Thermo-Optische Molekülmanipulation

Stefan Duhr

Dissertation
an der Fakultät für Physik
der Ludwig-Maximilians-Universität
München

vorgelegt von
Stefan Duhr
aus Dinslaken

München, den 11. April 2007

Erstgutachter: Prof. Dr. Hermann E. Gaub

Zweitgutachter: Prof. Dr. Joachim Rädler

Tag der mündlichen Prüfung: 14.06.07

Inhaltsverzeichnis:

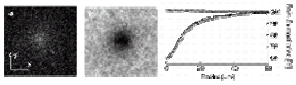

Publikation I, Seite 44
Stefan Duhr, Silvia Arduini and Dieter Braun
Thermophoresis of DNA determined by microfluidic fluorescence
Europ. Phys. J. E 15, 277-286 (2004)

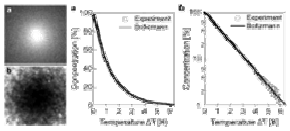

Publikation II, Seite 55
Stefan Duhr and Dieter Braun
Thermophoretic Depletion Follows Boltzmann Distribution
PRL 96, 168301 (2006)

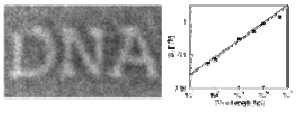

Publikation III, Seite 60
Stefan Duhr and Dieter Braun
Why molecules move along a temperature Gradient.
PNAS, 103, 19678-19682 (2006)

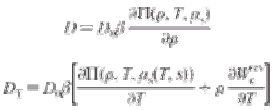

Publikation IV, Seite 66
Jan K. G. Dhont, Simone Wiegand, Stefan Duhr
and Dieter Braun
Thermodiffusion of Charged Colloids: Single Particle Diffusion
Langmuir 23 (4), pp. 1674-1683 (2007)

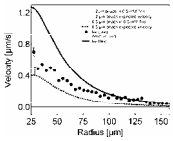

Publikation V, Seite 77
Stefan Duhr and Dieter Braun
Thermophoresis beyond local equilibrium
Physical Review Letters, eingereicht

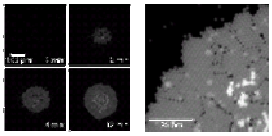

Publikation VI, Seite 86
Stefan Duhr and Dieter Braun
Two-dimensional colloidal crystals formed by thermophoresis and convection
Applied Physics Letters 86, 131921 (2005)

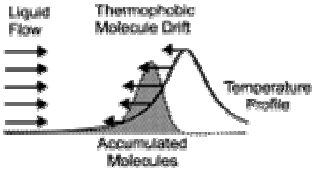

Publikation VII Seite 90
Stefan Duhr and Dieter Braun
Molecule accumulation by opposing fluid flow with thermophoretic drift
Physical Review Letters 97, 038103 (2006)

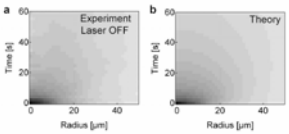

Publikation VIII, Seite 95
R. A. Sperling, T. Liedl, S. Duhr, S. Kudera, M. Zanella, C.-A. J. Lin, W. Chang, D. Braun, W. J. Parak
Size determination of (bio-) conjugated water-soluble colloidal nanoparticles - a comparison of different techniques
J. Phys. Chem. C, akzeptiert (2007)

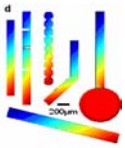

Publikation IX, Seite 104
Philipp Baaske, Franz Weinert, Stefan Duhr, Kono H. Lemke, Michael J. Russel and Dieter Braun
Extreme Accumulation of Nucleotides in Simulated Hydrothermal Pore Systems,
PNAS, 104, 9346–9351 (2007)

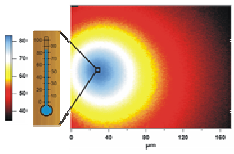

Publikation X, Seite 111
Philipp Baaske, Stefan Duhr and Dieter Braun
Melting Curve Analysis in a Snapshot
Applied Physics Letters, in Vorbereitung

Zusammenfassung

Seit mehr als 150 Jahren ist bekannt, dass Temperaturgradienten zu einer gerichteten Molekülbewegung führen. Jedoch ist deren Ursache in Flüssigkeiten bis heute umstritten. Ziel dieser Doktorarbeit ist es, einen Beitrag zum Verständnis der Wirkung von Temperaturgradienten auf Moleküle in Flüssigkeiten zu leisten und die gewonnenen Erkenntnisse in biotechnologische Anwendungen zu überführen. Die in dieser Arbeit entwickelte mikroskopische Theorie der Thermophorese basiert auf einem lokalen Gleichgewichtsansatz.

Der durch einen Temperaturgradienten induzierte Massefluss beruht demnach auf einer Maximierung der Solvatationsentropie eines Moleküls. Die Theorie ermöglicht die Vorhersage der Thermophorese von sehr unterschiedlichen Molekülen wie sphärischen Polystyren-Partikeln und flexiblen DNA-Polymeren.

Experimentell werden die Temperaturgradienten rein optisch durch Infrarot-Laser-Strahlung erzeugt, und die thermophoretische Molekülbewegung wird fluoreszenzmikroskopisch nachgewiesen und quantifiziert. Dieser Ansatz ermöglichte es erstmals den Drift einzelner Molekülen in Temperaturgradienten zu beobachten.

Es zeigte sich, dass selbst kleinste Moleküle mit einem Gewicht von nur wenigen Dalton mittels Temperaturverteilungen in Lösung beeinflusst werden können. Wie stark die erzeugte Konzentrationsänderung ist, hängt von molekularen Eigenschaften wie Ladung, Oberflächenchemie und Größe ab. Diese Sensitivität soll zukünftig den Nachweis von Interaktionen und Strukturänderungen von Biomolekülen durch Thermophorese ermöglichen.

In dieser Arbeit wird außerdem eine Anwendung vorgestellt, die die Relaxation eines thermophoretisch aufgebauten Konzentrationsgradienten nutzt, um die Diffusions-Koeffizienten gelöster Partikel zu bestimmen. Dadurch wird es möglich, den hydrodynamischen Radius von Molekülen in Lösungen schnell und präzise zu bestimmen, ohne dass besondere Ansprüche an die Konzentration oder Reinheit der Probe gestellt werden.

Weiterhin werden verschiedene Ansätze beschrieben, mit deren Hilfe Moleküle durch eine Kombination aus gerichteter Flüssigkeitsbewegung und thermophoretischer Drift stark angereichert werden können.

Temperaturverteilungen lassen sich jedoch auch ohne eine induzierte Molekülbewegung verwenden, um Informationen über Biomoleküle zu gewinnen. Die optisch erzeugten Temperaturgradienten liegen fast instantan vor, während die thermophoretische Drift in einem längeren Zeitintervall stattfindet. Diese

Tatsache kann genutzt werden um schnelle biochemische Reaktionen wie das Schmelzen von Doppelhelices zu messen und kinetische und thermodynamische Parameter zu bestimmen.

Abstract

The Soret effect in aqueous soutions is known for more than 150 years now, but the microscopic mechanism behind it remains elusive. The aim of this work is to contribute to the ongoing debate by deriving a general explanation for the directed motion of molecules in liquids induced by temperature gradients. Since systems with an inherent temperature gradient are clearly dissipative in nature no thermodynamic potentials are applicable. However, a nonequilibrium system can be devided in sub volumes for which thermodynamic variables are locally defined. The local equilibrium theory presented here directly connects the entropy of solvation to the drift of particles in a temperature field. In this sense particles drift to maximize the respective entropy of their interaction with the solvent.

The experimental setup used throughout this work makes use of an infrared laser to heat aqueous solutions. The dissolved molecules are detected optically by fluorescence microscopy. This all optical setup made it possible to collect high quality data for a broad set of different molecules.

It can be stated that it is possible to manipulate even very small molecules with optically induced temperature gradients. This sets the stage for new ways of molecule accumulation and characterisation. In the appendix of this work beside the publication on theory the first published examples for applications of thermophoresis in the field biological sciences are presented.

1 Einleitung

Temperaturgradienten in Lösungen oder Gasen führen nicht nur zu einem Wärmefluss, sondern auch zu einem Molekülfluss, der Konzentrationsgradienten erzeugt. Die Kopplung von einem Materietransport an einen Wärmefluss ist auch unter dem Namen Thermophorese, Thermodiffusion oder Ludwig-Soret-Effekt bekannt. Bereits im Jahr 1856 publizierte Carl Ludwig unter dem Titel „Diffusion zwischen ungleich erwärmten Orten gleich zusammengesetzter Lösungen“ den ersten Aufsatz, der sich der Thermodiffusion widmete [*Ludwig 1856]*. Aus ersten systematischen Experimenten von Charles Soret wurden 20 Jahre später die bis heute verwendeten Arbeitsgleichungen abgeleitet *[Soret 1879]*. Obwohl die frühen Arbeiten die Thermophorese in Flüssigkeiten beschrieben, wurde die erste Theorie für Gase entwickelt, noch bevor Chapman im Jahre 1917 den experimentellen Nachweis erbrachte *[Chapman 1917]*. Die mikroskopische Ursache für dieses Phänomen in Flüssigkeiten blieb dagegen weiter unklar und wird bis heute stark debattiert. Viele Klärungsansätze beruhen dabei auf hydrodynamischen Kräften, die auf Grund eines temperaturbedingten Energiegradienten an der Oberfläche von gelösten Partikeln auftreten [*Brenner 2006, Dhont 2004, Parola 2004, Piazza 2002, Rauch 2002, Ruckenstein 1981, Schimpf 2000*]. Allerdings ist auf diese Weise nicht gelungen eine Beschreibung zu finden, die in der Lage ist alle experimentellen Ergebnisse zu Thermophorese in Flüssigkeiten zu erklären. Da sich Systeme, in denen thermophoretische Drift stattfindet, nicht im Gleichgewicht befinden, wurden thermodynamische Ansätze bis auf wenige Ausnahmen nicht in die Betrachtungen mit einbezogen. Dieses kann auch damit begründet werden, dass die Entwicklungen in der klassischen Thermodynamik sich lange Zeit weitestgehend auf die Beschreibung von reversiblen Prozessen beschränkten. Systeme mit Temperaturgradienten sind per Definition dissipativ und daher nur eingeschränkt mit Methoden der Gleichgewichtsthermodynamik zu analysieren. Es zeigt sich jedoch, das viele Nicht-Gleichgewichtssysteme unter der Annahme, dass sich kleinste Teilvolumen im thermischen Gleichgewicht befinden, mit thermodynamischen Methoden beschreiben lassen *[Astumian 2006, Prigogine 1999]*. In der Vergangenheit zeigte sich, wie schwer es ist, eine einheitliche mikroskopische Theorie für den thermophoretischen Transport zu finden *[Wiegand 2006]*. In dieser Arbeit wurde mittels Fluoreszenzmessung, Mikrofluidik und lokalen Temperaturverteilungen auf der Mikrometerskala eine breite und verlässliche Datenbasis der Thermophorese in wässrigen Lösungen gebildet. Dieses hat es ermöglicht, eine

auf lokalem Gleichgewicht basierende mikroskopische Theorie der Thermophorese zu entwickeln, die generell das Verhalten von geladenen oder ungeladenen Molekülen in Flüssigkeiten beschreibt (**Publikation III**). Die Untersuchung von Thermophorese auf Basis eines solchen lokalen Gleichgewichtes kann auch zu Erkenntnissen über den Zusammenhang zwischen Gleichgewicht, lokalem Gleichgewicht und Nicht-Gleichgewicht führen. Auf Basis einer allgemein gültigen Theorie soll Thermophorese zur Manipulation und Charakterisierung von Biomolekülen eingesetzt werden.

2 Thermophorese im Fluoreszenzmikroskop

Durch die Kombination von Fluoreszenzmikroskopie und optisch implementiertem Heizen durch Infrarot-Laser (IR-Laser) ist es möglich, den thermophoretischen Massentransport mit hoher Präzision auf Einzelmolekülebene zu analysieren.

Aufgrund ihrer häufigen Anwendung in den Biowissenschaften sind Fluoreszenzmethoden etabliert und es steht eine breite Auswahl an Modellsystemen zur Verfügung. Diese reichen von sphärischen Polystyren-Partikeln über vergleichsweise kleine fluoreszenzmarkierte DNA-Moleküle bis hin zu Nanokristallen. Gleichzeitig können Experimente bei geringer Probenkonzentration (1 nM – 1 µM) durchgeführt werden, wodurch intermolekulare Wechselwirkungen weitestgehend ausgeschlossen werden können.

Die Fluoreszenzdetektion der Moleküle und die optische Manipulation durch einen Temperaturgradienten finden auf einer Längenskala von wenigen hundert Mikrometern statt. Dadurch kann der gesamte Messbereich mit hoher Auflösung auf eine CCD-Kamera abgebildet werden. Ursachen für Messartefakte wie z.B. Verunreinigungen können mit dieser Messanordnung sofort erkannt werden.

Durch die Verwendung von dünnen mikrofluidischen Messkammern können Nebeneffekte der Temperaturverteilung wie die Konvektion effektiv unterdrückt werden, so dass die thermophoretisch etablierten Konzentrationsgradienten nicht beeinflusst werden. Zusätzlich erlauben die dünnen mikrofluidischen Strukturen eine zweidimensionale Beschreibung der Messkammer. Der im Folgenden vorgestellte Aufbau wird detailliert in **Publikation I** beschrieben.

2.1 Optische Detektion

An einem Standard Fluoreszenzmikroskop, dem AxioTech Vario (Zeiss AG, Jena), werden verschiedene Modifikationen vorgenommen. Als Beleuchtungsquelle wird eine Hochleistungs-LED (Light Emitting Diode, LXHL-LX5C, Luxeon) mit einer zentralen Anregungswellenlänge von 500 nm verwendet, die in das Gehäuse einer Halogenlampe eingebaut ist und mit einer Stromversorgung (ILX Lightwave LD-3565) bei 30-700 mA betrieben wird. Die LED hat bei 500 nm eine etwa 5x geringere Intensität als die verwendete Halogenlampe, ist dafür aber wesentlich rauschärmer. Insbesondere bei kurzen Belichtungszeiten ist die zeitlich stabile LED-Anregung von Vorteil. Die

Anregungs- und Emissionsfiltersätze für FITC und Cy-3 Fluoreszenz wurden von AHF Analysetechnik bezogen (F41-001 (*HQ 480/40, Q 505 LP, HQ 535/50*); F41-007 (*HQ 545/30, Q 570 LP, HQ 610/75*)).

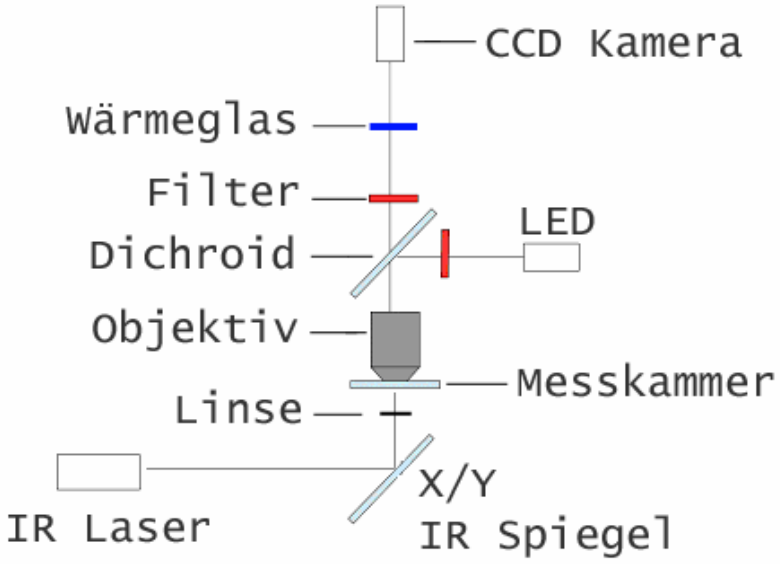

Abbildung 1. Optischer Aufbau. Die Abbildung zeigt eine Skizze des fluoreszenzmikroskopischen Aufbaus. Die Fluoreszenz wird durch eine LED über ein Objektiv in der Messkammer angeregt. Die Abbildung der Fluoreszenz auf die CCD-Kamera erfolgt über dasselbe Objektiv, einen Strahlteiler (Dichroid), Filtersätze und ein Wärmeglas (IR-Filter). Von der Unterseite der Messkammer wird ein Infrarotlaser über zwei spannungsgesteuerte Spiegel mittels einer Linse in die Kammer fokussiert.

Das Anregungslicht wird über einen Strahlteiler durch das verwendete Objektiv in die Kammer fokussiert. Die in dieser Arbeit verwendeten Objektive sind ein 40x Öl Immersions (Fluor NA:1.3, Zeiss) und ein 32x Luft Objektiv (LD-A-Plan NA:0.4, Zeiss), die als gut korrigierter Kondensor dienen. Die langwelligere Fluoreszenz wird über das Objektiv auf eine CCD-Kamera abgebildet (Sensicam qe, PCO). Der CCD-Chip besitzt 1376x1040 Pixel mit einem variablen Binning von bis zu 16x8 Pixel. Ohne Binning wird bei Verwendung eines 40x Objektivs ein Bereich von ca. 160x160 nm auf einen Pixel abgebildet. Bei maximalem Binning können 48 Bilder pro Sekunde aufgenommen werden. So ist es möglich, selbst die Kinetik schneller Transportprozesse zu analysieren. Die spektrale Sensitivität liegt zwischen 260 nm und 1100 nm, wobei die maximale Quanteneffizienz von 60% bei 500 nm liegt. Typischerweise wird ein Probenbereich von 400x400µm abgebildet.

Unterhalb der Messkammer ist eine IR-Laser-Scan Einheit eingebaut, über die ein Infrarot-Laser in die Kammer fokussiert werden kann. Zum Schutz der CCD-

Kamera vor der infraroten Strahlung des Lasers wird ein Wärmeglas im Strahlengang eingebaut (Abbildung 1).

2.2 Optisches Heizen

Lokales und kontaktfreies Heizen wird durch die Fokussierung von IR-Laser-Strahlung in eine wässrige Lösung realisiert. Wellenlängen im infraroten Bereich, also von mehr als etwa 1 µm, sind bei den verwendeten Leistungen nicht energiereich genug, um elektronische Übergänge in Molekülen zu erzeugen. Die Absorption dieser Strahlung hebt, abhängig von der Wellenlänge, Elektronen auf verschiedenste Schwingungsenergieniveaus. Das Dipolmoment ist dabei ein Maß für die Fähigkeit eines Moleküls, mit der elektromagnetischen Strahlung in Wechselwirkung zu treten. Zur Absorption von IR-Strahlung muss die zu induzierende Schwingung das Dipolmoment des Moleküls verändern. Dieses ist bei den meisten asymmetrischen Molekülen der Fall. Das H_2O Molekül absorbiert auf Grund seiner strukturellen Asymmetrie sowie des starken Dipolmomentes ($6.1 \cdot C/m$) sehr stark IR-Strahlung von mehr als 1000 nm Wellenlänge. Aus dem Lambert-Beer-Bouguer Gesetz $I/I_0 = \exp(-\alpha \cdot d)$ folgt, dass bei einem Absorptionskoeffizienten α von 3400 m^{-1} bei 1480 nm die Intensität beim Durchgang durch Wasser innerhalb einer Strecke d =350 µm auf 30% ($1/e$) abgefallen ist (Abbildung 2). Die Absorptionslänge ist für das Design der Messkammern von großer Bedeutung, da sie in den meisten Fällen ein oberes Limit für die Höhe der Kammern vorgibt. Kammern, die wesentlich dünner als die Absorbtionslänge sind garantieren, dass das Wasser entlang der Lasereinfallsrichtung homogen geheizt wird.

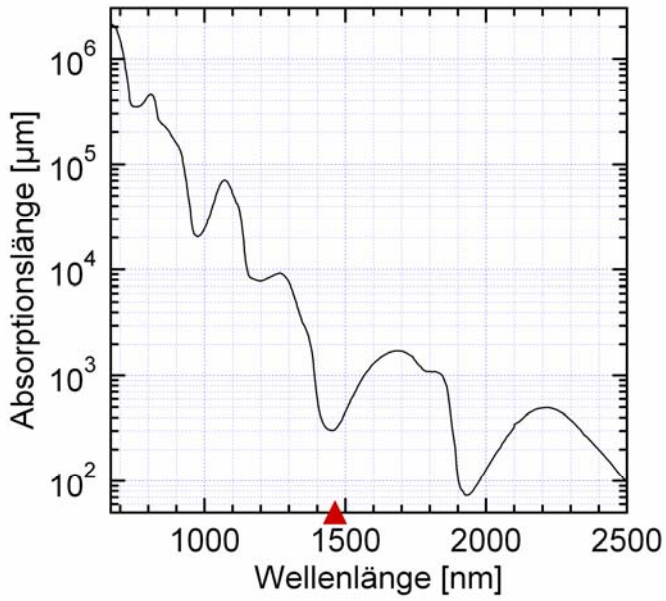

Abbildung 2. Wellenlängenabhängigkeit der Absorptionslänge in Wasser. Im infraroten Wellenlängenbereich steigt der Absorptionskoeffizient stark an. Die Absorptionslänge sinkt dadurch auf 350 µm bei 1480 nm (rot). Innerhalb dieser Länge werden etwa 70% der Laserleistung absorbiert.

Als IR-Strahlungsquellen wurden Laser zweier unterschiedlicher Leistungsklassen verwendet.

Für Messungen, in denen eine wässrige Lösung lokal auf etwa 20 K über Raumtemperatur aufgeheizt werden soll, wird ein 320 mW Dioden-Laser mit einer zentralen Wellenlänge von 1480 nm (FOL1405-RTV-317, CW, Furukawa) verwendet. Die Leistung und Kühlung des Lasers werden durch ein ILX-Lightwave LDC-3744B Modul reguliert. Die Spannung wird mit einer digital-analog Firewire basierten I/O-Karte (DAQPAD-6070E) kontrolliert werden. Für Temperaturerhöhungen über 20 K wird ein Raman-Faser-Laser (Raman Fibre Laser, cw, IPG Laser) bei 1450 nm verwendet. Dieser Dioden gepumpte Ytterbium Festkörperlaser emittiert zwischen 1050 nm und 1120 nm. Diese Strahlung wird durch einen Raman-Effekt zu längeren Wellenlängen verschoben.

Aus beiden Lasern wird die Strahlung mittels einer single-mode Faser ausgekoppelt. Die bei einer Numerischen Apertur von 0.1 mit etwa 6° leicht divergent aus der Faser austretende Strahlung wird mittels eines Kollimators auf ein 1 mm breites Strahlprofil parallelisiert ($\exp(-2) \approx 13\%$). Die IR-Strahlung wird von der Unterseite, also gegenüber der Detektions/Illuminations Seite in die Messkammer eingekoppelt. Dieses ermöglicht eine von der Detektion unabhängige Wahl der optischen Komponenten für die Laserpositionierung und Laserfokussierung. Standardmäßig wird der Laser über eine Linse (C240TM-C,

Thorlabs) mit einer Numerischen Apertur von 0.5 und Brennweite von 8 mm in die Messkammer fokussiert. Da nur etwa 1/8 der gesamten Linse ausgeleuchtet wird, ergibt sich nach $\omega_0 \approx f\lambda / D$ ein minimaler Gausscher-Strahlradius von ω_0 $\approx$10 µm ($\exp(-2)$). Aus dem Rayleigh-Kriterium $z_0 = 2\pi\omega_0^2 / \lambda$ ergibt sich eine Fokustiefe von 250 µm. Der Strahlradius nimmt innerhalb dieser Länge auf $\sqrt{2}\omega_0$, also um etwa 4 µm zu. Experimentell lässt sich die Temperaturverteilung durch eine stärkere Ausleuchtung der Linse ebenso wie durch einen Verschub des Fokus mittels eines z-Translationselementes beeinflussen.

Zwei IR-Strahlung reflektierende spannungsgesteuerte Spiegel (Cambridge Technology 6200-XY Scanner, Driver 67120) erlauben die Mikrometer genaue Positionierung des Lasersfokus in der X/Y-Ebene der Messkammer. Der Winkel, mit dem die IR-Strahlung auf die Linse trifft, wird in eine laterale Positionsänderung des Fokus umgesetzt.

2.3 Messkammern

Um die Vorteile der rein optischen Thermophoresemessung nutzen zu können, ist die Messkammergeometrie von entscheidender Bedeutung. Die Absorptionslänge des IR-Lasers und die Unterdrückung der Konvektion sind dabei, neben der Fokustiefe, die entscheidenden Kriterien für die optimale Kammerhöhe in Lasereinfallsrichtung (z-Richtung). Diese sollte weit unterhalb der Absorptionslänge von 350 µm liegen, da nur so die Leistungsabnahme beim Durchlaufen der Probe vernachlässigbar ist. Gleichzeitig nimmt mit zunehmender Schichtdicke auch die Geschwindigkeit der Konvektion stark zu. Simulationen zeigen, dass die maximale Konvektionsgeschwindigkeit in 10 µm hohen Kammern bei Temperaturerhöhungen von 1-2 K unter 100 nm/s liegt (siehe Publikation I, Fig. 3). Auch der Zusammenhang zwischen Konzentration und gemittelter Fluoreszenzintensität ist nur als linear anzunehmen, wenn die Kammerhöhe wesentlich geringer ist als die Gaussche-Fokustiefe des Objektivs. Dieses liegt beispielsweise für das häufig verwendete 32x Luft Objektiv bei σ = 680 µm [Braun 2002].

Beim Design der Mikrofluidik ist neben der Konvektion auch noch die Lösungsmittelverdunstung als Quelle für eine ungewollte Flüssigkeitsbewegung zu beachten.

2.3.1 Herstellung der Stempelstrukturen

Ein Material, welches wegen seiner guten Handhabbarkeit häufig Anwendung zur Herstellung von mikrofluidischen Messkammern findet, ist das auf Silikon basierende Polymer Poly-(dimethylsiloxan) (PDMS, Sylgard 184, Dow Corning). Es ist im sichtbaren Spektralbereich und auch bei Wellenlängen im infraroten Bereich transparent.

Um die Mikrofluidikkammern herzustellen, werden aus PDMS negative Abdrücke einer Stempelstruktur erstellt. Die Stempel werden im Reinraum aus SU-8 Photolack (Epoxid Harz, Microchem Corp.) mittels eines sog. Spin-Coaters auf einen 4-Zoll einseitig polierten Silizium-Wafer aufgebracht. Die Höhe der Struktur wird durch die Viskosität des Photolacks (SU-8 2; SU-8 10) und die Rotationsgeschwindigkeit zwischen 5 und 20 µm variiert (Tabelle 1). Im ersten Schritt des zweistufigen Spin-Coatings werden 3 ml des Photolacks zentral auf den rotierenden Wafer gegeben.

Höhe	SU-8	V (ml)	1.Schritt	t(s)	2.Schritt	t(s)
5 µm	SU-8 2	3 ml	500 rpm	20 s	750 rpm	30 s
10 µm	SU-8 10	3 ml	1000 rpm	20 s	4000 rpm	30 s
100 µm	SU-8 10	3 ml	600 rpm	20 s	600 rpm	30 s

Tabelle 1: Parameter für das Aufbringen des Photolacks auf einen 4 Zoll Wafer mit anschließendem Spin Coating. Um verschiedene Höhen des SU-8 Harzes zu erreichen wurden Photolacke mit unterschiedlicher Viskosität bei vorher kalibrierten Umdrehungsgeschwindigkeiten des Spin-Coaters verwendet.

Nach dem Aufbringen des Photolackes wird dieser 2 min bei 50°C auf einer Heizplatte vorgeheizt, innerhalb von 4 min auf 90°C erhitzt und 1 min bei 90°C gehalten. Um Spannungsrisse durch zu schnelles Abkühlen zu vermeiden, wird der Wafer auf einem Textiltuch noch 1 min bei 90°C auf der Heizplatte belassen und dann eine Stunde bei 40°C in einen Umluftofen gegeben. Zur Belichtung des Photolackes wird ein Karl Suss MA4 mit einer Wellenlänge 350 nm (Quecksilber Bande) bei 21 mW/cm^2 verwendet. Die Maske wurde mit einer Auflösung von 5000 dpi auf eine transparente Folie gedruckt (Farbsatz, München). Dieses erlaubt Auflösungen von 1-2 µm Genauigkeit. Die Folie wird mit der bedruckten Seite auf den Wafer gelegt und mit einer Glasplatte beschwert, um guten Kontakt zu gewährleisten. Das SU-8 Harz wird 80 s (5 µm und10 µm) oder 120 s (100 µm) belichtet. Der beschriebene Heizprozess wird erneut durchgeführt und der Wafer anschließend für 120 s in die erste und dann für 120 s in eine weitere SU-8 Entwicklerlösung getaucht. Die Reste von Entwickler und Photolack werden bei 500 rpm für 20 s mit Isopropanol abgewaschen. Die entstandenen stabilen, positiven Strukturen sind in Abbildung 4 gezeigt.

2.3.2 Herstellung der Mikrofluidik

Die eigentlichen Mikrofluidikkammern werden aus dem negativen PDMS-Abdruck der SU-8-Struktur hergestellt. Dazu werden 30 ml einer 20:1 Mischung aus PDMS und dem zugehörigen Vernetzungsagens in einen Exikator gegeben und für 30 min bei 0.2 mbar entgast. Der Wafer wird in eine nur wenig größere Zellkulturschale (Carl-Roth GmbH, Karlsruhe) gelegt, und das entgaste PDMS wird darüber gegossen. Aus dem verwendeten Volumen ergibt sich eine PDMS-Schichtdicke von etwa einem Zentimeter. Die Schale wird verschlossen und für 2 Stunden bei 60°C in einen Inkubationsofen gestellt, wo die temperaturinduzierte Polymerisation beginnt. Nachdem etwa 1 Stunde der Inkubationszeit verstrichen ist, wird zusätzlich noch eine 5:1 PDMS-Mischung auf dieselbe Weise angesetzt. Davon wird 1 ml auf 24x40 mm Deckgläser (Carl-Roth GmbH, Karlsruhe) gegeben, und das Polymer wird mittels eines Spin-Coaters bei 600 rpm (30 s) und 2000 rpm (30 s) auf dem Deckglas verteilt. Dieses Protokoll ist anhand der Dichte des PDMS auf 10 µm Schichtdicke kalibriert worden. Das PDMS auf den Deckgläsern wird anschließend für 15 min bei 70°C leicht polymerisiert.

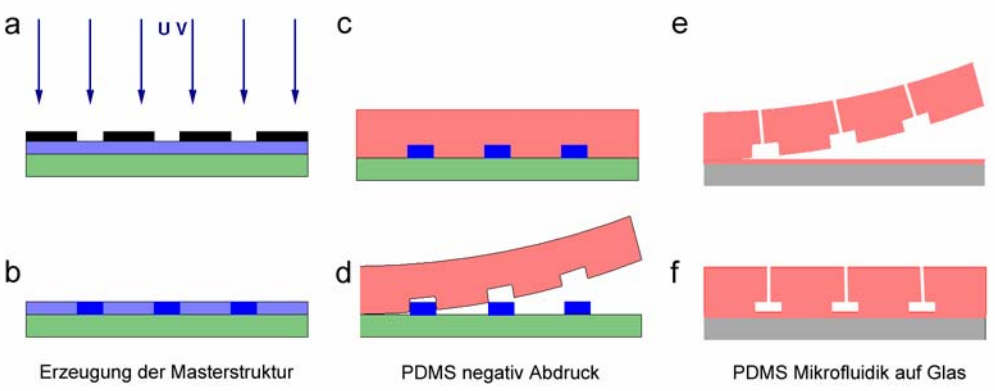

Abbildung 3. Herstellung der Mikrofluidik Stempelstrukturen. (a)Auf einen Silizium-Wafer (grün) wird SU-8 Photolack aufgetragen (hellblau). (b) Durch eine Maske (schwarz) wird der Lack mittels UV Strahlung ausgehärtet (dunkelblau). (c) Der nicht ausgehärtete Photolack wird abgewaschen und auf die verbleibende Stempelstruktur wird PDMS (rot) gegeben. (d) Das ausgehärtete PDMS wird vom Stempel entfernt. (e,f) Mit einer Kanüle werden die Zuflüsse für das Befüllen der Messkammer hergestellt und der PDMS-Block auf ein ebenfalls mit PDMS beschichtetes Deckglas (grau) gegeben.

Die negativen PDMS-Abdrücke der Mikrofluidikstruktur werden mit einem Skalpell ausgeschnitten, die Kanäle mit einer Kanüle von der Innenseite her angestochen und der Abdruck auf ein Deckglas gegeben. Das nicht vollständig ausgehärtete PDMS verbindet die beiden Hälften augenblicklich miteinander, so dass sich ein

geschlossener Mikrofluidik-Chip ergibt, der über die durch die Kanüle gestochenen Kanäle von außen zu befüllen ist (Abbildung 3). Um eine durch Verdunstung induzierte Drift zu unterdrücken, haben sich einseitig geöffnete Messkammern bewährt (Abbildung 4). Diese können unter leichtem Überdruck befüllt werden, da das ausgehärtete PDMS für Gase durchlässig ist. Das Verdunsten der Flüssigkeit wird verhindert, indem der Zufluss mit Immersionsöl verschlossen wird.

2.3.3 Spezielle Mikrofluidik

Die unter 2.3.2 beschriebenen Mikrofluidik-Kammern zeichnen sich durch eine gute Reproduzierbarkeit der Höhe aus. Gleichzeitig sind die Temperaturen durch die geringe Wärmeleitfähigkeit des PDMS ($\lambda_{PDMS} = 0.18 \cdot W/mK$) selbst bei Schichtdicken um 10 µm weitgehend homogen in z-Richtung (Abbildung 5). Allerdings sind PDMS Oberflächen sehr hydrophob, was zu einer starken Wechselwirkung mit Polystyren-Partikeln führt. Die Thermophorese reagiert sehr empfindlich auf äußere Faktoren wie die Salzkonzentration und Lösemittelzusammensetzung *[Wiegand 2006]*. Daher ist die Veränderung der Oberflächeneigenschaften der Kammer mittels chemischer Modifikation nicht möglich, da die einseitig befüllbaren Kammern nur schwer zu spülen sind.

Daher wurden für das Modellsystem der Polystyren-Partikel Mikrofluidik-Kammern so hergestellt, dass sich deren Hydrophobizität sich mittels eines Plasmareinigers verringern lässt.

Die Kammern werden erstellt indem ein definiertes Volumen auf eine 1 mm dicke Polystyrenschale (PS) (Zellkulturschale, Carl-Roth GmbH, Karlsruhe) gegeben wird. Anschließend wird ein quadratisches Deckplastik (ibidi GmbH, München) von 10 mm Kantenlänge und 150 µm Dicke darauf gelegt. Die Flüssigkeit verteilt sich gleichmäßig und die so entstandene Kammer wird mit Nagellack verschlossen, um Drift durch verdunstendes Wasser zu verhindern. Die Kammerhöhen werden durch das Flüssigkeitsvolumen definiert. Im Zentrum lassen sich die Höhen zwischen 10 µm und 20 µm mit einer Genauigkeit von etwa 10% reproduzieren (siehe Publikation I, Fig. 1). Die Oberflächen werden vor der Erstellung der Kammer 10 min im Plasmareiniger (Harrick, 10 W, 0.2 mbar) behandelt, um sie ausreichend hydrophil zu machen.

Für Untersuchungen der Interaktion zwischen einem Konvektionsstrom und dem thermophoretischem Fluss (**Publikation VI**) werden Kammern mit Höhen von bis zu 500 µm benötigt.

Dazu wird ein Abstandhalter aus Silikon (McMaster, New York) von 500 µm Dicke auf einen Objektträger gelegt. Die Messkammer wird mit ausreichend Flüssigkeit gefüllt und mit einem Deckglas verschlossen (siehe Publikation VI, Fig. 1). Eine weitere Abdichtung hat sich in diesen Fällen als unnötig erwiesen.

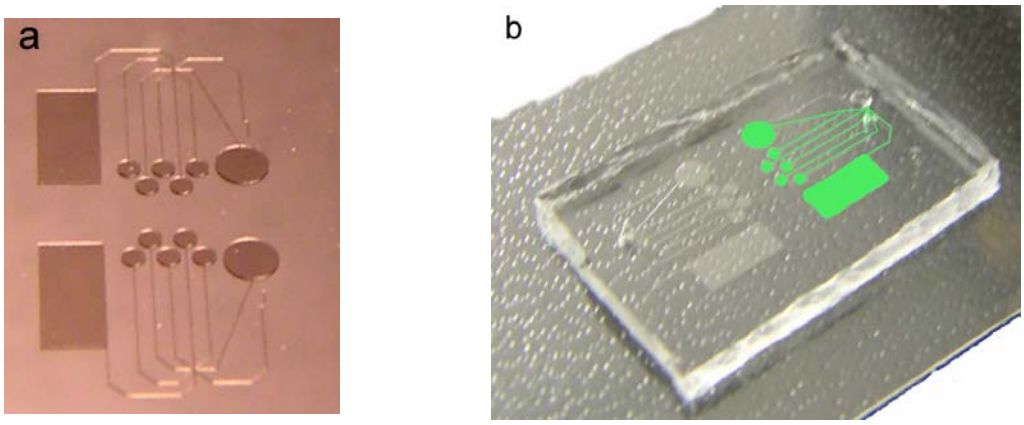

Abbildung 4. Beispiel einer SU-8 Stempelstruktur und Mikrofluidik Kammer. (a) Eine 10 µm hohe SU-8 Struktur ist auf einem Silizium-Wafer aufgebracht worden. (b) Im zugehörigen PDMS-Abdruck entstehen zwei einseitig offenen Kanal-/Kammersysteme. Die IR Strahlung wird von der hier oben liegenden Seite in die Kammern fokussiert. Die Fluoreszenzmessung findet durch dass dünne Deckglas der gegenüberliegenden Seite statt.

2.4 Fluoreszenzmessungen

Die präzise Bestimmung der räumlichen Verteilung von Temperatur und Konzentration ist entscheidend für die Charakterisierung der thermophoretischen Eigenschaften von Molekülen. Die Temperatur wird anhand der temperaturabhängigen Fluoreszenz des Farbstoffes BCECF (B-1151 mixed isomers, Molecular Probes) in 10 mM Tris-Puffer bestimmt, die in einer unabhängigen Fluorimetermessung kalibriert worden ist. Zusätzlich zur Temperaturabhängigkeit wird auch die Thermophorese der Farbstoffmoleküle selbst berücksichtigt.

Die relative Konzentration ist direkt proportional zur Fluoreszenz der markierten Moleküle. Allerdings muss auch hier eine Temperaturabhängigkeit des Fluoreszenzmarkers in die Bestimmung des Konzentrationsgradienten miteinbezogen werden.

Vor Beginn einer quantitativen Auswertung wird noch eine Korrektur der inhomogenen Anregungsverteilung vorgenommen. Die LED als Lichtquelle hat

den Vorteil eines zu Quecksilberdampflampen vergleichsweise sehr geringen Rauschens. Sie erzeugt jedoch eine räumlich variierende Anregungsintensität, da es sich nicht um eine perfekte punktförmige Lichtquelle handelt. Experimentell werden räumliche Intensitätsschwankungen von etwa 10% auf etwa 200 µm gemessen, die nicht auf Änderungen der Schichtdicke zurückzuführen sind. Daher wird die Fluoreszenz eines jeden Pixels zu Beginn einer Messung auf 100% Konzentration bzw. Raumtemperatur normiert.

Auch an der zeitlichen Entwicklung der Intensitätsverteilung müssen meist leichte Korrekturen vorgenommen werden, da der Farbstoff im angeregten Zustand photochemisch zerstört wird. Dieses macht sich als lineare Abnahme der Fluoreszenz über die Zeit bemerkbar. Die Rate, mit der die Fluoreszenz abnimmt, ist Konzentrationsunabhängig und kann damit leicht aus den experimentellen Daten ermittelt und als lineare Korrektur hinzugefügt werden. Die Rate des Bleichens kann sowohl aus der Differenz zwischen Anfangs- und Endzustand als auch von Bild zu Bild bestimmt werden.

Zusätzlich wird die Hintergrundintensität der CCD-Kamera bei ausgeschalteter Anregungslichtquelle bestimmt und pixelspezifisch abgezogen.

Typische Messungen beinhalten daher eine Sequenz von „Dunkelbildern“ gefolgt von Bildern mit LED-Anregung zur Bestimmung des Fluoreszenzausgangslevels. Bei eingeschaltetem IR-Laser werden dann so lange Bilder aufgenommen bis sich das System im Fließgleichgewicht befindet. Nach Abschalten des Lasers wird das schnelle Auskühlen der Kammer, gefolgt von der langsamen Rückdiffusion der Moleküle, abgewartet. Daraus können Informationen über die Größe der Moleküle gewonnen werden.

2.4.1 Optische Temperaturbestimmung

Die Temperaturverteilung wird mit Hilfe des pH-sensitiven Fluoreszenzfarbstoffes BCECF bestimmt. Die Konzentration des Farbstoffes wird auf 50 µM in 10 mM Tris-HCl Puffer eingestellt. Veränderungen der Temperatur beeinflussen das Dissoziationsgleichgewicht des Puffers. Eine Erhöhung der Temperatur um 1 K verschiebt den pH-Wert des Puffers instantan um etwa -0.03 pH Einheiten. Die BCECF Fluoreszenz sinkt durch schnelle Protonenübertragung bei nicht zu starken Temperaturerhöhungen linear mit der Temperatur um -0.95%/K. Diese Temperaturabhängigkeit wurde durch eine unabhängige Messung in einem Fluorimeter bestimmt (siehe Publikation I, Fig. 1). Neben der Temperaturabhängigkeit geht auch noch die durch thermophoretische Drift

bedingte Konzentrationsänderung des Farbstoffes in die Fluoreszenzabnahme bei einer lokalen Temperaturerhöhung mit ein. Der Soret-Koeffizient, der die Stärke der Thermophorese im Fließgleichgewicht bestimmt, liegt für den Farbstoff BCECF unter den gegebenen Bedingungen bei S_T=0.003/K.

Durch Labview-Programme (National Instruments) wird aus der Fluoreszenzverteilung die Temperaturverteilung bestimmt. Dabei ist zu berücksichtigen, dass die gemessene Fluoreszenzintensität einen Kammermittelwert repräsentiert. Abhängig von der Höhe der Messkammer und der Temperaturleitfähigkeit des verwendeten Kammermaterials weicht die maximale Temperatur in der Kammermitte teils deutlich vom gemessenen Mittelwert ab (Abbildung 5).

Mit Hilfe der Finite-Elemente Simulations-Software (FemLab, Comsol) können die Bedingungen in der Mikrofluidik-Kammer in Abhängigkeit von verschiedenen Kammermaterialien simuliert werden. Details der Simulation sind in **Publikation I** beschrieben. Wie in Abbildung 5 gezeigt, ist auf Grund der geringen Wärmeleitfähigkeit im Falle von PDMS[1] die Temperatur weitgehend unabhängig von der Kammerhöhe. Glas[1] führt wegen der höheren Wärmeleitfähigkeit zu einem vergleichsweise starken Abfall der Temperatur an der Grenzfläche um 15%, verglichen mit der Maximaltemperatur in der Kammermitte. Saphir[1] führt die Wärme so gut ab, dass die Grenzfläche fast Umgebungstemperatur besitzt. Dieser starke Temperaturgradient an Oberflächen kann, wie in **Publikation VI** gezeigt, zur Anreicherung von Molekülen genutzt werden (siehe Publikation VI, Fig. 2) *[Braun 2002]*.

Zur Aufklärung der mikroskopischen Ursache des Soret-Effekts muss die thermophoretische Moleküldrift in Richtung der Oberflächen unterdrückt werden, da nur laterale Molekülbewegungen in ausreichendem Maße aufgelöst werden können. Um Temperaturgradienten in z-Richtung zu minimieren, werden daher Kunststoffe wie PDMS oder Polystyren als Kammermaterial verwendet.

[1] $\lambda_{PDMS} = 0.18 \frac{W}{m \cdot K}$, $\lambda_{glas} = 1.4 \frac{W}{m \cdot K}$, $\lambda_{saphir} = 34 \frac{W}{m \cdot K}$, $\lambda_{H_2 0} = 0.54 \frac{W}{m \cdot K}$

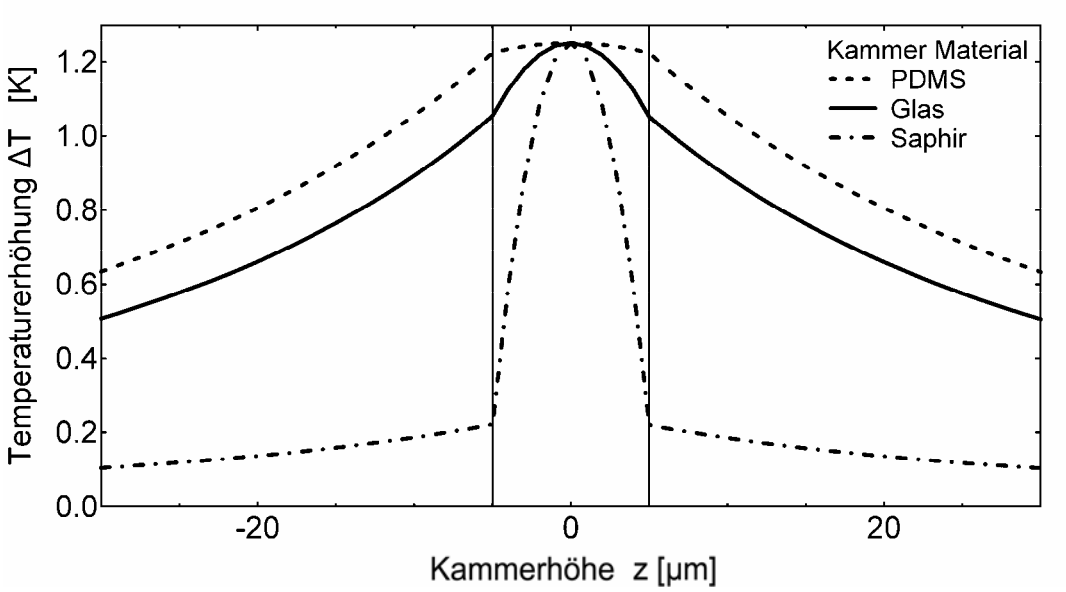

Abbildung 5. Temperaturprofile im Kammerquerschnitt. Während die laterale Temperaturverteilung durch die Wärmeleitfähigkeit des Wassers bestimmt wird, ist in z-Richtung das Kammermaterial von Bedeutung. Die Abbildung zeigt das parabolische Gleichgewichts-Temperaturprofil in einer 10 µm hohen Kammer in Abhängigkeit von der Wärmeleitfähigkeit des begrenzenden Materials. Im Fall von PDMS (und anderen Kunststoffen wie PS) ist die Temperatur im Kammerquerschnitt konstant.

2.4.2 Optische Konzentrationsbestimmung

Auch für die auf Fluoreszenz basierende Konzentrationsmessung gilt, dass die gemessene Konzentration einen Kammermittelwert darstellt. Da jedoch das Temperaturprofil in Lasereinfallsrichtung weitestgehend konstant ist, repräsentiert dieser Mittelwert sehr gut die Verhältnisse in der dünnen Flüssigkeitsschicht. Bei einer nur geringen Störung des Systems gleichen sich die Fehler durch die Höhenabhängigkeit von der Temperatur und der Konzentration aus (siehe Publikation I, Section 4). Die Abnahme der Fluoreszenz beruht neben der Konzentrationsänderung auch noch auf einer Temperaturabhängigkeit der Markerfluoreszenz. Da diese im Fluorimeter unabhängig bestimmt wurde, kann dieser Effekt bei bekannter Temperaturverteilung leicht korrigiert werden.

3 Transportphänomene im Lokalen Gleichgewicht

Viele Systeme sind nicht im thermischen Gleichgewicht. Die Erde selbst unterliegt der ständigen Einstrahlung von Energie durch die Sonne. Aber auch die meisten Systeme unter Laborbedingungen befinden sich im Nicht-Gleichgewicht, da die beobachteten Prozesse unendlich langsam ablaufen müssten, um reversibel zu sein. Ein Grund für den Erfolg der Gleichgewichtsthermodynamik in der Beschreibung dieser Systeme liegt darin, dass sich diese fast ausnahmslos in einem lokalen Gleichgewicht befinden.

3.1 Nicht-Gleichgewichtsthermodynamik

In dieser Arbeit wird ein lokaler Gleichgewichtsansatz verwendet, um eine mikroskopische Theorie für den thermophoretischen Massentransportes in einem Nicht-Gleichgewichtssystem zu entwickeln. Dieses bedeutet, dass die Temperatur und andere thermodynamische Variablen jeweils nur einem kleinen Teilvolumen des Systems zugeordnet werden *[Prigogine 1999]*. Die intensiven thermodynamischen Größen Temperatur (T), Druck (p) und chemisches Potential (μ) sind dadurch räumlich (x) und zeitlich (t) veränderlich:

(1) $$T = T(x,t) \qquad p = p(x,t) \qquad \mu = \mu(x,t)$$

Die extensiven Größen S (Entropie), U (Innere Energie) und N_k (Molenzahl) werden durch die jeweiligen Dichten s, u und n_k ersetzt. Die Gibbs-Relation $dU = TdS - Vdp + \sum_1^n \mu_n dN_k$ mit $U = Vu$, $S = Vs$ und $N_k = Vn_k$ besitzt dabei für kleine, miteinander in Kontakt stehende Volumenelemente weiterhin Gültigkeit.
Dieses wird durch Molekulardynamik-Simulationen unterstützt, die zeigen, dass die Maxwellsche Geschwindigkeitsverteilung sich etwa 10 mal schneller einstellt als die mittlere Zeit zwischen zwei Molekülkollisionen in einem Gas *[Alder 1958]* bei 1 bar Druck sind dies etwa 10^{-8} s. In Flüssigkeiten ist diese Zeitspanne noch wesentlich kürzer. Da Stöße mit gelösten Molekülen in einer ähnlichen Größenordnung stattfinden, ist anzunehmen, dass sich auch die Geschwindigkeitsverteilung der Atome des Soluten sehr im Gleichgewicht befindet. Daher müssen Störungen, die dazu führen, dass die Temperatur der Teilvolumen nicht mehr definiert ist, ebenfalls sehr schnell stattfinden.

Auch extensive Größen, wie die Anzahl der Gas-/Lösemittelmoleküle in kleinsten Volumenelementen, stützen die These des lokalen Gleichgewichtes. Die Fluktuationen der Zahl von Gas-/Lösungsmittelmolekülen in einem Volumenelement ist gegeben durch $\partial\widetilde{N} = \widetilde{N}^{1/2}$. Die relative Fluktuation $\partial\widetilde{N} / \widetilde{N} = \widetilde{N}^{-1/2}$ in einem Volumen von 1 µm^3 eines Gases bei 1 bar und 278 K ergibt sich zu 4x10^{-7}. In Flüssigkeiten entspricht dieser Wert noch einem wesentlich kleineren Volumen. Für die weitaus geringere Anzahl an Soluten in einer Lösung ist die Gültigkeit jedoch nicht offensichtlich. In **Publikation II** wird gezeigt, dass sich lokale Gleichgewichtsbedingungen auch bei geringen Konzentrationen gelöster Partikel anwenden lassen (siehe Publikation 2, Fig. 4).
Die Annahme eines lokalen Gleichgewichtes gilt für die meisten Systeme und verliert seine Gültigkeit erst, wenn die Gradienten, wie im Falle von Schockwellen, sehr stark sind oder die Volumenelemente eines Systems für gegebene Gradienten nicht klein genug definiert werden können.

3.2 Molekültransport durch Diffusion

Beispiele für Transportphänomene sind Diffusion, Wärmeleitung und Viskosität. In diesen Fällen führt der Gradient einer Größe zu einem Transport einer anderen. Eine räumlich inhomogene Temperatur führt zum Transport von Wärmeenergie, während ein Konzentrationsgradient zu einem Molekülfluss führt.
Die Diffusion entlang eines Konzentrationsgradienten wird als Ficksche Diffusion bezeichnet. Die Teilchenstromdichte $\vec{j}_n$ ist gegeben durch $\vec{j}_n = -D \cdot \nabla n$ mit dem Diffusions-Koeffizienten als Proportionalitätsfaktor zwischen Fluß und Konzentrationsgradient. Zur Beschreibung des thermophoretischen Molekültransports ist es sinnvoll, den diffusiven Transport auf der Basis von irreversiblen Prozessen und des chemischen Potentials zu beschreiben.
Irreversible Prozesse wie die Ficksche-Diffusion können durch thermodynamische Kräfte und thermodynamische Flüsse beschrieben werden *[Prigogine 1999]*. Die Entropieproduktion durch irreversible Vorgänge $d_i S$ ist dabei gleich dem Produkt aus Kraft (F) und Fluss (dX): $d_i S = F dX$. Im Folgenden soll die Entropieproduktion eines irreversiblen Prozesses anhand der Diffusion verdeutlicht werden.

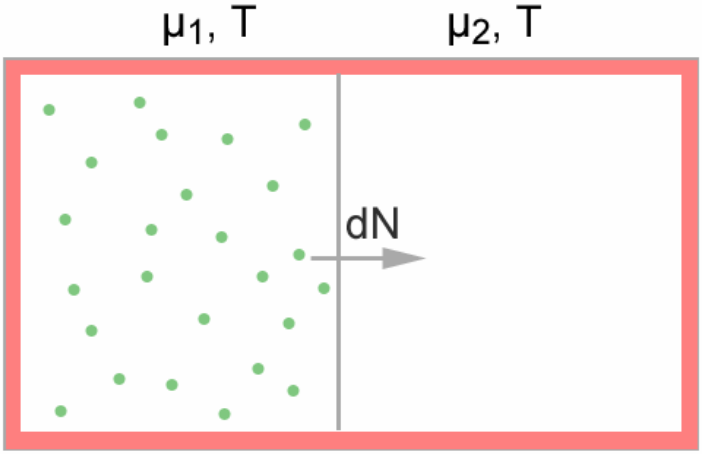

Abbildung 6. Diffusion als irreversibler Prozess. Der Übertritt von Partikeln in ein ehemals abgetrenntes Kompartiment gleicher Temperatur kann durch eine Reaktionsrate dN beschrieben werden. Ist das System isoliert, so kann die irreversible Entropieänderung des Systems auf das chemische Potential zurückgeführt werden.

Diffusion beschreibt den Stofftransport auf Grund eines makroskopischen Konzentrationsgradienten. Ebenso wie chemische Reaktionen mit dem chemischen Potential μ beschrieben werden können, ist dieses auch für die Diffusion möglich. Wie in Abbildung 6 dargestellt, gibt es in einem Gefäß einen Bereich mit dem chemischen Potential μ_1 und der Menge N_1 gelöster Teilchen. Getrennt davon gibt es einen Bereich gleicher Temperatur aber mit einem chemischen Potential μ_2 und der Menge N_2 gelöster Teilchen. Wie dies für chemische Reaktionen üblich ist, kann auch die „Reaktion“ des Übertritts von Teilchen von einem Kompartiment in ein anderes mit einem „Reaktionsfortschritt“ ($d\xi$) beschrieben werden:

(1) $$-dN_1 = dN_2 = d\xi$$

Für ein geschlossenes System, in dem es keinen Massenaustausch mit der Umgebung gibt, gilt für die innere Energie:

(2) $$dU = TdS - pdV + \sum_1^n \mu_n dN_k$$

$$dU = T(d_eS + d_iS) - pdV + \sum_1^n \mu_n dN_k$$

Findet zusätzlich auch kein Energieaustausch mit der Umgebung statt ($dU = dV = 0$), so kann auch kein reversibler Entropieaustausch mit der

Umgebung stattfinden ($d_e S = 0$). Die irreversible Entropieproduktion des Partikeltransports kann geschrieben werden als *[De Donder 1936]:*

(3)
$$d_i S = \frac{dU + pdV}{T} - \left(\frac{\mu_1 - \mu_2}{T} \right) d\xi$$
$$d_i S = -\left(\frac{\mu_1 - \mu_2}{T} \right) d\xi > 0$$

Die Zunahme der Entropie spiegelt dabei den irreversiblen Partikeltransport von Orten eines hohen chemischen Potentials zu Orten mit einem niedrigeren chemischen Potential wider. Die Energiezunahme $Td_i S$ macht sich als Wärmeerzeugung auf Grund von Reibung bemerkbar. Wie bereits erwähnt, lassen sich irreversible Prozesse generell durch thermodynamische Flüsse und die sie bedingenden thermodynamischen Kräfte darstellen. Im Falle der Diffusion ist die Kraft gegeben durch $F = (\mu_1 - \mu_2)/T$ und der Fluss durch $dX = d\xi$. Es wird deutlich, dass ein Diffusionsstrom nur solange getrieben wird, wie $\mu_1 - \mu_2 \neq 0$ ist. Die Reaktion ist im Gleichgewicht, wenn die chemischen Potentiale ausgeglichen sind. Im Gleichgewicht ist $d_i S / dt = 0$ und die Entropie maximal.

In welchem Verhältnis steht dieser allgemeine Ausdruck für den Diffusionstransport zu den phenomenologischen Fickschen Gesetzen? Gleichung (3) lässt sich für eine einzelne Komponente (k) in einem eindimensionalen chemischen Potential folgendermaßen umformlieren:

(4)
$$\frac{d_i s(x)}{dt} = -\frac{1}{T} \left(\frac{\partial \mu_k}{\partial x} \right) J_k$$

Nahe dem Gleichgewicht ist anzunehmen, dass die Kraft direkt proportional zum Fluß ist, was im Folgenden als lineares Regime der Nicht-Gleichgewichtsthermodynamik bezeichnet werden soll. Daher wird ein linearer Proportionalität-Koeffizient eingeführt, der den Fluß in Verbindung zur Kraft setzt und in Relation zum Fickschen-Diffusions-Koeffizienten steht.

(5)
$$J_k = -L_k \frac{1}{T} \left(\frac{\partial \mu_k}{\partial x} \right)$$

Man kann nun das chemische Potential durch den im 1.Fickschen Gesetz verwendeten Konzentrationgradienten ersetzen. Die Konzentrationsabhängigkeit des chemischen Potentials läßt sich durch $\mu(p,T,x_k) = \mu(p,T) + RT \cdot \ln\{x_k\}$

beschreiben. Dabei ist x_k der Molenbruch aus n_k / n_{tot}. Der Zusammenhang zwischen Konzentrationsgradienten und Massefluß ergibt sich bei konstantem n_{tot} zu:

(6) $$J_k = -L_k R \cdot \frac{1}{n_k}\left(\frac{\partial n_k}{\partial x}\right) = -D_k \nabla n_k \text{ , mit } D_k = \frac{L_k R}{n_k}$$

Anzumerken ist, dass der Ausdruck in Gleichung (5) allgemeingültiger ist als das Ficksche-Diffusionsgesetz in Gleichung (6). Sind beispielsweise zwei Phasen miteinander im Gleichgewicht, so sind die chemischen Potentiale ausgeglichen, es existiert jedoch meist ein Konzentrationgradient, was nach dem Fickschen-Diffusionsgesetz zu einem Nettofluss führen würde.
Für die im weiteren dargestellte Herleitung einer mikroskopischen Theorie der Thermophorese ist es interessant, dass Diffusionsgesetz aus Gleichung (5) um ein mit einem Feld $\partial\psi$ assoziiertes Potential zu erweitern:

(7) $$J_k = -L_k \frac{1}{T}\left(\frac{\partial \mu_k}{\partial x}\right) = -L_k R \cdot \left(\frac{1}{n_k}\frac{\partial n_k}{\partial x} + \frac{\tau_k}{T}\frac{\partial \psi}{\partial x}\right)$$

Wobei τ_k der Interaktionsenergie pro Mol der Moleküle mit dem Feld entspricht. Der allgemeine Ausdruck $\vec{J}_{Feld} = -\Gamma_k \cdot n_k \cdot \partial\psi / \partial x$ setzt einen Fluss in Relation zur Mobilität Γ_k. Der Quotient aus Mobilität und Diffusions-Koeffizienten, also zwei Transportkoeffizienten, ist eng verknüpft mit der Interaktionsenergie/Interaktionsentropie des Moleküls mit dem Feld:

(8) $$\frac{\Gamma_k}{D_k} = \frac{\tau_k}{RT}$$

Dieses allgemeine Herleitung ist aufschlussreich für die Beschreibung der Thermophorese als Partikelbewegung in einem Temperaturfeld unter der Annahme eines lokalen Gleichgewichtes (siehe Die Mikroskopische Theorie der Thermophorese und Publikation III, Equation 1).

3.3 Gekoppelter Transport

Wie bereits für die Diffusion gezeigt, kann in Systemen nahe dem Gleichgewicht die Entropieproduktion auf folgende Weise geschrieben werden:

(9) $$\sigma = \sum_k J_k \cdot F_k$$

Weiterhin ist davon auszugehen, dass die Flüsse linear mit den Kräften über phenomenologische Koeffizienten verknüpft sind:

(10) $$J_k = \sum_j L_{kj} \cdot F_j$$

Aus Gleichung (10) ist bereits ersichtlich, dass z.B. ein Temperturgradient nicht nur einen Wärmefluss erzeugen kann, sondern auch noch andere Flüsse antreibt. Beispiele hierfür sind der Thermoelektrische-Effekt, wobei ein Wärmefluss den Fluss von Elektronen bedingt, aber auch der Peltier-Effekt, bei dem ein Stromfluss einen Wärmefluss bedingt. Der durch einen Temperaturgradienten bedingte Massentransport ist unter dem Namen Soret-Effekt oder Thermophorese bekannt.

3.3.1 Wärmeleitung und Thermophorese im Lokalen Gleichgewicht

Ein Wärmefluss löst einen Massenfluss aus (Soret-Effekt, Thermophorese) aber auch der reziproke Effekt, der durch einen Massentransport erzeugte Wärmefluss ist bekannt (Dufour-Effekt). Die Entropieproduktion durch Wärme- und Massenfluss lässt sich folgendermaßen formulieren:

(11) $$\sigma = \vec{J}_u \cdot \nabla\left(\frac{1}{T}\right) - \sum_{k=1}^{w} \vec{J}_k \cdot \nabla\left(\frac{\mu_k}{T}\right)$$

(12) $$= \left(\vec{J}_u - \sum_{k=1}^{w} \vec{J}_k \cdot \mu_k\right) \nabla\left(\frac{1}{T}\right) - \sum_{k=1}^{w} \vec{J}_k \cdot \frac{1}{T} \nabla \mu_k$$

Diese Form der Entropieproduktion erlaubt jedoch noch keine Trennung zwischen Temperaturgradient und Konzentrationsgradient, da $\nabla \mu_k$ eine Funktion von Konzentration, Druck und Temperatur ist.

Mit der partiellen molaren Entropie $s_k = (\partial s / \partial n_k)_{p,T}$ und der Vorraussetzung, dass das System im mechanischen Gleichgewicht ist ($\Delta p = 0$), ergibt sich der Ausdruck für die lokale Entropieproduktion nach einigen Umformungen *[Prigogine 1999]* zu:

(13) $$\sigma = \left(\vec{J}_u - \sum_{k=1}^{w} \vec{J}_k \cdot (\mu_k + T s_k) \right) \nabla \left(\frac{1}{T} \right) - \sum_{k=1}^{w} \vec{J}_k \cdot \frac{1}{T} (\nabla \mu_k)_{p,T}$$

wobei nun temperaturabhängige und konzentrationsabhängie Kräfte getrennt voneinander aufgeführt sind. Mit der partiellen molaren Enthalpie $h_k = \mu_k - s_k T$ kann der Wärmefluss unter Einbeziehung eines Massenflusses beschrieben werden als:

(14) $$\vec{J}_q = \vec{J}_u - \sum_{k=1}^{w} \vec{J}_k \cdot h_k$$

In einem geschlossenen System und bei konstantem Druck ist die Änderung der Enthalpie gleich der Wärmemenge, die mit der Umgebung ausgetauscht wird. In einem offenen System bei konstantem Volumen ist die ausgetauschte Wärmemenge gleich der Änderung der Energie abzüglich der Änderung der Enthalpie auf Grund eines Masseflusses aus dem System. Der Vektor $\vec{J}_q$ wird daher auch als reduzierter Wärmefluss bezeichnet.
Betrachtet man ein Zweikomponentensystem (z.B. Colloidale Partikel und Lösungsmittel), so kann man für die Formulierung der Entropieproduktion die Gibbs-Duhem-Relation nutzen:

(15) $$n_1 (\nabla \mu_1)_{p,T} = n_2 (\nabla \mu_2)_{p,T}$$

sowie die Bedingung, dass das Volumen durch die Flüsse nicht beeinflusst wird:

(16) $$\vec{J}_1 \upsilon_1 = \vec{J}_2 \upsilon_2$$

mit dem partiellen molaren Volumen υ. Daraus ergibt sich folgende Formulierung für die Entropieproduktion:

(17) $$\sigma = \vec{J}_q \cdot \nabla \left(\frac{1}{T} \right) - \frac{1}{T} \left(1 + \frac{\upsilon_1 n_1}{\upsilon_2 n_2} \right) \vec{J}_1 \cdot (\nabla \mu_1)_{p,T}$$

Nun lassen sich die phenomenologischen Gesetze für die Kopplung von Wärme und Molekülfluss formulieren. Ein interessanter Punkt bei der Formulierung der Kopplungen ist das Symmetrie-Prinzip *[Curie 1908]*, dessen Aussage den Ausschluss einiger Kopplungen zulässt. Es besagt, dass skalare Kräfte (z.B. die isotrope Affinität ($\Delta\mu$)) keine gerichteten Flüsse (z.B. den anisotropen Wärmefluss) erzeugen können. Für Temperatur- und Konzentrationsgradienten sind daher alle Kopplungen zu beachten. Die reziproken Onsager-Relationen lauten daher:

(18)

$$\vec{J}_q = L_{qq} \cdot \nabla\left(\frac{1}{T}\right) - L_{q1} \cdot \frac{1}{T}\left(1 + \frac{\upsilon_1 n_1}{\upsilon_2 n_2}\right) \cdot (\nabla\mu_1)_{p,T}$$

$$\vec{J}_1 = L_{1q} \cdot \nabla\left(\frac{1}{T}\right) - L_{11} \cdot \frac{1}{T}\left(1 + \frac{\upsilon_1 n_1}{\upsilon_2 n_2}\right) \cdot (\nabla\mu_1)_{p,T}$$

Dabei ist L_{qq} der Transportkoeffizient für Wärmetransport und L_{11} der Transportkoeffizient für den diffusiven Materietransport. L_{1q} ist der Koeffizient für den thermophoretischen Transport, und L_{q1} für den Dufour-Effekt. Stellt die zweite Komponente n_2 das im Überschuss vorhandene Lösungsmittel dar, so kann der Quotient $\upsilon_1 n_1 / \upsilon_2 n_2$ vernachlässigt werden und der Massenfluss in Anwesenheit eines Temperaturgradienten kann in Form eines erweiterten 1.Fickschen Gesetzes geschrieben werden. Dabei ist D_T der Koeffizient der thermophoretischen Mobilität:

(19)

$$\vec{J}_1 = \frac{L_{1q}}{T^2} \cdot \nabla T - L_{11} \cdot \frac{1}{T}\left(1 + \frac{\upsilon_1 n_1}{\upsilon_2 n_2}\right) \cdot \nabla n_1 = -n_1 D_T \cdot \nabla T - D \cdot \nabla n_1$$

4 Die Mikroskopische Theorie der Thermophorese

Die Nicht-Gleichgewichtsthermodynamik erlaubt die Beschreibung von irreversiblen Prozessen solange lineare phenomenologische Gesetze gültig sind *[Prigogine 1999, S. 351]*. Aus Gleichung (19) lässt sich die Konzentration im Fließgleichgewicht bei $\vec{J}_1 = 0$ bestimmen:

(20)

$$\frac{n}{n_0} = 1 - \frac{D_T}{D} dT = 1 - S_T dT$$

Allerdings ist diese Relation nur für kleine Konzentrations- und Temperaturunterschiede gültig.

Als erster Schritt soll eine allgemeine Beschreibung gefunden werden, die über einen großen Konzentrations- bzw. Temperaturbereich Gültigkeit besitzt.

In **Publikation II** wird die Abhängigkeit zwischen Konzentration und Temperaturerhöhung im Fließgleichgewicht untersucht. Dafür wird die Temperatur lokal um maximal 10 K erhöht. Dieses führt bei den verwendeten Molekülen zu einer Konzentrationsabsenkung um bis zu zwei Größenordnungen unter die Ausgangskonzentration. Gleichung (20) ist in diesem Regime nicht mehr für das gesamte System gültig. Die Integration von Gleichung (19) (bei konstanten Transportkoeffizienten und geringer Soluten-Konzentration) ergibt eine exponentielle Abhängigkeit zwischen Konzentration und Temperatur, ähnlich einer Boltzmannverteilung. Diese exponentielle Verteilung konnte experimentell bestätigt werden (siehe Publikation II, Fig. 3,4):

(21)
$$\frac{n}{n_0} = \exp\left[-S_T\left[T_n - T_0\right]\right]$$

Dieses exponentiell von der Temperatur abhängige Fließgleichgewicht lässt sich durch die Verkettung vieler kleiner Volumenelemente beschreiben, in denen jeweils die linearisierte Form (20) gilt (Abbildung 7).

Die Volumenelemente stehen mittels Diffusion miteinander in Kontakt. Sind die Größen der Boxen so gewählt, dass die Temperaturänderung zwischen zwei Boxen im ganzen System gleich ist, so lässt sich die Konzentration des n-ten Elementes durch die Multiplikation der Konzentrationen aller vorrausgegangenen Elemente bestimmen.

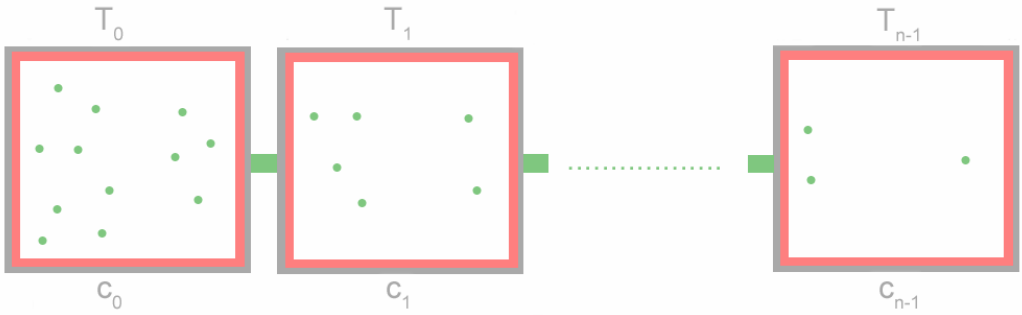

Abbildung 7. Lokale Thermophorese. Die Verkettung kleiner Volumenelemente, in denen eine lineare Beziehung zwischen Temperaturerhöhung und Konzentration besteht, ergeben für das Gesamtsystem einen exponentiellen Zusammenhang zwischen Temperatur und Konzentration.

Bei einer genügend großen Anzahl von Elementen folgt die exponentielle Abhängigkeit aus dem Grenzwertsatz der Exponentialfunktion.
Ein System mit einem Temperaturgradienten ist nicht im thermodynamischen Gleichgewicht, allerdings können auch hier Volumenelemente definiert werden, in denen ein lokales Gleichgewicht vorliegt. Dieses bedeutet, dass für die Beschreibung des mikroskopischen Mechanismus der Thermophorese thermodynamische Potentiale benutzt werden können. Unter der Bedingung, dass in jeder der Boxen ein lokales Gleichgewicht vorliegt kann der Exponent auch in Form einer Differenz in der Gibbschen-Freien-Energie formuliert werden:

(22) $$\frac{n_n}{n_0} = \left[1 - S_T \frac{T_N - T_0}{N}\right]^N \rightarrow \exp\left[-S_T\left[Tn - T_0\right]\right] = \exp\left[-\left[\frac{G(x) - G_0(x_0)}{kT}\right]\right]$$

Die Verknüpfung der experimentell bestätigten exponentiellen Konzentrationsabhängigkeit und der Boltzmannverteilung erlaubt eine Formulierung des Soret-Koeffizienten mit Hilfe eines thermodynamischen Potentials. Unterstützt wird dieses durch den experimentellen Nachweis das der Soret-Koeffizient mit der Oberfläche von sphärischen Partikeln skaliert: $S_T \propto a^2$ (siehe Publikation II, Fig. 5). Dieses deutet daraufhin, dass die temperaturabhängige Interaktionsenergie zwischen Partikel und Lösungsmittel, die Solvatationsenergie, von entscheidender Bedeutung ist.

In **Publikation III** wird der Zusammenhang zwischen der Solvatation von Molekülen und ihrem thermophoretischen Verhalten im Temperaturgradienten hinsichtlich des mikroskopischen Mechanismus näher untersucht. Als Modellsystem dienen sphärische Polystyren-Partikel mit 20 nm bis 2 µm Durchmesser, deren Oberfläche mit Carboxylgruppen modifiziert wurde, um sie in wässrigen Suspensionen zu stabilisieren. Als Modellsystem für Polymer-Thermodiffusion werden monodisperse DNA-Moleküle von 50-50.000 bp Länge verwendet.
Aus (20) kann folgender Zusammenhang zwischen kleinen Konzentrationsänderungen und kleinen Änderungen des thermodynamischen Potentials formuliert werden:

(23) $$\frac{\delta n}{n} = -S_T \delta T = \frac{\delta G}{kT}$$

Der Soret-Koeffizient läßt sich nun als Ableitung der Gibbsschen-Freien-Energie $dG = -SdT + Vdp + \mu dN$ nach der Temperatur schreiben. Die lokale Anwendung des thermodynamischen Potentials führt zu folgendem Ausdruck für das gesamte System:

(24) $$S_T = -\frac{\Delta S}{kT}$$

Dieser Ausdruck wird in **Publikation III** experimentell bestätigt. Es zeigt sich, dass die Maximierung der Solvatationsentropie zum Fluss der Partikel im Temperaturgradienten führt.

Dabei erweist sich die Entropie der Debye-Hückel-Abschirmung bei geladenen Molekülen meist als dominant. Neben den Ladungseffekten ist auch die Orientierung von Lösemittelmolekülen an der Oberfläche des Soluten, die sog. Hydratationsentropie, von Bedeutung [Israelachvili 1992] (Abbildung 8).

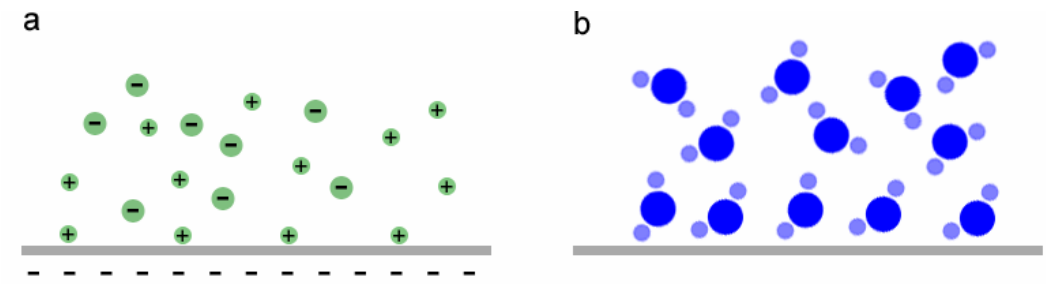

Abbildung 8. Die Solvatationsentropie in Wasser. Die Solvatationsentropie geladener Moleküle in Wasser setzt sich aus zwei Anteilen zusammen. (a) Die Oberflächenladung wird durch kondensierte und freie Ionen abgeschirmt, wobei die Abschirmlänge der freien Ionen temperaturabhängig ist. (b) Die Freiheitsgrade der Wassermoleküle sind an der Oberfläche der gelösten Moleküle eingeschränkt. Auch diese nicht-ionische Hydratationsentropie trägt zur Solvatationsentropie bei.

Die geladene Oberfläche der Moleküle kann mitsamt der abschirmenden Ionenhülle als Kapazität betrachtet werden, deren Energie temperaturäbhängig ist. Daher kann der Soret-Koeffizient aus der Entropieänderung eines einzelnen geladenen Moleküls wie folgt berechnet werden:

(25) $$S_T = \frac{A}{kT}\left(-s_{hyd} + \frac{\beta\sigma_{eff}^2}{4\varepsilon\varepsilon_0 T}\cdot\lambda_{DH}\right),$$

mit der auf die Oberfläche normierten Entropie s_{hyd}, der Temperaturabhängigkeit der Dielektrizitätskonstante β, der effektiven Ladung σ_{eff} und der Debye-Hückel Abschirmlänge λ_{DH}. Diese mittels Entropie hergeleitete Theorie beschreibt die experimentellen Ergebnisse, einschließlich des Vorzeichenwechsels (siehe Publikation III, Fig. 1) des Soret-Koeffizienten, sehr genau. Der Anteil der Hydratationentropie am Soret-Effekt ist abhängig von den jeweiligen Oberflächeneigenschaften und kann nur experimentell bestimmt werden (siehe Publikation III, Fig. 2).

Weiter unterstützt werden die Ergebnisse aus **Publikation II** und **III** durch eine theoretische Arbeit **(Publikation IV).** Basierend auf einem Ansatz aus Kraftgleichgewicht auf der Zeitskala der Brownschen Molekularbewegung und Thermodynamik wird eine Theorie entwickelt, die auf der reversiblen Arbeit beruht, die benötigt wird, um den Partikel samt seiner Solvatationshülle aufzubauen. Die Resultate stehen im Einklang mit der entropischen Theorie der Thermophorese, die in **Publikation II** und **III** beschrieben wurde.

5 Die Grenze des Lokalen Gleichgewichtes

Um eine mikroskopische Theorie der Thermophorese zu entwickeln, wurden in der Vergangenheit fast ausschließlich hydrodynamische Methoden angewandt, die Druckgradienten oder Volumenkräfte beschrieben, die zu einer Bewegung im Temperaturgradienten führen [Ruckenstein 1981, Piazza 2002, Schimpf 2000]. Ihren Ursprung haben diese Kräfte in der ungleichmäßigen Verteilung von Solventmolekülen um ein gelöstes Partikel oder in der temperaturabhängigen Änderung der Partikel-Solvent-Interaktion.

Wie gezeigt, läßt sich Thermophorese jedoch präzise mit Mitteln der Thermodynamik beschreiben, solange kleinen Volumenelementen thermodynamische Variablen zugeordnet werden können.

Es ist anzunehmen, dass eine Grenze existiert, ab der diese Annahme die Verhältnisse in dem System nicht mehr zutreffend beschreibt. Dieses kann auf Basis der Onsager-Relationen als eine nichtlineare Proportionalität zwischen Kraft und Fluß bezeichnet werden. Im Falle des thermophoretischen Transportes lässt sich die Grenze zwischen einem lokalen Gleichgewicht und lokalem Nicht-Gleichgewicht anhand von zwei Transportmechanismen auf unterschiedlichen Zeitskalen verdeutlichen *[Astumian 2007]*. Betrachtet man die deterministische Thermodiffusion, so ist die Zeit um eine Strecke der Länge des Partikelradius a zurückzulegen gegeben durch $\Delta t_T = a/(D_T \nabla T)$. Im Gegensatz dazu steht die charakteristische Zeit $\Delta t_D = a^2 / D$, die ein Molekül benötigt, um dieselbe Strecke rein diffusiv zurückzulegen. Die in dieser Arbeit angelegten Temperaturgradienten sind klein genug, so dass der auf Diffusion basierende Mechanismus auf der Längenskala des Partikelradius dominiert. Dieses bedeutet, dass die Moleküle die Energielandschaft diffusiv erkunden und in Bereichen (meist) niedriegerer Temperatur stabilisiert werden.

Beobachtet man allerdings vergleichsweise große Partikel mit einer dementsprechend großen thermophoretischen Mobilität (z.B.Partikel mit einem Durchmesser von 2 µm) in starken Temperaturgradienten, so kann der deterministische Transport dominieren. In diesem Falle gelten Modelle, die Thermophorese mittels am Partikel angreifenden mechanischen Kräften beschreiben. Der Temperaturgradient, ab dem der deterministische Transport überwiegt, ist gegeben durch:

(26) $$\nabla T > \frac{1}{a \cdot S_T}$$

Für einen Partikel mit dem Radius a und dem zugehörigen Soret-Koeffizienten ist es zu erwarten, dass ab diesem Gradienten die lineare Relation $v = -D_T \nabla T$ zwischen Geschwindigkeit und Temperaturgradient nicht mehr gültig ist oder eine Linearität mit deutlich anderem Proportionalitätsfaktor vorliegt.

Publikation V (eingereicht) untersucht Thermophorese von großen Partikeln bei sehr starken Temperaturgradienten. Eine Abweichung von $v = -D_T \nabla T$, die bei niedrigen Temperaturgradienten Gültigkeit besitzt (siehe Publikation III), konnte experimentell nachgewiesen werden. Die Frage ob jenseits dieses Limits wieder eine lineare Abhängigkeit zwischen Temperaturgradient und Geschwindigkeit besteht, oder ob die thermophoretische Geschwindigkeit auf Grund von gegenläufigen Effekten in Sättigung geht bleibt jedoch weiterhin offen.

6 Auf Thermophorese basierende Anwendungen

Bis heute gibt es nur wenige technologische Anwendungen von Thermophorese. Von Bedeutung ist aktuell nur die Thermische-Feld-Fluss-Fraktionierung (ThFFF). Dieses ist eine Chromatographiemethode, bei der die Molekülretention durch die thermophoretische Beeinflussung der Partikelposition in einem parabolischen Flussprofil erreicht wird. Ein Temperaturgradient liegt dabei quer zur Flussrichtung in einer nur wenige hundert Mikrometer breiten Kapillare. Die Verteilung von Molekülen mit einem ausgeprägten thermophoretischen Effekt ist dabei stärker zu einer Wand des Kanals verschoben als dieses bei Molekülen mit schwacher Thermophorese der Fall ist. Anwendung findet ThFFF neben der Polymerchemie auch bei der quantitativen Aufreinigung von Proteingemischen *[Williams 2006]*. Temperaturgradienten erlauben generell Beeinflussung von kleinsten Molekülen in ihrer wässrigen Umgebung. Durch eine rein optische Implementierung gelingt dies kontaktfrei in geringsten Volumen von wenigen hundert Nanolitern.

6.1 Zweidimensionale Kristalle

Im Falle der ThFFF stehen die Vektoren des thermophoretischen- und des Lösemittelflusses in einem rechten Winkel zueinander. In **Publikation VI** wird eine ähnliche Situation *[Braun 2002]* zur Bildung von zweidimensionalen Kristallen aus runden Polystyrene-Partikeln genutzt. Flüssigkeitsschichten von etwa 500 µm Höhe werden lokal mit einem IR Laser geheizt (siehe Publikation VI, Fig. 1). Dadurch wird ein Konvektionsstrom erzeugt, der konzentrisch auf das Zentrum des Heizfokus zuläuft. Der Konvektionsstrom allein führt jedoch nicht zu einer Entmischung von Lösungsmittel und Partikeln. Zusätzlich gibt es noch anisotrope Temperaturgradienten. Auf Grund der relativ geringen Wärmeleitfähigkeit von Wasser sind laterale Temperaturgradienten klein im Vergleich zu den Gradienten, die senkrecht zur stark wärmeleitenden Glas- oder Saphiroberfläche stehen (siehe Publikation VI, Fig. 3). Die Kristalle bilden sich, da Moleküle, die im Konvektionsstrom zirkulieren, durch den starken senkrechten Temperaturgradienten zur Oberfläche transportiert werden. Im Zentrum des Heizfokus und nahe der Oberfläche ist dieser Temperaturgradient sehr stark und der Konvektionsstrom vergleichsweise schwach. Daher werden die Moleküle effektiv auf der Oberfläche in einer aus zwei Flüssen gebildeten, optisch erzeugten Falle gefangen (Abbildung 9).

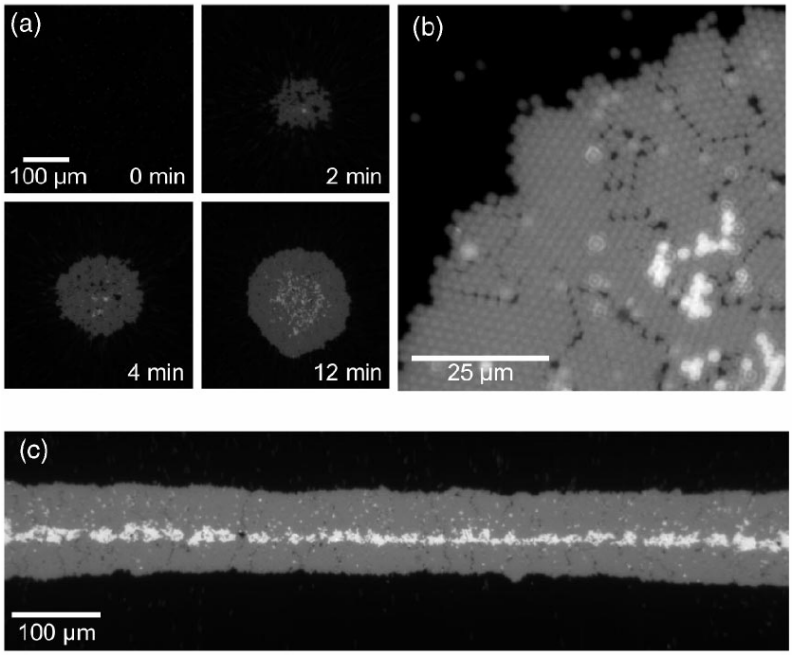

Abbildung 9. Zweidimensionale Kristalle auf Oberflächen. (a) Durch eine Kombination von Konvektion und Thermophorese lassen sich Zweidimensionale Kristalle Kollidaler Partikel auf Oberflächen erzeugen. (b) Hochaufgelöst lassen sich auch Fehlstellen und deren Dynamik beobachten. (c) Die Form der Kristalle ist nur abhängig von der Geometrie des geheizten Bereiches. So können Partikel auch entlang einer Linie akkumuliert werden.

6.2 Molekülanreicherung in Mikrofluidik-Kanälen

Der unter 6.1 beschriebene Ansatz zur Aufkonzentrierung ist nur für große Partikel ab etwa 0,5 µm Durchmesser effektiv. Die Anreicherung von wesentlich kleineren Molekülen lässt sich dadurch erreichen, dass eine Flüssigkeitsströmung und thermophoretischer Transport gegenläufig ausgerichtet werden (siehe Publikation VII, Fig. 1).

Bei kleinen Molekülen wirkt die Diffusion allerdings einer Aufkonzentrierung entgegen, weshalb besondere Anforderungen an die Geometrie der Flußkammer gestellt werden müssen. Wie in Abbildung 10 gezeigt, findet der Prozess in einem dünnen mikrofluidischen Kanal von 10x10 µm statt (siehe Publikation VII, Fig. 2). Das Kammermaterial PDMS sorgt durch seine geringe Wärmeleitfähigkeit dafür, dass die Kammertemperatur homogen im Kammerquerschnitt ist. Dieser Kanal kann mittels Gravitationsfluss aus einem großen Reservoir für lange Zeit unter einen konstanten Fluss gesetzt werden. Abbildung 10 zeigt die zeitabhängige Konzentrationveränderung, wenn eine Lösung von 10.000 bp DNA mit weniger als 1 µm/s durch einen Heizspot von maximal 16 K fließt. Die Situation kann mit Hilfe eines Potentialbildes analysiert werden, welches

einerseits durch die Fließgeschwindigkeit aber auch durch die thermophoretische Drift bestimmt wird. Moleküle bewegen sich auf den Punkt erhöhter Temperatur zu, werden jedoch durch den thermophoretischen Gegenfluss vor dem Heizpunkt angereichert. In **Publikation VII** wird eine analytische Theorie für die Anreicherung von DNA-Molekülen vorgestellt und die Abhängigkeit von der Driftgeschwindigkeit, dem Temperaturgradienten, sowie den Thermodiffusions- und Diffusions-Koeffizienten der Moleküle analysiert.

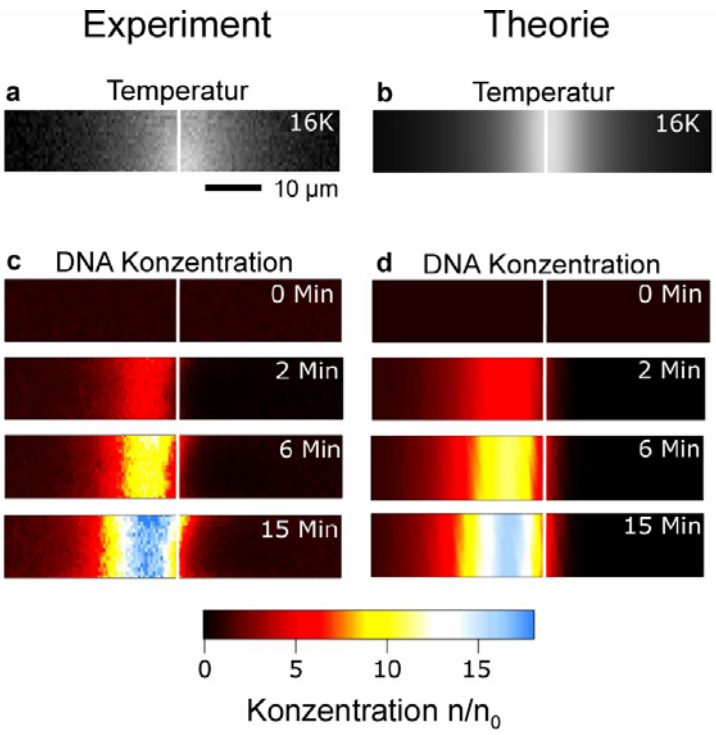

Abbildung 10. Experiment und Theorie der Thermo-Optischen Molekülanreicherung. (a,c) Sind ein thermophoretischer Fluss und eine Flüssigkeitsbewegung antiparallel orientiert, so können Moleküle vor einem Heizpunkt in einem dünnen Kanal aufkonzentriert werden. (b,d) Diese Ergebnisse können mit einer 3-D-Simulation erklärt werden.

6.3 Größenbestimmung von Nanokristallen

In **Publikation VIII** (akzeptiert) wird Thermophorese verwendet um den hydrodynamischen Radius von Nanokristallen zu bestimmen, die mit verschiedenen organischen Modifikationen versehen sind.

Die zur Charakterisierung von anorganischen Kristallen häufig angewendeten Methoden führen oft nicht zu den gewünschten Ergebnissen. Dieses liegt zum einen daran, dass Methoden wie Röntgenbrechung die organischen Strukturen nicht abbilden können. Zum anderen aber auch an den Inhomogenitäten, die

durch die Modifikation auftreten können und die abhängig von der Methode das Ergebnis unterschiedlich stark beeinflussen. Der thermophoretischen Messmethode liegt zu Grunde, dass Temperaturgradienten einen Konzentrationsgradienten aufbauen, dessen Relaxation gemessen werden kann. Wird die Wärmequelle ausgeschaltet, so sinkt die Temperatur der Messkammer innerhalb von etwa 100 ms auf die Umgebungstemperatur ab. Daran anschließend wird die vergleichsweise langsame Rückdiffusion der Moleküle auf einer Zeitskala von etwa 1-20 s beobachtet. Auf Grund des runden Heizfokus ist das System radialsymmetrisch und der Konzentrationsgradient lässt sich auf einen eindimensionalen radialen Mittelwert reduzieren (siehe Publikation VIII, Fig. 4). Ein Polynomfit des Gradienten wird als Randbedingung für eine eindimensionale Finite-Elemente-Simulation (Femlab, Comsol) der Relaxation des Konzentrationsprofils verwendet. Der Diffusions-Koeffizient wird dabei solange angepasst, bis Simulation und Experiment in ihrer zeitlichen Entwicklung übereinstimmen. Über die Stokes-Einstein-Relation kann der hydrodynamische Radius bestimmt werden *[Einstein 1905]*. Insgesamt zeigt sich die Methode konkurrenzfähig mit den in **Publikation VIII** dargestellten etablierten Techniken. Ein großer Vorteil des hier vorgestellten Ansatzes ist es, dass der effektive Radius problemlos auch in einer weniger reinen Probe über einen weiten Konzentrationsbereich bestimmt werden kann.

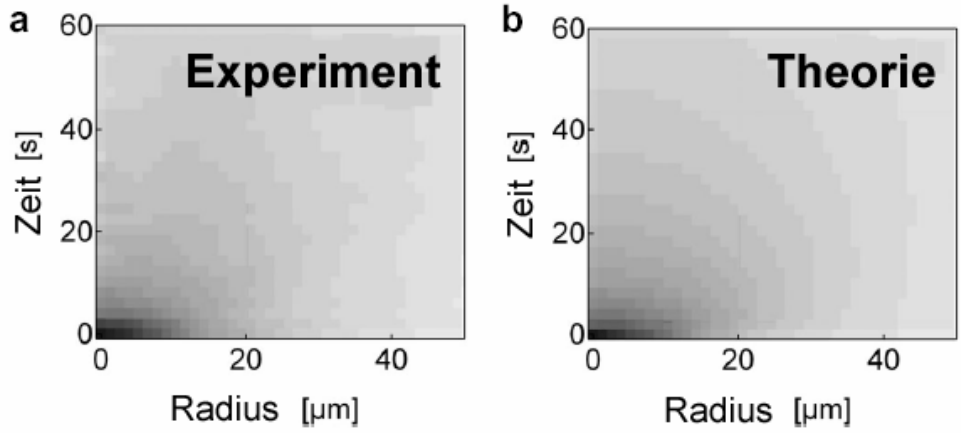

Abbildung 11. Größenbestimmung anhand der Relaxation des Konzentrationsgradienten. In der Abbildung sind radiale Konzentrationsmittelwerte über die Zeit gezeigt (schwarz = niedrige Konzentration, weiß = hohe Konzentration) (a) Durch Thermophorese wird ein Konzentrationsgradient aufgebaut, der nach dem Abschalten des Heizlasers abgebaut wird. (b) Eine Simulation der Entwicklung des radialen Konzentrationsmittels über die Zeit wird verwendet, um den Diffusions-Koeffizienten zu bestimmen.

7 Biomolekül Akkumulation in Hydrothermalen-Quellen

Eine sehr starke Anreicherung von Molekülen kann durch besondere geometrische Bedingungen erreicht werden, wie sie das erste Mal von Klaus Clusius *[Clusius 1938]* beschrieben wurden. Die Kombination von Flüssen und Temperaturgradienten in langen dünnen Röhren erlaubt die Anreicherung von kleinen Molekülen wie z.B. einzelnen Nukleotiden. Die Gleichgewichtskonzentration am kalten, geschlossenen Ende von sogenannten Clusius-Röhren kann wie folgt beschrieben werden:

(27) $$\frac{n_{unten}}{n_{oben}} = \exp[0.42 \times S_T \Delta T \times r]$$

Ein Röhre (r, Seitenverhältnis Länge/Breite) wird entlang einer langen Seite geheizt und auf der gegenüberliegenden Seite wird Wärme abgeführt. Das Volumen der Röhre wird dabei durch einen Konvektionsfluss permanent umgewälzt. Im Temperaturgradienten bewegen sich die Moleküle, ähnlich wie es bei der ThFFF-Technologie (siehe Abschnitt 6) geschieht, zu einer der begrenzenden Wände. Der laminare Fluss bewegt dabei die Moleküle immer wieder durch den Temperaturgradienten. Am unteren Ende scheiden sich die Moleküle ähnlich dem Mechanismus in **Publikation VI** an der Oberfläche ab. Da das Seitenverhältnis in den Exponenten der Gleichgewichtskonzentration eingeht, können in langen Röhren geringen Durchmessers auch kleine Moleküle mit geringen Soret-Koeffizienten exponentiell angereichert werden.

Mögliche natürliche Vorkommen dieses Anreicherungsszenarios sind hydrothermale Quellen in der Tiefsee. Die Randbedingungen für eine Clusius-Röhre, wie starke Temperaturunterschiede und poröses Gestein, liegen hier vor. In **Publikation IX** wird die Rolle von Thermophorese bei der Entstehung des Lebens diskutiert. Der Akkumulationsmechanismus ist eine plausible Möglichkeit das Grundproblem vieler Szenarien der molekularen Evolution in den Ozeanen zu lösen: Die tieferen Schichten der Ozeane schützen zwar organische Moleküle vor den herrschenden Umweltbedingungen wie z.B. starker UV-Strahlung, jedoch müssen diese Moleküle in gewissen Konzentrationen vorliegen, damit ein früher Metabolismus entstehen kann. Bei freier Diffusion in den Ozeanen ist dies jedoch praktisch unmöglich. Die Anreicherung im Gestein der hydrothermalen Quellen ist ein möglicher Ansatz, dieses Konzentrationsproblem auf der frühen Erde zu lösen.

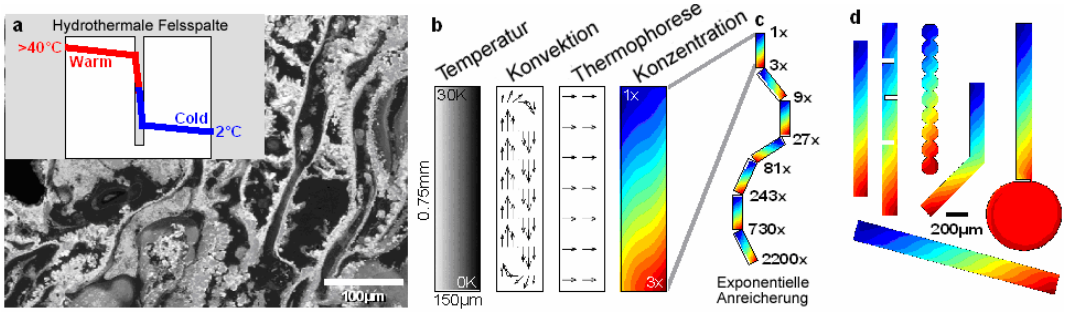

Abbildung 12. Molekülakkumulation in Hydrothermalen Felsspalten. (a) Das poröse Gestein hydrothermaler Quellen enthält dünne Kanäle mit großem Verhältnis von Länge zu Breite. Es können Temperaturunterschiede von mehr als 40 K über den Durchmesser der Kanäle erreicht werden. (b) Die Abbildung zeigt die Ergebnisse von Simulationen der Anreicherung in den Kanälen von hydrothermalen Quellen (1000 bp DNA). (c,d) Die Akkumulation ist weitgehend unabhängig von Störungen im Verlauf der Kapillaren im Fels.

8 Anwendungen von Lokalen Temperaturverteilungen

Bisher wurden in dieser Arbeit die Anwendungsmöglichkeiten von Temperaturgradienten zur Erzeugung von Konzentrationsverteilungen vorgestellt. Aber auch ohne einen Massefluss ist es möglich, eine lokale Temperaturverteilung für eine Molekülcharakterisierung zu nutzen. Zum Beispiel können chemische Reaktionen beeinflusst werden. Naheliegend für einen solchen Vorgang sind sogenannte Schmelzübergänge von Nukleinsäuren oder Proteinen. Temperaturverteilungen lösen in diesen Fällen Strukturänderungen des Moleküls und eine Bewegung im Temperaturgradienten aus. Beide Effekte finden aber auf unterschiedlichen Zeitskalen statt und können gut voneinander getrennt werden. Die Reaktionsraten des Nukleinsäureschmelzübergangs sind in den meisten Fällen ausreichend hoch, so dass der Messzeitraum so gewählt werden kann, dass thermophoretische Molekülbewegungen vernachlässigbar sind. In **Publikation X** (in Vorbereitung) wird erstmals eine durch Infrarot-Laser induzierte Temperaturverteilung verwendet, um die Stabilität von Biomolekülen innerhalb von 50 ms ortsaufgelöst zu bestimmen.

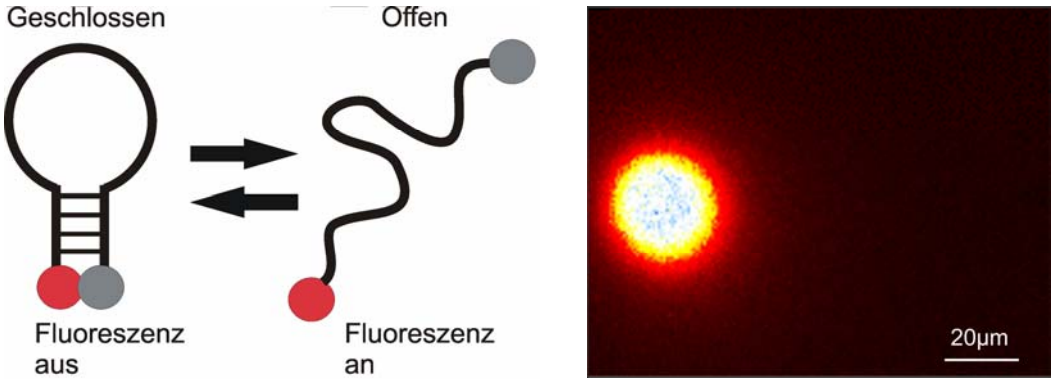

Abbildung 13. Zustandsverteilung eines DNA-Hairpins. (a) Die Fluoreszenz eines DNA-Hairpins ist bei niedrigen Temperaturen, im hybridisierten Zustand gering. Beim Temperaturbedingten Aufschmelzen der doppelsträngigen Strukturanteile nimmt die Fluoreszenz stark zu. (b) Durch lokales heizen mit einem IR-Laser können alle Temperaturen zwischen Raumtemperatur (außen) und 100°C (im Zentrum des Laserfokus) gleichzeitig erzeugt werden. Das schnelle Fluoreszenzsignal des Aufschmelzens erlaubt die Messung der Stabilität als Maß für die Stabilität eines Biomoleküls in nur 50 ms.

9 Ausblick

Die Aufklärung der mikroskopischen Ursache thermophoretischer Molekülbewegung stand im Mittelpunkt dieser Arbeit. Darüber hinaus machen es die optisch erzeugten Temperaturgradienten auch möglich neue Anwendungen für Biowissenschaften und Biotechnologie zu entwickeln.

Der Soret-Koeffizient ist ein Marker für die Oberflächeneigenschaften von gelösten Molekülen, wodurch intermolekulare Wechselwirkungen und Änderungen der Partikel Oberfläche/Struktur detektiert werden können. Die Messung mittels Temperaturgradienten unterscheidet sich darin deutlich von vielen gängigen Messprinzipien: Es können auch Änderungen der Eigenschaften eines Moleküls nachgewiesen werden können, die nicht auf einer Größenänderung beruhen. Erste Vorversuche zeigen, dass die Bindung von PEG-Molekülen (5-20 kDa) an Nanokristalle nachgewiesen und die Anzahl der gebundenen Moleküle bestimmt werden kann. Dieses erlaubt außerdem eine Quantifizierung der Solvatationsentropie dieser Moleküle und lässt den Schluss zu, dass auch die Bindung von Proteinen, die meist ein höheres Molekulargewicht besitzen, ebenfalls auf diese Weise nachgewiesen werden kann.

In ersten Experimenten konnten auch größenneutrale Bindungsereignisse, wie die Bindung einer kurzen einzelsträngigen DNA von 40 Basen Länge an einen wesentlich größeren 25 nm großen Nanopartikel, nachgewiesen werden. Die Änderung der Solvatationsentropie durch die Bindung manifestiert sich in diesem Fall in einem größeren Soret-Koeffizienten, der innerhalb von wenigen Sekunden gemessen werden kann.

In diesem Zusammenhang soll zukünftig ebenfalls die Sequenzabhängigkeit der Thermophorese von kurzen DNA Molekülen analysiert werden. Längerfristig sollen auf diese Weise Modifikationen der DNA durch mutagene Substanzen wie Zytostatica nachgewiesen werden.

Bei Molekülen mit komplexen Faltungsstrukturen, wie dieses z.B. bei Proteinen der Fall ist, lassen sich mittels Thermophorese Strukturänderungen messen. Ein einzelner Fluoreszenzmarker genügt dabei, um Information über das gesamte Molekül zu erhalten, da der Soret-Koeffizient die Solvatationsenergie des gesamten Moleküls widerspiegelt. Dieser Zusammenhang zwischen Thermophorese und Proteinstruktur konnte in einem Vorversuch verifiziert werden. Die Strukturänderungen eines Proteins bei unterschiedlichen Temperaturen konnte gemessen werden.

Die schnellen Heiz- und Kühlraten, die beim optischen Heizen dünner Flüssigkeitsschichten erreicht werden, können weiterhin genutzt werden, um Zeitkonstanten für chemische Reaktionen, wie das Hybridisieren von komplementären DNA-Strängen nach thermischer Denaturierung zu erhalten.
In Kombination mit den wesentlichen Vorteilen der thermophoretischen Molekülcharakterisierung, wie Kontaktfreiheit und hoher Messgeschwindigkeit, können die Eigenschaften von Biomolekülen effizient auf neue Art und Weise untersucht werden.

10 Literaturverzeichnis

[Alder 1958]
Alder B. J. and Wainright T., *Transport Processes in Statistical Mechanics*, New York: Interscience (1958)

[Astumian 2006]
Astumian R.D., *The unreasonable effectiveness of equilibrium theory for interpreting nonequilibrium experiments*, Am. J. Phys., 74 (8) (2006)

[Astumian 2007]
Astumian R.D., *Commentary: Coupled transport at the nanoscale: The Unreasonable Effectiveness of equilibrium theory*, PNAS (104), p. 3-4 (2007)

[Braun 2002]
Braun D., Libchaber A., *Trapping of DNA by Thermophoretic Depletion and Convection*, Phys. Rev. Lett. 89, 188103 (2002)

[*Brenner 2006]*
Brenner H., *Elementary kinematical model of thermal diffusion in liquids and gases,* Phys. Rev. E 74, 036306 (2006)

[Chapman 1917]
Chapman S. and Dootson F.W., *A note on thermal diffusion*, Phil. Mag. 33, 248-253 (1917)

[Clusius 1938]
Clusius K., Dickel G., *Neues Verfahren zur Gasentmischung und Isotopentrennung*, Naturw. **26**, 546 (1938)

[Curie 1908]
Curie P., *Oeuvres de Pierre Curie*, Paris, Gaulthier-Villars (1908)

[De Donder 1936]
De Donder T. and Van Rysselberghe P., *Affinity*, Menlo Park CA: Stanford University Press (1936)

[Dhont 2004]
Dhont J.K.G., T*hermodiffusion of interacting colloids. I. A statistical thermodynamics approach*, Journal of Chemical Physics 120, 1632-1641, (2004)

[Einstein 1905]
Einstein A., *Über die von der molekulartheoretischen Theorie derWärme geforderten Bewegung von in ruhenden Flüssigkeiten suspendierten Teilchen*, Annalen der Physik **17**: p. 549-560 (1905).

[*Israelachvili 1992*]
Israelachvili J, *Intermolecular and Surface Forces*, (Academic, New York), 2nd Ed. (1992)

[Ludwig 1856]
Ludwig C., *Diffusion zwischen ungleich erwärmten Orten gleich zusammengesetzter Lösungen*, Akad. Wiss. Wien. Math.-Nat. Wiss. Kl. **20**, 539 (1856)

[Parola 2004]
Parola A. and Piazza R., *Particle Thermophoresis in Liquids*, Eu. Phys. Journal E, **15** (2004)

[Piazza 2002]
Piazza R, Guarino A., Soret *Effect in Interacting Micellar Solutions*, Phys. Rev. Lett. 88, 208302 (2002)

[Prigogine 1999]
Prigogine I., *Modern Thermodynamics*, John Wiley & Sons, ISBN: 0 471 97393 9 (1999)

[Rauch 2002]
Rauch J., Köhler W., *Diffusion and Thermal Diffusion of Semidilute to Concentrated Solutions of Polystyrene in Toluene in the Vicinity of the Glass Transition*, Phys. Rev. Lett. 88, 185901 (2002)

[Ruckenstein 1981]
Ruckenstein E., *Can phoretic motions be treated as interfacial tension gradient driven phenomena?,* J. Colloid Interface Sci. 83, 77-85 (1981)

[Schimpf 2000]
Schimpf M.E., Semenov S.N., *Mechanism of Polymer Thermophoresis in Nonaqueous Solvents*, J. Phys. Chem. B 104, 9935-9942 (2000)

[Soret 1879]
Soret C., *Sur L'etat d'équilibre que prend au point de vue de sa concentration une dissolution saaline primitivement homo géne dont deux parties sont portées a des températures différentes*, Arch. Geneve 3, 48-64 (1879)

[Wiegand *2006]*
Wiegand S., *150 Jahre Ludwig-Soret Effekt*,
Bunsen-Magazin 8.Jahrgang 5/2006

[Williams 2006]
Williams S.K.R., Lee D, *Field-Flow Fractionation of Proteins, Polysaccharides, Synthetic Polymers, and Supramolecular Assemblies*, J. Sep. Sci., 29, 1720 – 1732 (2006)

11 Danksagung

Bei folgenden Menschen möchte ich mich für ihre Unterstützung bedanken:

Bei Dr. Dieter Braun, der mir die Möglichkeit gegeben hat, in einem für mich völlig neuen Feld zu arbeiten, und der auch die Arbeit an anwendungsbezogenen Projekten immer unterstützt hat.

Bei Prof. Dr. Hermann E. Gaub für sein Interesse an der Umsetzung der auf Thermophorese basierenden Analyseverfahren und die freundliche Unterstützung.

Ich möchte mich bei den Mitarbeitern am Lehrstuhl von Prof. Dr. Hermann E. Gaub für die gute Arbeitsatmosphäre bedanken, besonders aber bei Philipp Baaske, Franz Weinert und Christoph Wienken, mit denen ich mir Schreibtisch und Labor in den letzten Jahren geteilt habe. Bei Angelika Kardinal für die Präparation von verschiedensten DNA Proben.

Bei Dr. Ullrich Rothbauer und Prof. Dr. Heinrich Leonhardt für fluoreszenzmarkierte Antikörper, und bei Ralph Sperling und Prof. Dr. Wolfgang Parak für die Zusammenarbeit bei der thermophoretischen Charakterisierung von Nanokristallen.

Bei meiner Familie.

Bei meinen Eltern.

Bei Nadine.

12 Anhang: Publikationen

Publikation I: Thermophoresis of DNA determined by microfluidic fluorescence, **Europ. Phys. J. E** 15, 277-286 (2004), Stefan Duhr, Silvia Arduini and Dieter Braun

Eur. Phys. J. E **15**, 277–286 (2004)
DOI 10.1140/epje/i2004-10073-5

THE EUROPEAN PHYSICAL JOURNAL E

Thermophoresis of DNA determined by microfluidic fluorescence

S. Duhr, S. Arduini, and D. Braun[a]

Dissipative Biosystems Lab, Applied Physics, Ludwig Maximilians Universität München, Amalienstr. 54, 80799 München, Germany

Received 6 September 2004 and Received in final form 14 October 2004 /
Published online: 17 November 2004 –

Abstract. We describe a microfluidic all-optical technique to measure the thermophoresis of molecules. Within micrometer-thick chambers, we heat aqueous solutions with a micrometer-sized focus of infrared light. The temperature increase of about 1 K is monitored with temperature-sensitive fluorescent dyes. We test the approach in measuring the thermophoresis of DNA. We image the concentration of DNA in a second fluorescence-color channel. DNA is depleted away from the heated spot. The profile of depletion is fitted by the thermophoretic theory to reveal the Soret coefficient. We evaluate the method with numerical 3D calculations of temperature profiles, drift, convection and thermophoretic depletion using finite element methods. The approach opens new ways to monitor thermophoresis at the single molecule level, near boundaries and in complex mixtures. The flexible microfluidic setting is a good step towards microfluidic applications of thermophoresis in biotechnology.

PACS. 87.23.-n Ecology and evolution – 82.70.Dd Colloids – 82.60.Lf Thermodynamics of solutions

1 Thermophoresis of biomolecules

Separation techniques such as gel electrophoresis are at core of modern DNA and protein biotechnology. However, electrophoresis is hard to miniaturize due to electrochemical effects at the metal-buffer interface and the tedious preparation of gel phases. We follow a new approach by driving biomolecules with strong but microscopic temperature gradients. Although the basic effect of this movement —called thermophoresis or Soret effect [1–5]— is now known for almost 150 years, the effect was only recently applied by us to DNA [6]. Our aim is to elucidate novel approaches to make use of thermophoretic driving forces in miniaturized biotechnology devices. Thermophoresis has an interesting history in applied chemistry and physics. For example, Clusius in 1938 found that convection can couple to thermophoresis in a way that highly amplifies the accumulation effect [7, 8]. The approach, called Clusius separation tube (Trennrohr) or gravitational column, is still used to measure thermophoretic constants of highly diffusive components. On the other hand, non-aqueous polymers were separated by thermal field flow (TFF) separation [9]. Recently, a miniaturized design was made by the group of Frazier with chamber dimensions as low as $2 \times 40 \times 0.03\,\mathrm{mm}$. It was used to separate beads in water [10,11]. In a recent speculation, we argued that thermophoresis could have played a role in molecular evolution near hydrothermal vents [12]. Here we will discuss novel all-optical approaches in thin microfluidics to measure and apply thermophoresis for biomolecules in tiny volumes. We used the aforementioned approach to estimate thermal diffusion coefficients of DNA [6]. Working at the boundary between disciplines, we use fluorescence microscopy from biology, infrared heating from applied optics and complex liquid handling from microfluidics. Our approach can apply very strong temperature gradients ($> 1\,\mathrm{K}/\mu\mathrm{m} = 10000\,\mathrm{K/cm}$) in flexible microfluidic settings under excellent fluorescence microscopy conditions. We detect both temperature and particle concentration by fluorescence. This yields a flexible experimental platform to confirm basic characteristics of thermophoresis. Microscopic imaging allows to measure slowly diffusing molecules within reasonable times. For example, 50.000 base pair λ-DNA (diffusion constant of $D = 10^{-12}\,\mathrm{m^2\,s^{-1}}$) can be measured within 300 s. Since we microscopically image the sample, artefacts such as dirt or sample inhomogeneity are immediately recognized. Also liquid movement such as convection or drift yields precise fingerprints in the concentration image. Moreover, with the fluorescence approach, we have the prospect of following thermophoresis down to the single molecule level. We are not only motivated by possible applications of thermophoresis. To our day, the theoretical description of thermophoresis in liquids is not yet understood. The out-of-equilibrium nature of thermophoresis makes its description difficult to be described. The recent work of many labs and researchers, for example of Werner

[a] e-mail: dieter.braun@physik.lmu.de, mail@dieterb.de

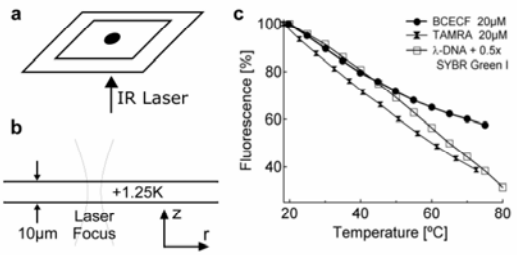

Fig. 1. Temperature control for all-optical imaging of thermophoresis. (a) A thin chamber is sandwiched between glass cover slides. The center of the chamber is locally heated by a a moderately focussed infrared laser. (b) We choose a chamber thickness of 10 μm and heat moderately in the center by 1.25 K. (c) The local temperature is inferred from the temperature dependence of pH-dependent fluorescent dyes in TRIS buffer as measured independently in a fluorometer. The negative slopes mean that a darkening in the fluorescent image can be interpreted as increase in temperature.

Köhler [13,14] and Roberto Piazza [15–17] shed new light into the mechanics of thermophoresis of polymers, micelles and proteins in aqueous solutions. Only by collecting thermophoresis data in as diverse as possible situations we can hope to understand the effect.

2 Materials and method

2.1 Chamber

For a most simple measurement approach, we enclose 2 μl of sample between 0.17 mm thick cover slips (Roth Laborbedarf). The sample is placed on a 24×40 mm cover slip and closed by pressing a smaller 18 mm $\times$ 18 mm cover slip from the top. The liquid stops at the boundary of the smaller cover slip and wets its area. Then it is sealed with immersion oil at the periphery (Fig. 1a). Based on the volume-area ratio, we expect a sample film of 6 μm thickness. However, since the immersion oil creeps into the chamber from the sides, the chamber might be 1–2 μm thicker. It should be noted that the method does not sensitively depend on the precise knowledge of the chamber thickness. After 20 minutes of equilibration, drifts in the chamber drop typically below 0.03 μm/s.

2.2 Microfluidics

For more sophisticated geometries, we use the well-known PDMS-SU-8 microfluidics. The low IR-absorption and low thermal conductivity ($\lambda = 0.18\,\mathrm{W\,m^{-1}\,K^{-1}}$) makes PDMS a perfect material for infrared heating. The connection between PDMS microfluidics and the glass needs however special care to be reliable and non-leaking. We use PDMS-PDMS bonding, but change the protocol of Quake's group [18] to keep the chamber compatible with oil objectives. The process is as follows. A thin layer of 1 : 5 PDMS is spin coated on 24×40 mm cover slips at 2000 rpm, leading to a film of about 20–30 μm as measured by weighing the slides. After curing for 15 min on a 70 °C hot plate, the PDMS is solid but still sticky to glue upon contact to the 1 : 10 bulk PDMS. The channels seal fully after curing at 60 °C for 2 h.

2.3 Infrared heating (Fig. 1a,b)

The fiber-coupled solid-state laser Furukawa FOL1405-RTV-317 yields a center wavelength of $\lambda = 1480$ nm at 320 mW maximum power. It is mounted on an ILX Lightwave LDM-4984 and current and cooling controlled by an ILX Lightwave LDC-3744B. The current can be modulated from the analog output of a computer-controlled digital-analog DAQPAD-6070E Firewire-based I/O-card from National Instruments using LabView 7.0. The infrared light is coupled out of the fiber to a $1/e^2$ diameter of 3 mm with a Thorlabs output coupler F260FC-C and then scanned by a Cambridge Technology 6200-XY Scanner with Driver 67120. After fully expanding the beam to 6 mm by a 19 mm/40 mm focal distance beam expander (Thorlabs), it is focussed with a infrared corrected Mitutoyo objective NIR 5× with working distance 38 mm and numerical aperture 0.14. We achieve a minimal Gaussian $1/e$ profile width of 8 μm (Fig. 1b). The focus can be easily broadened by moving the thin chamber along the optical axis in z-direction. Water highly absorbs at this wavelength with an attenuation length of $k = 400\,\mu$m.

2.4 Fluorescence imaging of temperature (Fig. 1c)

We exploit the pH drift of 10 mM TRIS buffer upon temperature change. The drift is measured by a pH-sensitive fluorescent probe. This allows usage of highly soluble fluorescent probes. All optical probes of temperature pursued previously only worked for non-aqueous solutions. The temperature dependence of the dye was measured with a temperature-controlled fluorometer (Fig. 1c). Near 20 °C, we obtain temperature sensitivities of $B = -1.13\%/\,\mathrm{K}$ for TAMRA (20 μM, C-300, molecular probes), $B = -0.95\%/\,\mathrm{K}$ for BCECF (20 μM, B-1151 mixed isomers, molecular probes).

2.5 DNA and DNA staining

We use the DNA of the bacteria-attacking virus lambda (λ). λ-DNA has a length of 48502 base pairs. We stain DNA with low concentrations of SYBR Green I (S-7563, molecular probes). Starting from 0.46 μg/μl (14 nM) stock solution (Invitrogen/Gibco BRL, Cat. No. 25250-010), we dilute the DNA 1 : 10 into a 10 mM TRIS-HCl buffer (pH 7.8). Short DNA with a length of 27 base pairs was hybridized from synthetically produced oligomers

(IDTDNA) and diluted to 10 μM. We add 2× SYBR-Green and 20 μM of TAMRA. The dye intercalates into DNA, but changes the overall DNA characteristics only minimally. For example, SYBR-stained DNA can still be replicated with a PCR reaction.

2.6 Fluorescence imaging and bleaching correction

We use the microscope Zeiss Axiotech Vario with objective Plan Fluar 40×, NA 1.3 oil. For illumination, a Luxeon High power LEDs LXHL-LX5C was built into a standard halogen lamp housing and driven at 30–700 mA by an ILX Lightwave LD-3565 current source. Fluorescence filters were from AHF-Analysentechnik, Tübingen for FITC (HQ F41-001). Detection was provided with a 12-bit camera PCO Sensicam QE 670KS with 65% quantum efficiency. The camera has a linear light response at negligible background levels. For slow diffusing specimen, the illumination was switched off during equilibration to reduce bleaching. Fluorescence imaging averages the fluorescence across chambers thinner than about 30 μm. This can be demonstrated by focussing a layer of adsorbed fluorescent beads. For objectives with low numerical aperture, averaging spans almost 1 mm as documented in [6]. However, we had to check that this averaging across the chamber is independent of lateral temperature gradients. These can bend the light rays of excitation and emission from their optimal configuration, leading to a defocussed image and lower fluorescence readings. Note that this lensing effect differs from thermal lensing methods which measure the focal length of the created lens in the far field. Since defocussing-induced fluorescence imaging artefacts are small at NA = 0.4 due to the large averaging focus, we can use it as reference. We compared fluorescence images of the same radial temperature profiles measured at NA = 0.4 and NA = 1.3. Both images differed only in the central 10 μm region relative to each other by 5%. We therefore infer that averaging fluorescence across thin chambers is reliable even under lateral temperature gradients used in our experiments. To be independent of inhomogeneous fluorescence illumination, images in the heated state are normalized against previously taken cool pictures. Also, a cool picture after measurement is taken to allow for a linear bleaching correction over time. In all experiments, illumination intensity is low such that bleaching was below 20% and linear bleaching correction was applicable.

3 Numerical simulations

3.1 3D simulation of temperature profile (Fig. 2)

We calculate the shape of the temperature profile across the chamber. Since the fluorescence measurements average all fluorescence across the chamber, its exact profile should not affect the result. The laser focus is described with a minimal $1/e^2$-radius of $\sigma_0 = 8\,\mu$m, attenuation length $k = 400\,\mu$m, refractive index of water $n = 1.333$ focussed

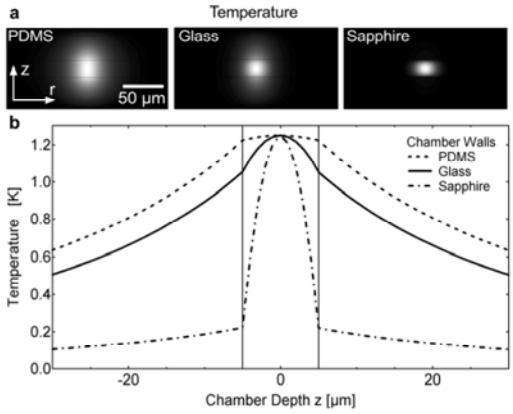

Fig. 2. Temperature profile in a 10 μm thin chamber (theory). (a) The recorded fluorescence images average across the thin chamber. The detailed temperature profile across the chamber was calculated for different chamber wall materials. (b) Whereas low thermal conductive PDMS leads to almost constant temperature profile across the z-axis, the increased thermal conductivity of glass or even sapphire yields steeper parabolic temperature profiles.

at height $z = z_0$ in the center of the chamber with a numerical aperture of NA = 0.14 with Gaussian shape in geometrical approximation. We obtain the absorbed light power density $I(r, z)$:

$$\sigma = \sigma_0 + \tan\left[\arcsin\left(\frac{\mathrm{NA}}{n}\right)\right] \times |z - z_0|\,,$$
$$I(r,z) \propto \sigma^2 \times \exp\left(-\frac{2r^2}{\sigma^2}\right) \times \exp\left[-\frac{(z-z_0)}{k}\right]\,. \qquad (1)$$

It should be noted that the chamber thickness below 10 μm is much smaller than the attenuation length of the light. Therefore, the focus can be approximated by

$$I \propto \exp\left(-\frac{2r^2}{\sigma^2}\right)\,. \qquad (2)$$

The total absorbed laser power is adjusted to increase the chamber liquid temperature in the center by 1.25 K above room temperature in all shown simulations. The light pressure pushes the liquid with a radiation force density f obtained from dividing the absorbed light intensity I by the light velocity c_0:

$$f = \frac{I}{c_0}\,. \qquad (3)$$

All numerical calculations are done with the finite element simulator Comsol Femlab 2.3.154 + Chemical Engineering Module. The physical parameters of the materials were as follows. For water, density $\rho = 1000\,\mathrm{kg\,m^{-3}}$, heat capacity $c = 4200\,\mathrm{J\,kg^{-1}K^{-1}}$ and heat conductivity $\lambda = 0.54\,\mathrm{W\,m^{-1}K^{-1}}$; for PDMS, $\rho = 1030\,\mathrm{kg\,m^{-3}}$, $c = 1260\,\mathrm{J\,kg^{-1}K^{-1}}$ and $\lambda = 0.18\,\mathrm{W\,m^{-1}\,K^{-1}}$; for glass, $\rho =$

$2600\,\mathrm{kg\,m^{-3}}$, $c = 780\,\mathrm{J\,kg^{-1}K^{-1}}$ and $\lambda = 1.4\,\mathrm{W\,m^{-1}K^{-1}}$ and for sapphire, $\rho = 3980\,\mathrm{kg\,m^{-3}}$, $c = 750\,\mathrm{J\,kg^{-1}K^{-1}}$ and $\lambda = 34\,\mathrm{W\,m^{-1}K^{-1}}$. All FEMLab model files can be obtained from the authors. To show the influence of heat conductivity of the chamber on the temperature profile, we simulated the temperature in a $10\,\mu$m thick water film between $170\,\mu$m thick chamber walls. All calculations were done in cylinder coordinates and therefore reflect a full 3D model. The simulation of temperature across the chamber is seen in Figure 2. The liquid temperature is almost constant across the chamber for isolating PDMS chamber walls. It becomes parabolic with small tails for glass walls and is reduced for sapphire chamber to almost perfect parabolic shape. Profiles of the temperature across the chamber in the heating center are shown in Figure 2b. To reach the same temperature, the laser power has to be increased 4.7-fold as we go from PDMS to glass and again 4.7-fold as we change from glass to sapphire.

3.2 Theory of thermophoresis (Fig. 3)

Thermophoresis is described by a phenomenological term that extends Fick's first law. The concentration current density j depends on the concentration c given in the molar ratio of molecules *versus* liquid molecules as follows:

$$j = -D[\nabla c + S_T c(1-c)\nabla T] \tag{4}$$

The Soret coefficient S_T is the ratio of the thermal diffusion coefficient D_T and the diffusion coefficient D: $S_T = D_T/D$. The description of thermophoresis by equation (4) is phenomenological and still lacks a microscopic understanding. Further measurements of thermal diffusion coefficients D_T are important to reveal the detailed mechanism underlying thermophoresis.

We use equation (4) to simulate thermophoresis in 3D by finite element methods in cylinder coordinates. The result is shown in Figure 3. The water in the chamber is heated to a peak temperature increase of 1.25 K (Fig. 3a). With the diffusion constant of λ-DNA [19] of about $D = 1 \times 10^{-12}\,\mathrm{m^2\,s^{-1}}$ and the thermal diffusion coefficient $D_T = 0.4 \times 10^{-12}\,\mathrm{m^2\,K^{-1}\,s^{-1}}$ that we measure later, we find the thermophoretic depletion of Figure 3b. The concentration of DNA in the center of the chamber drops to 60% with a spatial distribution directly governed by equation (5). It is derived for small probe concentrations c and constant D_T in non-moving liquids from equation (5):

$$\frac{c}{c_0} = e^{-S_T(T-T_0)} \approx 1 - S_T(T-T_0)\,. \tag{5}$$

For small temperatures $\Delta T D_T/D \ll 1$, the linear extension is valid and will be used heavily in the derivations of the following section in fluorescence imaging corrections.

Any central heating leads to thermal convection from lateral temperature gradients. The measurement idea is to choose a thin chamber to highly dampen convection. The convection is driven in the same direction both by thermal expansion of water under gravity and by light pressure of the heating infrared light. We solve the Navier-Stokes equations for water together with heat transfer and the diffusion equation of DNA. The maximal convection speed is found to be $0.055\,\mu$m/s. This convection has the potential to perturb the concentration profile shaped by thermophoresis. However, even for slow-diffusing species such as λ-DNA, the simulation shows that convection is not fast enough to change the concentration profile. The concentration profile shows the same shape as the temperature profile and can be still directly inferred from non-flow conditions given by equation (5).

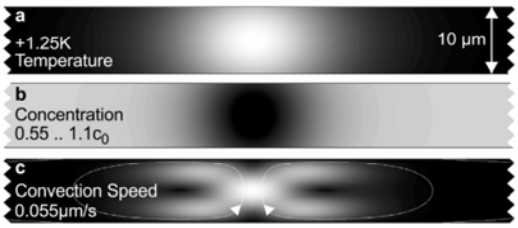

Fig. 3. Convection and thermophoresis in thin chamber (theory). Any central heating leads to thermal convection from lateral temperature gradients. The measurement idea is to choose a thin chamber to damp convection. The validity of the approach is tested by finite element solutions of the Navier-Stokes equation. We find a maximal convection speed of $0.055\,\mu$m/s. Even for slow-diffusing species such as λ-DNA ($D = 1 \times 10^{-12}\,\mathrm{m^2/s}$), convection is not fast enough to perturb the concentration profile.

3.3 Temporal response and equilibration time (Fig. 4)

Under conditions of small temperature differences and low convection, we can reduce the description to a one-dimensional axial model. We add a linear cooling term to model the surface cooling of the chamber. It is adjusted to obtain the radial temperature profile of the 3D calculation. The reduction of the theoretical model to one dimension allows easy simulations of the temporal response in the experiment. The radial depletion of λ-DNA can already be seen after seconds and develops into a steady-state profile after several 100 s (Fig. 4a). We find a similar temporal response also in the experiments. The final depletion reflects the applied temperature increase of 1.25 K above room temperature according to equation (5). The temporal drop of the concentration of DNA in the center of the chamber is a non-trivial function of time due to the radial geometry of the measurement (Fig. 4b). The final central concentration drops to 60% of the initial concentration after more than 100 s.

3.4 Convection artefact in thicker chambers (Fig. 5)

Thicker chambers increase the speed of convection and can even turn thermophoretic depletion into accumulation [6]. We keep the heating of the chamber constant

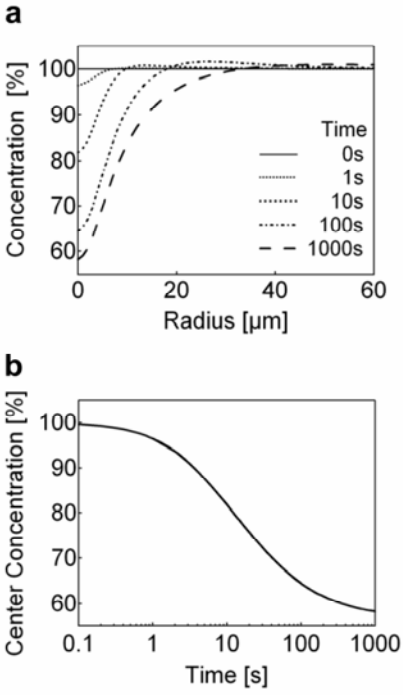

Fig. 4. Thermophoresis over time (theory). Under conditions of small temperature and low convection, we can reduce the description to an axial model with only one radial dimension. This allows for simulations of the temporal response of thermophoretic depletion. (a) The radial profile reaches steady state for λ-DNA after several 100 s. It reflects the applied temperature profile according to equation (5). (b) The concentration of DNA in the center of the chamber drops with a non-trivial characteristics due to the Gaussian radial heating geometry of the measurement. The final central concentration drops to 60% of the initial concentration after more than 100 s.

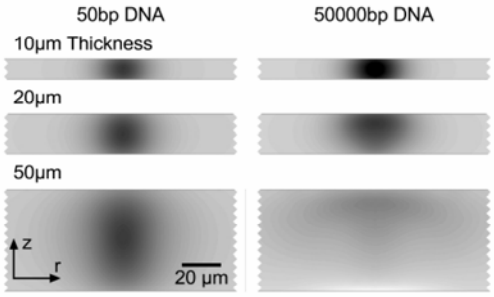

Fig. 5. From depletion to accumulation by convection in thicker chambers (theory). We keep the heating of the chamber constant at 1.25 K above ambient temperature and increase the chamber thickness. For a fast-diffusing 50 base pair DNA, this has no effect on the central depletion profile of about 98%. However, for slow-diffusing λ-DNA, chamber thickness even at these low temperatures is crucial. Already at 20 μm the concentration profile becomes asymmetric at reduced minimal concentration. For a 50 μm thick chamber, we find conditions of enhanced concentration ($c = 1.1c_0$) at the lower chamber wall. This accumulation to a point by thermophoresis was reported earlier in thicker chambers under stronger heating [6]. The convection artefact of thicker chambers is easily seen experimentally when a concentration profile does not match the theoretical profile that is calculated from the measured temperature.

to 1.25 K above ambient temperature and increase the chamber thickness. As we choose chamber thicknesses of 10, 20 and 50 μm, the maximal convection speed has values of 0.055, 0.22 and 1.5 μm/s. The flow characteristics is similar to Figure 3c. We show two scenarios: fast-diffusing DNA of length around 50 base pairs with $D = 34 \times 10^{-12}\,\mathrm{m^2\,s^{-1}}$ (Fig. 5, left) and slow-diffusing DNA with about 50.000 base pairs $D = 1 \times 10^{-12}\,\mathrm{m^2\,s^{-1}}$ (Fig. 5, right). For both we assume the same thermal diffusion coefficient $D_T = 0.4 \times 10^{-12}\,\mathrm{m^2\,K^{-1}\,s^{-1}}$. Faster convection has no effect on the depletion profile and we can measure thermophoresis using equations (4–10). We might even enhance the temperature to obtain better signals. For slow-diffusing DNA, chamber thickness even at low temperatures is crucial. Already at 20 μm chamber thickness, the concentration profile becomes asymmetric and the center concentration is reduced. For a 50 μm thick chamber, we even find a 10% enhancement of concentration ($c = 1.1c_0$) at the lower chamber wall. This accumulation by thermophoresis and convection was experimentally found by us before [6]. In thermophoretic measurements, this convection artefact of thicker chambers can be seen in a concentration profile which then does not match the measured temperature profile. Therefore, the condition of a too thick chamber can be readily detected. The plume of convective-thermophoretic accumulation is similar in shape to the standing-wave oscillations studied by Lücke *et al.* [20]. In both cases, concentration differences created by thermophoresis are transported by convection. However, the detailed mechanism is different since here the convection is only driven by thermal expansion.

3.5 Influence of light pressure on convection (Fig. 6)

The effect of light pressure upon absorption is not negligible. Convection in thin chambers differ when infrared heating is applied from top or from the bottom. The effect can be experimentally seen for example when we directly put the end of the glass fiber of the laser into water: a flow that is driven by the light coming out the fiber is clearly visible. This light pressure effect has to be taken into account also in thermophoresis measurements by thermal lensing as we indicated to the authors of [17], where an estimate of the effect and a discussion of its dependence on the experimental conditions is given. We show here that the effect of light pressure can reduce the upward convection. It is even possible to invert the convection. However, we cannot directly balance convection by light pressure as shown in the following. For the simulation, we choose a

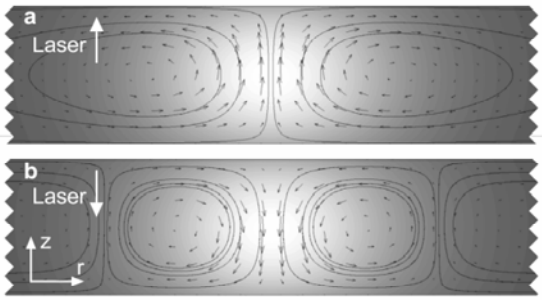

Fig. 6. Effect of light pressure on convection (theory). Momentum of light cannot be neglected when water is heated by infrared radiation. We give an example for a 50 μm thick chamber heated by 1.25 K in the center. Without light pressure, the maximal convection speed would be +0.15 μm/s. (a) If the light comes from below, the convection speed increases to 0.5 μm/s. (b) Light from above can invert the convection flow, forcing it down in the center with −0.2 μm/s. Only in the periphery it still convects upwards with +0.05 μm. Convection therefore is not balanced in detail, but reduced if IR-heating is applied from above.

50 μm thick chamber heated again to 1.25 K above ambient temperature in the center. Without light pressure, the maximal convection speed would be +0.15 μm/s. If the light comes from below, the convection speed increases to +0.5 μm/s (Fig. 6a). Light from above can invert the convection flow, forcing it down in the center with −0.2 μm/s. It convects only in the periphery upwards with +0.05 μm (Fig. 6b). These two counter-moving convection tubes are formed due to the different locations of force generation. Heat conduction broadens the temperature distribution as compared with the light radiation that heats and at the same time moves the liquid with its light pressure. Therefore, at the periphery, fluid flow is directed upwards since temperature is still increased, but light pressure from above is too low. In first order, the effect of convection reversal by light radiation is not depending on the chamber thickness. This is because the absorbed light radiation that pushes the liquid depends quadratically on the chamber thickness. The reason is that the system is dominated by the cooling walls and thus by quadratically scaling diffusion of heat diffusion to the walls. In a viscous laminar system, this is proportional to the speed of the liquid. Therefore, liquid flow from radiative pressure scales quadratically with the thickness of the chamber if the chamber is heated to the same temperature. On the other hand, thermal convection in a chamber heated to the same temperature scales quadratically with the chamber thickness as discussed in [17]. Therefore, both effects scale equally for thin chambers. However, in our full 3D simulations, the light pressure effect is decreasing more for thicker chambers. For example a 100 μm thick chamber yields a central downward flow of only −0.075 μm/s, yet heating with light from below gives an upward velocity of +2 μm/s.

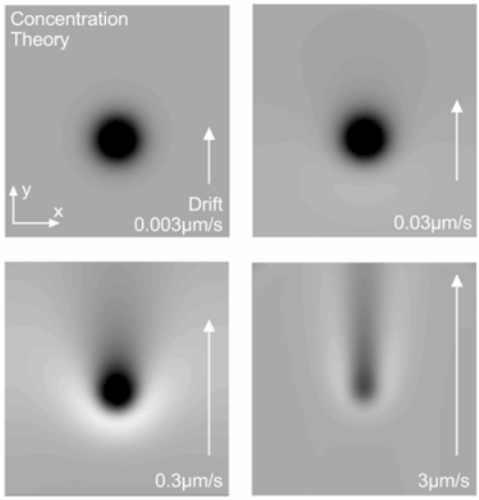

Fig. 7. Flow distortion by solution drift (theory). Besides convection, drift of the liquid in the chamber is a major source of artefact in a thermophoresis measurement. However, the imaging approach allows to detect this drift easily. We show 2D simulations of thermophoresis of λ-DNA for a liquid drift of 0.003, 0.03, 0.3 and 3 μm/s. The shown chamber section is 100 μm × 100 μm wide. The heating spot parameters are the same as in Figures 3–5. Already for drifts below 0.03 μm/s we see a noticeable distortion of the radial profile which increases as the drift velocity increases. At about 0.3 μm/s, a strong accumulation is found below the heating spot as thermophoretic drift and liquid drift counteract. Experimentally, drift-free chambers are prepared by sealing the chamber with oil and waiting 20 min to equilibrate.

3.6 Thermophoresis against horizontal drift (Fig. 7)

A small horizontal drift of the solution is commonly found under microfluidic conditions. Typically, it originates for example from external pressures, gravitational flow, evaporations at the openings of the chamber or simply from thermal expansion induced by inhomogeneous chamber temperatures. The drift distorts the depletion profile along the flow. Besides convection, drift of the liquid in the chamber is a major source of artefact in a thermophoresis measurement. The imaging approach allows to detect drift very easily from an asymmetric concentration image. This effect can be simulated when we extend the one-dimensional axial simulation used in Figure 4 to a 2D situation. We calculate the thermophoresis of λ-DNA for a central liquid drift of 0.003, 0.03, 0.3 and 3 μm/s. A 100 μm × 100 μm section of the chamber is shown in Figure 7. The heating parameters are identical to the ones used beforehand in Figures 3–5. For drifts below 0.03 μm/s we see a noticeable distortion of the radial profile which increases as the drift velocity increases. At about 0.3 μm/s, a strong accumulation is found in the region of the heating spot where thermophoretic drift and liquid drift have opposite direction. Here, thermophoretic drift and liquid

drift counteract. Experimentally, it is often a challenge to meet the drift-less criteria for slow-diffusing specimen. For chambers made out of cover slips, sealing the chambers with oil and waiting for 20 min yields drift-free chambers in most cases. The effect of drift can be much reduced by using dead end structures in microfluidic channels.

4 Fluorescence imaging of concentration and temperature

We will discuss in the following how concentration and temperature can be extracted from fluorescence images. As described in materials and methods, we measured fluorescence intensities F_T for the temperature dye and F_c for the DNA dye. Both are imaged in the cold state at T_0 —denoted by F_T^0, F_c^0— and later in the heated state at temperatures $T(x,y)$ —denoted by F_T, F_c. The temperature-sensitive dye depends on small temperature changes $T - T_0$ with a linear slope B given in percent fluorescence change per K temperature change [%/K] (Fig. 1c). The fluorescence intensity of the probe marker F_c reports the probe concentration c:

$$F_T = F_T^0[B(T - T_0) + 1] , \qquad F_c = F_c^0 \frac{c}{c_0} , \qquad (6)$$

F_c^0 is the fluorescence intensity of the probe marker at both background concentration c^0 and cold temperature T_0. Inserting equation (6) into the linearly approximated form of thermophoretic depletion given by equation (5) leads to a linear relationship between F_c and F_T:

$$\frac{F_c}{F_c^0} = 1 - \frac{S_T}{B} \frac{F_T - F_T^0}{F_T^0} . \qquad (7)$$

Both linear relationships, namely that of F_T to the temperature according to equation (6) and that of F_c to F_T according to equation (7) makes it possible to infer them from the images which inherently record a cross-chamber average. This means that averaging across the chamber, which we will denote by the operator $\langle\ \rangle$, leads to the same prefactor for both F_T and F_c since they integrate over the same functional shape. Thus, we can infer the Soret coefficient directly from the measured, averaged fluorescence intensities $\langle F_T \rangle$ and $\langle F_c \rangle$:

$$S_T = \frac{D_T}{D} = -\left(\frac{\langle F_c \rangle}{\langle F_c^0 \rangle} - 1 \right) \frac{\langle F_T^0 \rangle}{\langle F_T \rangle - \langle F_T^0 \rangle} B . \qquad (8)$$

To be more precise, we have to include into the description a possible temperature dependence of the probe marker itself. For example, SYBR-Green has a marked temperature dependence of $B^* = -0.96\%/\,\mathrm{K}$ (0.5× SYBR Green I with λ-DNA, Fig. 1c). We include this effect with the following substitution of the concentration fluorescence from equation (6):

$$F_c = F_c^0 \frac{c}{c_0} [B^*(T - T_0) + 1] . \qquad (9)$$

The problem is that this additional temperature dependence breaks the linear averaging argument used above. Now, other than in equation (7), F_c is a non-linear function of the relative temperature change $f_T = (F_T - F_T^0)/F_T^0$:

$$\frac{F_c}{F_c^0} = -\frac{S_T}{B} \left[f_T + f_T^2 \frac{B^*}{B} \right] . \qquad (10)$$

We have to consider this non-linearity especially for strong heating and have to take into account the precise temperature characteristic across the chamber. However, for our experiments with λ-DNA, the relative temperature change f_T is only 1.4%. This is much larger than the quadratic term $f_T^2 B^*/B = 0.017\%$, leading to an error if we neglect the effect of 1.2% in S_T. This deviation is however below our overall measurement precision.

We have to consider another possible source of error. In using temperature-sensitive dyes with characteristics measured in thermodynamic equilibrium in a fluorometer, we assume that thermophoretic depletion of the temperature dye itself can be neglected. In a preliminary estimation, the dye has a similar monomer thermodiffusion as the highly charged DNA, namely approximately $D_T = 0.4 \times 10^{-12}\,\mathrm{m^2\,K^{-1}\,s^{-1}}$. Together with the diffusion constant of a similar dye FITC, $D = 5.1 \times 10^{-10}\,\mathrm{m^2\,s^{-1}}$, we infer a Soret coefficient $S_T = 0.0008\,\mathrm{K^{-1}}$. Preliminary measurements confirm similar Soret coefficients for the used temperature dye. We can infer the Soret coefficient of the dye from fast recordings of the temperature fluorescence upon laser heating. After a fast fluorescence drop we find a slower response which we attribute to thermophoretic depletion. The ratio of the two drops allow to infer the Soret coefficient of the dye, very similar to beam deflection methods of Giglio and Vendramini [21]. We can take for example a temperature increase of 1 K above room temperature. The intensity of the dye decreases by about 1% due to its temperature sensitivity. Its concentration due to thermophoresis is depleted however by only 0.08%. Thus, our measurement of temperature using fluorescent dyes is 8% too high. Hence, thermal diffusion coefficients have the possibility to be systematically too low by 8%. The effect of this systematic error will be studied in more detail in the future since it can be suppressed by taking the temperature image at an optimal time after switching on the laser.

5 Measuring thermophoresis of DNA

5.1 Recapitulation of method

Until now we have checked that thermophoresis should be measurable by microfluidic fluorescence without artefacts. An infrared focus is heating water optically to a temperature which we detect by fluorescence imaging. It causes a thermophoretic depletion that is recorded by fluorescence at a different color. By comparing the temperature profile with the concentration profile in steady state, we can infer the Soret coefficient.

We have checked that both the temperature profile and the concentration profile across the chamber have the same parabolic shape. Since we are in the linear regime of equation (5), the averaging across the chamber performed by fluorescence imaging introduces no artefact. By using a $< 10\,\mu$m thin chamber, convection is too slow to introduce a detectable deviation even for slow-diffusing specimen. A drift across the chamber is easily detectable in the concentration image. Thermophoresis of the temperature dye and temperature dependence of the DNA stain are negligible. Our protocols correct for bleaching of fluorescence dyes and inhomogeneous fluorescence illumination.

5.2 Measuring thermophoresis of DNA (Fig. 8)

After checking for possible artefacts, we can now proceed to the experiment. We image the temperature of the infrared-heated water with the fluorescent dye TAMRA in the red-color channel. After bleaching and correcting for inhomogeneous illumination, we extract the temperature image given in Figure 8a. The center of the chamber reveals an increase of temperature by a cross-chamber average of 1.25 K above room temperature. In the green-color channel, we image λ-DNA with the dye SYBR-Green, prepared as described in the methods section. We take the cold image, heat for 300 s without illumination and take a hot image. After correcting for bleaching and the temperature sensitivity of SYBR-Green, we can extract the relative concentration image of DNA (Fig. 8b). DNA is depleted to a cross-chamber average of 60% at the center. Note that the grainy image is not noise, but already the fingerprint of highly diluted single λ-DNA molecules. We do radial averaging of both images (Fig. 8c). This is especially necessary for the noisy temperature image. We fit the radial concentration profile (circles) with the theoretical concentration profile (solid line). The theoretical expectation is inferred from the measured temperature profile with equation (10). We find a nearly perfect fit between measured and calculated concentration profiles for a Soret coefficient $S_T = 0.4\,\mathrm{K}^{-1}$. A full numerical correction of the parabolic z-profile in the chamber changes the result only within experimental noise.

We could infer the diffusion constant of λ-DNA by following the backdiffusion. However, this measurement is quite noisy since the slow diffusion leads to considerable bleaching of SYBR. In future measurements this will be better optimized as we will change to a geometry that is more easily accessible by theory. We will then take images at specific times of the initial depletion to also infer the diffusion constant. Here, we confirmed qualitatively that diffusion is similar to the value of about $D = 1 \times 10^{-12}\,\mathrm{m}^2\,\mathrm{s}^{-1}$ published for λ-DNA [22] and rely on the fact that diffusion of molecules is not changed much near a surface [23]. We therefore obtain a thermal diffusion coefficient $D_T = 0.4 \times 10^{-12}\,\mathrm{m}^2\,\mathrm{K}^{-1}\,\mathrm{s}^{-1}$. We repeat the experiment, adding 500 mM of NaCl. No thermophoretic depletion can be seen (Fig. 8c, triangles). This indicates that DNA probably follows a similar salt dependence as reported for SDS-micelles [15].

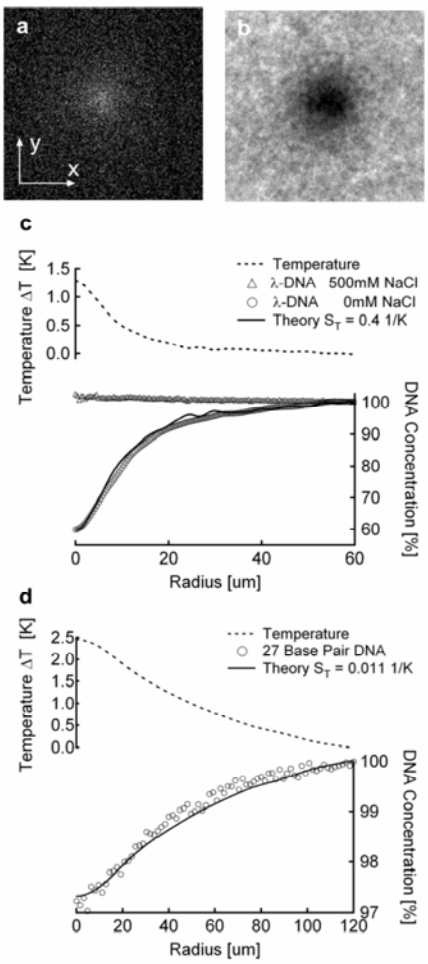

Fig. 8. All-optical thermophoresis measurement of λ-DNA. (a) We image the temperature of the infrared-heated water with the fluorescent dye TAMRA in the red-color channel. After bleaching and illumination correction, we can extract a temperature image. We find the center of the chamber to be heated by 1.25 K above room temperature. (b) In the green-color channel, we image λ-DNA with the dye SYBR-Green I. After bleaching correction and correction for the temperature sensitivity of SYBR, we compute the relative concentration image of DNA. It is depleted to 60% in the heated center. Note that the grainy image is no noise, but the fingerprint of single λ-DNA molecules. (c) Quantitative evaluation is done by radial averaging of above images. Fitting the radial concentration profile with equation (10), using the temperature from the radially averaged temperature image, we find a very good match. The only fitting parameter is the Soret coefficient $S_T = 0.4\,\mathrm{K}^{-1}$. If we add 500 mM of NaCl, no thermophoretic depletion can be seen. We wait 300 s for the equilibration. Evaluation with full correction of the z-profile in the chamber changes the result only within the noise of the experiment. (d) Also short DNA of 27 base pairs can be measured. The depletion is much less pronounced: we find a Soret coefficient $S_T = 0.011\,\mathrm{K}^{-1}$.

The method is not restricted to large molecules. In Figure 8d, we measured the thermophoresis of a 27 base pair DNA. As expected, the depletion is significantly smaller. The DNA concentration in the center drops only by 2%. The numerical fit (Fig. 8d, solid line) yields a Soret coefficient $S_T = 0.011\,\mathrm{K}^{-1}$. Together with the literature value for the diffusion of DNA of this size [22] of $D = 36 \times 10^{-12}\,\mathrm{m}^2\,\mathrm{s}^{-1}$, we can infer a thermal diffusion coefficient $D_T = 0.4 \times 10^{-12}\,\mathrm{m}^2\,\mathrm{K}^{-1}\,\mathrm{s}^{-1}$. Note that we broadened the heating profile by defocussing the heating laser spot. In this way, we obtain better statistics in the central pixels of the depletion.

5.3 Estimation of error

We give a short overview over the possible error influences discussed beforehand. First of all, the CCD Camera is working at the photon shot noise limit and records intensities with a typical error of 0.5% per pixel. Radial averaging reduces this error greatly down to about 0.05%. This translates to concentration measurement precision of 0.05% and a temperature error of about 0.05 K. This means that Soret coefficients S_T have statistical errors ranging from 2% for large molecules up to 5% for small molecules. As discussed, S_T might be systematically too low by up to 8% as we neglected the thermophoresis of the temperature dye itself. Also, quadratic corrections in the temperature correction of the concentration fluorescence signal can introduce systematic errors of about 1.2%. So far, the method relies on lieterature values for the diffusion coefficient D, which introduces systematical errors of perhaps 30–40%. Small changes in the chamber thickness are not expected to influence the measurement. Therefore, we expect for the method as presented here a precision of about 40% for our measurements. Most of the above error sources will be further optimized in the future. Nevertheless, we accept the above drawbacks since the fluorescence approach gives direct microscopic control over thermophoresis measurements. First of all, fluorescence detection is highly sensitive and allows to measure very low concentrations, down to detecting single molecules. Moreover, we can do thermophoretic measurements in tiny volumes of about $20 \times 20 \times 10\,\mu\mathrm{m}$ (4 femtoliters), opening thermophoretic approaches for highly precious samples. Additionally, the method is selective and only measures thermal diffusion coefficients of the stained molecule even in very complex mixtures. Last but not least, the imaging allows for easy detection of preparation artefacts such as inhomogenous samples, dirt, liquid drift or convection.

5.4 Thermophoresis of DNA under liquid flow (Fig. 9)

We have observed in simulations (Figs. 5 and 7) that thermophoretic depletion can lead to accumulation when the liquid flow works in the opposing direction. Here we show two cases. In both, heating generates a counteracting flow simply by convection. Therefore, only local heating can lead to accumulation of DNA. It opens to interesting dynamics as convection interacts with thermophoretic drift that is generated from the identical heat source.

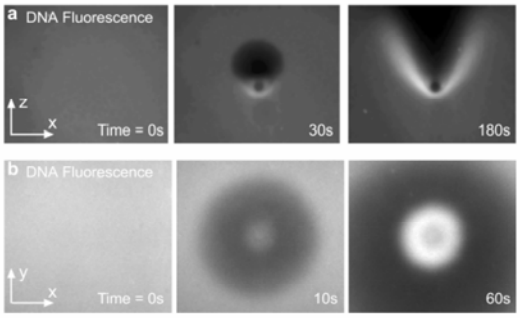

Fig. 9. Accumulation from thermophoresis working against convection. We have seen in simulations (Figs. 5 and 7) that thermophoretic depletion leads to accumulation when the liquid flow works in the opposing direction. We show two cases, where heating generates this flow by convection. Both cases show how convection geometries interact with the thermophoretic drift generated from the same heat source. (a) A vertically oriented glass chamber (80 μm thick, 500 μm image width) generates a convection pattern in the shape of "∞" . At the heating spot, fluid therefore flows from below, slightly from the left and the right side. Since thermophoresis of DNA is opposed, we find a V-shaped pattern, reminiscent of the drift simulation of Figure 7 where the liquid flow is only directed upwards. (b) A similar situation was discussed in detail in equation (6). In a geometry similar to the simulation of Figure 5, a rather thick chamber (50 μm) is heated from below. Thermophoresis and convection lead to a ring-shaped accumulation of DNA near the bottom chamber wall.

In Figure 9a, we see a vertically oriented glass chamber of 80 μm thickness that generates a convection pattern in the shape of "∞". At the heating spot, fluid flows from below, slightly from the left and the right side. Since thermophoresis of DNA is opposing the convection, we find a V-shaped pattern, reminiscent of the drift simulation of Figure 7 where the liquid flow is only directed upwards.

In a second case (Fig. 9b), discussed in more detail in [6], a geometry is studied that is similar to the simulation in Figure 5. A rather thick chamber (50 μm) is heated from below. Thermophoresis and convection leads to a ring-shaped accumulation of DNA near the bottom chamber wall. Both examples show that DNA accumulates in conditions where thermophoretic drift opposes convection flow.

6 Conclusions

We discussed how microfluidic fluorescence under infrared heating can be used to infer thermophoretic constants all-optically. The microscopic setting gives fast equilibration times. The thin chamber efficiently quenches convection below detectable limits. Fluorescence gives optical

resolution ($< 1\,\mu$m) and allows to reach single-molecule sensitivity. Moreover, we can measure thermophoresis of selected molecules in complex and viscous fluid mixtures. Thermophoresis is traditionally used to measure diffusion of molecules [21], an approach which will be accessible also to the femtoliter-sized microfluidic volumes used in this study. Since fluorescence and infrared heating can be performed by a laser scanner in complicated microfluidic designs, the method presented here is able to apply thermophoretic effects in a wide range of interesting settings. The approach will be useful for basic research questions such as single-particle tracking under thermophoresis to resolve the underlying microscopic dynamics of thermophoresis. Moreover, it allows to study thermophoresis near surfaces. With the shown methods, thermophoresis can be applied to various microfluidic applications, such as sorting molecule mixtures by size. In this way, thermophoresis could be an important new biocompatible driving force in microfluidic technologies.

References

1. C. Ludwig, Sitzungsber. Akad. Wiss. Wien, Math.-Naturwiss. Kl. **20**, 539 (1856).
2. C. Soret, Arch. Sci. Phys. Nat. Genève **3**, 48 (1879).
3. J.C. Maxwell, J.C. Collected Papers II, 681-712 (1879) (Cambridge University Press, 1890).
4. P.S. Epstein, Z. Phys. **54**, 537 (1929).
5. S.R. de Groot, P. Mazur, *Non-Equilibrium Thermodynamics* (North-Holland, Amsterdam, 1969).
6. D. Braun, A. Libchaber, Phys. Rev. Lett. **89**, 188103 (2002).
7. K. Clusius, G. Dickel, Z. Phys. Chem. B **44**, 397, (1939).
8. K. Clusius, M. Huber, Z. Naturforsch. A **10**, 230 (1955).
9. M.E. Schimpf, J.C. Giddings, J. Polym. Sci. B **28**, 2673 (1990).
10. B.K. Gale, K.D. Caldwell, A.B. Frazier, IEEE Trans. Biomed. Eng. **45**, 1459 (1998).
11. T.L. Edwards, B.K. Gale, A.B. Frazier, Anal. Chem. **74**, 1211 (2002).
12. D. Braun, A. Libchaber, Phys. Biol. **1**, 1 (2004).
13. W. Köhler, P. Rossmanith, J. Phys. Chem. **99**, 5838 (1995).
14. C. Debuschewitz, W. Köhler, Phys. Rev. Lett. **87**, 055901 (2001).
15. R. Piazza, A. Guarino, Phys. Rev. Lett. **88**, 208302 (2002).
16. S. Iacopini, R. Piazza, Europhys. Lett. **63**, 247253 (2003).
17. R. Rusconi, L. Isa, R. Piazza, J. Opt. Soc. Am. B. **21**, 605 (2004).
18. T. Thorsen, S.J. Maerkl, R. Quake, Science **298**, 580 (2002).
19. A. Pluen, P.A. Netti, R.K. Jain, D.A. Berk, Biophys. J. **77**, 542552 (1999).
20. P. Matura, D. Jung, M. Lücke, Phys. Rev. Lett. **92**, 254501 (2004).
21. M. Giglio, A. Vendramini, Phys. Rev. Lett. **38**, 26 (1977).
22. A. Pluen, P.A. Netti, R.K. Jain, D.A. Berk, Biophys. J. **77**, 542 (1999).
23. A. Pralle, E.-L. Florin, E.H.K. Stelzer, J.K.H. Hörber, Appl. Phys. A **66**, S71-S73 (1998).

Publikation II: Thermophoretic Depletion Follows Boltzmann Distribution, **PRL** 96, 168301 (2006), Stefan Duhr and Dieter Braun

PRL 96, 168301 (2006) PHYSICAL REVIEW LETTERS week ending 28 APRIL 2006

Thermophoretic Depletion Follows Boltzmann Distribution

Stefan Duhr and Dieter Braun

Applied Physics, Center for Nanoscience, Ludwig Maximilians University München, Amalienstr. 54, D-80799 München, Germany

(Received 26 December 2005; published 27 April 2006)

Thermophoresis, also termed thermal diffusion or the Soret effect, moves particles along temperature gradients. For particles in liquids, the effect lacks a theoretical explanation. We present experimental results at moderate thermal gradients: (i) Thermophoretic depletion of 200 nm polystyrene spheres in water follows an exponential distribution over 2 orders of magnitude in concentration; (ii) Soret coefficients scale linearly with the sphere's surface area. Based on the experiments, it is argued that local thermodynamic equilibrium is a good starting point to describe thermophoresis.

DOI: 10.1103/PhysRevLett.96.168301 PACS numbers: 82.60.Lf, 82.70.Dd, 87.23.−n

Introduction.—Temperature gradients can move particles, a phenomenon called the Soret effect. Experimentally, the effect has been known for 150 years [1]. Particles typically deplete from regions of enhanced temperature, but the inverted effect of thermophilic behavior is also found [2–4]. Thermophoresis is theoretically not yet understood. Experimental methods to measure thermophoresis of colloids in aqueous and nonaqueous suspensions are quite diverse and use thermal field flow fractionation (ThFFF) [5,6], beam deflection [2,4,7], holographic scattering [3,8,9], thermal lensing [10], and optical heating in microfluidics [11,12]. Thermophoresis has the potential to analyze the particle-solvent interaction of nanoscaled particles and biomolecules. Moreover, it is a versatile tool to manipulate or concentrate molecule concentrations in solution [12,13]. In addition to biotechnological applications, a natural thermophoretic setting is found in pores of rock near hot springs on the floor of the ocean, possibly involved in molecular evolution [14,15].

A generally applied assumption for describing thermophoresis is that it should be treated as a transport phenomenon using, for example, microscopic particle-particle potentials, hydrodynamics, or effective force fields [16–19]. Here, experimental evidence is presented, which explains thermophoresis for moderate temperature gradients by local thermodynamic equilibrium which diffusively connects to an exponential Boltzmann steady state distribution.

The local thermal equilibrium picture of thermophoresis leads to a scaling prediction of thermophoresis over the radius of solid particles. We confirm the prediction for polystyrene (PS) beads in water ranging from 40 nm to 2 μm in diameter. Despite the fact that temperature is not homogeneous, our experiments argue towards a local thermodynamic equilibrium description of thermophoresis. Similar arguments have been discussed recently by Astumian [20].

Theory.—The process in which a temperature gradient induces a mass transport is termed thermophoresis and is described by linear phenomenological relations. Combined with diffusive back flow we find, for molecules of low concentration [21], the drift current density

$$j = j_D + j_{TD} = -D\nabla c - D_T c \nabla T \tag{1}$$

with diffusion coefficient D, molecule concentration gradient ∇c, thermal diffusion coefficient D_T (also termed thermophoretic mobility) and temperature gradient ∇T. Since $j = vc$, the thermophoretic molecule drift velocity is linear to the temperature gradient:

$$v = -D_T \nabla T. \tag{2}$$

In the steady state, both currents compensate ($j = 0$), leading to

$$\frac{dc}{c} = -S_T dT \tag{3}$$

for small temperature differences dT with the Soret coefficient $S_T = D_T/D$. For a constant S_T, the integration of Eq. (3) yields an exponential steady state distribution:

$$\frac{c(\vec{x})}{c_0(\vec{x}_0)} = \exp[-S_T[T(\vec{x}) - T_0(\vec{x}_0)]]. \tag{4}$$

The concentration $c(\vec{x})$ exponentially depends on temperature $T(\vec{x})$. The relation is normalized by an arbitrarily defined location $\vec{x}_0$ with a concentration c_0 and temperature T_0. We experimentally test Eq. (4), made possible by a recently developed method to image thermophoresis with microfluidic fluorescence [11,12].

The exponential steady state distribution can be understood from concatenating local equilibria by diffusion. Let us consider an arbitrary division of space into smaller regions (Fig. 1) and assume that the division is sufficiently small to obtain local equilibrium in each of the regions. The ratio of end concentration c_N and start concentration c_0 can be multiplied from local concentration ratios of neighboring chambers c_{i+1}/c_i, subsequently expressed by local laws of linear thermophoresis:

$$\frac{c_N}{c_0} = \prod_{i=0}^{N-1} \frac{c_{i+1}}{c_i} = \prod_{i=0}^{N-1} 1 - S_T(T_{i+1} - T_i). \tag{5}$$

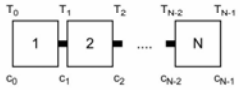

FIG. 1. Construction of a global exponential steady state by concatenation of local linear thermophoresis. At the local level, concentration ratios are proportional to temperature differences. Diffusive coupling of concentrations between local descriptions leads to a global exponential steady state distribution.

After assuming equal spacing in temperature $\Delta T = (T_N - T_0)/N$ we can, for large N, apply the limit definition of the exponential function:

$$\frac{c_N}{c_0} = \left[1 - S_T \frac{T_N - T_0}{N}\right]^N \rightarrow e^{-S_T(T_N - T_0)}. \quad (6)$$

The above derivation illustrates how local thermodynamic equilibria assemble into a global exponential steady state despite nonequilibrium conditions.

Methods.—We used microfluidic fluorescence [11,12] to put the above exponential steady state relation to an experimental test. Temperature differences are created by an infrared laser (Furukawa FOL1405-RTV-317, 1480 nm, 25 mW) moderately focused by an aspheric lens with 8 mm focal distance (Thorlabs, C240TM-C) Water strongly absorbs at this wavelength with an attenuation length of $\kappa = 320\ \mu$m. A 10 μm thin water chamber was formed by polystyrene slides. Imaging was performed by a 32× air objective (Zeiss LD-A Plan $NA = 0.4$) in a fluorescence upright microscope (Zeiss Axiotech) equipped with a CCD camera (PCO Sensicam QE)

Temperatures were measured by the dye BCECF used with 50 μM concentration in 10 mM TRIS buffer [11,12] with temperature sensitivity of $-2.8\%/\mathrm{K}$. The heated spot showed temperatures of $\Delta T = 8$ K with a full width at half maximum of 40 μm. We measured thermophoresis of 200 nm diameter carboxyl-modified polystyrene beads (Molecular Probes, F-8811), diluted to 0.02% solid in 1 mM Tris buffer. Their thermophoretic properties were measured for a small temperature difference of 1.2 K to $D_T = 1.4\ \mu\mathrm{m}^2/(\mathrm{sK})$ and $D = 2.1\ \mu\mathrm{m}^2/\mathrm{s}$, yielding $S_T = 0.7\ \mathrm{K}^{-1}$.

Concentration of particles was averaged from an image stack of 50 images, each with an exposure time of 10 seconds, recorded at 12-bit resolution. The imaging protocol consisted of three time steps: first without heating, second in steady state after 20 min of laser heating, and third after 20 min of backdiffusion to correct for fluorescence bleaching of the beads. Bleaching could be corrected linearly; inhomogeneous illumination was removed by dividing with the initial, unheated image stack. Radial concentration profiles were extracted from the averaged image stacks. Background fluorescence was subtracted as inferred from the central depleted region.

Several possible artifacts were excluded by the experimental design. The 32× air objective averages the concentration profile in z direction [12]. We simulated the experiment using finite element calculations (FEMlab 2.3, Comsol) for Navier-Stokes flow superposed with heat transfer, thermal expansion, gravity, photonic momentum, molecule diffusion, and thermophoresis. The numerical approach was benchmarked previously against experiments [11,22]. The temperature profile across the chamber is flat due to the low thermal conductivity of the PS chamber walls [Fig. 2(a)]. Small deviations from a constant z profile of both temperature and concentration automatically compensate in first order [11]. The simulation does not detect a noticeable disturbance of the concentration profile by thermal convection [Fig. 2(b)]. This is understood since the latter has a maximal speed of only 5 nm/s, mostly due to the thin chamber size and the broad laser focus [Fig. 2(c)].

Results and discussion.—The radial temperature distribution of the heated solution was measured by BCECF fluorescence [Fig. 3(a)]. An individual image of the beads is shown in Fig. 3(b), while a logarithmic plot of the reconstructed bead concentration from the full measurement protocol is given in Fig. 3(c). Three beads which stick to the chamber surface can be seen; however, their fluorescence has no statistical significance in the final result. The remaining inhomogeneities in the center are due to insufficient averaging over the beads' movement and excluded in the analysis. Radial averages of temperature and

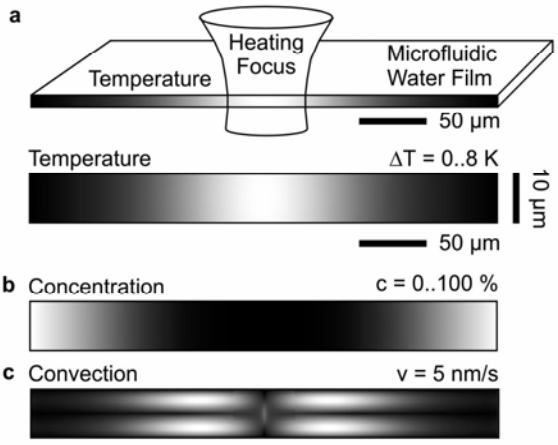

FIG. 2. Details of the experimental approach. (a) A 10 μm thin water film is enclosed between PS walls. Low thermal conduction of the chamber walls allow a thickness independent temperature profile, confirmed by the shown finite element calculation. (b) As a result, the thermophoretic depletion profile equally shows no thickness profile. (c) Convection is slow at maximal velocities of 5 nm/s due to thin chamber and comparable broad heating focus.

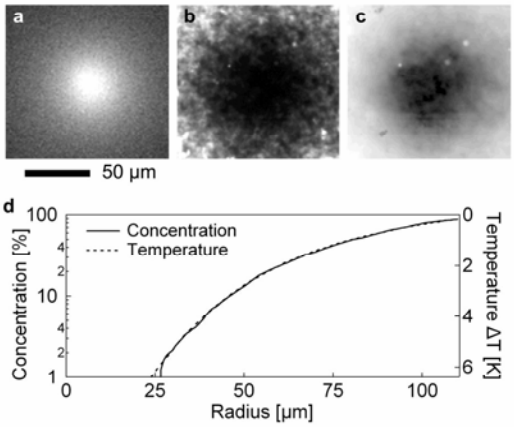

FIG. 3. Exponential thermophoretic depletion. (a) Temperature measured from BCECF fluorescence. (b) Single image of thermophoretic depleted polystyrene beads. (c) Logarithmic bead concentration image, averaged from 50 single images and after bleach and illumination correction. (d) Radial averages of particle concentration (logarithmic) and temperature (linear).

concentration are given in Fig. 3(d), notably with a logarithmic scale for concentration (left) and linear, inverted scale for temperature (right). Since both measurements correspond in the plot, we directly see that the concentration scales exponentially with temperature.

By removal of the common radius coordinate, the bead concentration is plotted over the applied temperature increase ΔT in Fig. 4. The exponential dependence is fitted by Eq. (4) with the Soret coefficient $S_T = 0.72/\mathrm{K}$ (solid line) and holds well over the large concentration range from $c/c_0 = 100\%$ down to 1%. The fitted S_T is very close to the value of $0.7/\mathrm{K}$ measured before at only a 1.2 K elevated temperature. Carboxyl-modified polystyrene beads show a comparably low temperature dependence of

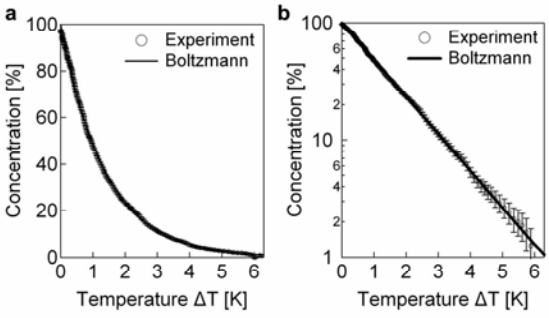

FIG. 4. Exponential concentration distribution. (a) In steady state, thermophoretic depletion results in an exponential distribution, compatible with an energetic Boltzmann distribution. (b) The logarithmic plot reveals the quality of the exponential fit over 2 orders of magnitude in concentration.

the Soret coefficient $S_T(T) = S_T(T_0)(1 + \gamma[T - T_0])$, measured independently to $\gamma = 2.2\%/\mathrm{K}$. The experimental results can be equally described with or without above slight temperature dependence of S_T.

In hindsight, we can test the division of the nonequilibrium system into a succession of local equilibria brought forward in Eqs. (5) and (6). Locally, temperature and concentration differences are small and a linearized Boltzmann distribution holds:

$$\frac{dc}{c} = \frac{dG}{kT} = -S_T dT. \tag{7}$$

As seen, we can equate the local Boltzmann law with Eq. (3) to connect the Soret coefficient S_T with Gibbs free enthalpy G. The latter is used for the experimental condition of constant pressure and nearly constant temperature.

The finest division into local equilibria systems is limited by the finite size of the particle itself. Even at the experimentally steepest temperature gradient of $\nabla T = 0.1\ \mathrm{K}/\mu\mathrm{m}$, the energy difference over the radius a of the particle is

$$a \times \nabla G = a \times S_T \nabla T kT = 0.01kT. \tag{8}$$

The energetic asymmetry across the particle is only 2% of the particle's thermal fluctuations, which, according to Einstein [23], is $kT/2$. On the other side, the total energetic difference in the experiment was $\Delta G = k\bar{T}\ln(c_{\min}/c_{\max}) = 4.6k\bar{T}$, well beyond local equilibrium. This means that the partitioning introduced in Eqs. (5) and (6) and Fig. 1 can be applied with at least $N = 4.6/0.01 = 460$, yielding a well converged exponential steady state distribution in Eq. (6).

Based on experimental evidence, it is tempting and along the lines of Astumian [20] to describe thermophoretic steady states by a Boltzmann distribution for cases where local thermodynamic equilibrium can be assumed:

$$\frac{c}{c_0} = \exp[-S_T(T - T_0)] = \exp\left[-\frac{G(T) - G(T_0)}{k\bar{T}}\right]. \tag{9}$$

The linear relation between the Soret coefficient S_T and particle energy G in Eq. (7) leads to a scaling prediction of thermophoresis over particle size. For solid particles, only the solvation energy at their surface can be temperature dependent. Therefore, based on Eq. (7), the Soret coefficient must scale with particle surface area. Since $D \propto a^{-1}$, D_T scales with a particle radius:

$$S_T \propto \frac{\partial G}{\partial T} \propto a^2, \qquad D_T \propto D\frac{\partial G}{\partial T} \propto a. \tag{10}$$

We measured Soret coefficients for carboxyl-modified polystyrene beads of various size (Molecular Probes, F-8888, F-8823, F-8827, F-8795, and F-8823) in 1 mM TRIS buffer. Measurements for beads larger than 200 nm in diameter were obtained from single particle tracking [24]. The measurements are well fitted with the scaling

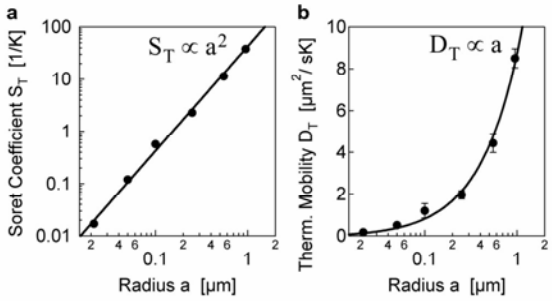

FIG. 5. Scaling of the Soret coefficient S_T and thermophoretic mobility D_T with particle size. (a) The Soret coefficient of carboxyl-modified beads of different radius a scale with its particle surface area, confirming a local equilibrium description of thermophoresis. (b) Accordingly, thermophoretic diffusion coefficient D_T scales linearly with radius.

of Eq. (10) (Fig. 5, solid lines). Hydrodynamic theories [16–19] predict particle-size independent D_T and thus $S_T \propto a$, in contradiction to the experimental data.

Similar particle-solvent systems have been analyzed with ThFFF [5,6]. ThFFF uses exceptionally strong thermal gradients of up to 1 K/μm and leads to values for S_T and D_T for small polystyrene beads that are comparable to our measurements. However, for larger particles in ThFFF, the energetic difference of Eq. (8) exceeds kT and local equilibrium cannot be assumed. This transition, given by $a \times S_T \Delta T = 1$ strongly depends on particle size ($\nabla T \propto a^{-3}$) due to Eq. (10). Incidentally, measurements of ThFFF versus particle size, typically for diameters between 50 and 400 nm, are performed near the transition. Often, saturation of retention times t_R/t_0 over particle radius is found and results in a hard to explain scatter in size scaling laws for different particle systems [5,6] and in contradiction to our results.

Based on recent findings [24], the contradiction, however, can be readily resolved. We find using single particle tracking that the linearity $v = -D_T \nabla T$ does not hold out of local equilibrium. The relation saturates nonlinearly for larger thermal gradients. Since evaluations of ThFFF assume a linear transport relation, apparent values for D_T and S_T decrease beyond the transition. This probably leads to the discrepancy of size scaling measured with ThFFF and our method (Fig. 5), where considerable smaller thermal gradients were used to ensure local equilibrium.

To conclude, we collected experimental evidence in favor of describing thermophoresis by local thermodynamic equilibrium. Under moderate thermal gradients, thermophoretic depletion follows an exponential steady state distribution over 2 orders of magnitude. Identification with a local Boltzmann distribution leads to a scaling law of the Soret coefficient for solid particles, which is confirmed experimentally, but contradicts hydrodynamic transport models of thermophoresis [16–19].

We thank Jan Dhont, Werner Köhler, and Simone Wiegand for discussions and Hermann Gaub for hosting our Emmy-Noether Group which was funded by the Deutsche Forschungsgemeinschaft DFG.

[1] C. Ludwig, Sitzber. Kaiserl. Akad. Wiss. Math.-Natwiss. Kl. (Wien) **20**, 539 (1856).
[2] M. Giglio and A. Vendramini, Phys. Rev. Lett. **38**, 26 (1977).
[3] B.-J. de Gans, R. Kita, B. Müller, and S. Wiegand, J. Chem. Phys. **118**, 8073 (2003).
[4] S. Iacopini and R. Piazza, Europhys. Lett. **63**, 247 (2003).
[5] S. J. Jeon, M. E. Schimpf, and A. Nyborg, Anal. Chem. **69**, 3442 (1997).
[6] P. M. Shiundu, G. Liu, and J. C. Giddings, Anal. Chem. **67**, 2705 (1995).
[7] R. Piazza and A. Guarino, Phys. Rev. Lett. **88**, 208302 (2002).
[8] J. Rauch and W. Köhler, Phys. Rev. Lett. **88**, 185901 (2002).
[9] S. Wiegand and W. Köhler, in *Thermal Nonequilibrium Phenomena in Fluid Mixtures* (Springer, Berlin, 2002), p. 189.
[10] R. Rusconi, L. Isa, and R. Piazza, J. Opt. Soc. Am. B **21**, 605 (2004).
[11] S. Duhr, S. Arduini, and D. Braun, Eur. Phys. J. E **15**, 277 (2004).
[12] D. Braun and A. Libchaber, Phys. Rev. Lett. **89**, 188103 (2002).
[13] A. Voit, A. Krekhov, W. Enge, L. Kramer, and W. Köhler, Phys. Rev. Lett. **94**, 214501 (2005).
[14] Dieter Braun and Albert Libchaber, Physical Biology **1**, P1 (2004).
[15] Dieter Braun, Noel L. Goddard, and Albert Libchaber, Phys. Rev. Lett. **91**, 158103 (2003).
[16] K. I. Morozov, J. Exp. Theor. Phys. **88**, 944 (1999).
[17] M. E. Schimpf and S. N. Semenov, J. Phys. Chem. B **105**, 2285 (2001).
[18] A. Parola and R. Piazza, Eur. Phys. J. E **15**, 255 (2004).
[19] J. R. Bielenberg and H. Brenner, Physica (Amsterdam) **356A**, 279 (2005).
[20] R. D. Astumian, Am. J. Phys. (to be published).
[21] S. R. de Groot and P. Mazur, *Non-Equilibrium Thermodynamics* (North-Holland, Amsterdam, 1962).
[22] S. Duhr and D. Braun, Appl. Phys. Lett. **86**, 131921 (2005).
[23] A. Einstein, Ann. Phys. (Berlin) **22**, 569 (1907).
[24] S. Duhr and D. Braun (to be published).

Publikation III: Why molecules move along a temperature gradient. **PNAS**, 103, 19678-19682 (2006), Stefan Duhr and Dieter Braun

Why molecules move along a temperature gradient

Stefan Duhr and Dieter Braun*

Chair for Applied Physics, Ludwig Maximilians Universität, Amalienstrasse 54, 80799 Munich, Germany

Edited by Leo P. Kadanoff, University of Chicago, Chicago, IL, and approved October 12, 2006 (received for review May 26, 2006)

Molecules drift along temperature gradients, an effect called thermophoresis, the Soret effect, or thermodiffusion. In liquids, its theoretical foundation is the subject of a long-standing debate. By using an all-optical microfluidic fluorescence method, we present experimental results for DNA and polystyrene beads over a large range of particle sizes, salt concentrations, and temperatures. The data support a unifying theory based on solvation entropy. Stated in simple terms, the Soret coefficient is given by the negative solvation entropy, divided by *kT*. The theory predicts the thermodiffusion of polystyrene beads and DNA without any free parameters. We assume a local thermodynamic equilibrium of the solvent molecules around the molecule. This assumption is fulfilled for moderate temperature gradients below a fluctuation criterion. For both DNA and polystyrene beads, thermophoretic motion changes sign at lower temperatures. This thermophilicity toward lower temperatures is attributed to an increasing positive entropy of hydration, whereas the generally dominating thermophobicity is explained by the negative entropy of ionic shielding. The understanding of thermodiffusion sets the stage for detailed probing of solvation properties of colloids and biomolecules. For example, we successfully determine the effective charge of DNA and beads over a size range that is not accessible with electrophoresis.

DNA | fluorescence | microfluidic | Soret | thermodiffusion

Thermodiffusion has been known for a long time (1), but its theoretical explanation for molecules in liquids is still under debate. The search for a theoretical understanding is motivated by the fact that thermodiffusion in water might lead to powerful all-optical screening methods for biomolecules and colloids. Equally well, thermodiffusion handles and moves molecules all-optically and therefore can complement well established methods: for example, electrophoresis or optical tweezers. For the latter, forces of optical tweezers scale with particle volume and limit this method to particles of only >500 nm. Electrophoresis does not suffer from force limitations but is difficult to miniaturize because of electrochemical reactions at the electrodes.

On the other hand, thermodiffusion allows the microscale manipulation of small particles and molecules. For example, 1,000-bp DNA can be patterned arbitrarily in bulk water (Fig. 1). The temperature pattern "DNA," heated by 2 K, was written into a water film with an infrared laser scanning microscope. The concentration of 1,000-bp DNA was imaged by using a fluorescent DNA tag. In an overall cooled chamber at 3°C, DNA accumulates toward the heated letters "DNA" (negative Soret effect), whereas at room temperature DNA is thermophobic (positive Soret effect) as seen by the dark letters.

In the past, the apparent complexity of thermodiffusion prevented a full theoretical description. As seen for DNA in Fig. 1, molecules characteristically deplete from regions with an increased temperature, but they can also show the inverted effect and accumulate (2, 3). Moreover, the size scaling of thermodiffusion recorded by thermal field flow fractionation showed fractional power laws with a variety of exponents that are hard to interpret (4, 5). The latter effect might be resolved by revealing nonlinear thermophoretic drift for the strong thermal gradients used in thermal field flow fractionation (our unpublished observations).

A variety of methods were used to measure thermodiffusion, mostly in the nonaqueous regime, ranging from beam deflection (2, 3, 6), holographic scattering (7–9), electrical heating (10), to thermal lensing (11). Recently we have developed a fluorescence microfluidic imaging technique (12, 13) that allows the measurement of thermodiffusion over a wide molecule size range without artifacts induced by thermal convection. Highly diluted suspensions can be measured; therefore, particle–particle interactions do not have an influence. We only apply moderate temperature gradients. In the following study, we used this method to confirm a straightforward theoretical explanation of thermodiffusion.

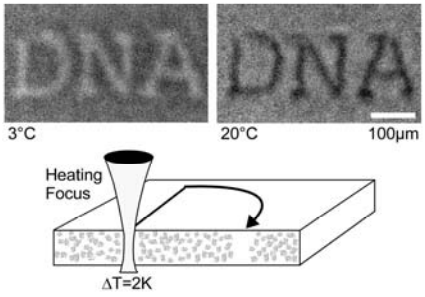

Fig. 1. Thermodiffusion manipulates the DNA concentration by small temperature differences within the bulk solution. A thin water film is heated by 2 K along the letters "DNA" with an infrared laser. For a cooled chamber at 3°C, fluorescently tagged DNA accumulates at the warm letters. However, at room temperature, DNA moves into the cold, showing reduced fluorescence. The chamber is 60 μm thin, containing 50 nM DNA in 1 mM Tris buffer. Every 50th base pair is labeled with TOTO-1 (for details, see supporting information).

Theoretical Approach

For diluted concentrations, it is generally assumed (14) that the thermodiffusive drift velocity $\vec{v}$ depends linearly on the temperature gradient ∇T with a proportionality constant which equals the thermodiffusion coefficient D_T: $\vec{v} = -D_T \nabla T$. In steady state, thermodiffusion is balanced by ordinary diffusion. Constant diffusion and thermodiffusion coefficients both lead to an exponential depletion law (15) $c/c_0 = \exp[-(D_T/D)(T - T_0)]$, with the concentration c depending on the temperature difference $T - T_0$ only. The concentration c is normalized by the boundary condition of the concentration c_0 with temperature T_0. The Soret coefficient is defined as ratio $S_T = D_T/D$, which determines the magnitude of thermodiffusion in the steady state. Although the above exponential distribution could motivate an approach based on Boltzmann equilibrium statistics, it is commonly argued that thermodiffusion without exception is a local nonequilibrium effect that requires fluid dynamics, force fields, or particle–solvent potentials (16–20). However, in a previous paper (15), we demonstrated that for moderate temperature

Author contributions: D.B. designed research; S.D. and D.B. performed research; S.D. and D.B. analyzed data; and S.D. and D.B. wrote the paper.

The authors declare no conflict of interest.

*To whom correspondence should be addressed. E-mail: dieter.braun@lmu.de.

www.pnas.org/cgi/doi/10.1073/pnas.0603873103

gradients the thermal fluctuations of the particle are the basis for a local equilibrium. This allows the description of the thermodiffusive steady state by a succession of local Boltzmann laws, yielding $c/c_0 = \exp[-(G(T) - G(T_0))/kT]$, with G being the Gibbs-free enthalpy of the single particle–solvent system. Such an approach is valid only if the temperature gradient ∇T is below a threshold $\nabla T < (aS_T)^{-1}$, which is given by the particle fluctuations with the hydrodynamic radius a and Soret coefficient S_T, as shown recently (15). In the present study, temperature gradients below this limit were used so that thermodiffusion is measured at local thermodynamic equilibrium conditions.

Local thermodynamic equilibrium allows the derivation of a thermodynamic foundation of the Soret coefficient. The local Boltzmann distribution relates small concentration changes δc with small Gibbs-free energy differences: $\delta c/c = -\delta G/kT$. We equate this relation with a locally linearized thermodiffusion steady state given by $\delta c/c = -S_T \delta T$ and thus find the Soret coefficient by the temperature derivative of G:

$$S_T = D_T/D = (kT)^{-1} \times \partial G/\partial T. \qquad [1]$$

Whereas the above relation is sufficient for the following derivation, it can be generalized by locally applying the thermodynamic relation $dG = -SdT + Vdp + \mu dN$. For single particles at a constant pressure we find that the Soret coefficient equals the negative entropy of the particle–solvent system S according to $S_T = -S/kT$. This relation is not surprising given that the entropy is by definition related with the temperature derivative of the free enthalpy.

The above general energetic treatment is inherent in previously described approaches based on local equilibrium (14, 21, 22), including the successful interpretation of thermoelectric voltages of diluted electrolytes (23, 24), which are described by energies of transfer. Recently, the nonequilibrium approach by Ruckenstein (25) was applied to colloids (26) with the characteristic length l assigned to the Debye length λ_{DH}. If instead one would assign the characteristic length according to $l = 2a/3$ with the particle radius a, the Ruckenstein approach would actually confirm the above local equilibrium relation (1) for the Soret coefficient. Measurements on SDS micelles (26) appeared to confirm this nonequilibrium approach, but for the chosen particles the competing parameter choices $l = 2a/3$ and $\ell = \lambda_{DH}$ yielded comparable values. Thus, the experiments could not distinguish between the competing theories.

We will use the above local equilibrium relations to derive the Soret coefficient for particles larger than the Debye length in aqueous solutions and put the results to rigorous experimental tests. Two contributions dominate the particle entropy S in water (Fig. 2*a*): the entropy of ionic shielding (Fig. 2a *Left*) and the temperature-sensitive entropy of water hydration (Fig. 2*a Right*). The contribution from the entropy of ionic shielding is calculated with the temperature derivative of the Gibbs-free enthalpy (26, 27) $G_{ionic} = Q_{eff}^2 \lambda_{DH}/[2A\varepsilon\varepsilon_0]$ with the effective charge Q_{eff} and particle surface A. Alternatively, this enthalpy can be interpreted as an electrical field energy $G_{ionic} = Q_{eff}^2/[2C]$ in the ionic shielding capacitor C. We neglect the particle–particle interactions because the fluorescence approach allows the measurement of highly diluted systems. To obtain the Soret coefficient, temperature derivatives consider the Debye length $\lambda_{DH}(T) = \sqrt{\varepsilon(T)\varepsilon_0 kT/(2e^2 c_S)}$ and the dielectric constant $\varepsilon(T)$. Both temperature derivatives give rise to a factor $\beta = 1 - (T/\varepsilon)\partial\varepsilon/\partial T$. The effective charge Q_{eff} is largely temperature-insensitive, which was confirmed by electrophoresis independently (28). Such a dependence would be unexpected because the strongly adsorbed ions dominate the value of the effective charge. Experimentally, we deal with colloids exhibiting flat surfaces, i.e., the particle radius is larger than λ_{DH}. In this case, charge renormalization does not play a role and we can introduce an effective surface charge density $\sigma_{eff} = Q_{eff}/A$ per molecule area A. From the temperature derivation according to Eq. **1**, the ionic contribution to the Soret coefficient is $S_T^{(ionic)} = (A\beta\sigma_{eff}^2\lambda_{DH})/(4\varepsilon\varepsilon_0 kT^2)$. A similar relation was derived for charged micelles recently (22), although without considering the temperature dependence of the dielectric coefficient ε. Next, the contribution to the Soret coefficient from the hydration entropy of water can be directly inferred from the particle-area-specific hydration entropy $s_{hyd} = S_{hyd}/A$, namely $S_T^{(hyd)} = -As_{hyd}(T)/kT$. Finally, the contribution from the Brownian motion is derived as $S_T = 1/T$ by inserting the kinetic energy of the particle $G = kT$ into Eq. **1**. However, this contribution is very small ($S_T = 0.0034$/K) and can be neglected for the molecules under consideration. The contributions from ionic shielding and hydration entropy add up to

$$S_T = \frac{A}{kT}\left(-s_{hyd} + \frac{\beta\sigma_{eff}^2}{4\varepsilon\varepsilon_0 T} \times \lambda_{DH}\right). \qquad [2]$$

The Soret coefficient S_T scales linearly with particle surface A and Debye length λ_{DH}. We tested Eq. **2** by measuring S_T versus salt concentration, temperature, and molecule size. In all cases, thermodiffusion is quantitatively predicted without any free parameters. We used fluorescence single-particle tracking to follow carboxyl-modified polystyrene beads (catalog no. F-8888, Molecular Probes, Eugene, OR) with diameters of 1.1 and 0.5 at 25 aM dialyzed into 0.5 mM Tris·HCl at pH 7.6. Thermodiffusion of particles ≤ 0.2 μm is measured by the fluorescence decrease that reflects the bulk depletion of the particles (12). The chamber thickness of 20 μm damped the thermal convection to negligible speeds (15). The experimental design also excludes thermal lensing and optical trapping (15). Debye lengths λ_{DH} were titrated with KCl (see the supporting information, which is published on the PNAS web site).

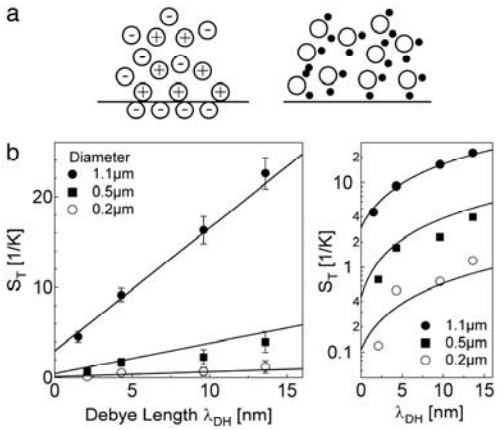

Fig. 2. Salt dependence. (*a*) Thermodiffusion in water is dominated by ionic shielding (*Left*) and water hydration (*Right*). (*b*) Soret coefficient S_T versus Debye length for carboxyl-modified polystyrene beads of diameter 1.1, 0.5, and 0.2 μm. Linear plot (*Left*) and logarithmic plot (*Right*). The Soret coefficients are described by Eq. **2** with an effective surface charge of $\sigma_{eff} = 4{,}500$ e/μm^2 known from electrophoresis. The intercept $S_T(\lambda_{DH} = 0)$ is fitted with a hydration entropy per particle surface of $s_{hyd} = -1{,}400$ J/(mol·K·μm^2).

Salt Dependence. Fig. 2*b* shows the Soret coefficients of polystyrene beads with different sizes versus λ_{DH}. The Soret coefficients

PHYSICS

BIOCHEMISTRY

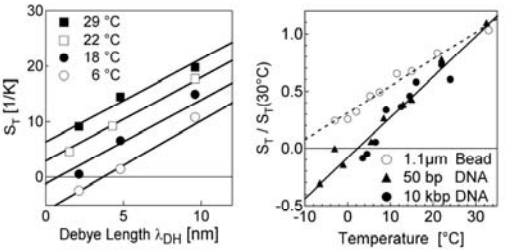

Fig. 3. Temperature dependence. (*a*) The temperature dependence is dominated by the linear change in the hydration entropy S_{hyd}. It shifts the salt-dependent thermodiffusion $S_T(\lambda_{DH})$ to lower values. The particle size is 1.1 μm. (*b*) The Soret coefficient S_T increases linearly with the temperature as expected for a hydration entropy $S_{hyd}(T)$. It depends on the molecule species, not its size, as seen from the rescaled Soret coefficients for DNA with different lengths.

scale linearly with a small intercept at $\lambda_{DH} = 0$ and confirm the λ_{DH}-dependence of Eq. 2. For smaller-diameter beads, the Soret coefficients scale with the particle surface area A (Fig. 2), as expected from Eq. **2**. To check whether Eq. **2** also quantitatively explains the measured Soret coefficients, we inferred the effective charge of the beads by electrophoresis (see supporting materials). By using 40-nm beads with identical carboxyl surface modifications at $\lambda_{DH} = 9.6$ nm, we fluorescently observed free-flow electrophoresis and corrected for electroosmosis, finding an effective surface charge density of $\sigma_{eff} = 4{,}500 \pm 2{,}000$ e/μm^2. This value is virtually independent from the used salt concentrations (28). With this inferred effective charge, Eq. **2** fits the Soret coefficient for various bead sizes and salt concentrations well (Fig. 2*b*, solid lines).

The intercept $S_T(\lambda_{DH} = 0)$, where ionic contributions are zero, also scales with particle surface and is described by a hydration entropy per particle surface of $s_{hyd} = -1{,}400$ J/(mol·K·μm^2). The value matches the literature values for similar surfaces reasonably well (29–31). For example, dansyl-alanine, a molecule with surface groups comparable with polystyrene beads, was measured to have a hydration entropy (29) of -0.13 J/(mol·K) at a comparable temperature. Linear scaling with its surface area by using a radius of $a = 2$ nm results in a value of $s_{hyd} = -2{,}500$ J/(mol·K·μm^2), in qualitative agreement with our result. The hydration entropy is a highly informative molecule parameter that is notoriously difficult to measure, yielding an interesting application for thermodiffusion.

Temperature Dependence. Hydration entropies S_{hyd} in water are known to increase linearly with decreasing temperatures (29–31). Because the slope of the ionic contribution of S_T versus λ_{DH} is with high-precision temperature insensitive for water [$\beta(T)/(\epsilon T^2) \cong$ const], only the intercept is expected to decrease as the overall temperature of the chamber is reduced. This is indeed the case, as seen from the temperature dependence of beads with diameters of 1.1 μm ($T = 6$–29°C) (Fig. 3*a*). We infer from the intercept $S_T(\lambda_{DH} = 0)$ that the hydration entropy changes sign at ≈20°C. As seen for DNA in Fig. 1, hydration entropy can dominate thermodiffusion at low temperatures and move molecules toward the heat ($D_T < 0$).

The properties of hydration entropy lead to a linear increase of S_T over temperatures at a fixed salt concentration as measured for 1.1-μm beads and DNA (Fig. 3*b*). We normalized S_T by dividing by S_T(30°C) to compensate for molecule surface area. The slopes of S_T over temperature differ between beads and DNA. However the slope does not differ between DNA of different size (50 bp versus 10,000 bp). Based on Eq. **2**, this is to be expected because the temperature dependence of the hydration entropy depends only on the type of surface of the molecule, not its size. We measured the diffusion coefficients of the DNA species at the respective temperature independently. Within experimental error, changes in the diffusion coefficient D match with the change of the water viscosity without the need to assume conformational changes of DNA over the temperature range. Please note that the change of the sign of the DNA Soret coefficient is situated near the point of maximal water density only by chance. There, the two entropic contributions balance. For polystyrene beads at $\lambda_{DH} = 2$ nm for example, the sign change is observed at 15°C (Fig. 3*a*). An increased Soret coefficient over temperature was reported for aqueous solutions before (3), however with a distinct nonlinearity that we attribute to remnant particle–particle interactions.

Size Dependence of the Beads. The Soret coefficient was measured for carboxyl-modified polystyrene beads in diameters ranging from 20 nm to 2 μm. Beads with diameters of 0.2, 0.1, 0.04, and 0.02 μm were diluted to concentrations of 10 pM, 15 pM, 250 pM, and 2 nM, and their bulk fluorescence was imaged over time to derive D_T and D (12, 15) from the depletion and subsequent back-diffusion. Larger beads with diameters of 1.9, 1.1, and 0.5 μm were diluted to concentrations of 3.3 aM, 25 aM, and 0.2 pM and measured with single-particle tracking. The solutions were buffered in 1 mM Tris (pH 7.6) with $\lambda_{DH} = 9.6$ nm. In all cases, interactions between particles can be excluded. Care was taken to keep the temperature gradient in the local equilibrium regime.

We find that the Soret coefficient scales with particle surface over four orders of magnitude (Fig. 4*a*). The data are described well with Eq. **2** with an effective surface charge density of $\sigma_{eff} = 4{,}500$ e/μm^2 and neglected hydration entropy contribution. The 5-fold too-low prediction for the smallest particle (20 nm in diameter) can be explained by charge renormalization because its radius is smaller than λ_{DH}.

The diffusion coefficient D for spheres is given by the Einstein relation and scales inversely with radius $D \propto 1/a$. Inserting Eq. **2** into $S_T = D_T/D$, the thermodiffusion coefficient D_T is expected to scale with particle radius a. This is experimentally confirmed over two orders of magnitude (Fig. 4*b*). These findings contradict several theoretical studies claiming that D_T should be independent of particle size (16–20, 26), based on ambiguous experimental results from thermal field flow fractionation (4) that were probably biased by nonlinear thermodiffusion in large thermal gradients (15).

Size Dependence of DNA. Whereas polystyrene beads share a very narrow size distribution as a common feature with DNA molecules, beads are a much less complicated model system. Beads are rigid spheres that interact with the solvent only at its surface. In addition, the charges reside on the surface, where the screening takes place. Thus, the finding that thermodiffusion of flexible and homogeneously charged DNA is described equally well with Eq. **2** is not readily expected and quite interesting (Fig. 4 *c* and *d*).

We measured DNA with sizes of 50–48,502 bp in 1 mM Tris buffer ($\lambda_{DH} = 9.6$ nm) at low molecule concentrations between 1 μM (50 bp) and 1 nM (48,502 bp). Only every 50th base pair was stained with the TOTO-1 fluorescent dye. The diffusion coefficient was measured by back-diffusion after the laser was turned off and depends on the length L of the DNA in a nontrivial way. The data are well fitted with a hydrodynamic radius scaling $a \propto L^{0.75}$. This scaling represents an effective average over two DNA length regimes. For DNA molecules longer than ≈1,000 bp, a scaling of 0.6 is found (32), whereas shorter DNA scales with an exponent of ≈1 (see the supporting information).

We can describe the measured Soret coefficient over three

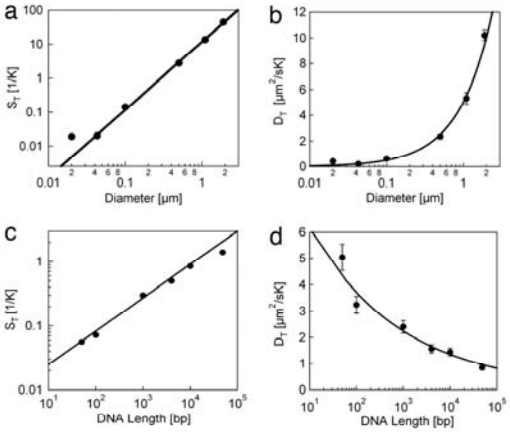

Fig. 4. Size dependence. (*a*) For polystyrene beads, the Soret coefficient scales with the particle surface over four orders of magnitude. Measurements are described by Eq. **2** with an effective surface charge density of σ_{eff} = 4,500 e/μm^2 (2) and negligible hydration entropy. The deviation for the bead with a diameter of 20 nm can be understood from an increased effective charge due to the onset of charge normalization for $a \leq \lambda_{DH}$. (*b*) Accordingly, the thermodiffusion coefficient D_T scales linearly with bead diameter. (*c*) The Soret coefficient of DNA scales according to $S_T \propto \sqrt{L}$, with the length L of the DNA based on Eq. **2** with an effective charge per base pair of 0.12 e. (*d*) Thermodiffusion coefficient D_T decreases over DNA length with $D_T \propto L^{-0.25}$, caused by the scaling of diffusion coefficient $D \propto L^{-0.75}$.

orders of magnitude of DNA lengths with Eq. **2** if we assume that effective charge of the DNA is shielded at the surface of a sphere with the hydrodynamic radius a. Because of the low salt concentration (λ_{DH} = 9.6 nm), such globular shielding is reasonable. Not only is the experimentally observed scaling of the Soret coefficient with the square root of its length correctly predicted based on Eq. **2** ($S_T \propto Q_{eff}^2/a^2 \propto L^2/L^{1.5} \propto L^{0.5}$), but the Soret coefficient also is fully described in a quantitative manner (Fig. 4*c*, solid line), with an effective charge of 0.12 e per base, matching well with literature values (33) ranging from 0.05 e/bp to 0.3 e/bp.

As shown in Fig. 4*d*, the thermodiffusion coefficient for DNA drops with DNA length according to $D_T = DS_T \propto Q_{eff}^2/a^3 \propto L^2/L^{2.25} \propto L^{-0.25}$. Thus, shorter DNA actually drifts faster in a temperature gradient than longer DNA. It is important to point out that this finding is in no way contradictory to experimental findings of a constant D_T over polymer length in nonaqueous settings (8). According to Eq. **1**, the thermodynamic relevant parameter is the Soret coefficient, which is determined by the solvation energetics. The argument (19) that polymers have to decouple into monomers to show a constant D_T merely becomes the special case where the solvation energetics determine both S_T and D with equal but inverted size scaling. In accordance with our local energetic equilibrium argument, S_T and not D_T dominates thermodiffusion also for nonaqueous polymers near a glass transition (8). Here, S_T is constant, whereas D_T and D scale according to an increased friction. However, for a system of DNA in solution, for which long-ranging shielding couples the monomers, a constant D_T over polymer length cannot be assumed *a priori* (Fig. 4*d*).

Effective Charge. The effective charge Q_{eff} is a highly relevant parameter for colloid science, biology, and biotechnology. So far it only could be inferred from electrophoresis, restricted to

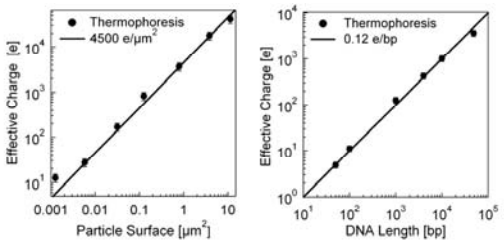

Fig. 5. Effective charge from thermodiffusion. Effective charge is inferred from thermodiffusion using Eq. **3**. Polystyrene beads (20–2,000 nm) (*a*) and DNA (50–50,000 bp) (*b*) were measured over a large size range, which is impossible with electrophoresis. As expected, the effective charge of the beads scales with particle surface and linearly with the length of DNA.

particles smaller than the Debye length ($a \leq 3\lambda_{DH}$) (34). Unfortunately, many colloids are outside this regime. As shown before, a similar size restriction does not hold for thermodiffusion. In many cases, the hydration entropy s_{hyd} contributes <15% (Fig. 2) and can be neglected at moderate salt levels. Thus, we can invert Eq. **2** to obtain the effective charge Q_{eff} for spherical molecules from

$$Q_{eff} = \frac{2T^2}{3\eta D}\sqrt{\frac{\varepsilon\varepsilon_0 k^3 S_T}{\beta\pi\lambda_{DH}}}. \quad [3]$$

The effective charge derived from thermodiffusion measurements of polystyrene beads and DNA is plotted in Fig. 5 over several orders of magnitude in size. The effective charge of beads scales linearly with particle surface, with a slope confirming the effective surface charge density of σ_{eff} = 4,500 e/μm^2, which was inferred from electrophoresis only for small particles. Average deviations from linear scaling are <8% (Fig. 5*a*). The effective charge inferred from thermodiffusion measurements of DNA using Eq. **3** scales linearly with DNA length with an effective charge of 0.12 e/bp. The length scaling is confirmed over four orders of magnitude with an average error of 12% (Fig. 5*b*). Thus, thermodiffusion can be used to infer the effective charge with low errors for a wide range of particle sizes. This is even more interesting for biomolecule characterization because measurements of thermodiffusion can be performed all-optically in picoliter volumes.

Conclusion

We describe thermodiffusion, the molecule drift along temperature gradients, in liquids with a general, microscopic theory. Applied to aqueous solutions, this theory predicts thermodiffusion of DNA and polystyrene beads with an average accuracy of 20%. We experimentally validate major parameter dependencies of the theory: linearity against screening length λ_{DH} and molecule hydrodynamic area A, quadratic dependence on effective charge, and linearity against temperature. Measurements of thermodiffusion can be miniaturized to the micrometer scale with the all-optical fluorescence technique and permit microscopic temperature differences to manipulate molecules based on their surface properties (Fig. 1). The theoretical description allows the extraction of solvation entropy and the effective charge of molecules and particles over a wide size range.

Materials and Methods

Infrared Temperature Control. The temperature gradients used to induce thermodiffusive motions were created by aqueous absorption of an infrared laser (Furukawa Electric, Tokyo, Japan) at a wavelength of 1,480 nm and 25 mW of power. Water strongly

absorbs at this wavelength with an attenuation length of $\kappa = 320$ μm. The laser beam was moderately focused with a lens of 8-mm focal distance. Typically, the temperature in the solution was raised by 1–2 K in the beam center with a $1/e^2$ diameter of 25 μm, measured with the temperature-dependent fluorescence signal of the dye 2′,7′-bis(carboxyethyl)-5(6)-carboxyfluorescein (12). Thin chamber heights of 10–20 μm and moderate focusing removed possible artifacts from optical trapping, thermal lensing, and thermal convection (12). For temperature-dependent measurements, both the objective and the microfluidic chip were tempered with a thermal bath. Imaging was provided from an AxioTech Vario fluorescence microscope (Zeiss, Oberkochen, Germany), illuminated with a high-power light-emitting diode (Luxeon, Calgary, Canada), and recorded with the CCD camera SensiCam QE (PCO, Kelheim, Germany).

Molecules. Highly monodisperse and protein-free DNA of 50, 100, 1,000, 4,000, 10,000, and 48,502 bp (Fast Ruler fragments and λ-DNA; Fermentas, St. Leon-Rot, Germany) were diluted to 50 μM base pair concentration, i.e., the molecule concentration was between 1 μM (50 bp) and 1 nM (48,502 bp). DNA was fluorescently labeled by the intercalating TOTO-1 fluorescent dye (Molecular Probes) with a low dye/base pair ratio of 1:50. Carboxyl-modified polystyrene beads with diameters of 2, 1, 0.5, 0.2, 0.1, 0.04, and 0.02 μm (catalog nos. F-8888, F-8823, F-8827, F-8888, F-8795, F-8823, and F-8827; Molecular Probes) were dialyzed (Eluta Tube mini; Fermentas) in distilled water and diluted in 1 mM Tris (pH 7.6) to concentrations between 3.3 aM (2 μm) and 2 nM (0.02 μm).

Concentration Imaging Over Time. Either the method of concentration imaging (12) or single-particle tracking was used to measure thermodiffusion at low concentrations, namely <0.03 g/liter for DNA and 10^{-5} g/liter for beads. At higher concentrations, we found profound changes of thermodiffusion coefficients. DNA and polystyrene beads of <0.5 μm in diameter were imaged over time (12) by bright-field fluorescence with a ×40 oil-immersion objective. Concentrations inferred after correcting for bleaching, inhomogeneous illumination, and temperature-dependent fluorescence (12) were fitted with a finite element theory. The model captures all details of both thermodiffusive depletion and back-diffusion to measure D_T and D independently (see supporting information). Measurements were performed in microfluidic chips 10 μm in height with polydimethylsiloxane on both sides.

Single-Particle Tracking. Polystyrene particles of >0.5 μm in diameter were measured by single-particle tracking due to the slow equilibration time and risk that steady-state depletion is disturbed by thermal convection. The thermodiffusive drift was imaged with a ×32 air objective at 4 Hz at an initial stage of depletion in a 20-μm-thick chamber. Averaging over the z position of the particles removed effects from thermal convection. The drift velocity versus temperature gradient of 400 tracks were linearly fitted by $v = -D_T \nabla T$ to infer D_T. The diffusion coefficients D of the particles were evaluated based on their squared displacement, matching within 10% the Einstein relationship.

We thank Klaus Stierstadt, Jan Dhont, and Werner Köhler for discussions and Julia Morfill and Veronica Egger for comments on the manuscript. Our Emmy-Noether Group is funded by the Deutsche Forschungsgemeinschaft and hosted by Hermann Gaub.

1. Ludwig C (1856) *Sitzungber Bayer Akad Wiss Wien Math-Naturwiss Kl* 20:539.
2. Giglio M, Vendramini A (1977) *Phys Rev Lett* 38:26–30.
3. Iacopini S, Piazza R (2003) *Europhys Lett* 63:247–253.
4. Jeon SJ, Schimpf ME, Nyborg A (1997) *Anal Chem* 69:3442–3450.
5. Shiundu PM, Liu G, Giddings JC (1995) *Anal Chem* 67:2705–2713.
6. Piazza R, Guarino A (2002) *Phys Rev Lett* 88:208302.
7. de Gans BJ, Kita R, Müller B, Wiegand S (2003) *J Chem Phys* 118:8073–8081.
8. Rauch J, Köhler W (2002) *Phys Rev Lett* 88:185901.
9. Wiegand S, Köhler W (2002) in *Thermal Nonequilibrium Phenomena in Fluid Mixtures* (Springer, Berlin), p 189.
10. Putnam SA, Cahill DG (2005) *Langmuir* 21:5317–5323.
11. Rusconi R, Isa L, Piazza R (2004) *J Opt Soc Am B* 21:605–616.
12. Duhr S, Arduini S, Braun D (2004) *Eur Phys J E* 15:277–286.
13. Braun D, Libchaber A (2002) *Phys Rev Lett* 89:188103.
14. de Groot SR, Mazur P (1969) *Nonequilibrium Thermodynamics* (North–Holland, Amsterdam).
15. Duhr S, Braun D (2006) *Phys Rev Lett* 96:168301.
16. Emery AH, Jr, Drickamer HG (1955) *J Chem Phys* 23:2252–2257.
17. Ham J (1960) *J Appl Phys* 31:1853–1858.
18. Morozov KI (1999) *J Exp Theor Phys* 88:944–946.
19. Schimpf ME, Semenov SN (2000) *J Phys Chem B* 104:9935–9942.
20. Voit A, Krekhov A, Enge W, Kramer L, Köhler W (2005) *Phys Rev Lett* 92:214501.
21. Dhont JKG (2004) *J Chem Phys* 120:1632–1641.
22. Fayolle S, Bickel T, Le Boiteux S, Würger A (2005) *Phys Rev Lett* 95:20830.
23. Agar JN, Turner JCR (1960) *Proc R Soc London Ser A* 255:307–329.
24. Snowdon PN, Turner JCR (1960) *Trans Faraday Soc* 56:1409–1418.
25. Ruckenstein E (1981) *J Colloid Interface Sci* 83:77–85.
26. Piazza R, Guarino A (2002) *Phys Rev Lett* 88:208302.
27. Israelachvili J (1992) *Intermolecular and Surface Forces* (Academic, New York), 2nd Ed.
28. Lin W, Galletto P, Borkovec M (2004) *Langmuir* 20:7465–7473.
29. Haidacher D, Vailaya A, Horváth C (1996) *Proc Natl Acad Sci USA* 93:2290–2295.
30. Southall NT, Dill KA, Haymet ADJ (2002) *J Phys Chem B* 106:521–533.
31. Kronberg B, Costas M, Silveston R (1995) *Pure Appl Chem* 67:897–902.
32. Pluen A, Netti PA, Jain RK, Berk DA (1999) *Biophys J* 77:542–552.
33. Smith SB, Bendich AJ (1990) *Biopolymers* 29:1167–1173.
34. O'Brien RW, White LR (1978) *J Chem Soc Faraday Trans 2* 74:1607–1626.

Publikation IV: Thermodiffusion of Charged Colloids: Single Particle Diffusion, **Langmuir** 23 (4), pp. 1674-1683 (2007), Jan K. G. Dhont, Simone Wiegand, Stefan Duhr and Dieter Braun

1674 *Langmuir* **2007,** *23,* 1674−1683

Thermodiffusion of Charged Colloids: Single-Particle Diffusion

Jan K. G. Dhont,*,† S. Wiegand,† S. Duhr,‡ and D. Braun‡

Forschungszentrum Jülich, Institute für Festkörper Forschung (IFF), Weiche Materie, D-52425 Jülich, Germany, and Ludwig Maximilians University, Applied Physics, Amalienstrasse 54, D-80799 München, Germany

Received July 25, 2006. In Final Form: October 25, 2006

An expression for the single-particle thermal diffusion coefficient of a charged colloidal sphere is derived on the basis of force balance on the Brownian time scale in combination with thermodynamics. It is shown that the single-particle thermal diffusion coefficient is related to the temperature dependence of the reversible work necessary to build the colloidal particle, including the core, the solvation layer, and the electrical double layer. From this general expression, an explicit expression for the contribution of the electrical double layer to the single-particle thermal diffusion coefficient is derived in terms of the surface charge density of the colloidal sphere, the electrostatic screening length, and its core radius, to within the Debye-Hückel approximation. This result is shown to explain experimental data, for both thin and thick double layers. In addition, a comparison with other theories is made.

1. Introduction

Spherical colloids are excellent model systems to gain understanding concerning the microscopic mechanism that underlies collective diffusion and thermal diffusion. The coupling of a temperature gradient to diffusion in a multicomponent mixture was observed for the first time 150 years ago in salt solutions by Lugwig.[1] Up to a decade ago, thermal diffusion of simple molecular systems has been extensively studied. Due to the recent development of new experimental techniques to probe thermal diffusion, macromolecular systems have become of increasing interest. In recent years, several experimental[2−6,16] and theoretical[7−10] studies are devoted to the determination of the thermal diffusion coefficient D_T of macromolecules, micelles, and colloids. Here, one should differentiate between highly diluted and concentrated solutions. For very dilute systems, the thermal diffusive behavior is dominated by single-particle properties, related to the core material, the electric double layer, and the solvation layer. For concentrated systems, in addition to single-particle properties, interactions between the macromolecules need to be considered. In the present paper, the contribution of the electric double layer to the single-particle thermal diffusion coefficient will be considered.

In two earlier papers of one of the present authors,[9,10] the contribution to the thermal diffusion coefficient of colloids that arises from colloid−colloid interactions was discussed. In the present paper, we consider very dilute suspensions where these interactions do not contribute. There is one section in ref 9, however, where the single-particle thermal diffusion coefficient is claimed to vary proportionally to the temperature derivative of the chemical potential of the "complexed colloidal particle", which includes the solvation layer and electrical the double layer. As shown in the present paper, however, this is not correct. It will be shown that, instead of the derivative of the chemical potential, the temperature derivative of the reversible work to create such a complexed colloidal particle determines the single-particle diffusion coefficient.

When gradients in concentration and temperature and deviations from their mean values are small, the phenomenological equation of motion for the number density ρ of a given species that incorporates temperature-induced diffusion is of the form

$$\frac{\partial}{\partial t}\rho(\mathbf{r}, t) = D\nabla^2\rho(\mathbf{r}, t) + D_T\nabla^2 T(\mathbf{r}, t) \qquad (1)$$

where D is the collective diffusion coefficient and D_T is the thermal diffusion coefficient. The thermal diffusion coefficient describes the coupling of a spatially varying temperature $T(\mathbf{r}, t)$ and the density of a given species. Equation 1 will be derived in the present paper from thermodynamic arguments and force balance on the Brownian time scale, leading to explicit expressions for the thermal diffusion coefficient D_T. These expressions are explicitly evaluated as far as the electrical double layer contributions are concerned in terms of charge, core radius, and Debye screening length. The theoretical prediction will be compared to experiments on a micellar system[11] and a colloidal system of polystyrene particles of varying sizes.[12] Moreover, our analysis will be compared to other recent theories on charged colloids.[7,8,13]

2. Basic Idea for the Calculation of D_T for Colloids

The starting point for the explicit calculation of the thermal diffusion coefficient of colloids is the continuity equation for the number density $\rho(\mathbf{r}, t)$ of colloidal spheres

$$\frac{\partial}{\partial t}\rho(\mathbf{r}, t) = -\nabla\cdot[\mathbf{v}(\mathbf{r}, t)\rho(\mathbf{r}, t)] \qquad (2)$$

where ∇ is the gradient operator with respect to position $\mathbf{r}$ and $\mathbf{v}$ is the thermally averaged translational velocity of a colloidal

* E-mail: j.k.g.dhont@fz-juelich.de.
† Forschungszentrum Jülich.
‡ Ludwig Maximilians University.

(1) Ludwig, C. *Sitzungsber. Akad. Wiss. Wien Math. Naturwiss. Kl.* **1856**, *20*, 539.
(2) Piazza, R. *Philos. Mag.* **2003**, *83*, 2067−2085.
(3) Morozov, K. I. *J. Magn. Magn. Mater.* **1999**, *201*, 248−251.
(4) Putnam, S. A.; Cahill, D. G. *Langmuir* **2005**, *21*, 5317−5323.
(5) Rauch, J.; Köhler, W. *Phys. Rev. Lett.* **2002**, *88*, art. no. 185901.
(6) Duhr, S.; Arduini, S.; Braun, D. *Eur. Phys. J. E* **2004**, *15*, 277−286.
(7) Bringuier, E.; Bourdon, A. *Phys. Rev. E* **2003**, *67*, 011404.
(8) Parola, A.; Piazza, R. *Eur. Phys. J. E* **2004**, *15*, 255−263.
(9) Dhont, J. K. G. *J. Chem. Phys.* **2004**, *120*, 1632−1641.
(10) Dhont, J. K. G. *J. Chem. Phys.* **2004**, *120*, 1642−1653.
(11) Piazza, R.; Guarino, A. *Phys. Rev. Lett.* **2002**, *88*, 208302.
(12) Duhr, S.; Braun, D. *PNAS*, accepted.
(13) Fayolle, S.; Bickel, T.; Le Boiteux, S.; Würger, A. *Phys. Rev. Lett.* **2005**, *95*, 208301.

10.1021/la062184m CCC: $37.00
Published on Web 12/23/2006

sphere. The velocity of a colloidal particle will be calculated on the basis of thermodynamic arguments. This can be done on the diffusive time scale (typically on the order of a few nanoseconds), where inertial forces on colloidal spheres can be neglected. The noninertial forces thus add up to zero, which is known as "force balance".[14,15] There are generally two noninertial forces to be distinguished: the force **F** that arises from direct, nonhydrodynamic interactions between colloidal particles and its surroundings in a concentration and temperature gradient and the force $\mathbf{F}^{\mathrm{h}}$ due to hydrodynamic friction of the colloidal sphere with the solvent. Hydrodynamic interactions between colloidal spheres need not be considered here for single-particle diffusion (for interacting colloids, these hydrodynamic interaction contributions can be included on the basis of the Smoluchowski equation as discussed in ref 10). The hydrodynamic force is then proportional the velocity of the sphere

$$\mathbf{F}^{\mathrm{h}}(\mathbf{r}, t) = -\gamma \mathbf{v}(\mathbf{r}, t) \tag{3}$$

where γ is the friction coefficient. In the case of a charged colloidal particle, the electrolyte contribution to the friction coefficient is at most on the order of a few percent. Electrolyte friction will therefore be neglected, so that the friction coefficient is simply equal to the friction coefficient of the core with the solvent

$$\gamma = 6\pi\eta_0 R \tag{4}$$

where η_0 is the shear viscosity of the solvent and R the radius of the colloidal spheres. Force balance implies that

$$0 = \mathbf{F}(\mathbf{r}, t) + \mathbf{F}^{\mathrm{h}}(\mathbf{r}, t) \tag{5}$$

From eqs 5 and 3, it follows that

$$\mathbf{v}(\mathbf{r}, t) = \mathbf{F}(\mathbf{r}, t)/\gamma \tag{6}$$

An equation of motion for the colloid density is thus obtained from eqs 2 and 6 once an expression for **F** is found. This force will be obtained from thermodynamics and will turn out to be equal to a linear combination of gradients in colloid density and temperature, rendering eq 2 of the form in eq 1. This then leads to expressions for the thermal diffusion coefficient of a colloidal particle.

The force can be obtained from thermodynamics as follows. Like in ref 9, the system under consideration is divided into subsystems, which will be referred to hereafter as "boxes". These boxes are assumed to be large enough to allow them to be treated as thermodynamic systems on their own. Each box can be regarded in internal equilibrium when gradients in density and temperature are small enough to ensure a very slow evolution of the global colloid concentration and a slow heat transport. Gradients are supposed to be sufficiently small so that the largest internal relaxation time of a box is small compared to mass and heat transport times. Consider two neighboring boxes "1" and "2". Their volumes are equal to V, while the prescribed and fixed temperature in box 1 is equal to T and in box 2 equal to $T + \delta T$. There are N_1^{c} colloidal particles in box 1 and N_2^{c} in box 2. For simplicity, we shall consider the case where only H^+ ions dissociate from the surfaces of colloids and where an acid HA is added to the solution, which completely dissociates into H^+ and A^-. The final expression for the thermal diffusion coefficient is also valid for other types of ions. The number of H^+ ions in a box is denoted as N_1^+ for box 1 and N_2^+ for box 2. Likewise, the number of A^- ions is denoted as N_1^- and N_2^-, and the number of solvent molecules in boxes 1 and 2 is denoted as N_1^{s} and N_2^{s}, respectively. We have to calculate the reversible work δw^{rev} necessary to displace, in a quasi-static manner, δN^{c} colloidal spheres from box 1 to box 2. That is, an external force, that is infinitesimally less in amplitude than the force $-\mathbf{F}$, acts on the colloidal spheres, which are then quasi-statically transported in the direction in which they will diffuse if no external force would be present. The reversible work

$$\delta W^{\mathrm{rev}} = \delta w^{\mathrm{rev}}/\delta N^{\mathrm{c}} \tag{7}$$

per moved colloidal particle is related to the force **F**, which we set out to calculate as

$$\delta W^{\mathrm{rev}} = -\mathbf{L}\cdot\mathbf{F} \tag{8}$$

where **L** is the distance between the centers of box 2 and box 1, which is the distance over which the colloidal particles are displaced when moved from box 1 to box 2. Hence

$$\mathbf{F} = -\nabla W^{\mathrm{rev}}(\mathbf{r}) = -\left[\frac{\partial W^{\mathrm{rev}}}{\partial \rho}\nabla\rho + \frac{\partial W^{\mathrm{rev}}}{\partial T}\nabla T\right] \tag{9}$$

Substitution into eqs 6 and 2 and comparing to eq 1 leads to[17]

$$D = D_0\beta\rho\frac{\partial W^{\mathrm{rev}}}{\partial \rho}$$

$$D_{\mathrm{T}} = D_0\beta\rho\frac{\partial W^{\mathrm{rev}}}{\partial T} \tag{10}$$

where $D_0 = k_{\mathrm{B}}T/\gamma$ is the Einstein diffusion coefficient (with k_{B} Boltzmann's constant). In the derivation of these expressions, only the leading order terms in deviations from mean values of the density and temperature are accounted for. Terms like $|\nabla\rho|^2$ and $(\nabla T)\cdot(\nabla\rho)$ are thus neglected.

It should be noted that the definition of the thermal diffusion coefficient used in this paper complies with the equation of motion (eq 1). Different definitions are sometimes used, where, for example, D_{T} in eq 1 is replaced by ρD_{T}, or $c(1-c)D_{\mathrm{T}}$ in case of binary mixtures (with c the molar fraction of one of the species).

A thermodynamic approach relies on the assumption that there is local equilibrium, which is the case when gradients in temperature and concentration are small. Nonlinear effects for large temperature gradients have been observed experimentally in ref 16.

3. Force on a Colloidal Sphere: Heuristic Considerations

Before giving a more systematic derivation of an explicit expression for the reversible work, the intuitive approach given below readily leads to the correct result.

Imagine the following pathway to move a colloidal particle from box 1 to box 2. First, a force is applied which reversibly breaks off the interface. That is, the solvation layer is forced to attain the bulk solvent structure, and ions are attached to the surface of a colloidal sphere to render it uncharged. The reversible work to do this is minus the reversible work $W_i^{\mathrm{rev}}(T)$ involved in building up the interface at temperature T. Then, the core

(14) Batchelor, G. K. *J. Fluid Mech.* **1976**, *74*, 1.

(15) Dhont, J. K. G. *An introduction to dynamics of colloids*; Elsevier: Amsterdam, 1996.

(16) Duhr, S.; Braun, D. *Phys. Rev. Lett.* **2006**, *96*, 168301.

(17) In a comment in ref 9 section VI, this expression for the single-particle thermal diffusion coefficient was cited, except that instead of W^{rev} the chemical potential $\mu_{\mathrm{cs}}^{\star}$ for the "complexed colloidal sphere" appears. This is not correct: only that part of the chemical potential related to reversible work appears in the expression for the single-particle thermal diffusion coefficient.

material of the colloidal particle is reversibly heated to establish a raise in temperature of δT, which requires no work as far as the interface is concerned. The core is then moved to box 2, which requires no work as far as the interface is concerned, because the interface is simply nonexistent during this displacement. Then, the solvation layer is restructured and the electrical double layer is recharged, which requires work equal to $W_i^{\rm rev}(T + \delta T)$. On moving the colloid from box 1 to box 2, reversible work is done against gradients in the osmotic pressure Π. For noninteracting colloids, $\Pi = \rho k_{\rm B}T$, so that the accompanied body force is equal to $-\nabla\Pi = -k_{\rm B}[T\nabla\rho + \rho\nabla T]$. The work per colloidal particle is thus equal to $-k_B[T\nabla \ln\{\rho\} + \nabla T]$. This work includes the displacement of an equal volume of electrolyte solution in opposite direction. Hence

$$\mathbf{F} = -k_{\rm B}T\nabla \ln\{\rho\} - \left[k_{\rm B} + \frac{\partial W_i^{\rm rev}(T)}{\partial T}\right]\nabla T \qquad (11)$$

This leads to the following expressions for the diffusion coefficients[17]

$$D = D_0$$

$$D_{\rm T} = D_0\left[\frac{\rho}{T} + \beta\rho\frac{\partial W_i^{\rm rev}(T)}{\partial T}\right] \qquad (12)$$

The first term within the square brackets for $D_{\rm T}$ is the "ideal gas" contribution, and the second term is the contribution due to the presence of the double layer.

Besides the reversible work involving the solvation layer and the double layer, there are two additional types of internal degrees of freedom which require work (i) to build up the structured solid colloidal material in contact with electrolyte solution in the immediate vicinity of the surface of the colloidal sphere and (ii) work to build up the bulk solid core material of the colloidal particle including the accompanied replacement of solvent by the solid colloidal material. These two types of degrees of freedom can be incorporated in the reversible work and can simply be added in eq 12. The bulk contribution (ii) has been discussed in detail in ref 18.

The result (eq 12) will be derived in the following section in a more systematic way.

4. Force on a Colloidal Sphere: Thermodynamics

The following is an extension of the discussion in ref 10, where now the solvent molecules and ions are explicitly accounted for.

The reversible work $\delta w^{\rm rev}$ necessary to achieve the displacement of colloidal spheres from box 1 to box 2 is equal to $\delta F + S_1\delta T_1 + S_2\delta T_2$, where δF is the accompanied change in Helmholtz free energy. The entropy S_1 is the entropy carried by the material that is taken from box 2 to box 1 on moving the colloids from box 1 to box 2, and $\delta T_1 = -\delta T$ is the accompanied change of temperature of that material. Similarly, S_2 is the entropy carried by the material moved from box 1 to box 2, and $\delta T_2 = \delta T$ is the temperature change of that material. These entropic terms cancel against similar contributions in the Gibbs−Duhem relation that will be used later in our analysis (as is shown in the Appendix). For brevity, we shall therefore not denote these entropic terms in equations here after. All entropic contributions of the form $S\delta T$ cancel at the end. Hence

$$\delta w^{\rm rev} = \delta F\ (+\ \text{entropic contributions}) \qquad (13)$$

The Helmholtz free energy of each of the two boxes is a function of the number of solvent molecules, ions, and colloidal particles in the box, its volume, and the temperature. Let $\delta N_j^{\rm s}$ and $\delta N_j^{\pm}$ denote the change of the number of solvent molecules and ions (H^+ and A^-) in box j associated with an exchange of $\delta N^{\rm c}$ colloidal particles. The reversible work necessary for the above-described process is then equal to

$$\delta w^{\rm rev} = \delta F = F(N_1^{\rm c} - \delta N^{\rm c}, N_1^{\rm s} - \delta N_1^{\rm s}, N_1{}^+ - \delta N_1{}^+, N_1{}^- - \delta N_1{}^-, V, T) + F(N_2^{\rm c} + \delta N^{\rm c}, N_2^{\rm s} + \delta N_2^{\rm s}, N_2{}^+ + \delta N_2{}^+, N_2{}^- + \delta N_2{}^-, V, T + \delta T) - F(N_1^{\rm c}, N_1^{\rm s}, N_1{}^+, N_1{}^-, V, T) - F(N_2^{\rm c}, N_2^{\rm s}, N_2{}^+, N_2{}^-, V, T + \delta T) \qquad (14)$$

Expansion of the free energies with respect to $\delta N^{\rm c}$, $\delta N_j^{\rm s}$, and $\delta N_j^{\pm}$, using $\partial F/\partial N_j^{\rm c} = \mu_{{\rm c},j}$, with $\mu_{{\rm c},j}$ the chemical potential of the colloidal particles in box j, and similarly for the solvent molecules and the ions, gives

$$\delta w^{\rm rev} = \{\mu_{\rm c,2} - \mu_{\rm c,1}\}\delta N^{\rm c} + \mu_{\rm s,2}\delta N_2^{\rm s} - \mu_{\rm s,1}\delta N_1^{\rm s} + \mu_2^+\delta N_2^+ + \mu_2^-\delta N_2^- - \mu_1^+\delta N_1^+ - \mu_1^-\delta N_1^- \qquad (15)$$

The chemical potentials appearing in eq 15 are interpreted as follows. The chemical potential of a colloidal sphere is understood to be the difference in free energy of an uncharged colloid in its "dry state" and in the dissolved state in the suspension. It contains therefore two contributions: (i) the free energy that is released on spontaneous formation of the solvation layer and the double layer on transferring a "dry" colloidal sphere to the suspension and (ii) the gain in entropy of a colloidal sphere due to its freedom to take any position in the suspension. In particular, the gain in entropy of ions that are dissociated from the surface of a colloidal sphere is included in the chemical potential of a colloid. Similarly, the chemical potential of an added salt molecule is defined as the free energy change on dissolving a "dry" salt molecule. The separate chemical potentials μ_j^+ and μ_j^- of H^+ and A^- are therefore not independent and will only occur in the combination $\mu_{{\rm salt},j} \equiv \mu_j^+ + \mu_j^-$, which will be referred to as "the chemical potential of a salt molecule".

With the above definitions of chemical potentials, the changes $\delta N_j^{\pm}$ are changes solely due to transport of $H^+ - A^-$ pairs, that is, of salt molecules. It follows from electroneutrality that $\delta N_j^+ = \delta N_j^-$, which will be denoted simply as $\delta N_j^{\rm salt}$. This is the change of the number of salt molecules in box j. Hence, from eq 15

$$\delta w^{\rm rev} = \{\mu_{\rm c,2} - \mu_{\rm c,1}\}\delta N^{\rm c} + \mu_{\rm s,2}\delta N_2^{\rm s} - \mu_{\rm s,1}\delta N_1^{\rm s} + \mu_{{\rm salt},2}\delta N_2^{\rm salt} - \mu_{{\rm salt},1}\delta N_1^{\rm salt} \qquad (16)$$

The number of solvent molecules and the number of ion pairs $H^+ - A^-$ that is transported is connected to the number of colloidal particles that are moved from box 1 to box 2. On moving a colloidal particle from box 1 to box 2, an equal volume of electrolyte solution will be moved from box 2 to box 1, when thermal expansion of colloidal material and solvent is neglected. The total number of bulk solvent molecules within the volume of a colloidal sphere in box j is equal to $v_{\rm c}^0\rho_{{\rm s},j}^0\delta N^{\rm c}$, where $v_{\rm c}^0$ is the volume occupied by the core of a single colloidal sphere and $\rho_{{\rm s},j}^0$ is the bulk concentration of solvent in box j, that is, the

(18) Würger, A. *Europhys. Lett.* **2006**, *74*, 658−664.

concentration of solvent outside the solvation layer. The molar volume v_c^0 of the colloids is taken independent of the colloid concentration and temperature, as indicated by the superscript 0. The molar volume v_c^0 is to a good approximation simply equal to the volume of a colloidal sphere, where the relatively small differences due to thermal expansion of the colloidal material are neglected. There is an excess number of molecules Γ^s within the solvation layer that is attached to each colloidal sphere. The free energy connected to the formation of this solvation layer is already incorporated in the chemical potential of a colloidal particle, as discussed above. The changes of the number of solvent molecules δN_j^s in eq 16 do therefore not include the excess amounts of solvent molecules within the solvation layers. Hence

$$\delta N_j^s = -v_c^0 \rho_{s,j}^0 \delta N^c \tag{17}$$

This equation allows one to express δN_j^s in eq 16 in terms of δN^c. A similar relation can be derived for the change of the number of ions. Hence, just as for the solvent molecules we have

$$\delta N_j^{salt} = -v_c^0 \rho_{salt,j}^0 \delta N^c \tag{18}$$

where $\rho_{salt,j}^0$ ($= \rho_{\pm}^0$) is the number concentration of ion pairs (= salt molecules) outside the double layer.

Substitution of eqs 17 and 18 into eq 16 gives

$$\delta w^{rev}/\delta N^c = \mu_{c,2} - \mu_{c,1} - v_c^0[\rho_{s,2}^0 \mu_{s,2} - \rho_{s,2}^0 \mu_{s,1} + \rho_{salt,2}^0 \mu_{salt,2} - \rho_{salt,1}^0 \mu_{salt,1}] \tag{19}$$

or, in obvious notation

$$\delta w^{rev}/\delta N^c = \delta\mu_c - v_c^0 \delta[\rho_s^0 \mu_s] - v_c^0 \delta[\rho_{salt}^0 \mu_{salt}] \tag{20}$$

Here, the δ's refer to the differences between box 2 and box 1.

The expression (eq 20) includes both single-particle and interaction contributions. In order to separate these two contributions, the chemical potential of the solvent molecules and the ions within the suspension are defined through an osmotic equilibrium. That is, we shall imagine each box to be in osmotic equilibrium with a reservoir of electrolyte solution with the corresponding temperature, where the membrane is permeable for solvent and ions but not for colloids. The physics behind the introduction of such a reservoir is as follows. The dynamics of the small species (the solvent molecules and the ions) are much faster compared to the colloidal particles. These small species are therefore always in equilibrium with the field imposed by the instantaneous configuration of colloidal particles, provided that each box is itself in internal equilibrium. In particular, the small species inside the solvation layer and the double layer are in equilibrium with the small species outside these layers. The solvent molecules and ions outside the solvation layer and double layer are now formally regarded as an osmotic reservoir. The Gibbs−Duhem relation for the suspension reads (entropic contributions are again not denoted here, since these cancel against the entropic contributions in eq 13, as shown in the Appendix)

$$0 = V\delta p - N^c \delta\mu_c - N^s \delta\mu_s - N^{salt} \delta\mu_{salt} \tag{21}$$

where p is the mechanical pressure within the suspension with volume V. Note that, as for eq 19, the differences δ refer to the differences between box 2 and box 1. Since differences between the two boxes are (infinitesimally) small, the number N^c of colloidal particles in eq 21 is "the average" of the number of particles in the two boxes, and similarly for the other extensive quantities. The corresponding Gibbs−Duhem relation for differences between the reservoirs of boxes 2 and 1 is

$$0 = V^r \delta p_r - N_r^s \delta\mu_s - N_r^{salt} \delta\mu_{salt} \tag{22}$$

where a sub- or superscript "r" of "reservoir" is added to indicate that these quantities relate to the osmotic reservoir. This index is missing on μ_s and μ_{salt}, since these are equal in the suspension and the osmotic reservoir. Since the osmotic pressure is defined as

$$\Pi = p - p_r \tag{23}$$

it follows from eqs 21 and 22 that

$$\delta\mu_c = \frac{1}{\rho}\delta\Pi + \frac{1}{\rho}(\rho_{s,r} - \rho_s)\delta\mu_s + \frac{1}{\rho}(\rho_{salt,r} - \rho_{salt})\delta\mu_{salt} \tag{24}$$

where $\rho = N^c/V$ and $\rho_{salt} = N^{salt}/V$ are the number densities of colloids and salt molecules, respectively. Substituting this expression for $\delta\mu_c$ into eq 19 leads to

$$\delta w^{rev}/\delta N^c = \frac{1}{\rho}\delta\Pi - v_c^0 \delta[\rho_s^0 \mu_s] - v_c^0 \delta[\rho_{salt}^0 \mu_{salt}] + \frac{1}{\rho}(\rho_{s,r} - \rho_s)\delta\mu_s + \frac{1}{\rho}(\rho_{salt,r} - \rho_{salt})\delta\mu_{salt} \tag{25}$$

The number density ρ_s^0 of solvent molecules outside the solvation layer is different from the "thermodynamic" density $\rho_s = N^s/V$ in the suspension. There is an excess number of molecules Γ^s within the solvation layer that is attached to each colloidal sphere. This excess amount of solvent molecules in the solvation layer of a colloidal sphere is defined as

$$\Gamma^s = \int_{r>R} \mathrm{d}\mathbf{r}[\rho_s(r) - \rho_s^0] \tag{26}$$

where $\rho_s(r)$ is the local solvent molecule concentration at a radial distance r from the center of a colloidal sphere. The Gibbs dividing surface is defined here such that the adsorbed amount of solid colloidal core material is zero. Since the total number $V\rho_s$ of solvent molecules is equal to $N^c\Gamma^s + (V - N^c v_c^0)\rho_s^0$, it follows that

$$\rho_s = \rho\Gamma^s + (1 - \varphi)\rho_s^0 \tag{27}$$

where $\varphi = v_c^0\rho$ is the volume fraction of colloids.

Due to electroneutrality of the colloidal surface plus its double layer, the excess amount of H^+ ions is equal to $-Z$, where Z is the valence of a colloidal sphere (including the sign of the charge). In the present case, where H^+ ions dissociate from the surface, Z is a negative number. The number of adsorbed salt molecules Γ^{salt} in a single double layer is thus equal to

$$\Gamma^{salt} = \Gamma^- = \Gamma^+ + Z \tag{28}$$

where

$$\Gamma^{\pm} = \int_{r>R} \mathrm{d}\mathbf{r}[\rho_{\pm}(r) - \rho_{\pm}^0] \tag{29}$$

are the excess amounts of H^+ or A^- ions in the double layer. Here, $\rho_{\pm}(r)$is the local number concentration of H^+ and A^- around a colloidal sphere, which can be calculated within the scope of the Debye−Hückel theory for small surface potentials. Similarly as for solvent molecules, the thermodynamic concentration of

salt is equal to

$$\rho_{\text{salt}} = \rho\Gamma^{\text{salt}} + (1 - \varphi)\rho^0_{\text{salt}} \tag{30}$$

where $\rho^0_{\text{salt}} = \rho^0_{\pm}$ is the concentration of salt molecules outside the double layer.

The chemical potential of solvent molecules away from a colloidal particle, outside the solvation layer, is equal to that of the osmotic reservoir. The concentration ρ^0_s of such solvent molecules is therefore equal to the concentration $\rho_{s,r}$ of solvent molecules in the reservoir for incompressible solvents. With the neglect of the small contribution of thermal expansion of bulk material (so that $\delta\rho^0_s = 0$), using eq 27 gives

$$-v^0_c\delta[\rho^0_s\mu_s] + \frac{1}{\rho}(\rho_{s,r} - \rho_s)\delta\mu_s = -\Gamma^s\delta\mu_s \tag{31}$$

Similarly, the concentration ρ^0_{salt} outside the double layer is equal to the salt concentration $\rho_{\text{salt,r}}$ in the osmotic reservoir, so that it follows from eq 30 that

$$-v^0_c\delta[\rho^0_{\text{salt}}\mu_{\text{salt}}] + \frac{1}{\rho}(\rho_{\text{salt,r}} - \rho_{\text{salt}})\delta\mu_{\text{salt}} = -\Gamma^{\text{salt}}\delta\mu_{\text{salt}} \tag{32}$$

Substitution of eqs 31 and 32 into eq 25 gives

$$\delta w^{\text{rev}}/\delta N^c = \frac{1}{\rho}\delta\Pi - \Gamma^s\delta\mu_s - \Gamma^{\text{salt}}\delta\mu_{\text{salt}} \tag{33}$$

This result can be written in an alternative form with the use of the Gibbs adsorption equation

$$-\Gamma^s\delta\mu_s - \Gamma^{\text{salt}}\delta\mu_{\text{salt}} = 4\pi R^2\delta\gamma + S_i\delta T \tag{34}$$

where R is the radius of a colloidal sphere, γ is the surface tension, and S_i is the entropy of a single interface between the colloidal material and the electrolyte solution, including the solvation layer and double layer. As before, the location of the Gibbs dividing surface is chosen such that the amount of adsorbed solid colloidal material vanishes. The surface tension γ is well-defined for both thin and thick double layers. Since $4\pi R^2\gamma$ is equal to the free energy of the interface, it follows that

$$-\Gamma^s\delta\mu_s - \Gamma^{\text{salt}}\delta\mu_{\text{salt}} = \delta W_i^{\text{rev}} \tag{35}$$

where W_i^{rev} is the reversible work involved in building up a single interface, including the solvation layer and the electrical double layer. The reversible work $W^{\text{rev}} = \delta w^{\text{rev}}/\delta N^c$ necessary to move a single colloidal sphere (see eq 8) thus follows from eqs 33 and 35 as

$$\delta W^{\text{rev}} = \frac{1}{\rho}\delta\Pi + \delta W_i^{\text{rev}} \tag{36}$$

The first term on the right-hand side describes the energy necessary to displace a colloidal particle against gradients in the osmotic pressure. The second term is related to the work that is involved in changing the temperature of a solvation layer and a double layer and of the immediate surface of the colloidal sphere.

For very dilute suspensions, where colloidal spheres do not interact with each other, $\Pi = \rho k_B T$. From eqs 10 and 36, the following expressions for the diffusion coefficients are then found

$$D = D_0$$

$$D_T = D_0\left[\frac{\rho}{T} + \beta\rho\frac{\partial W_i^{\text{rev}}(T)}{\partial T}\right] \tag{37}$$

which reproduces eq 12.

The interaction contributions to the osmotic pressure[9,10] should be added to the above results for concentrated colloids.

As mentioned before, what has been neglected are the degrees of freedom associated with the bulk material of the core of a colloidal particle. The reversible work that is required to build up the solid bulk core material of a colloidal sphere (and the accompanied displacement of solvent) can simply be added to the work in eq 37.

5. Double-Layer Free Energy and Reversible Work

In order to compare the prediction (eqs 12 and 37) for the thermal diffusion coefficient to experiments, the reversible work W_i^{rev} involved in creating an interface must be expressed in terms of, for example, salt concentration and the radius of the colloidal sphere. In the present section, only the double-layer contribution $W_{\text{dl}}^{\text{rev}}$ to the interface work is considered.

It will be assumed that the dielectric constant within the core of a colloidal sphere is constant and there are no charges inside the core of the colloidal particle, that is, all charges are assumed to be located on its surface.

When the dielectric constant within the core of the colloidal particle is homogeneous, independent of position, the surface charge σ is proportional to the radial derivative of the electric potential Φ at the surface of the colloidal particle, that is, at the radial distance $r = R$, with R the radius of the colloidal sphere, $\sigma = -\epsilon(\mathrm{d}\Phi(r)/\mathrm{d}r)_{|r=R}$, with ϵ the dielectric constant of the solvent. For moderate electric surface potentials, the electric potential Φ within the double layer is equal to[19]

$$\Phi(r) = \Phi_s\frac{\exp\{-\kappa(r - R)\}}{r/R} \quad (r \geq R) \tag{38}$$

where $\Phi_s = \Phi(r = R)$ is the surface potential and

$$\kappa = \sqrt{\frac{e^2}{k_B T\epsilon}\sum_j \rho^0_j z_j^2} \tag{39}$$

is the reciprocal Debye length, with $e > 0$ the elementary charge, k_B Boltzmann's constant, ρ^0_j the number density of ions of species j outside the double layer, which carry z_j elementary charges.

The surface potential can be expressed in terms of the total charge $Q = 4\pi R^2\sigma$ on a colloidal sphere from the relation between the charge density and the radial derivative of the potential at the colloidal surface as mentioned above

$$\Phi_s = \frac{Q}{4\pi\epsilon R}\frac{1}{1 + \kappa R} \tag{40}$$

For some colloidal particles (like carboxyl-modified polystyrene), the surface groups are fully dissociated, whereas for other systems (like bare silica), the surface groups are only partially dissociated, depending on the pH.

The free energy of a colloidal particle is, by definition, the change in free energy on immersion of a colloid in its "dry state" into the dispersion. This free energy is either the Helmholtz free

(19) Verwey, E. J. W.; Overbeek, J. Th. G. *Theory of the stability of lyophobic colloids*; Dover publications: New York, 1999.

energy under constant volume or the Gibbs free energy under constant pressure. Before immersion, the colloidal particle is not solvated and surface groups are not dissociated. On immersion, the colloidal particle will gain entropy since it is free to move through the dispersion, the surface of the particle will be solvated, and ions will be released from the surface while building up the double layer. The free energy to build up the double layer consists of two parts: (i) the free energy that it takes to create the ion cloud around the colloid and to charge its surface, which can be calculated via a "charging process"; and (ii) the gain in entropy on release of ions from the surface of the colloidal particle on charging the surface. These two contributions have been discussed in detail in chapter 3 of the classic book of Verwey and Overbeek.[19] The charging process costs an energy in the form of reversible work $W_{\mathrm{dl}}^{\mathrm{rev}}$ equal to

$$W_{\mathrm{dl}}^{\mathrm{rev}} = \frac{1}{2} Q\Phi_{\mathrm{s}} \tag{41}$$

The change in free energy due to the release of ions from the surface is equal to $-Q\Phi_{\mathrm{s}}$. The double-layer free energy F_{dl} (relative to the "dry" colloidal particle) is thus equal to

$$F_{i,\mathrm{dl}} = -\frac{1}{2} Q\Phi_{\mathrm{s}} \tag{42}$$

The free energy of the double layer must be negative, since otherwise the double layer would be unstable: the free energy would be lowered by decharging the colloidal particle if the free energy were positive. The reversible work is thus equal but opposite in sign to the free energy, as a result of the entropic contribution due to the release of ions from the colloid surface.

Note that, according to eq 42, the contribution γ_{dl} of the double layer to the interfacial tension is equal to

$$\gamma_{\mathrm{dl}} = -\frac{1}{8\pi R^2} Q\Phi_{\mathrm{s}} = -\frac{\epsilon}{2R}(1+\kappa R)\Phi_{\mathrm{s}}^2 \tag{43}$$

within the Debye−Hückel approximation, where in the second line eq 40 has been used. For thin double layers, this reduces to $\gamma_{\mathrm{dl}} = -\epsilon\kappa\Phi_{\mathrm{s}}^2/2$, which is the expression that is used in, for example, refs 11 and 20 (in Gaussian units).

6. Explicit Expression for the Soret Coefficient

Explicit expressions for the double-layer contribution to the single-particle diffusion coefficient are obtained by substitution of eqs 39−41 into eq 37. Again neglecting small contributions from thermal expansion, it is found that the double-layer contribution to the Soret coefficient $S_{\mathrm{T}}^{(\mathrm{dl})} = D_{\mathrm{T}}/\rho D$ is given by

$$TS_{\mathrm{T}}^{(\mathrm{dl})} = 1 + \frac{1}{4}\beta Q\Phi_{\mathrm{s}} \frac{\kappa R}{1+\kappa R}\left[1 - \frac{\mathrm{d}\ln\epsilon}{\mathrm{d}\ln T}\left(1+\frac{2}{\kappa R}\right)\right] + \beta Q\Phi_{\mathrm{s}} \frac{\mathrm{d}\ln Q}{\mathrm{d}\ln T} \tag{44}$$

The "ideal gas" contribution (the first term on the right-hand side in eq 44) stems from work against the osmotic pressure, where additional terms should be accounted for when intercolloidal interactions become important at higher concentrations (see refs 9 and 10). The last term in this equation is only important when the total charge on the colloidal spheres is temperature-dependent. This is generally the case for colloidal particles where the surface groups are only partially dissociated.

(20) Rückenstein, E. *J. Colloid Interface Sci.* **1981**, *83*, 77−81.

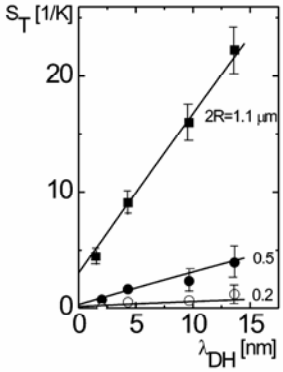

Figure 1. The Soret coefficient at room temperature $T = 298$ K as a function of the Debye−Hückel screening length $\lambda_{\mathrm{DH}} = \kappa^{-1}$ for carboxyl-modified polystyrene spheres with a surface charge of $\sigma = 4500\ e/\mu\mathrm{m}^2$, or, equivalently, $4\pi l_{\mathrm{B}}^2\sigma/e = 0.029$. The radii of the spheres are 550, 250, and 100 nm, as indicated in the figure. The solid lines are the predictions from eq 45 with $\mathrm{d}Q/\mathrm{d}T = 0$, and the data points are for polystyrene spheres.[12] The only adjustable parameter for each curve is the offset for zero Debye length, which is related to the solvation layer contribution and the contribution associated with the degrees of freedom within the bulk solid core material of a colloidal sphere.

In order to compare with experiments, where the dependence of the Soret coefficient on the Debye length $\lambda_{\mathrm{DH}} = \kappa^{-1}$ and the radius R of the colloidal spheres is probed, eq 44 is more conveniently written as

$$TS_{\mathrm{T}}^{(\mathrm{dl})} = 1 + \frac{1}{4}\left(\frac{4\pi l_{\mathrm{B}}^2\sigma}{e}\right)^2 \frac{\kappa R}{(1+\kappa R)^2}\left(\frac{R}{l_{\mathrm{B}}}\right)^3 \times \left[1 - \frac{\mathrm{d}\ln\epsilon}{\mathrm{d}\ln T}\left(1+\frac{2}{\kappa R}\right)\right] + \left(\frac{4\pi l_{\mathrm{B}}^2\sigma}{e}\right)^2 \frac{1}{1+\kappa R}\left(\frac{R}{l_{\mathrm{B}}}\right)^3 \frac{\mathrm{d}\ln Q}{\mathrm{d}\ln T} \tag{45}$$

where $l_{\mathrm{B}} = \beta e^2/4\pi\epsilon$ is the Bjerrum length (which is 0.71 nm for water at room temperature). This result is valid for arbitrary Debye screening lengths. Note that the dimensionless combination $4\pi l_{\mathrm{B}}^2\sigma/e$ is the number of unit charges on a fictitious sphere with radius l_{B} with the same charge density as the colloids. As will be seen in section 7, where a comparison with experiments is made, the values that this dimensionless group takes vary from about 0.01 for polystyrene spheres to 1 for SDS micelles. The temperature dependence of the dielectric constant cannot be neglected, since for water at room temperature, $\mathrm{d}\ln\epsilon/\mathrm{d}\ln T = -1.34$.

7. Comparison with Experiments and Other Theories

In this section, we shall compare the theoretical predictions in eq 45 with experiments on two different types of systems: carboxyl-modified polystyrene spheres of various radii but equal charge density[12] and (ii) a SDS micellar solution.[11] In particular, the salt concentration dependence of the Soret coefficient will be discussed as well as its colloid size dependence. The polystyrene spheres are always large compared to the Debye length, while for the micellar system, the Debye length is comparable to or larger than the size of the micelles. The table gives the parameters for the two systems that are needed for a quantitative comparison.

A comparison with experiments on colloidal polystyrene spheres with identical surface chemistry but differing radii is given in Figure 1, where data are taken from ref 12. Here, the Soret coefficient is plotted against the Debye−Hückel screening

Table 1. System Parameters

system	radius [nm]	σ	$4\pi l_B^2\sigma/e$	$d \ln \epsilon / d \ln T$	l_B [*nm*]
polystyrene	550/250/100	4500 $e/\mu m^2$	0.029	−1.34	0.71
SDS micelles	2.7	0.218 e/nm^2	1.38	−1.34	0.71

length $\lambda_{DH} = \kappa^{-1}$. The surface charge density of the spheres as measured with electrophoresis is equal to $\sigma = 4500\ e/\mu m^2$, and hence, $4\pi l_B^2\sigma/e = 0.029$. Since the surface groups for these particles are fully dissociated, the charge is independent of temperature, that is $dQ/dT = 0$. The Bjerrum length for water at room temperature is 0.71 nm and $d \ln \epsilon / d \ln T = -1.34$.

The only adjustable parameter in a comparison of experimental values for the Soret coefficient and eq 45 is the offset for zero Debye length, which is related to the contribution of the solvation layer to the reversible work W_i^{rev} to create an interface and the contribution associated with the degrees of freedom within the bulk solid core material of the colloidal sphere. The solid curves in Figure 1 correspond to eq 45 with $dQ/dT = 0$. As can be seen, the agreement with the experiments is quite reasonable, both for the salt-concentration dependence of the Soret coefficient and for the dependence on the radii of the colloids.

The variation of the offset in Figure 1 with the radius of the colloidal spheres indicates that the solvation layer is the main additional contribution to the single-particle Soret coefficient and that the contribution from colloidal bulk-material is much less important. This is analyzed in more detail in ref 12.

Thermodiffusion of SDS micellar particles has been explored in ref 11. These particle are much smaller than the polystyrene spheres discussed above. For this system, the particle radius is $R = 2.7$ nm and the charge density is 0.218 e/nm^2, and hence, $4\pi l_B^2\sigma/e = 1.38$.[21] This system thus covers an entirely different part of parameter space as compared to the above-mentioned polystyrene spheres. For the SDS micelles, it is reasonable to assume that the surface groups are dissociated to an extent that allows the neglect of the temperature dependence of the charge in eq 45. Care should be taken when comparing these experiments with the prediction in eq 45, since now, according to eq 40, the dimensionless parameter $\beta e\Phi_s$ can be large, which invalidates the Debye−Hückel approach (for $\lambda_{DH} = 0.63$ nm, $\beta e\Phi_s = 1$, and for $\lambda_{DH} = 1.07$ nm, we have $\beta e\Phi_s = 1.5$). The above theory is thus certainly not applicable when λ_{DH} is larger than about 1 nm. For such small Debye lengths, the continuum Poisson−Boltzmann approach might be questionable. Nontheless, we compare the prediction in eq 45 with the experimental data in Figure 2. As can be seen, the salt concentration dependence of the Soret coefficient is correctly predicted for Debye lengths where the Debye−Hückel theory is valid. The theory and experimental data begin to deviate from the experimental data at a Debye length above which $\beta e\Phi_s$ becomes larger than unity, as expected. As before, the offset is an adjustable parameter. In ref 11, it is stated that, even for potentials such that $\beta e\Phi_s$ is much larger than unity, the Debye−Hückel theory is still applicable when an "effective charge" is used. In the above comparison, we used the charge density as reported in ref 21 for this system for lower potentials and refrained from using an "effective charge".

On the basis of a capacitor analogon with the electric-double-layer/charged-colloid system, the following expression for the Soret coefficient may be obtained[12]

$$TS_T^{(dl)} = 1 + \frac{1}{4}\left(\frac{4\pi l_B^2\sigma}{e}\right)^2 \frac{R^2}{\kappa l_B^3}\left\{1 - \frac{d \ln\{\epsilon\}}{d \ln\{T\}}\right\} \quad \text{(from ref 12)} \qquad (46)$$

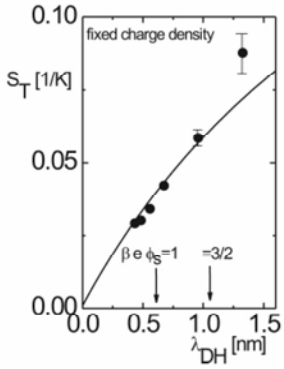

Figure 2. The Soret coefficient at room temperature $T = 298$ K as a function of the Debye−Hückel screening length $\lambda_{DH} = \kappa^{-1}$ for SDS micelles with a surface charge of $\sigma = 0.218\ e/nm^2$, or, equivalently, $4\pi l_B^2\sigma/e = 1.38$. The radii of the spheres are 2.7 nm. The solid lines are the predictions from eq 45 with $dQ/dT = 0$. The experimental data are taken from ref 11. As before, the only adjustable parameter is the offset at zero Debye length. The verticle arrows indicate the Debye lengths where $\beta e\Phi_s$ is 1 and $^3/_2$, beyond which the Debye−Hückel approach becomes invalid.

where the "ideal-gas contribution" has been added. This expression is precisely the result in eq 45 in the limit of thin double layers, where $\kappa R \gg 1$. Note that the polystyrene particles are very large in comparison to the double-layer thickness. The experimental results in Figure 1 can therefore also be described on the basis of the capacitor model.

In ref 20, an expression for the thermophoretic velocity is derived for thin double layers on the basis of a Navier−Stokes equation together with thermodynamic relations. By combining eq 27 from ref 20 and eq 43 for the double-layer contribution to the surface tension with $\kappa R \gg 1$, it is found that

$$TS_T^{(dl)} = 1 + \frac{3\pi}{4}\left(\frac{4\pi l_B^2\sigma}{e}\right)^2 \frac{R}{l_B^3\kappa^2} \quad \text{(from ref 20)} \qquad (47)$$

This expression is used in ref 11 to interpret the experimental data on SDS micelles discussed above. It predicts that the Soret coefficient is a quadratic function of the Debye screening length. This result does not agree with our prediction in eq 45, not for thin and also not for extended double layers. The reasons for this are (i) that it is not the free energy but only the reversible work that determines the Soret coefficient and (ii) that eq 47 assumes thin double layers, whereas the double layer thickness for the micellar SDS system is actually comparable to or larger than the size of the micelles. We therefore feel that the agreement between the proposed theory in ref 11 with their SDS micellar data is fortuitous.

Bringuier and Bourdon[7] propose an expression for the thermal diffusion coefficient in terms of the temperature derivative of the total internal energy (see their eq 13), based on arguments that are put forward by van Kampen.[22] Disregarding the temperature dependence of the total charge, which amounts to taking the limit $E \to \infty$ in their eq 17, where E is the energy related to the thermally activated desorption of ions from the surface of the colloids, and using their expression 16 for U in

(21) Bucci, S.; Fagotti, C. *Langmuir* **1991**, *7*, 824.
(22) van Kampen, N. G. *J. Phys. Chem. Solids* **1988**, *49*, 673−677.

their eq 13 gives, for small colloid concentrations

$$TS_T^{(dl)} = 1 + \frac{1}{4}\left(\frac{4\pi l_B^2 \sigma}{e}\right)^2 \frac{1}{(1+\kappa R)^2}\frac{\kappa R^4}{l_B^3}$$

(from ref 7 with $E \to \infty$ and $\rho \to 0$) (48)

Here, the temperature dependence of the total charge as well as the dielectric constant have been neglected. Within this approximation, the above expression is in accordance with our expression (eq 45), for both thin and thick double layers. The correspondence between this single-particle result for charged colloids from ref 7 and our expression (eq 45) for the Soret coefficient is quite satisfactory in view of the fundamentally different approaches that have been employed. For interacting systems, however, there is a difference between the general result in eq 13 of ref 7 and what is said in the present paper and refs 9 and 10. According to refs 9 and 10, interaction contributions are related to temperature and density derivatives of the osmotic pressure rather than derivatives of the internal energy (for the isothermal collective diffusion coefficient, this is has long been known). The internal energy U due to intercolloidal interactions is introduced in ref 7 in a rather uncontrollable manner. If the reversible work is used instead of U, and one recognizes that reversible work is done (i) against gradients in the osmotic pressure which includes interaction contributions and (ii) to build up single-particle colloidal complexes, the expression that would have been obtained in ref 7 fully agrees with the results of the present paper and refs 9 and 10.

Similar considerations as in ref 7 based on van Kampen's work[22] lead to the correct expression for the Soret coefficient in ref 18 (the expression between their eqs 4 and 5), provided that the "energy" u is interpreted as the reversible work to build up a colloidal sphere. The contribution to the reversible work associated with the bulk core material of a colloidal sphere and the displaced amount of solvent by the core has been extensively discussed in ref 18.

8. Summary and Conclusions

On the basis of force balance on the Brownian time scale in combination with thermodynamic considerations concerning the force on a colloidal sphere resulting from gradients in concentration and temperature, it follows from the present analysis and what has been said in ref 9 that the collective diffusion coefficient D and the thermal diffusion coefficient D_T are given by

$$D = D_0\beta\frac{\partial\Pi(\rho, T, \mu_s)}{\partial\rho}$$

$$D_T = D_0\beta\left[\frac{\partial\Pi(\rho, T, \mu_s(T,s))}{\partial T} + \rho\frac{\partial W_c^{rev}}{\partial T}\right] \qquad (49)$$

where Π is the osmotic pressure (which is a function of the colloid number density ρ, the temperature T, and the chemical potential μ_s of the solvent). In the temperature derivative of Π in the expression for D_T, the derivative also acts on the temperature dependence of the chemical potential of the solvent (the variable s represents the other variables on which μ_s depends besides the temperature). Furthermore, D_0 is the Einstein diffusion coefficient and $\beta = 1/k_BT$ (where k_B is Boltzmann's constant). The first term on the right-hand side of the expression for D_T accounts for direct interactions between colloidal particles and includes the "ideal gas" contribution, while the second term is the single-particle contribution. Here, W_c^{rev} is the reversible work that is needed to build up a colloidal particle. This includes the creation of (i) the solid bulk core material of the colloid and the associated displacement of solvent, (ii) the structured layer of solid material in the immediate vicinity of the solvent, (iii) the solvation layer, and (iv) the electrical double layer. The results in eq 49 reproduce the expression for the Soret coefficient given in ref 18 (see the equation between their eqs 4 and 5), provided that the energy u is interpreted as the reversible work to build up a colloidal sphere.

What is neglected in eq 49 is thermal expansion of colloidal core material and solvent and, more importantly, hydrodynamic interactions between the colloidal spheres. Hydrodynamic interactions become significant at higher colloid concentrations and can be accounted for in a microscopic approach as described in ref 10.

The single-particle contribution to the Soret coefficient related to the electric double layer is calculated within the Debye−Hückel approximation, leading to eqs 44 and 45. This prediction is shown to be in accordance with experiments on polystyrene spheres (thin double layers) and micelles (thick double layers), within the parameter range where the Debye−Hückel approximation is valid. There is a single adjustable parameter when comparing with experiments where the salt concentration is varied. This is the intercept at zero Debye length, which is related to the remaining contributions to W_c^{rev} mentioned above.

Acknowledgment. This work has benefited from several discussions with Wim Briels, Eric Bringuier, Werner Köhler, and Marianne Hartung, part of which resulted in the material of section 3 and the Appendix.

Appendix: The Entropic Contributions

It will be shown here that the entropic contributions to eq 13 and those arising from the Gibbs−Duhem relations for the suspension and the osmotic reservoir cancel, provided that thermal expansion is neglected and the solvent is incompressible. In ref 9, these entropic contributions were simply omitted.

For reversible isothermal changes, the reversible work is equal to the change in free energy. The process considered here is also isothermal (since the temperature of the two boxes is fixed). However, in exchanging matter between the two boxes, this matter experiences a change in its temperature. The free energy must be corrected for these temperature changes in order to obtain the reversible work. Since the change δF in free energy is equal to $\delta F = \delta w^{rev} - S\delta T$, we have to add the contribution $S\delta T$ to the calculated δF in order to obtain the reversible work δw^{rev}.

There is a single-particle contribution to the reversible work that is related to the change in temperature of matter that is exchanged. For example, the reversible work involved in building up an electrical double layer is temperature-dependent. In changing the temperature of a double layer, part of the exchanged heat in order to change the temperature is therefore converted into work. This latter contribution to the reversible work is a single-particle contribution which will be denoted in this Appendix as δw_c^{rev} (where the subscript "c" stands for "colloid"). The total reversible work is thus written as

$$\delta w^{rev} = \delta F + S\delta T + \delta w_c^{rev} \qquad (50)$$

The free energy and entropy are now understood to exclude the single-particle internal degrees of freedom, which relate to the solvation layer, the electrical double layer, and the solid material of which the core of the colloids consists. Changes related to these internal degrees of freedom of the "complexed colloidal particles" are lumped into the single-particle contribution δw_c^{rev}

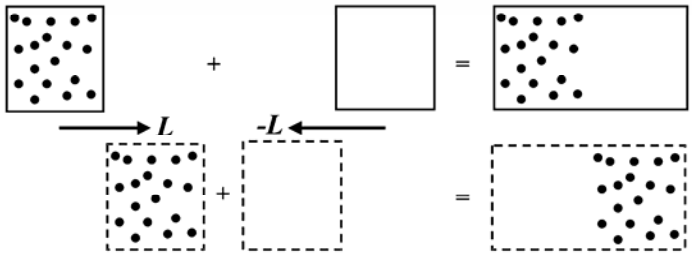

Figure 3. The left two figures depict the process of moving all colloidal particle from box 1 to box 2. The middle two figures depict the accompanied opposite displacement of pure solvent. The right two figures depict the resulting total process. Not depicted are the colloidal particles which are also displaced simultaneously during thermodiffusion (for example, from box 2 to box 3).

to the total work. It is precisely this single-particle contribution that is considered explicitly in the present paper. The corresponding degrees of freedom related to the electrical double layer are treated explicitly in the present paper by explicitly accounting for the electrolyte species that build the double layer in thermodynamic relations. In this appendix, we shall disregard these "internal degrees of freedom" of colloidal spheres, which are responsible for single-particle thermal diffusion, and simply lump them all together into δw_c^{rev} without further specification. The similar "entropic contributions" of the form $S\delta T$ that are connected to the internal, single-particle degrees of freedom can be treated similarly. Including these contributions would unnecessary complicate notation: all species that are involved in these internal degrees of freedom must be taken into account explicitly in all equations. We shall therefore discuss only the "interaction contributions" of the form $S\delta T$ of the solvent and of the colloids in this appendix. As mentioned above, contrary to the free energy in eq 50, the change in free energy in eq 13 in the main body of the present paper includes the internal colloidal particle degrees of freedom, which are lumped in eq 50 into the contribution δw_c^{rev}. Here, we will show that the remaining entropic contribution $S\delta T$ in eq 50 cancels against similar contributions arising from Gibb−Duhem relations and that the change in free energy δF in eq 50 is connected to interaction contributions (except for the "ideal gas contribution").

The "entropic contribution" $S\delta T$ can be obtained by considering the exchange of matter between the two boxes in more detail. What is actually happening during thermodiffusion is that all particles drift coherently from one box to the other. Consider therefore the process where all particles from box 1 drift to box 2. During the same time span, all particles within the neighboring box (box 0, for example) diffuse to box 1, and all particles from box 2 are displaced to the neighboring box (box 3, say). Since the gradients in concentration and temperature are constant over the length scale set by the size of the boxes, effectively $\delta N_c = N_{c,2} - N_{c,1}$ particles are moved from box 0 to box 1, from box 1 to box 2, and from box 2 to box 3. In the main text and in ref 9, the change in free energy is calculated for a displacement of these δN_c particles from box 1 to box 2. This is sufficient to obtain an expression for the force acting on a particle, once the entropic contributions are omitted. To include the entropic contributions $S\delta T$, however, we have to consider the whole cascade of coherent displacements of colloidal particles, where it suffices to ask for the change in free energy that is required to move all particles from box 1 to box 2. The similar contributions to the change in free energy from the entire cascade of displacements can simply be added to obtain the change of free energy of the whole system.

When thermal expansion of colloidal material and solvent is neglected, the movement of colloidal spheres from box 1 to box 2 is accompanied by the movement of an equal volume of solvent from box 2 to box 1. The process is sketched in the Figure 3. The entropic contribution is now unambiguously defined as $S_s\delta T - S_l\delta T$, where S_s is the entropy of the suspension and S_l is the entropy of an equal volume of pure solvent (note that the temperatures of boxes 1 and 2 are T and $T + \delta T$, respectively). It is very difficult to specify the entropic contributions if one considers the displacement of just a subcollection of particles from box 1 to box 2.

According to eq 50, we thus have (with V the volume of the boxes)

$$\delta w^{rev} = \delta F + V[s_s - s_l]\delta T + \delta w_c^{rev} \tag{51}$$

where s_s and s_l are the entropy of the suspension and pure solvent per unit volume.

The change in free energy $\delta F/\delta N_c$ per colloidal particle is calculated in ref 9

$$\delta F/\delta N_c = \delta\nu \tag{52}$$

where

$$\nu \equiv \mu_c - \frac{v_c^0}{v_s^0}\mu_s \tag{53}$$

The δ on $\delta\nu$ now refers to the difference between box 2 and box 1.

The Gibbs−Duhem relation for the suspension reads

$$0 = S_s\delta T - V\delta p + N_c\delta\mu_c + N_s\delta\mu_s \tag{54}$$

where S_s is the entropy of the suspension, V the volume, and p the mechanical pressure. The Gibbs−Duhem relation for the osmotic reservoir (that was already introduced in section 4, see eq 22) reads

$$0 = S_r\delta T - V_r\delta p_r + N_{s,r}\delta\mu_s \tag{55}$$

where the index "r" refers to the reservoir. It follows from these two relations and the definition of ν in eq 53 that

$$\delta\nu = \frac{V}{N_c}[s_r - s_s]\delta T + \frac{V}{N_c}\delta\Pi \tag{56}$$

where s_r is the entropy of the pure solvent in the reservoir per unit volume and $\Pi = p - p_r$ is the osmotic pressure. In deriving this equation, it is considered that the suspension is space-filling (that is, $N_c v_c^0 + N_s v_s^0 = V$) and the fluid in the reservoir is space-filling (that is $N_{s,r} v_s^0 = V_r$).

Combining eqs 51, 52, and 56 thus leads to the following expression for the reversible work δW^{rev} per colloidal particle

$$\delta W^{rev} = \frac{V}{N_c}[s_r - s_l]\delta T + \frac{V}{N_c}\delta\Pi + \delta W_c^{rev} \qquad (57)$$

where δW_c^{rev} is the single-particle reversible work for a single colloidal sphere. The entropy densities of pure liquid in the suspension (outside the solvation and double layers of the colloids) and of pure solvent in the osmotic reservoir differ from each other due to the pressure difference Π in the suspension and the osmotic reservoir. Now, according to the Gibbs−Duhem relation for the pure solvent, there are only two independent intrinsic variables. The entropy per unit volume, being an intrinsic variable, is therefore a function of two intrinsic variables only. Both s_r and s_l can thus be regarded as functions of either the intrinsic variables T, p or T, ρ_s (with $\rho_s = N_s/V$ the number concentration of pure solvent). For the same reason, the number density is a function of T and p. Hence

$$s_r(p_r, T) - s_l(p, T) = \int_p^{p_r} dp' \frac{\partial s(p', T)}{\partial p'} = \int_p^{p_r} dp' \frac{\partial s(\rho_s(p', T), T)}{\partial \rho_s} \frac{\partial \rho_s(p', T)}{\partial p'} \qquad (58)$$

For nearly incompressible solvents, $\partial\rho_s(p', T)/\partial p'$ is very small, so that the difference in entropy density can be neglected, provided that $\Pi \times$ a typical value of $\partial s(\rho_s, T)/\partial\rho_s$ is not inversely proportional to $\partial\rho_s(p', T)/\partial p'$. Since $\partial s(\rho_s, T)/\partial\rho_s = S/V - (V/N_s)\partial S(N, V, T)/\partial V$, and both terms on the right-hand side are perfectly well-defined also for incompressible solvents, there is no reason for $\partial s(\rho_s, T)/\partial\rho_s$ to diverge for incompressible solvents.

This shows that the entropy contributions to the reversible work on the right-hand side of eq 13 cancel against those arising from the Gibbs−Duhem relations for the suspension and the osmotic reservoir, provided that thermal expansion is neglected and the solvent is incompressible.

With the neglect of the entropy contribution for incompressible solvents and without the single-particle contribution, we thus recover from eq 57 the result $\delta W^{rev} = (V/N_c)\delta\Pi$ of ref 9 for the interaction contribution to the reversible work per colloidal sphere.

LA062184M

Publikation V: Thermophoresis beyond local equilibrium, **PRL**, **eingereicht**, Stefan Duhr and Dieter Braun

Nonlinear Thermophoresis beyond Local Equilibrium Criterion

Stefan Duhr and Dieter Braun

Applied Physics, Center for Nanoscience,
Ludwig Maximilians University München
Amalienstr. 54, D-80799 München, Germany

Thermophoresis (thermodiffusion, Soret effect) moves molecules along thermal gradients. We measure its phenomenological linear drift relation by single particle tracking in convection-free settings. For moderate thermal gradients, drift velocity depends linearly on the gradient. However, for strong thermal gradients, we find a nonlinear dependence of the drift on the applied gradient for large Soret coefficient and particle radius. Interestingly, the onset of the nonlinearity coincides with a local disequilibrium of the particle. Nonlinear thermophoresis resolves several fundamental contradictions between thermophoretic experiments and theory.

PACS: 87.23.-n, 82.70.Dd, 82.60.Lf

Introduction. Nonlinear transport effects are encountered in many fields of physics. Deviations from linear response typically points towards previously unconsidered physics. In the past, thermophoretic transport, in our case the movement of particles in liquids along a temperature gradient[1-3], was treated as linear response between temperature gradient ∇T and particle drift velocity v with thermal diffusion coefficient D_T:

$$v = -D_T \nabla T \tag{1}$$

We show here for the first time nonlinear transport in thermophoresis. The finding is of interest since despite ongoing experimental efforts[4-13], a generally successful theoretical explanation is lacking[14-25]. We test the linear transport of equation (1) for large particles, big Soret coefficients and steep thermal gradients by using single particle tracking. We find that for thermal gradients exceeding a distinct threshold the linearity assumption breaks down and thermophoretic drift becomes nonlinear. Interestingly, the onset of nonlinearity coincides with a transition from local thermodynamic equilibrium of the particle to local disequilibrium.

Measurement technique. A temperature field is generated by heating water with an infrared laser and measured microscopically with a temperature sensitive fluorescent dye[8,11,18]. We track the average velocity of single particles in a temperature gradient by fluorescence microscopy (Fig. 1a,b) and evaluate their drift velocity v against thermal gradient ∇T to test the linearity of equation (1). Imaging allows to detect particles which stick to the walls of the chamber. Thermal convection is suppressed by working in a 20 µm thin chamber, low heat conducting plastic walls (Ibidi, Munich) ensure a temperature gradient which is parallel to the chamber. The method allows to measure thermophoresis for large particles without artifacts from thermal convection.

A strong temperature gradient in a 20 µm thin water film is created optically by aqueous absorption of infrared light (Fig. 1a). A fiber coupled infrared solid state laser (Furukawa FOL1405-RTV-317, 1480 nm, 25 mW) is moderately focussed to prevent optical tweezing. Temperature is increased by 8 K in a 35 µm wide Lorentzian shape, establishing temperature gradients in the range of $\nabla T = 0...0.11$ K/µm . Heating is measured with micrometer resolution by temperature dependent fluorescence of the dye BCECF (Molecular Probes, B-1151), diluted to 50 µM in 10 mM TRIS buffer. It shows a temperature sensitivity of 2.8 %/K, consisting of 1.3 %/K pH sensitivity and thermophoresis of the dye with $S_T = 1.5\%\ K^{-1}$. Imaging and bleaching correction have been described previously[11].

Fluorescein labelled, carboxyl modified polystyrene beads of diameter 0.5 µm and 1.9 µm (Molecular Probes, F-8827, F-8888) are desalted and diluted to picomolar concentrations to avoid particle-particle interactions. The solution is buffered in 0.5 mM TRIS at pH 7.8. At this ion concentration, particles do not stick to the chamber surfaces. Fluorescence particle images are taken at 4 IIz through a 32 x air objective (microscope Zeiss Axiotech, camera PCO SensiCam_QE) with a large depth of focus[8], allowing z-independent particle detection (Fig. 1b). Particle positions are inferred with <10 nm precision by two-dimensionally fitting the fluorescence maxima. The diffusion coefficient is inferred from unheated particle tracks and matches within 3 % the manufacturer specifications with D=0.226 $\mu m^2/s$ (1.9 µm diameter) and D=0.858 $\mu m^2/s$ (0.5 µm). Particles at random initial position are subjected to above-described temperature gradient which is established within <10ms. Each recording evaluated 300 single particle tracks.

To test for possible artifacts, we calculate the 3-dimensional temperature field and thermal convection flow (Fig. 2) in radial coordinates[11] using finite elements (Femlab 2.3, model file can be obtained). Simulation results are given over the experimentally used radius r = 30..150 µm. The temperature profile shows a marked horizontal and a

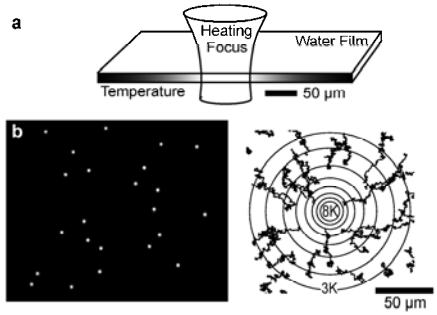

FIG. 1. ***Experimental setup.*** (a) A 20 µm thin water film is locally heated by infrared light. (b) The drift of single polystyrene beads is tracked in the created thermal gradient, indicated by isothermal rings (1.9 µm diameter beads in 0mM KCl).

negligible, 10-fold smaller vertical thermal gradient, leading to radial thermophoretic particle drift (Fig. 2b). Convection is sufficiently suppressed by the thin chamber, peaking at 0.05 µm/s and thus 10-fold lower than corresponding thermophoretic drift (Fig. 2c). Notably, single particle tracking cancels inward and outward convection flow to first order. Optical trapping forces were calculated[26] and yield in the worst case at the chamber center a drift of 0.01µm/s, less than 3% of the measured drift (Fig. 2d).

At various radius, we collect particle drift velocities within 50 s after application of the temperature gradient (Fig. 3a,c). The time limitation ensures that the system is far from the steady state and diffusive backflow is a minor contribution: equilibration time constant is given by b^2/D with an 1/e focus diameter of b ~ 35 µm leading to values of 1500 s and 5500 s for 0.5 µm and 1.9 µm particle diameters. For both particle sizes, the diffusive backflow $j = -D\nabla c$ is less than 10-times smaller than the thermodiffusive drift $j = -D_T c\nabla T$ as confirmed by numerical calculations. The steady state depletion in the heated center is estimated based on linear thermophoresis to 10^{-13} of bulk concentration for the small 0.5 µm diameter particles and 10^{-165} for 1.9 µm particles in the linear regime, rendering measurements of the steady state concentration profile prohibitive. The temperature dependence of D_T of the chosen beads is rather low[18] with -2.2 %/K. To conclude, the used experimental setting allows to measure thermophoretic velocity for large single particles in strong thermal gradients without significant artifacts.

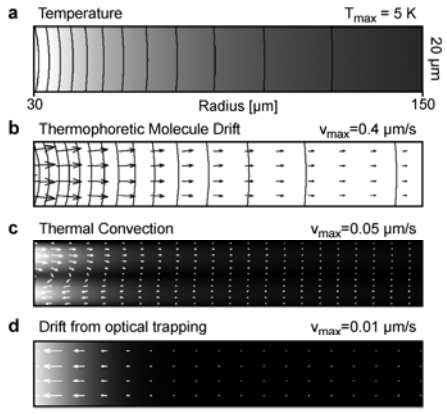

FIG. 2. ***No artifacts from vertical temperature gradient or thermal convection.*** (a) A 3-dimensional model of the experiment was simulated with finite element numerics. (b) The radial temperature drop dominates, leading to mostly lateral thermophoretic drift. (c) Thermal convection is 10-fold slower than thermophoretic drift. (d) Drift from optical trapping can be neglected.

Results. We measured the drift velocity of 0.5 μm beads in the temperature gradient and plot the results both versus experimental radius (Fig 3a) and logarithmic temperature gradient (Fig 3b). The drift velocity decreases over radius. The linear prediction of velocity v given by equation (1) with $D_T = 3.2\ \mu m^2/(sK)$ is plotted as solid line and fits the drift velocities very well (Fig 3a,b). This confirms the long held assumption that thermophoresis is governed by the linear approach of equation (1). However if we choose to measure larger beads with 1.9 μm diameter, the linearity breaks down. Linear scaling with $D_T = 9.8\ \mu m^2/(sK)$ is only found for low temperature gradients $\nabla T < 0.02$ K/μm at radius r > 100 μm (Fig. 3c). At lower radius and increased temperature gradient, the linear prediction of equation (1) is violated and beads drift with 2-fold slower than expected velocity at $\nabla T - 0.1$ K/μm (Fig. 3d).

The shape of nonlinear thermophoretic transport is extracted in Figure 4 by removing the common radius dependence and plotting versus temperature gradient ∇T. To compare experiments, drift velocity v is scaled by D_T of the linear regime to units of a thermal gradient K/μm. For small particles, the experiment confirms the linear drift relation of equation (1) (Fig. 4a, black), whereas for 1.9 μm particles the relation deviates nonlinearly towards slower drift velocities (Fig. 4a, white). Linear thermophoresis of 1.9 μm particles is reestablished by adding 20 mM KCl,

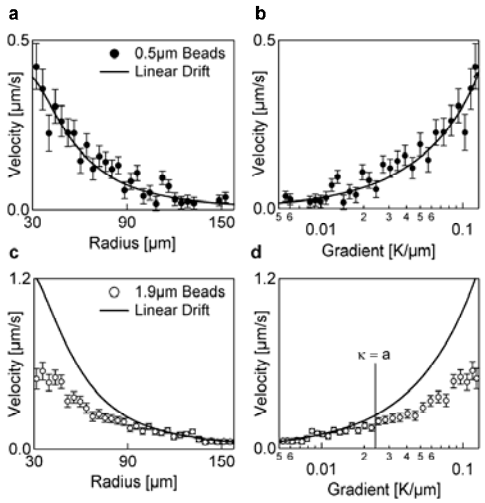

FIG. 3. ***Drift velocity versus radius and temperature gradient.*** (a,b) Raw data of thermophoretic drift of 0.5 μm polystyrene beads match linearly with the applied temperature gradient, both seen in the raw data over radius and a logarithmic plot against applied thermal gradients. (c,d) However, thermophoretic drift of 1.9 μm beads deviates from linear relationship for radius r = 30..100 μm where the thermal gradient exceeds 0.02K/μm.

which decreases the thermodiffusion coefficient from $D_T = 9.8\ \mu m^2/(sK)$ down to $D_T = 2.2\ \mu m^2/(sK)$ (Fig. 4b, black). Thus, nonlinear thermophoresis is not only a function of particle radius a, but also of thermodiffusion coefficient.

Discussion. To date, the theoretical foundation of thermophoresis in liquids is under debate. We show here that the generally held assumption of linear response does not apply to thermophoresis of large particles in strong thermal gradients. We believe the findings can be coherently interpreted at three different levels of description as follows.

Coarse graining length scale. We start our discussion from the well documented linear gradient at low thermal gradients. As generally assumed in the past[3] and checked experimentally for shallow thermal gradients[18], the thermodiffusive steady state follows an exponential distribution

$$c/c_0 = \exp[-S_T(T - T_0)] \tag{2}$$

as the result of linear thermophoretic drift and backdiffusion. This is valid for low particle concentrations (volume ratio << 1) and temperature independent coefficients D_T and D. The parameters are particle concentration c, temperature T, their boundary values c_0, T_0 and Soret coefficient $S_T = D_T/D$. The length scale κ in the form $c \propto \exp(-x/\kappa)$ of above exponential steady state is given by $\kappa = (S_T \nabla T)^{-1}$ with S_T from the linear regime. We compare this depletion length with the particle radius a and find two regimes: $\kappa \gg a$ describes a flat distribution

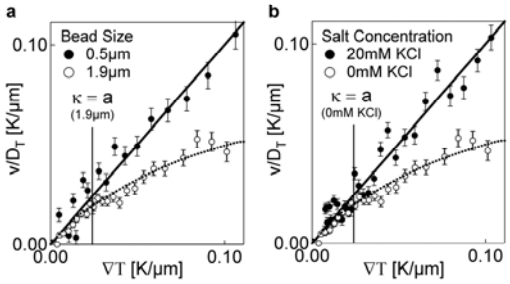

FIG. 4. ***Nonlinear thermophoresis.*** Normalized thermophoretic drift v/D_T versus temperature gradient ∇T. (a) Beads with diameter 1.9 µm show nonlinear thermophoresis while linear transport is observed for 0.5 µm beads. (solid line: linear fit, dashed line: spline fit to guide the eye) (b) Adding 20 mM KCl switches nonlinear thermophoresis of 1.9 µm beads back to linear thermophoresis parallel to the salt-induced drop of the Soret coefficient. (solid line: linear fit, dashed line: spline fit to guide the eye)

whereas for $\kappa \ll a$ the distribution falls off steeper than the particle size itself. Interestingly, with considerable precision, the limiting case

$$\kappa \approx a \tag{3}$$

determines the temperature gradient above which thermophoretic drift becomes nonlinear. For example, for 1.9 µm particles, the limit is given by $\nabla T = 0.024\,\mathrm{K/\mu m}$ (Fig. 4a,b, horizontal line) based on the experimental values of $a = 0.95$ µm and $S_T = 43\ \mathrm{K^{-1}}$. The value coincides with the onset of nonlinear thermophoresis. This implies that on the other side, nonlinear thermophoresis is expected for 0.5 µm particles beyond 1.1 K/µm ($S_T = 3.7\ \mathrm{K^{-1}}$) and for 1.9 µm particles in 20 mM KCl beyond 0.11 K/µm ($S_T = 9.7\ \mathrm{K^{-1}}$). Both limiting gradients are not experimentally accessible and linear thermophoresis is found below these values (Figure 4a,b). Thus both for variations of particle radius a and Soret coefficient S_T, the criteria (3) is confirmed by experiment.

We think, this finding tells us important things about the theoretical foundation of thermophoresis. While reasoning solely on coarse graining can be considered quite formal, it readily relates to discussions on the Onsager relations by van Kampen[19] and dissections of the thermophoretic steady state[18]. We provide additional physical insight with a ballistic and a thermodynamic interpretation of the onset of nonlinear thermophoresis below.

Ballistic interpretation. Let us compare the particle diffusion against the drift speed in the thermal gradient. In Fig. 1b, only central particles in the strong thermal gradient show an appreciable directed drift. More to the periphery, the particle's movement is dominated by diffusion and for short times, the particles nearly reversibly move back and forth along the gradient. To distinguish between ballistic and diffusive movement let us consider the time Δt the diffusion needs to broaden the position probability distribution to the size of the particle radius: $\Delta t = a^2/D$. After Δt, linear thermophoresis moves the particle over the distance $\Delta x = v\Delta t = D_T|\nabla T|\Delta t$. If this drift is larger than the diffusive broadening $\Delta x \gg a$, we call it ballistic and if it is smaller $\Delta x \ll a$, we call it diffusive. As we see, the distinction requires again the introduction of a finite length scale, namely the radius of the particle.

The ballistic regime is arithmetically equivalent to the steep distribution limit $\kappa \ll a$ with nonlinear thermophoresis and the diffusive regime is identical to the flat distribution limit $\kappa \gg a$ with linear thermophoresis. We argue as follows. In the ballistic regime, the particles drift irreversibly along the gradient in one direction whereas in the diffusive regime, the particles move in good approximation reversibly. They fluctuate back and forth along the gradient almost like a thermally equilibrated particle. It is thus tempting to approach the linear thermophoresis regime with a local thermodynamic, "local" being defined as the length scale of the particle.

Equilibrium interpretation. We start by assuming that local equilibration holds in the linear thermophoresis regime. As a result, the exponential distribution (2) can be directly interpreted as Boltzmann distribution[18]

$$c/c_0 = \exp[-[G(T) - G(T_0)]/k\bar{T}] \tag{4}$$

with G(T) the Gibbs-free enthalpy of a particle in its local temperature T. However, the assumption of local equilibrium sets a limit to the gradient of G, namely that G changes less than kT over the size of the particle: $a\nabla G \ll kT$.

The equivalence of equations (2) and (4) translates such criterion to thermophoretic variables of S_T and ∇T. Interestingly, it sets the onset of local disequilibrium at $\kappa \ll a$. Experimentally, we thus find linear thermophoresis under conditions of local equilibrium. Nonlinear thermophoresis is found beyond local thermodynamic equilibrium. Above argument also motivates why the thermodynamically related Soret coefficient S_T and not D_T determines the limit equation (3).

Towards a unified theory. The experiments point towards combining two competing theories of thermophoresis. Below the nonlinear onset, local equilibrium theories[18,22-25] describe thermophoresis. Above the limit we propose that linear nonequilibrium theories apply which typically use fluid dynamic approaches[15-17]. Such nonequilibrium theories predict considerable slower thermal drift for the measured particles, in accordance with the nonlinear slow down of thermophoresis (Fig. 4). We think that nonlinear thermophoresis is therefore the crossover point between two linear theories: a local thermodynamic description at low thermal gradients and a nonequilibrium description at strong thermal gradients. Whether the latter is linear at even stronger temperature gradients is difficult to access by experiment.

Scaling with particle size. Experiments on small particles show that thermophoretic drift rises with the radius of a particle[18]. But then, large objects would move very fast in even minute thermal gradients, in strong contradiction to everyday experience. For moderate temperature gradients, the Soret coefficients of polystyrene beads were measured[18] to scale according to $S_T \propto a^2$. From equation (3) follows $\nabla T \propto a^{-3}$ and the onset of nonlinear thermophoresis becomes strongly size dependent. Macroscopic objects, even for minute gradients, then fall into the regime of nonequilibrium models where thermophoretic drift does not depend on particle size. Nonlinear thermophoresis therefore resolves the large particle paradox of local equilibrium theories.

Most techniques measure thermophoresis well below the limit given by equation (3). Only thermal field flow fractionation (TFFF)[4,6] uses exceptionally large gradients of up to 1 K/μm. In contradiction to recent measurements[18], Soret coefficients found by TFFF[20,21] scale with particle size with a variety of power laws. We see however, that the onset of nonlinear thermophoresis is highly particle size dependent ($\nabla T \propto a^{-3}$) and the nonlinearity limit is reached for larger particles by TFFF. Therefore we can expect that nonlinear thermophoresis will resolve inconsistencies between measured size scaling laws.

To conclude, we used single particle tracking to microscopically access the non-equilibrium system of particle drift in a temperature gradient. Thermophoretic drift of particles with large Soret coefficients up to S_T=45 K^{-1} was measured. We test the linearity of thermophoretic transport and find nonlinear thermophoresis for temperature gradients above $(aS_T)^{-1}$ with a the radius of the particle. We argue that this limit marks the transition from local equilibrium[18] to local disequilibrium of particles in a thermal gradient. As a result, for the typically used tempera-

ture gradients, thermophoresis should be described by local thermodynamic equilibrium[22-25] in contrast to competing theoretical approaches[15-17].

We thank Werner Köhler and Jan Dhont for discussions and Hermann Gaub for hosting our Emmy-Noether Group, which was funded by the Deutsche Forschungsgemeinschaft DFG.

1 C. Ludwig, Sitzber. Akad. Wiss. Wien, Math.-naturw. Kl. 20, 539 (1856)

2 C. Soret, Arch. Geneve 3, 48 (1879)

3 de Groot, S. R. & Mazur P. *Non-equilibrium Thermodynamics,* North-Holland, Amsterdam, 1969

4 J. C. Giddings, M. E. Hovingh and G. H. Thompson, J. Phys. Chem. 74, 4291 (1970)

5 M. Giglio and A. Vendramini, Phys. Rev. Lett. 38, 26 (1977)

6 M. E. Schimpf and J. C. Giddings, J. of Polymer Science B 27, 1317 (1989)

7 W. Köhler and P. Rossmanith, J. Phys. Chem. 99, 5838 (1995)

8 D. Braun and A. Libchaber, Phys. Rev. Lett. 89, 188103 (2002)

9 B.-J. de Gans, R. Kita, B. Müller and S. Wiegand, J. of Chem. Phys. 118, 8073 (2003)

10 J. Rauch and W. Köhler, Phys. Rev. Lett. 88, 185901 (2002)

11 S. Duhr, S. Arduini, and D. Braun, Eur. Phys. J. E 15, 277 (2004)

12 R. Rusconi, L.Isa, and R.Piazza, J. Opt. Soc. Am. B 21, 605 (2004)

13 S. Duhr and D. Braun, Appl. Phys. Lett. 86, 131921 (2005)

14 P. S. Epstein, Zeitschrift für Physik 54, 537 (1929)

15 K.I. Morozov, J. Experim. and Theor. Phys. 88, 944 (1999)

16 M. E. Schimpf and S. N. Semenov, J. Phys. Chem. B 105, 2285 (2001)

17 A. Parola and R. Piazza, Eur. Phys. J. E 15, (2004)

18 S. Duhr and D. Braun, Phys. Rev. Lett., 96, 168301 (2006)

19 N.G. van Kampen, J. Stat. Phys. 109, 471 (2002)

20 S. J. Jeon, M. E. Schimpf, and A. Nyborg, Anal. Chem. 69, 3442-3450 (1997)

21 P.M. Shiundu, G. Liu, and J.C. Giddings, Anal. Chem. 67, 2705-2713 (1995)

22 J.K.G. Dhont, J. of Chem. Phys. 120, 1632 (2004)

23 J.K.G. Dhont, J. Chem. Phys. 120, 1642 (2004)

24 Duhr and Braun, submitted

25 S. Fayolle, T. Bickel, S. Le Boiteux and A. Würger, Phys. Rev. Lett. 95, 208301 (2005)

26 Tsvi Tlusty, Amit Meller and Roy Bar-Ziv, Phys. Rev. Lett. 81, 1738 (1998)

Publikation VI: Two-dimensional colloidal crystals formed by thermophoresis and convection, **Applied Physics Letters** 86, 131921 (2005) Stefan Duhr and Dieter Braun

L ABSTRACT + LINKS

APPLIED PHYSICS LETTERS **86**, 131921 (2005)

Two-dimensional colloidal crystals formed by thermophoresis and convection

Stefan Duhr and Dieter Braun[a)]
Dissipative Biosystems Lab, Applied Physics, Ludwig Maximilians Universität München, Amalienstr. 54, 80799 München, Germany

(Received 29 November 2004; accepted 3 February 2005; published online 24 March 2005)

Temperature gradients can trap micrometer-sized particles into two-dimensional crystals. We form colloidal crystals from otherwise repellent 2 μm polystyrene beads in diverse thermal convection settings. Our experiments indicate that the accumulation is driven by particle thermophoresis. Particles move along the temperature gradient and are pushed out of the warm liquid to a cold wall. We find reduced accumulation for decreased surface temperature gradients and enhanced salt concentrations. Moreover, thermophoretic fluid dynamics calculations predict flat accumulation profiles with 10^7-fold enhanced concentrations that are consistent with our experiments. The accumulated crystals could be used as molecular sieves for microfluidic biotechnological applications. A natural environment for similar accumulations are pores of rock near hydrothermal vents. © *2005 American Institute of Physics*. [DOI: 10.1063/1.1888036]

We show how the combination of thermodiffusion and convection in a solution of polystyrene beads leads to the accumulation of a two-dimensional crystal at the cooling surface in a convective flow. This finding confirms the strong DNA accumulation found previously in a similar convection setting.[1] Here, however, the tendency to accumulate is so strong that particles are pushed out of the diluted solution into a crystal.

Thermophoresis,[2–6] the movement of particles along temperature gradients, is an interfacial force which in liquids still lacks detailed understanding.[7–11] It can be used to separate beads[12–14] and measure diffusion constants.[15] The combination of convection and thermophoresis to accumulate molecules has a long history in elongated thermogravitational columns.[16]

Formation of colloidal crystals[17–22] out of diluted solutions is of interest for molecular sieves, photonic crystals,[23] and chemical sensing.[24] Two-dimensional crystals can be used to explore statistical physics of defects.[25,26] Ways to efficiently accumulate molecules and particles out of solution are of great interest to enhance the sensitivity of diffusion limited surface biosensors. Moreover, the forces which drive colloidal crystals might be used to enhance the crystallization of proteins. Notably, the experimental temperature gradients used in our system are compatible with natural conditions in pores of rock around hydrothermal vents.[27–30] Thermophoretic trapping experiments have been performed in chambers of 500 μm in height and 6 mm in diameter (Fig. 1). On top, the chamber was sealed off by a cover glass slide (Roth No. 0657, 170 μm thickness). The sidewalls were formed by a silicon sheet of 500 μm thickness (McMaster, New York) while the bottom was sealed by default with a 1 mm sapphire window (Edmund Optics), but for some experimental setups polymethyl siloxane (PDMS, Sylgard 184, Dow Corning) or glass (No. 0656, Roth Laborbedarf) was used. The water of the chamber was heated from below with an infrared laser (FOL1405RTV-317, Furukawa, Japan) with

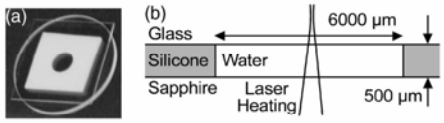

FIG. 1. Chamber. (a) Photograph of the convection chamber. (b) Liquid is filled between sapphire and glass, separated by 500-μm-thick silicone spacer with an open diameter of 6 mm. The center is heated by an infrared laser, inducing a toroidal convection flow.

a power of 100 mW. The lateral position of the laser focus could be moved by the use of two galvo-mirrors (6200-XY scanners with driver 67120, Cambridge Technologies) to form complex heating geometries. The laser beam was focused with a numerical aperture of 0.14 using a Mitutoyo near infrared-corrected 5× objective. The focus plane was placed 1000 μm above the top of the chamber to make heat-

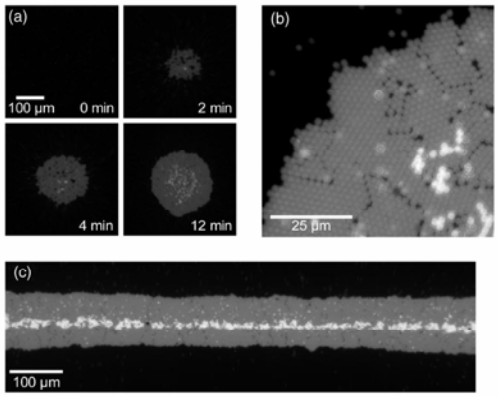

FIG. 2. Generation of two-dimensional colloidal crystal from thermophoresis and convection. (a,b) The chamber contains 2 μm polystyrene beads at low concentration. It is heated in the center by infrared absorption. Within 12 min, a two-dimensional colloidal crystal forms against the 5000-fold lower bead concentration in the liquid. (c) Heating along a line leads to the formation of an elongated crystal.

[a)]Author to whom correspondence should be addressed; electronic mail: dieter.braun@physik.lmu.de

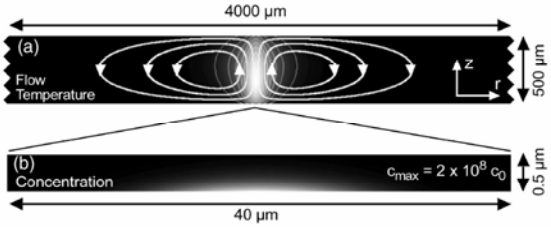

FIG. 3. Theory predicts strong and flat accumulation. (a) Heat transfer, bead diffusion, thermophoresis and Navier–Stokes flow are simulated in cylinder coordinates. We show the temperature profile and selected flow lines in a vertical cross section. (b) Predicted particle concentration reaches 2×10^8 times the bulk concentration in a very flat geometry at the lower chamber wall.

ing less focused. Due to a 6 mm $1/e^2$-diameter-Gaussian beam in front of the objective, we heat with a 2.8° opening angle in water.

For thermophoretic trapping, 1 and 2 μm fluorescently labeled polystyrene beads were used (2% solid, F-8823, F-8827, molecular probes) and diluted 1:500 and 1:100 in 0.1 mM Tris-HCl at *p*H 7.8, respectively. The lower chamber wall was imaged with a 10× or 32× objective using a fluorescent microscope (AxioTech Vario, Zeiss). Fluorescence was excited by a high-power LED (LXHL-LX5C, Luxeon) at a driving current of 35 mA with an ILX lightwave current source (ILX 3565). A charge coupled device camera (670KS, SensiCam QE, PCO, Kehlheim) was used to take pictures of the illuminated beads with a typical frame rate of 0.03 Hz (exposure 5 s delay, 25 s).

Figures 2(a) and 2(b) show the aggregation of a crystal within 12 min of laser heating. The thermophoretic trapping chamber is filled with 14 μl of diluted 2 μm polystyrene beads (45 000 spheres per μl). Laser heating immediately induces a toroidal convection, taking the beads along with the flow. After less than 12 min, a circular monolayer of fluorescently labeled beads is formed on the bottom sapphire chamber wall [Figs. 2(a) and 2(b)]. It has a maximum diameter of about 200 μm. The bead accumulation is limited only by closest crystal packing, leading to a 5000-fold increased concentration in the crystal as compared to the solution.

Two factors create the colloidal crystal. At the bottom of the chamber, convection transports the particles below the heated center. Nonslip boundary conditions force a slow flow near the chamber walls. Since sedimentation is negligible,

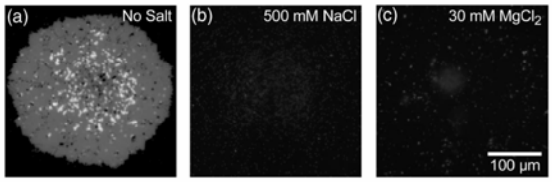

FIG. 4. No accumulation at high salt concentrations. (a-c) No accumulation is found for more than 500 mM NaCl or 30 mM $MgCl_2$. Thermophoresis vanishes at such high salt concentrations.

convection does not concentrate the particles. Accumulation is induced from a strong temperature gradient in *z* direction. Thermophoresis makes the particles follow the heat transport out of the chamber and pushes them to the lower chamber wall. The same effect is not seen at the top of the chamber since convection yields a divergent flow there.

Figure 2(c) shows how spreading the laser focus along a line leads to elongated accumulation of beads. The line was scanned my mirrors along 1.4 mm with 250 Hz and 160 mW laser power. The resulting linear accumulation demonstrates that radially convergent flow is not necessary to form a colloidal crystal.

A finite element calculation confirms the thermophoretic accumulation (Fig. 3). As described previously,[31] the numerical program FEMLAB allows parallel solving of Navier–Stokes flow, heat conductivity, diffusion, and thermophoresis. The convection takes place on the 1000 μm scale and the accumulation on the μm scale. Thus a highly adapted grid was necessary for the simulation. The diffusion constant for 2 μm spheres is $D=0.2\ \mu m^2/s$ according to the Stokes–Einstein relation $D=(k_BT)/(6\pi\eta r)$. As thermal diffusion coefficient we used $D_T=3\ \mu m^2/(s\,K)$ based on preliminary thermophoresis measurements using single particle tracking. No fitting parameters were used.

The simulation shows that the center of the chamber is heated to 62 °C and leads to a maximum convection speed of 580 μm/s. Temperature gradients in the central accumulation region are small in radial direction ($\partial_r T=10^3$ K/m) and strong vertically ($\partial_z T=8\times10^5$ K/m). Therefore the temperature gradient pushes the particles downwards with a drift velocity of $D_T\partial_z T=2.5\ \mu$m/s.

The simulation predicts very strong thermophoretic accumulation. We expect a 2×10^8-fold enhanced concentration near the lower chamber wall. The concentration falls off

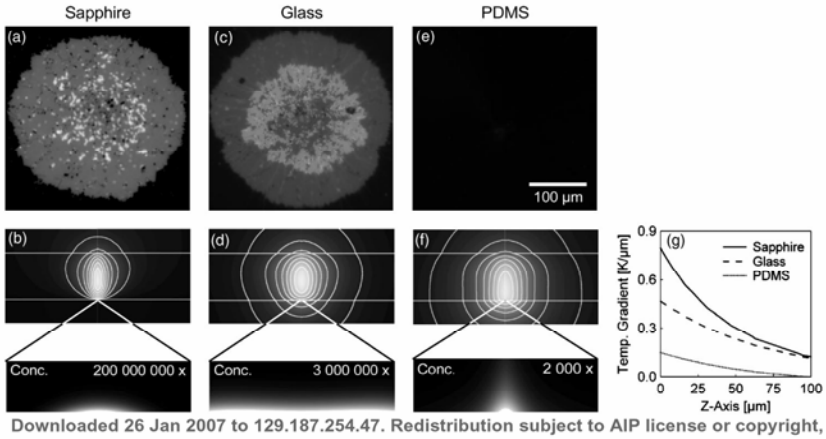

FIG. 5. Accumulation on different substrates. (a,c,e) The temperature gradient in *z* direction was modified by changing the substrate material from sapphire (a) to glass (c) and PDMS (e). The heat conductivity is decreased by more than two orders of magnitude. (b,d,f) Simulations show a strong change in the vertical temperature gradient. Concentration drops over five orders of magnitude from 2×10^8 over 3×10^6 down to 2×10^3 as we go from sapphire over glass to PDMS. (g) The central temperature gradients in *z* direction as obtained by the simulation.

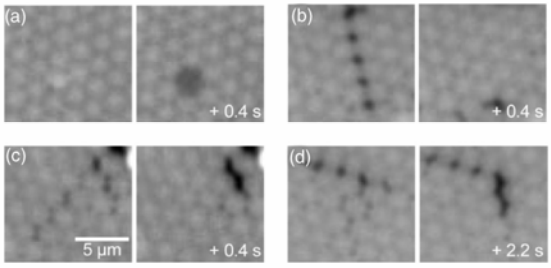

FIG. 6. Crystal defect dynamics. The accumulated crystal shows diverse defects with a fast and a rich dynamics. We show some examples. (a) A point defect builds up by the removal of a bead within 0.4 s. (b) A fault line closes within 0.4 s. (c) A fault line closes by opening a neighboring one. (d) Compression of unordered particles to a crystal.

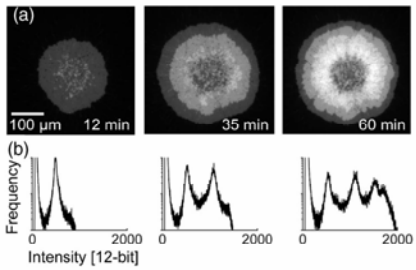

FIG. 7. Generation of multilayered crystal over time. Up to three crystal layers are formed within 60 min as seen as peaks in the intensity histograms.

to half its value within a diameter of 20 μm and a height of 0.5 μm. The height is fourfold smaller than the accumulated particles. The particles therefore effectively average the simulated concentration profile. In our experiments, the accumulation is 5000-fold since stronger accumulation is hindered sterically by the crystal.

Figure 4 shows how adding salt quenches the accumulation. We added 500 mM NaCl or 30 mM $MgCl_2$ where it is known that thermophoresis is quenched.[1,9] Although the particles have an enhanced tendency to stick to the surface under these conditions, accumulation vanishes. At high salt concentrations, convective flow alone does not lead to accumulation.

The temperature gradient near the lower wall is essential as seen in Fig. 5. Crystal formation vanishes if the heat conductivity of the lower substrate is reduced. This is done by replacing the lower chamber wall from sapphire [Fig. 5(a), heat conductivity $\lambda = 34\ \mathrm{Wm^{-1}K^{-1}}$] to glass [Fig. 5(c), $\lambda = 1.4\ \mathrm{Wm^{-1}\ K^{-1}}$] and PDMS [Fig. 5(e), $\lambda = 0.18\ \mathrm{Wm^{-1}\ K^{-1}}$]. Simulations of different bottom materials confirm this as the concentration drops over many orders of magnitude from 2×10^8 over 3×10^6 down to 2×10^3 (Figs. 5(b)–5(f)). This high sensitivity confirms the dominating role of the vertical temperature gradient [Fig. 5(g)].

Crystal defect dynamics can be observed as shown in Fig. 6. Point defects can appear by bead removal within 0.4 s [Fig. 6(a)], and line defects can rearrange within the same time span [Fig. 6(b)]. More complex rearrangements can also be seen [Figs. 6(c) and 6(d). These images demonstrate that the accumulated crystals can be used to simulate basic defect dynamics.

At incubation times longer than 12 min, up top three layers of beads accumulate to reach a steady state after 60 min [Fig. 7(a)]. The layers were observed in an intensity histogram as peaks [Fig. 7(b)]. A fourth layer does not nucleate into crystals, but consists only of loosely attached beads.

Our experiments demonstrate that micrometer-sized particles can be strongly accumulated by a combination of thermophoresis and convection. The mechanism has applications in microfiltration, particle accumulation, and molecular detection on surfaces. We expect that the demonstrated strong accumulation of particles can lead to a co-accumulation of molecules.

The authors thank Roberto Cerbino for discussions, the Deutsche Forschungsgemeinschaft (DFG) for funding through the Emmy Noether Program II, and Hermann Gaub for hosting our lab.

[1]D. Braun and A. Libchaber, Phys. Rev. Lett. **89**, 188103 (2002).
[2]C. Soret, Arch. Geneve **3**, 48 (1879).
[3]C. Ludwig, Sitzber. Akad. Wiss. Wien, Math.-Naturw. Kl. **20**, 539 (1856).
[4]J. C. Maxwell, *J.C. Collected Papers II* (Cambridge University Press, Cambridge), 1890, pp. 681–712
[5]P. S. Epstein, Z. Phys. **54**, 537 (1929).
[6]S. R. de Groot and P. Mazur, *Non-equilibrium Thermodynamics* (North-Holland, Amsterdam, 1969).
[7]W. Köhler and P. Rossmanith, J. Phys. Chem. **99**, 5838 (1995).
[8]C. Debuschewitz and W. Köhler, Phys. Rev. Lett. **87**, 055901 (2001).
[9]R. Piazza and A. Guarino, Phys. Rev. Lett. **88**, 208302 (2002).
[10]S. Iacopini and R. Piazza, Europhys. Lett. **63**, 247253 (2003).
[11]R. Rusconi, L. Isa, and R. Piazza, J. Opt. Soc. Am. B **21**, 605 (2004).
[12]M. E. Schimpf and J. C. Giddings, J. Polym. Sci., Part B: Polym. Phys. **28**, 2673 (1990).
[13]B. K. Gale, K. D. Caldwell, and A. B. Frazier, IEEE Trans. Biomed. Eng. **45**, 1459 (1998).
[14]T. L. Edwards, B. K. Gale, and A. B. Frazier, Anal. Chem. **74**, 1211 (2002).
[15]M. Giglio and A. Vendramini, Phys. Rev. Lett. **38**, 26 (1977).
[16]K. Clusius and G. Dickel, Z. Phys. Chem. Abt. B **44**, 397 (1939).
[17]I. M. Krieger and F. M. O'Neill, J. Am. Chem. Soc. **90**, 3114 (1968).
[18]N. A. Clark, A. J. Hurd, and B. J. Ackerson, Nature (London) **281**, 57 (1979).
[19]R. J. Carlson and S. A. Asher, Appl. Spectrosc. **38**, 297 (1984).
[20]D. J. W. Aastuen, N. A. Clark, L. K. Cotter, and B. J. Ackerson, Phys. Rev. Lett. **57**, 1733 (1986).
[21]E. A. Kamenetzky, L. G. Magliocco, and H. P. Panzer, Science **263**, 207 (1994).
[22]P. Schall, I. Cohen, D. A. Weitz, and F. Spaepen, Science **305**, 1944 (2004).
[23]J. E. G. J. Wijnhoven and W. L. Vos, Science **281**, 802 (1998).
[24]J. H. Holtz and S. A. Asher, Nature (London) **389**, 829 (1997).
[25]C. A. Murray, in *Bond-Oriented Order in Condensed Matter Systems*, edited by K. J. Strandburg (Springer, New York, 1992).
[26]K. Zahn, R. Lenke, and G. Maret, Phys. Rev. Lett. **82**, 2721 (1991).
[27]D. Braun and A. Libchaber, Physical Biology **1**, 1 (2004).
[28]M. J. Russell, A. J. Hall, A. G. Cairns-Smith, and P. S. Braterman, Nature (London) **336**, 117 (1988).
[29]N. G. Hohn (editor), Origins Life Evol. Biosphere **22**, 1 (1992).
[30]C. L. Van Dover, *The Ecology of Deep-Sea Hydrothermal Vents* (Princeton University Press, Princeton, NJ, 2000).
[31]S. Duhr, S. Arduini, and D. Braun, Eur. Phys. J. E **15**, 277 (2004).

Publikation VII Optothermal Molecule Trapping by Opposing Fluid Flow with Thermophoretic Drift, **PRL** 97, 038103, Stefan Duhr and Dieter Braun (2006)

PRL 97, 038103 (2006) PHYSICAL REVIEW LETTERS week ending 21 JULY 2006

Optothermal Molecule Trapping by Opposing Fluid Flow with Thermophoretic Drift

Stefan Duhr and Dieter Braun*

Biophysics, Ludwig Maximilians Universität München, Amalienstrasse 54, 80799 München, Germany

(Received 21 December 2005; published 21 July 2006)

Thermophoresis moves molecules along temperature gradients, typically from hot to cold. We superpose fluid flow with thermophoretic molecule flow under well-defined microfluidic conditions, imaged by fluorescence microscopy. DNA is trapped and accumulated 16-fold in regions where both flows oppose each other. Strong 800-fold accumulation is expected, however, with slow trapping kinetics. The experiment is equally described by a three-dimensional and one-dimensional analytical model. As an application, we show how a radially converging temperature field confines short DNA into a 10 μm small spot.

DOI: 10.1103/PhysRevLett.97.038103 PACS numbers: 87.23.−n, 82.60.Lf, 82.70.Dd

Introduction.—Contact-free methods to manipulate single particles are rare. Common tools are electrophoresis and optical tweezers. However, in optical trapping, forces scale with particle volume, limiting the method to particles larger than about 500 nm. A less well-known tool for optical molecule manipulation is thermophoresis [1,2], where molecules are moved by a thermal gradient. Laser heating, allows all-optical microscale access to small molecules, in contrast to electrophoresis. The achieved active accumulation of biomolecules helps to overcome diffusion limitations in both surface and bulk biochemical reactions. A well-known example is the diffusion limited reaction kinetics on DNA microarrays.

Recent advances in measuring thermophoresis using holographic scattering [3–6], optical lensing [7–9], beam deflection [10–12], and optothermal microfluidics [13,14] lead to a better understanding of thermophoresis [15–19]. Most experiments to measure thermophoresis [3,9–14] use conditions where fluid flow can be neglected. However, in elongated columns thermophoretic accumulation can be amplified by thermal convection [20–24], and flat geometries with toroidal convection flow yield point accumulations [13,25]. In thermal field flow fractionation (ThFFF), the fluid flows perpendicular to the temperature gradient and separates molecules by their respective thermophoretic response [26–28]. For the first time, we orient the fluid flow along the thermal gradient, made possible by optical heating with an infrared laser focus. The combination of thermophoresis and fluid flow results in strong trapping of small biomolecules (Fig. 1). As we will show, the experiments are equally described by three-dimensional (3D) or one-dimensional (1D) models.

Flow trap.—Molecules drift away from the heat by thermophoresis, counteracted by a passive liquid flow. As a result, molecules are trapped upstream of the warm spot. Generally accepted is a phenomenological foundation of the thermophoretic drift based on the Onsager theory of linear nonequilibrium thermodynamics. For low molecule concentrations the thermophoretic drift velocity v is proportional to temperature gradient ∇T:

$$\vec{v}_T = -D_T \nabla T \tag{1}$$

The coefficient D_T is termed the thermodiffusion coefficient with units $m^2/(s\,K)$ analog to the electrophoretic mobility μ with units $m^2/(s\,V)$. Thermophoresis extends Fick's law to

$$\vec{j} = -D\nabla c - (1-c)D_T c \nabla T, \tag{2}$$

with molecule concentration c and diffusion coefficient D. In steady state, with fluid at rest, diffusional and thermophoretic flow balance. We directly opposes a fluid flow with a thermal gradient in a microfluidic channel with 10 μm × 10 μm cross section [Fig. 2(a)]. The channel is surrounded by PDMS (Polydimethylsiloxane) silicone using a protocol described previously [14]. We oppose the flow of DNA containing water with a locally enhanced temperature gradient, created with a focused infrared laser (Furukawa FOL1405-RTV-317, 1480 nm). Fluid flow is controlled gravitationally by two open 5 μl syringes of defined height, connected to the microfluidics with silicone tubings (Carl Roth Laborbedarf).

The channel is imaged with a 40x oil objective on an AxioTech Vario fluorescence microscope (Zeiss), illuminated with a high power LED (Luxeon) and recorded with the CCD Camera SensiCam QE (PCO). Details of bleaching correction and temperature extraction were described previously [14]. The temperature increase is measured by

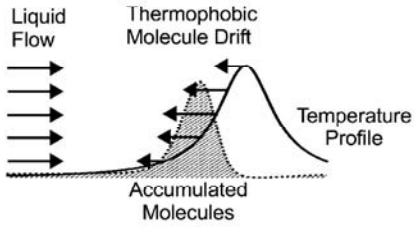

FIG. 1. Principle of thermophoretic flow trap. A warm spot repels molecules by thermophoresis. Counteracting fluid flow leads to accumulation of molecules upstream of the warm spot.

PRL 97, 038103 (2006) PHYSICAL REVIEW LETTERS week ending 21 JULY 2006

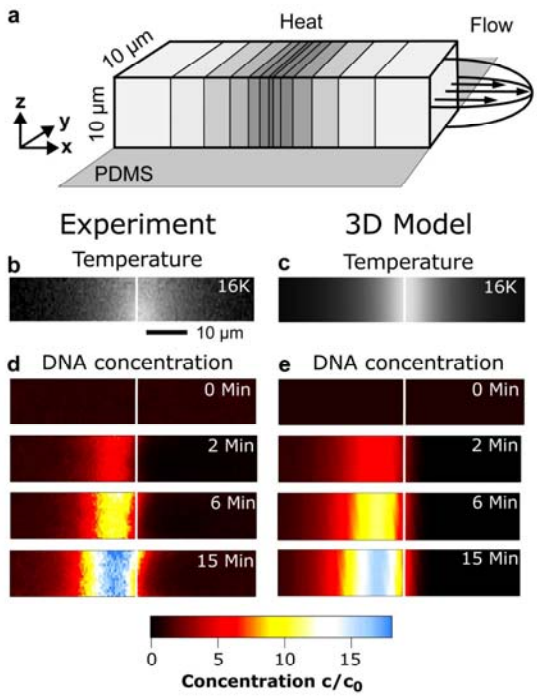

FIG. 2 (color online). Thermophoretic flow trap. (a) A warm spot (gray scale; $\Delta T_{\max} = 16$ K) repels molecules by thermophoresis. Countcracting parabolic fluid flow (black arrows; $v_{\max} = 0.55\ \mu$m/s) leads to accumulation of molecules upstream of the warm spot. (b) Cross chamber average of fluorescently measured temperature. (c) 3D temperature simulation of a heated water film between PDMS sheets. Low heat conductivity of PDMS leads to homogenous temperature across the channel. (d) The experiment shows that DNA is strongly accumulated 16-fold within 15 min. (e) 3D simulation of the microfluidic chamber using a parabolic flow profile. Kinetics and magnitude of accumulation fit the experiment.

the temperature dependent fluorescence signal of the dye BCECF, diluted to 50 μM in 10 mM Tris(hydroxymethyl)-aminomethan (TRIS) buffer. From the total BCECF temperature dependence of -2.4%/K, only -0.9%/K stems from pH drift of the used TRIS buffer. The remaining -1.5%/K are the result of thermophoresis of the dye itself [14]. Temperature was increased by 16 K in a Lorentzian-shaped focus of $T = T_0 + \Delta T/[1 + (x/b)^2]$ width $b = 12.2\ \mu$m [Fig. 2(b)]. DNA concentration was measured by fluorescence using an intercalating dye at low concentration. Highly monodisperse and protein-free DNA of 10 000 bp (Fermentas) was fluorescently labeled by using 1x SYBR-I (Molecular Probes, Oregon) which shows 1000x fluorescence increase when bound to DNA. DNA was diluted to 10 nM in 1 mM TRIS buffer.

DNA is flowing from the left with an effective velocity of 0.55 μm/s against the warm spot. Within 15 min, DNA accumulates 16-fold in the front, i.e., left of the warm spot. Images of DNA concentration recorded by fluorescence at different times are shown in Fig. 2(d). First, DNA is depleted at the warm spot (right side), followed by accumulation in front of the depletion (left side) as the water drift from the left brings in DNA. The depletion on the right is slowly fading in the progress of accumulation, filled by diffusion from the accumulated DNA. The effective fluid velocity was measured by the speed with which the accumulated DNA drifted to the right after the laser was switched off.

Three-dimensional model.—We first model the accumulation in three dimensions with a parabolic flow $\vec{v}(y, z)$ of peak velocity 0.55 μm/s. The extended Fick's law is given by

$$\vec{j} = \vec{v}(y, z)c - D\nabla c - D_T c\nabla T. \qquad (3)$$

We used the experimentally obtained Lorentzian temperature profile with a constant temperature in the y and z directions due to low thermal conductivity of PDMS [Fig. 2(b) and 2(c)]. Diffusion coefficient $D = 1.7\ \mu\text{m}^2/\text{s}$ and thermophoretic mobility $D_T = 1.1\ \mu\text{m}^2/(\text{s K})$ were taken from measurements on 10.000 base pair DNA in 1 mM TRIS buffer [15]. Convection has proven insignificant in these thin fluid films [14] with convection velocities on the order of nm/s. We plot the simulated cross section DNA concentrations over time next to the corresponding experimental results [Fig. 2(d) and 2(e)]. As expected, due to the fast diffusion relaxation time across the channel on the order of $\tau = \Delta x^2/D = 0.2$ min, the spacial inhomogenous velocity profile $\vec{v}(y, z)$ is smeared out in the accumulation and does not lead to a spacial inhomogeneity.

One-dimensional model.—The model can be reduced to one dimension due to fast diffusion across the channel. We will show that it describes the experiments equally well. We assume a plug flow instead of a parabolic flow profile $\vec{v}(y, z) = v_{\max}\vec{e}_x$. Figure 3 shows the DNA concentrations at the center of the channel at various times. The overlaid solid lines from the one-dimensional simulation fit the data very well. We see that thermophoresis opposed by a fluid flow can be described by straightforward superpositions of flows by Eq. (3). It leads to a fast and strong accumulation of DNA molecules. Accumulations at longer times in steady state can be described by an analytical model. Without fluid flow, thermophoresis and diffusion balance in steady state. For constant D and D_T at low DNA concentration, c compared to water molecules Eq. (2) can be integrated to

$$c(x) = c_0 e^{-U(x)}, \qquad U(x) = \frac{D_T[T(x) - T_0]}{D}, \qquad (4)$$

with boundary values for concentration c_0 and temperature T_0. Formally, the term $U(x)$ can be interpreted as thermodynamic potential. The local concentration c becomes a

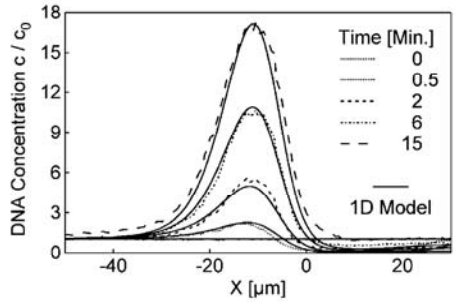

FIG. 3. 1D simulation describes experimental results. The experimental cross chamber average (dotted lines) match with theoretical results of a 1D time dependent simulation.

direct function of local temperature T, irrespective of the steepness of the temperature gradient ∇T. With fluid flow, the continuity equation $\partial c/\partial t + \nabla \cdot j = 0$ has to be taken into account. At steady state $\partial c/\partial t = 0$, the molecule flow j is constant given by $j_0 = vc_0$ with drift velocity v. An analytical solution of the steady state concentration profile $c(x)$ can be integrated:

$$c(x) = \frac{v}{D} e^{-U(x)} \int_x^\infty e^{U(x')} dx', \qquad U(x) = \frac{D_T[T(x) - T_0] - vx}{D}. \tag{5}$$

The term $U(x)$ can be interpreted as an effective potential. The normalization integral in Eq. (5) does not affect the shape of the accumulation profile near its peak. The potential allows a intuitive description of the accumulation: as the drift velocity increases, the initially depleting potential U for $v = 0$ builds up a potential trough upstream (left) of the warm spot [Fig. 4(a)]. The trough dimensions become smaller as the drift velocity v increases and is large in width and depth for small flow velocities. Based on the potential image, we understand the strong attraction of molecules in steady state calculated for low values of v [Fig. 4(b)]. The accumulation diminishes as drift v increases and the tilting of the potential by the term $-vx/D$ leads to a shallower and less wide potential trough. For the steady state solution in a one-dimensional model, accumulation is peaking for slower drift velocities. At $v = 0.04$ μm/s, accumulation is maximal with 820-fold DNA concentration in front of the heat spot [Fig. 4(b)]. While smaller drift v makes the potential deeper and accumulation stronger [Fig. 4(a) and 4(b)], considerably more time is needed to transport the DNA to the trap and reach a steady state. For example, the time to reach above $820x$ accumulation steady state is 1000 h or 41 days. The peak concentration is located with good approximation at the minimum of the effective potential $U(x)$; i.e., the maximal concentration is located at the point where thermophoretic drift $v_T = -D_T \nabla T$ and flow drift v exactly oppose each other:

$$\nabla U = 0 \Rightarrow v = D_T \nabla T. \tag{6}$$

Flow and gradient dependence.—The point of maximum accumulation is located closer to the heated center for higher velocities v [Fig. 4(a) and 4(b)], since the temperature gradient is stronger there. Figure 5(a) shows the velocity dependence of DNA accumulation within a short time of 15 min. To reach maximal accumulation of 10 kbp DNA within this time, $v = 0.55$ μm/s is optimal. Both faster and slower drift decreases the accumulation in the chosen finite time. The velocity for maximal accumulation efficiency barely depends on DNA length, allowing us to infer DNA size from the achieved accumulation at a constant drift v. As Fig. 5(b) shows, size selectivity and the magnitude of accumulation within the limited time span of 15 min, is exceptionally sensitive to focus width. Decreasing the focal width from 12 to 2 μm increases the accumulation of 10 kbp DNA within 15 min by an order of magnitude.

Radial flow trap in a sheet of liquid.—As temperature is created by optical means, we are not limited to a fixed focus in a microfluidic flow channel. For example, DNA in a two-dimensional 20 μm high water sheet can be accumulated by optically imposed circular heat rings which move concentrically towards a spot (Fig. 6). With a radial

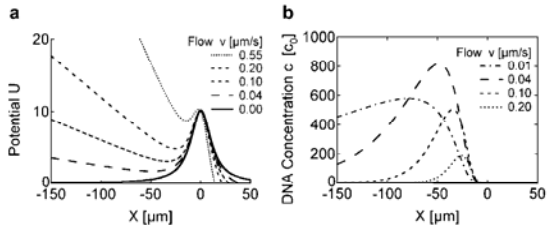

FIG. 4. Steady state accumulation. (a) In the potential image, introduction of flow corresponds to a tilting of thermophoretic depletion potential U, leading to a potential trough upstream of the warm spot. (b) The minimum of effective potential coincides with the maximum concentration in steady state. Accumulation peaks at $820x$ for $v = 0.04$ μm/s.

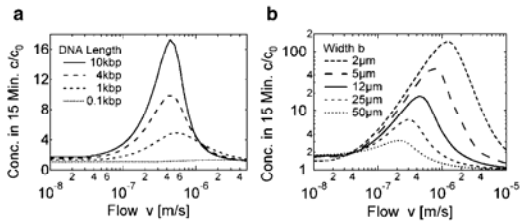

FIG. 5. Accumulation in finite time. (a) Maximal accumulation in finite time requires faster drift v than in steady state. The optimal velocity of 0.55 μm/s is only slightly shifted for shorter DNA. (b) Tighter focusing makes the potential steeper and leads to faster equilibration and considerably stronger accumulation within finite time.

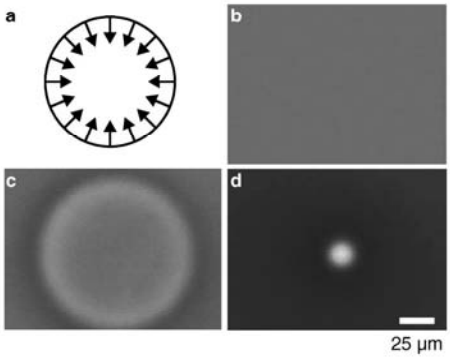

FIG. 6. Radial DNA accumulation. (a) A radial temperature circle is written into the chamber. It is closed radially over time and DNA becomes accumulated in the center. (b)–(d) Sequence of concentration of 1000 bp DNA at times 0, 20, and 80 s. Finally DNA is sixfold accumulated in a spot 10 μm in radius.

drift of $v = 2.3$ μm/s and an average temperature of $\Delta T_{\max} = 20$ K, short 1000 base pair DNA was accumulated sixfold in a spot of 10 μm radius within 80 scc. This result illustrates how optically triggered thermophoretic traps can accumulate molecules in a variety of geometries.

Conclusion.—Opposing thermophoretic flow against a fluid flow creates a molecule trap. Fluorescence measurements in a microfluidic channel agree well with the one-dimensional superposition of both flows. Within 15 min, 10.000 base pair DNA was accumulated 16-fold by a 16 K warm microscopic spot. We showed that 1000 base pair DNA can be sixfold accumulated to a spot by radially moving a circular temperature ring.

We thank Franz Weinert for assistance, Peter Fromherz for suggestions and Hermann Gaub for hosting the Emmy-Noether Nachwuchsgruppe which was funded by the Deutsche Forschungsgemeinschaft.

*Electronic address: dieter.braun@physik.lmu.de
Email address: mail@dieterb.de

[1] C. Ludwig, Sitzber. Akad. Wiss. Wien, Math.-Nat. Wiss. Kl. **20**, 539 (1856).
[2] C. Soret, Arch. Sci. Phys. Nat. Genève **2**, 48 (1879).
[3] J. Rauch and W. Köhler, Phys. Rev. Lett. **88**, 185901 (2002).
[4] C. Debuschewitz and W. Köhler, Phys. Rev. Lett. **87**, 055901 (2001).
[5] W. Köhler and S. Wiegand, in *Thermal Nonequilibrium Phenomena in Fluid Mixtures*, edited by W. Köhler and S. Wiegand (Springer-Verlag, Berlin, 2001), p. 190.
[6] B.-J. de Gans, R. Kita, B. Müller, and S. Wiegand, J. Chem. Phys. **118**, 8073 (2003).
[7] R. Rusconi, L. Isa, and R. Piazza, J. Opt. Soc. Am. B **21**, 605 (2004).
[8] S. Iacopini and R. Piazza, Europhys. Lett. **63**, 247 (2003).
[9] R. Piazza, S. Iacopini, and B. Triulzi, Phys. Chem. Chem. Phys. **6**, 1616 (2004).
[10] M. Giglio and A. Vendramini, Phys. Rev. Lett. **34**, 561 (1975).
[11] M. Giglio and A. Vendramini, Phys. Rev. Lett. **38**, 26 (1977).
[12] R. Piazza and A. Guarino, Phys. Rev. Lett. **88**, 208302 (2002).
[13] D. Braun and A. Libchaber, Phys. Rev. Lett. **89**, 188103 (2002).
[14] S. Duhr, S. Arduini, and D. Braun, Eur. Phys. J. E **15**, 277 (2004).
[15] S. Duhr and D. Braun (to be published).
[16] J. K. G. Dhont, J. Chem. Phys. **120**, 1632 (2004).
[17] J. K. G. Dhont, J. Chem. Phys. **120**, 1642 (2004).
[18] H. Brenner, Phys. Rev. E **72**, 061201 (2005).
[19] S. Fayolle, T. Bickel, S. Le Boiteux, and A. Würger, Phys. Rev. Lett. **95**, 208301 (2005).
[20] K. Clusius and G. Dickel, Naturwissenschaften **26**, 546 (1938).
[21] P. Debye, Ann. Phys. (Berlin) **36**, 284 (1939).
[22] H. Korsching and K. Wirtz, Naturwissenschaften **27**, 110 (1939).
[23] W. H. Furry, R. C. Jones, and L. Onsager, Phys. Rev. **55**, 1083 (1939).
[24] D. Jung and M. Lücke, Phys. Rev. Lett. **89**, 054502 (2002).
[25] S. Duhr and D. Braun, Appl. Phys. Lett. **86**, 131921 (2005).
[26] J. C. Giddings, M. Martin, and M. N. Myers, Sep. Sci. Technol. **14**, 611 (1979).
[27] O. Ecenarro, J. A. Madariaga, J. Navarro, C. M. Santamaria, J. A. Carrion, and J. M. Saviron, J. Phys. Condens. Matter **2**, 2289 (1990).
[28] J. K. Platten, M. M. Bou-Ali, and J. F. Dutrieux, J. Phys. Chem. B **107**, 11 763 (2003).

Publikation VIII: Size determination of (bio-) conjugated water-soluble colloidal nanoparticles - a comparison of different techniques, **J. Phys. Chem. C**, akzeptiert (2007), R. A. Sperling, T. Liedl, S. Duhr, S. Kudera, M. Zanella, C.-A. J. Lin, W. Chang, D. Braun, W. J. Parak, (2007)

Size Determination of (Bio)conjugated Water-Soluble Colloidal Nanoparticles: A Comparison of Different Techniques

R. A. Sperling,[†] T. Liedl,[†] S. Duhr,[†] S. Kudera,[†] M. Zanella,[†] C.-A. J. Lin,[†,‡] W. H. Chang,[‡] D. Braun,[†] and W. J. Parak*,[†]

Center for Nanoscience, Ludwig Maximilians Universität, München, Germany, and Center for Nano Bioengineering and R&D Center for Membrane Technology, Chung Yuan Christian University, Taiwan, R.O.C.

Received: February 5, 2007; In Final Form: April 21, 2007

The size of inorganic colloidal nanoparticles coated with organic layers of different thickness has been measured with different techniques, including transmission electron microscopy, gel electrophoresis, size exclusion chromatography, fluorescence correlation spectroscopy, and thermophoresis. The results are critically compared, and the advantages and disadvantages of the respective methods are discussed.

Introduction

In the last decades, improved synthesis techniques have significantly influenced research and applications of inorganic colloidal nanoparticles. This is mainly due to advances in the control of particle growth. Nowadays, samples with very narrow size distribution and controlled shape can be grown.[1−3] Colloidal stability is provided by a layer of organic molecules around the inorganic particle core. This layer can be either hydrophobic or hydrophilic, and the respective particles are soluble in organic solvents or aqueous solution. Naturally, this layer contributes to the overall diameter of the particles. Whereas the colloidal stability of particles in organic solvents is usually achieved by a monolayer of hydrophobic molecules,[4] thicker (hydrophilic) layers are often used to stabilize particles in aqueous solution, which in turn results in significantly increased particle diameters.[5,6] The effective diameter of the particles increases further when additional (biological) molecules are bound to the particle surface in order to provide functionality. In particular, for biological applications, it is important to know the effective diameter of the particles, as bigger particles, for example, might not be able to enter pores of a certain size. However, due to the composite nature of the particles—a "hard" inorganic core and a "soft" organic shell with attached biological molecules—this is not a trivial task. The problem is that some techniques are more sensitive for the inorganic part, and others may eventually influence the conformation and thus the size of the organic part.

The size of the first generation of colloidal semiconductor nanoparticles was investigated extensively several years ago by the group of Henglein and Weller.[7−9] These particles were directly synthesized in water, and the organic shell around the inorganic cores comprised just a monolayer of mercaptocarbonic acid molecules. In this study, we want to investigate the size of more complex nanoparticles that first have been synthesized in organic solvents, then have been transferred to aqueous solution by embedding them in a hydrophilic polymer shell,[10−13] and finally have been modified by the conjugation of polyethylene glycol (PEG) molecules with different molecular weight.[14] These particles represent the general case where the samples differ in the thickness of a (soft) organic shell, while the (hard) inorganic particle core is the same.

For this work, nanoparticle size was characterized by the following methods: transmission electron microscopy (TEM),[15−17] gel electrophoresis,[9,18−24] size exclusion chromatography (SEC),[7,8,21,25−35] fluorescence correlation spectroscopy (FCS),[11,36−44] and thermophoresis.[45−47] These and other relevant methods not used in this study are described in more detail in the Supporting Information (SI).

Materials and Methods

Particle Synthesis. CdSe/ZnS core/shell nanoparticles were synthesized in organic solvent according to standard protocols[48,49] and transferred to aqueous solution by embedding them in a shell of an amphiphilic polymer.[11] All protocols are reported in detail in the Supporting Information (SI §I.1−§I.5). The first exciton peak in the absorption spectrum of the CdSe cores was at 610 nm (corresponding to a diameter of the inorganic core of 4.7 nm[50]) and, after overcoating with the ZnS shell, at 614nm (see Table 1). PEG molecules of different molecular weight, which were modified with an amino group on one end, were attached at different ratios with standard EDC chemistry to the polymer shell around the nanoparticles[14] (SI §I.6). Sketches of the resulting particles are drawn in Table 2. For particles whose surfaces were saturated with PEG, unbound excess PEG molecules were removed in five subsequent purification steps with centrifuge filters. Mixtures of particles with a discrete number of PEG molecules attached per particle were first run on 1% agarose gels in order to separate particles with zero, one, two, and three PEG molecules attached per particle. After extraction of the particles from the gel, they were purified on a desalting column. As additional samples, Au nanoparticles[16,51] with the same modifications as those described for the CdSe/ZnS particles were also used. Detailed protocols have been published previously.[11,14] We also measured the diameter of commercially available quantum dots with and without streptavidin modification (Table 4).

Transmission Electron Microscopy. TEM images of CdSe/ZnS particles dissolved in chloroform and water were recorded before and after embedding them in a shell of amphiphilic

* Corresponding author. E-mail: Wolfgang.Parak@physik.uni-muenchen.de.
† Ludwig Maximilians Universität.
‡ Chung Yuan Christian University.

TABLE 1: The Inorganic Hard Core Diameter $\langle d \rangle$ of CdSe, CdSe/ZnS, and Au Particles (Drawn in Gray) Determined with Optical Methods[a] and by TEM Images[b]

particle type	$\langle d \rangle_{abs}$ [nm]	$\langle d \rangle_{TEM}$ [nm]	$\langle d_{eff} \rangle_{TEM}$ [nm] before polymer coating	$\langle d_{eff} \rangle_{TEM}$ [nm] after polymer coating[c]
CdSe	5.1	4.7	6.0	
CdSe/ZnS	5.3	5.3	6.4	9.6
Au		4.6	5.6	9.0

[a] For the CdSe particles, the diameter was derived from absorption spectra.[50] [b] By analyzing the spacing between the particles in the TEM images, the effective diameters $\langle d_{eff} \rangle$, which comprise the inorganic particles plus the organic layers (drawn in red and blue) attached to their surfaces, were determined before and after coating the particles with an amphiphilic polymer. Before the polymer coating, the particle is just surrounded by the hydrophobic surfactant layer (drawn in red). After the polymer coating, an amphiphilic polymer (with hydrophobic tails drawn in red and a hydrophilic backbone drawn in blue) is also wrapped around the particles.[11,14] [c] These values have to be considered as an approximation (see SI §II.2).

polymer. Drops of the particle solution were placed on TEM grids, and images were recorded after evaporation of the solvent. The distribution of the inorganic particle diameters and the distances between the centers of adjacent particles were derived from the images by an image analysis program (SI §II.1).

Gel Electrophoresis. CdSe/ZnS and Au particles saturated with PEG molecules of different length were run on agarose gels (1−2%, 1−2 h, 100 V). As a control, phosphine-stabilized 10 nm Au particles were also run on the same gel.[19,20] After running the particles on the gel, the bands of the CdSe/ZnS and Au particles were identified by their fluorescence and red color, respectively (see Figure 1) (SI §III). The mobilities of the different particles were determined from their position on the gel relative to the position where they had been loaded to the gel.[19,20] For CdSe/ZnS and Au particles with a discrete number of PEG molecules attached per particle, a low amount of PEG molecules of different length was reacted to the polymer-coated CdSe/ZnS and Au particles, and the reaction mixtures were run on agarose gels. After running the gel, discrete bands corresponding to CdSe/ZnS and Au particles with no, exactly one, exactly two, and exactly three PEG molecules bound per particle were observed as individual bands on the gel (see Figure 1).[19,20] The bands were extracted from the gel, and the obtained CdSe/ZnS− and Au−PEG conjugates with a different number of PEG molecules attached per particle were purified, desalting the column before using them for the SEC, FCS, and thermophoresis experiments. From gel electrophoresis, the mobilities m of all conjugates were then transformed in corresponding effective diameters d_{eff} by using a mobility−diameter calibration curve created with phosphine-stabilized Au nanoparticles[20] (SI §III):

$$d_{eff,1\%}(m) = -85.0 \cdot \ln[(m/m_{10nm,1\%})/1.05] + 6 \text{ [nm]}$$

$$d_{eff,2\%}(m) = -37.7 \cdot \ln[(m/m_{10nm,2\%})/1.12] + 6 \text{ [nm]} \quad \text{(Formula 1)}$$

Here, $m/m_{10nm,y}$ refers to the electrophoretic mobility of the conjugates (m) in relation to the mobility of 10 nm phosphine-stabilized Au particles ($m_{10nm,y}$) that have been run on a gel with the same agarose concentration y (y = 1% or 2%).[19,20]

Size Exclusion Chromatography. CdSe/ZnS and Au particles saturated with PEG molecules of different molecular weight were run on different high-performance liquid chromatography (HPLC) size exclusion columns, and the elution volume v_e (i.e., the total volume of the mobile phase when the particles come out of the column) of the particles was measured (similarly, elution times t_e, i.e., the time after which the particle fraction is eluted from the column, could have been measured) (see Figure 2) (SI §IV). In order to normalize the data to one universal curve, the elution volumes v_e were transformed into partition coefficients K_{SEC}.[52,53] The partition coefficient corresponds to the fraction of accessible pore volume for sample particles and can obtain values $0 \le K_{SEC} \le 1$. Very small particles or molecules can occupy the total pore volume (as they are small enough to fully penetrate the pores of the gel), and $K_{SEC} = 1$. Very large particles are totally excluded from the pore volume, and $K_{SEC} = 0$. In this way, the K_{SEC} value is a measure of the size of the particles: the smaller and larger the particles are, the closer their K_{SEC} values come to 1 and 0, respectively. In contrast to elution volumes or elution times, the K_{SEC} values are normalized quantities and thus do not depend in first order on experimental parameters such as sample volume, flow rate, or column geometry (SI §IV):

$$\begin{aligned} K_{SEC}(\text{particle}) &= [(t_e(\text{particle}) - t_e(\text{biggest particle})]/ \\ &\quad [(t_e(\text{smallest particle}) - t_e(\text{biggest particle})] \\ &= [(v_e(\text{particle}) - v_e(\text{biggest particle})]/ \\ &\quad [(v_e(\text{smallest particle}) - v_e(\text{biggest particle})] \\ &= [(v_e(\text{particle}) - v_0]/[v_t - v_0] \end{aligned} \quad \text{(Formula 2)}$$

The elution volume of the very small particles is referred to as the total liquid volume v_t, and the elution volume of the very large particles is referred to as dead or void volume v_0. In order to experimentally obtain v_t and v_0, aceton (a very small particle) and λ-DNA (a very big particle) were run, and their elution volumes (= v_t and v_0) were measured. For generating a calibration curve that relates partition coefficients K_{SEC} to effective diameters d_{eff}, protein standards were run through the columns, and their elution volumes were determined from the elution peak maxima and converted into partition coefficients. The size d_{eff} of each protein standard was estimated as 2 times the hydrodynamic radius of the protein.[53] By plotting the partition coefficients of different proteins versus their effective diameter and extrapolating these data, a calibration curve d_{eff}-(K_{SEC}) was obtained (see Figure 2). By using this calibration curve, the partition coefficients derived for the CdSe/ZnS−PEG and Au−PEG conjugates could be converted into effective diameters. As for the gel electrophoresis experiments, the effective diameters are obtained by a comparison with standard samples of known diameter. In the case of the gel electrophoresis experiments, phosphine-stabilized Au nanoparticles were used. These particles could not be used for the SEC measurements, as they got stuck in the columns. Therefore a series of globular proteins had to be used as standard samples for the SEC measurements.

Fluorescence Correlation Spectroscopy. Samples of CdSe/ZnS−PEG conjugates were mounted on an Axiovert200 confocal microscope with a 40× water immersion objective (C-Apochromat, NA = 1.2) and a ConfoCor2 FCS module (whole setup: Zeiss, Germany). Fluorescence was excited with the 488 nm line of an Ar ion laser. The focal volume was calibrated with Alexa488 (D = 316 $\mu m^2 s^{-1}$, Molecular Probes). The nanocrystals were diluted to a concentration of ~10 nM, which corresponds to roughly one particle per focal volume. Time traces of the fluorescence intensity were recorded with an

TABLE 2: Effective Diameters d_{eff} [nm] of CdSe/ZnS-PEG Conjugates[a]

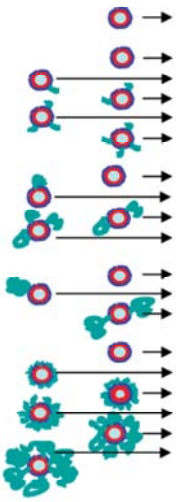

PEG/ polymer-coated CdSe/ZnS particle	M(PEG) [g/mol]	$\langle d_{eff}\rangle_{TEM}$ [nm]	$\langle d_{eff}\rangle_{gel,1\%}$ [nm]	$\langle d_{eff}\rangle_{gel,2\%}$ [nm]	$\langle d_{eff}\rangle_{SEC}$ [nm]	$\langle d_{eff}\rangle_{FCS}$ [nm]	$\langle d_{eff}\rangle_{Therm}$ [nm]
0	-	9.6[b]	14.5	-	-	20.5	-
0	5000	-	14.5	14.5	-	20.1	-
1	5000	-	24.5	19.3	-	22.8	-
2	5000	-	34.2	24.1	-	24.4	-
3	5000	-	43.6	28.5	-	25.8	-
4	5000	-	51.9[c]	32.8	-	-	-
0	10000	-	14.5	-	-	25.0	-
1	10000	-	29.4	-	-	25.8	-
2	10000	-	43.5	-	-	26.6	-
3	10000	-	56.5[c]	-	-	-	-
0	20000	-	14.5	-	-	22.2	8.2
1	20000	-	39.6	-	-	26.3	12.2
2	20000	-	62.7[c]	-	-	29.2	30.2
0	-	-	-	14.5	12.6	19.4	12.2
sat.	750	-	-	46.1[c]	14.6	25.4	22.0
sat.	2000	-	-	180.2[c]	18.3	25.6	23.6
sat.	5000	-	-	neg.[c]	23.9	27.6	25.0
sat.	10000	-	-	neg.[c]	26.2	30.2	30.0
sat.	20000	-	-	neg.[c]	34.8	34.2	40.0

[a] PEG molecules (drawn in green) of different molecular weight M_w have been attached to the surface of polymer-coated CdSe/ZnS particles, as already sketched in Table 1.[14] Either zero, one, two, three, or as many as possible ("sat.") PEG molecules were attached per particle, and the effective particle diameter $\langle d_{eff}\rangle$ was measured with TEM, gel electrophoresis ("gel",1% and 2% agarose concentration), FCS, SEC, and thermophoresis ("Therm"). The particles with single PEGs attached per particle (first 13 samples) had been separated with gel electrophoresis and subsequent extraction from the gel and purification before their diameters were measured with SEC, FCS, and thermophoresis. [b] This value has to be considered as approximation. [c] These values are not realistic (as they are either too big or negative) due to limitations of the applied technique (see SI §II.2).

TABLE 3: Effective Diameters d_{eff} [nm] of Au−PEG Conjugates[a]

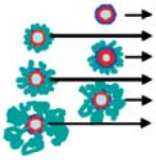

PEG/ polymer-coated Au particle	M(PEG) [g/mol]	$\langle d_{eff}\rangle_{TEM}$ [nm]	$\langle d_{eff}\rangle_{gel,1\%}$ [nm]	$\langle d_{eff}\rangle_{gel,2\%}$ [nm]	$\langle d_{eff}\rangle_{SEC}$ [nm]
0	-	8.6	12.7	12.5	-
0	5000	-	12.7	12.5	-
1	5000	-	26.3	18.4	-
2	5000	-	38.2[b]	24.5	-
3	5000	-	-	29.9	-
0	10000	-	13.4	12.5	-
1	10000	-	44.5[b]	21.6	-
2	10000	-	70.7[b]	29.3	-
0	20000	-	14.4	12.5	-
1	20000	-	52.5[b]	27.7	-
2	20000	-	83.5[b]	40.2	-
0	-	-	-	12.5	11.1
sat.	750	-	-	49.7[b]	12.5
sat.	2000	-	-	140.1[b]	16.5
sat.	5000	-	-	neg.[b]	21.0
sat.	10000	-	-	neg.[b]	28.8
sat.	20000	-	-	neg.[b]	34.8

[a] PEG molecules of different molecular weight M_w have been attached to the surface of polymer-coated Au particles.[14] Either zero, one, two, three, or as many as possible ("sat.") PEG molecules were attached per particle, and the effective particle diameter $\langle d_{eff}\rangle$ was measured with gel electrophoresis ("gel",1% and 2% agarose concentration) and SEC. [b] These values cannot be taken into account (as they are too big or negative) and demonstrate the limitations of gel electrophoresis for size measurements (see SI §II.2).

avalanche photodiode with single-photon sensitivity. From the fluorescence intensity traces, autocorrelation functions were calculated (see Figure 3) (SI §V). By fitting the experimentally obtained autocorrelation functions with model functions for freely diffusing particles, the diffusion coefficients of the particles were obtained as fit parameters.[37−39,54] The diffusion coefficients were then converted into effective diameters by using the Stokes−Einstein relation. In contrast to the gel

TABLE 4: Effective Diameters d_{eff} of Commercially Available Quantum Dots[a,b]

sample	$\langle d_{eff}\rangle_{gel,2\%}$ [nm]	$\langle d_{eff}\rangle_{SEC}$ [nm]	$\langle d_{eff}\rangle_{Therm}$ [nm]	$\langle d_{eff}\rangle_{mean-value}$ [nm]
QD655 carboxyl	16.6	11.8	14.0	14.1 ± 2.4[d]
QD655 SA	133.0[c]	20.5	25.6	23.1 ± 1.6

[a] Quantum Dot Corporation, 655 nm emission, polymer shell with carboxyl groups and with additional streptavidin (SA) modification (Qdot655 ITK carboxyl, #2132-1, and Qdot655 streptavidin conjugate, #1012-01). [b] The values were obtained with gel electrophoresis (2% agarose gels), SEC (Sephadex S-400 columns), and thermophoresis. [c] This value cannot be taken into account due to charge effects (see SI §II.2). [d] This value is in the same range as the diameter obtained for particles with slightly smaller cores from Pons et al.[24]

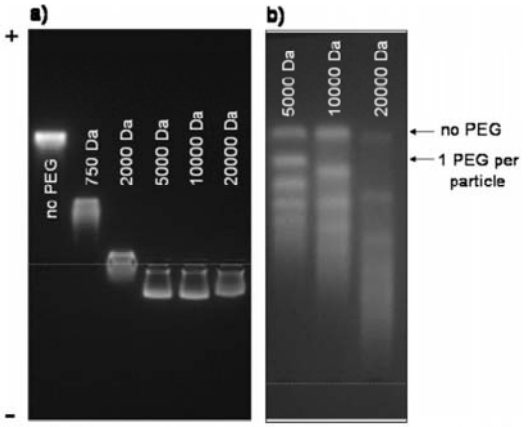

Figure 1. 1. Gel electrophoresis for polymer-coated CdSe/ZnS nanoparticles. The "+" and "−" symbols indicate the direction of the applied electric field, and the dashed line marks the position where the samples have been loaded into the wells of the gel. (a) 2% agarose gel with particles with no PEG and particles whose surface has been saturated with PEG of 750, 2000, 5000, 10000, and 20000 Da molecular weight. (b) 1% agarose gel of particles to whose surface only a few PEG molecules of different molecular weight have been bound. The particles with no, one, two, and so forth PEG molecules attached per particle yield discrete bands on the gel.

electrophoresis and HPLC measurements, the effective diameters obtained with FCS measurements are absolute values and do not depend on a direct comparison with standard samples of known diameter. However, the setup has to be calibrated with a dye of known diffusion constant for all measurements. Since the Au−PEG conjugates do not fluoresce, they could not be analyzed with FCS.

Thermophoresis. Strong local temperature gradients were used to manipulate concentration patterns in solution, all optically. Figure 4a shows the typical time course of an experiment. A solution of nanoparticles was continuously monitored by fluorescence microscopy, and the local fluorescence was used as measure for the particle concentration. An infrared laser was then used to introduce an inhomogeneous radial symmetric concentration pattern by inducing thermophoretic motion. After a few seconds, when the concentration in the center of the heat spot had decreased to at least 90% of the initial condition, the heating source was turned off. The temperature relaxed nearly instantaneously and was followed by the much slower flattening of the concentration profile by diffusion. These time-resolved concentration profile data were compared with data obtained in a one-dimensional (1D) radial simulation over time (Figure 4b). By comparison of the experimental and simulated data, the mean diffusion coefficient of the fluorescent particles in solution was obtained, and from this the hydrodynamic diameter of the particles was derived using the Stokes−Einstein relation (SI §VI). In contrast to the gel electrophoresis and HPLC measurements the effective diameters obtained with thermophoresis measurements do not depend on a comparison with standard samples of known diameter, but are absolute values. Since the Au−PEG conjugates do not fluoresce, they could not be analyzed with thermophoresis.

PEG Radius. The increase in size of particles with a PEG shell should correspond to the dimensions of the PEG molecules. The effective diameters of free PEG molecules can be calculated from Formula 3, which was obtained by SEC,[55] whereby r_h is the hydrodynamic radius, and M_w is the molecular weight of the PEG:

$$d_{eff,PEG} = 2r_h = 0.03824\, M_w^{0.559} \qquad \text{(Formula 3)}$$

Results and Discussion

Transmission Electron Microscopy. The results for the TEM analysis are summarized in Tables 1, 2, and 3. However, these values have to be considered as very rough estimates with only limited reliability (SI §II.2). First of all, measurements had to be performed on dried samples. While, in solution, the hydrophobic surfactant chains repel each other, on a TEM grid, the particles can come so close to each other that the surfactant chains intercalate. More severe, the size distribution after the polymer coating, that is, the size-distribution of the entire system inorganic core plus organic shell, is by far not as good as that of the original particle solution, and the particles therefore do not assemble anymore nicely into two-dimensional lattices. Therefore, the particle-to-particle distance curves are smeared out, and the derived effective particle diameters have to be interpreted with care. As the particles have to be measured in the dried state, the effective diameters as determined by TEM do not contain any interaction with the solvent (as, for example, a cloud of counterions). Therefore, the values obtained for the effective diameter for CdSe/ZnS as well as Au particles with TEM are significantly smaller than the effective diameters determined with methods in which the particles are dispersed in their solvents (see first lines of Tables 2 and 3).

Gel Electrophoresis. In Figure 1, examples for particles separated by gel electrophoresis are shown. As with SEC, not only can the particle diameter be estimated, but the particles can also be sorted and fractionated by size in small preparative scale. In comparison to SEC, the size resolution of gel electrophoresis is significantly better, as particles with zero, one, two, and so forth PEG molecules can be clearly separated by gel electrophoresis, but not with the columns used for SEC. However, there are severe limitations for the determination of effective diameters. The particles need to possess a very high colloidal stability in the electrolytic solution, which is needed to drive the current, otherwise they agglomerate and get stuck on the gel. The biggest problem, however, is obtaining an appropriate calibration curve that relates electrophoretic mobility to effective size. As electrophoretic mobility depends on both size and charge, any calibration curve for size can only be valid for objects of similar charge. Furthermore, the physical properties such as stiffness and flexibility of the particles used to obtain the calibration curve must be similar to those of the particles that are to be investigated. Basically, two different types of particles could be used in order to obtain calibration curves: biological macromolecules or colloidal nanoparticles. We have tried oligonucleotides[19,20] as well as proteins for calibration, but

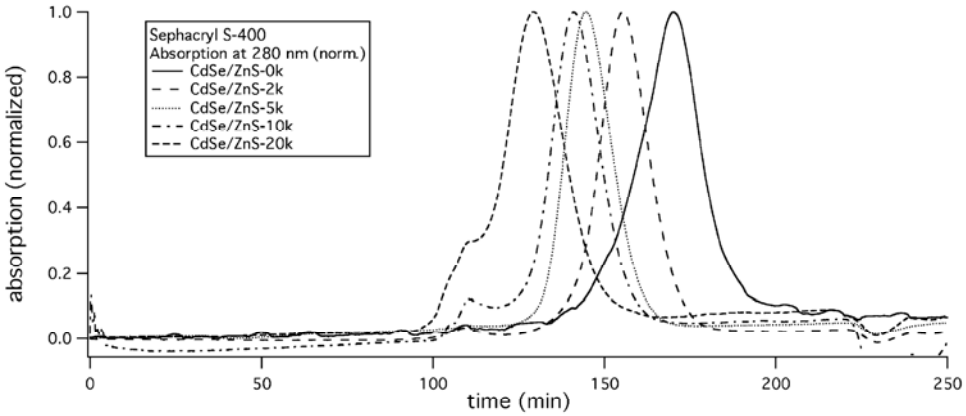

Figure 2. Size exclusion chromatograph (SEC) with a Sephacryl S-400 filled column of CdSe/ZnS nanoparticles whose surface is saturated with PEG molecules of different molecular weight (no PEG, 2 kDa, 5 kDa, 10 kDa, 20 kDa). Plotted is the absorption of the eluted solution versus elution time. The bigger the particles are, due to the attachment of PEG of higher molecular weight, the earlier they are eluted from the colu

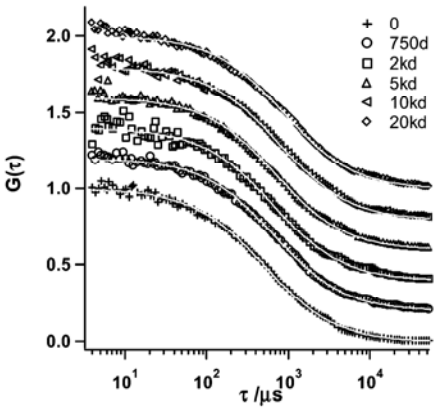

Figure 3. Autocorrelation functions $G(\tau)$ obtained from the FCS data for polymer-coated CdSe/ZnS particles whose surface is saturated with PEG molecules of different molecular weight (750 g/mol, 2 kg/mol, 5 kg/mol, 10 kg/mol, 20 kg/mol). The curves for the respective particles are shifted along the *y*-axis for the purpose of better visualization. The particles with no PEG attached are referred to as particles with PEG of molecular weight 0 (top graph). The experimental data were fitted with an analytical function (shown as gray lines), which yielded the effective diffusion coefficient as one fit parameter (see SI §V).

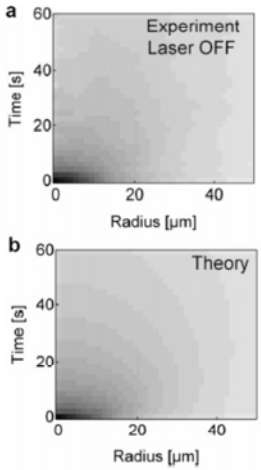

Figure 4. Thermophoresis and back-diffusion of nanometer-sized particles in solution. Thermodiffusion is used to form a concentration gradient in solution by heating a micrometer-sized spot. Graph a (experiment) shows the development of radial concentration averages over time after the heating laser is switched off (black: low concentration; gray: high concentration). As can be seen from the plot, the concentration inhomogeneity relaxes within 60 s. The data shown correspond to a particle size of approximately 30 nm in diameter. (b) (theory) The diffusion constant D is obtained by performing 1D finite element simulations with D as a free parameter, until the theory in b matches the experiment in a.

both yielded very different mobility values compared to the ones obtained for colloidal nanoparticles. As linear flexible molecules, oligonucleotides can move in a different way through the pores of a gel compared to rigid inorganic colloidal nanoparticles. On the other hand, the surface charge density of oligonucleotides is, in first order, constant, therefore oligonucleotides are sorted by size and not by charge. In contrast to average oligonucleotides, proteins possess a secondary and tertiary structure and can be thought of in crude approximation as elastic spherical particles. However, proteins can have different surface charge densities comprising the full spectra from negative to neutral to positive. Because it is hard to find a set of proteins with different sizes but with the same charge density as the particles that are to be investigated, proteins are also not suited as standard particles for obtaining a calibration curve that relates electrophoretic mobilities to size. Therefore we have chosen inorganic colloidal nanoparticles of different size but with identical negatively charged surface coatings (bis(*p*-sulfonatophenyl)-phenylphosphine dihydrate) as size standards. There are known problems for these standards as well. First, there is an inherent uncertainty in the standard, as the effective hydrodynamic diameter is not known and is assumed to be the hard core Au particle diameter plus 2 times the length of the phosphine molecules, without taking into account the cloud of counterions.[20] However, comparison with the literature data obtained from dynamic light scattering shows that they are in good agreement with the assumed values. Second, attached macromolecules (such as DNA[20]) form a soft shell around the hard inorganic core, which can be compressed by the gel. This can be seen in the data of Tables 2 and 3: the effective diameters derived from 1% agarose gels are always larger than the ones from 2% agarose gels, as the soft shell is compressed more on gels of higher percentage. This difference in data obtained with gels of different percentages has already been observed with DNA-modified sulfonate-stabilized Au particles.[20] Even in this case where there is only a minor influence of charge on the

electrophoretic mobilities, the diameters obtained with gels of different percentages differed significantly, whereby the differences were most significant for long DNA strands and particles with a lot of attached DNA (= thick soft shells). In this study, PEG molecules were used for particle modification. As has already been reported,[14] attachment of sufficient amounts of PEG to negatively charged polymer-coated particles can reverse the polarity of the particles to a positive net charge, so that they migrate toward the negative electrode during gel electrophoresis (see Figure 1). This effect might be due to positive ions adsorbed to the PEG.[56] At any rate, this charge effect makes the determination of effective diameters of PEGylated particles with gel electrophoresis almost impossible. Due to the charge effect, the derived diameters are too large, and, for particles saturated with long PEG, no diameter can be derived due to the change in polarity (see Tables 2 and 3). The more PEG is attached per particle and the higher the molecular weight of the PEG, the more unreliable the results become. Although, in our experience, gel electrophoresis is the most sensitive of the here-described methods to resolve changes in size (e.g., the attachment of a single molecule), reliable absolute numbers of effective diameters can be only derived under very restricted conditions when the charge density of the sample to be investigated is highly similar to that of the particles used as size standards.

Size Exclusion Chromatography. Analogous to gel electrophoresis, SEC is not only an analytical method, but particles of different diameter can be fractionated on a preparative scale. Here, sorting by size is also achieved by a porous matrix, but, in contrast to gel electrophoresis where particles are driven by an electric current and small particles run faster, in SEC smaller particles are retarded because they can access a larger pore volume of the column packing. For all the columns used in this study, the resolution by size was lower for SEC compared to gel electrophoresis, since, with SEC, particles with zero, one, two, three, and so forth PEG molecules bound per particle could never be separated, while this was easily achieved with gel electrophoresis. Size measurements with both methods rely on appropriate size standards. In SEC, charge effects, that is, electrostatic interaction of charged particles with charges in the gel, are typically reduced by a mobile phase with a high salt concentration that screens residual charges of the column material. Unfortunately, this rules out the use of the sulfonate-stabilized Au particles that were used for gel electrophoresis as size standards, as these particles tend to agglomerate at high salt concentrations and get stuck in the columns. We therefore used globular proteins as size standards, as we could exclude charge effects as in the case of gel electrophoresis. Good estimates for effective hydrodynamic diameters exist for many proteins. On the other hand, the size range of available proteins is limited. We were unable to find spherically shaped (globular) proteins with a diameter as large as the largest of our PEG-modified nanoparticles (ca. 40 nm). The derived effective diameters for PEGylated nanoparticles from the extrapolated calibration curve are therefore more reliable the smaller the particles are (see Tables 2 and 3 and Figure 2).

Fluorescence Correlation Spectroscopy. Unlike gel electrophoresis or SEC, FCS is a purely analytical method and does not allow for separation and subsequent collection of fractions of particles with different diameters. The effective diameters derived from the FCS measurements (see Table 2 and Figure 3) are consistent with our previous findings[11,41] and also consistent within themselves. The more and the longer PEG is added to the particles, the bigger the measured effective diameters are. Since FCS is based on single-particle experiments, each effective diameter reported in Table 2 corresponds to the mean value of the diameters of hundreds of particles from each sample. Within one sample series (i.e., different PEGs have been attached to the same batch of polymer-coated particles and the measurements were performed directly after each other with exactly the same FCS setup conditions), even the attachment of single PEG molecules could be resolved, that is, the resolution limit is better than that for the increase in diameters for particles upon attachment of zero, one, two, and three PEGs per particle (see Table 2). However, the absolute values of effective diameters that have been recorded on the same type of particles but under different experimental conditions (i.e., when the particles were extracted from different gels before the measurements, when the FCS setup was recalibrated, etc.) vary significantly. As an example, we take the mean diameters for plain polymer-coated particles (i.e., zero PEGs per particle) from the different series from Table 2. The mean effective diameter and standard deviation of the five different samples ($<d_{eff,FCS}>$ = <20.5 nm, 20.1 nm, 25.0 nm, 22.2 nm, 19.4 nm>) is 22.0 ± 2.8 nm. The standard deviation has to be seen as an error bar for absolute measurements. The error bar is in the same range as the increase in the particle diameter upon the attachment of individual PEG molecules per particle. We therefore conclude that, although relative changes in the effective particle diameter upon the attachment of molecules within the same batch of particles and under the same setup conditions can be resolved with good precision, there is a significant error of about 3 nm in the determination of absolute effective diameters. There are two main sources for systematic errors in deriving absolute effective diameters: (i) Although FCS does not need a size standard, the focal volume has to be calibrated for each set of measurements with a dye molecule of known diffusion constant and thus known hydrodynamic diameter. Each error of the calibration is propagated to the results of the following measurements. (ii) In contrast to organic fluorophores, colloidal quantum dots exhibit no exponential triplet state decay but rather blinking behavior on all time-scales, which influences the recorded florescence intensity time traces. To our knowledge, so far, no analytical expression has been derived to account for this fact.[11,41,42]

Thermophoresis. The values obtained by thermophoresis increase as expected with the molecular weight of the covalently coupled PEG molecules. The method measures the mean diffusion coefficients of the whole ensemble. Species without or with less surface modification would, in principle, lead to a higher overall diffusion coefficient and smaller radius, respectively. The sizes obtained for nanoparticles saturated with PEG molecules are listed in Table 2, and a typical experiment is shown in Figure 4. In contrast to gel electrophoresis and SEC, no calibration curve of size standards needed to be used for obtaining the effective diameters. Although thermophoresis, like FCS, is based on obtaining effective diameters by measuring the diffusion of the dispersed particles, the values obtained with both methods differ significantly (see Table 2). The standard deviation in the measurements between similar samples is in the same range as that with FCS (polymer-coated CdSe/ZnS with no PEG: $<d_{eff,Therm}>$ = <8.2 nm, 12.2 nm> = 10.2 ± 2.8 nm; see last column of Table 2; the deviations within one method are attributed to variations in the sample, e.g., due to differences in the gel extraction procedure). The difference in the effective diameter of about a factor of 2 ($<d_{eff,Therm}> \approx$ 10 nm; $<d_{eff,FCS}> \approx$ 22 nm) for plain polymer-coated nanoparticles as determined with thermophoresis and FCS can

TABLE 5: Polymer-Coated Au and CdSe/ZnSe Nanoparticles Coated with Saturated Layers of PEG Molecules of Different Molecular Weight M_w[a]

M_w (PEG) [g/mol]	$<d_{eff}>_{SEC}$ [nm] Au core	$<d_{eff}>_{SEC}$ [nm] CdSe/ZnS core	$<d_{eff}>_{FCS}$ [nm] CdSe/ZnS core	$<d_{eff}>_{Therm}$ [nm] CdSe/ZnS core	$1/2\Delta d_{eff,SEC}$ [nm] Au core	$1/2\Delta d_{eff,SEC}$ [nm] CdSe/ZnS core	$1/2\Delta d_{eff,FCS}$ [nm] CdSe/ZnS core	$1/2\Delta d_{eff,Therm}$ [nm] Au core	$1/2<\Delta d_{eff}>$ [nm]	$d_{eff,PEG}$ [nm]
0	11.1s	12.6	19.4	12.2						
750	12.5	14.6	25.4	22.0	0.7	1.0	3.0	4.9	2.4 ± 2.0	1.5
2000	16.5	18. 3	25.6	23.6	2.7	2.9	3.1	5.7	3.6 ± 1.4	2.7
5000	21.0	23.9	27.6	25.0	5.0	5.7	4.1	6.4	5.3 ± 1.0	4.5
10000	28.8	26.2	30.2	30.0	8.9	6.8	5.4	8.9	7.5 ± 1.7	6.6
20000	34.8	34.8	34.2	40.0	11.9	11.1	7.4	13.9	11.1 ± 2.7	9.7

[a] The first line hereby corresponds to plain polymer-coated nanoparticles without PEG modification. In columns 2−5, the mean effective diameters $<d_{eff}>$ of the particles as determined with different methods are listed. These values originate from the data in Tables 2 and 3. The thickness of the PEG layers of different molecular weight around polymer-coated particles are derived as half of the difference of the total diameters of PEG-coated and the plain polymer-coated particles: $1/2\Delta d_{eff}(M_w(PEG) = X) = (<d_{eff}(M_w(PEG) = X)> - <d_{eff}(M_w(PEG) = 0)>)/2$. These values are listed in columns 6−9. In column 10, the mean thickness of the PEG layers (as the average value of the different methods) $1/2\Delta d_{eff}$ is given. The last column shows the diameters of free PEG molecules as calculated with Formula 3.[55]

therefore not be explained by the resolution limit due to sample variations (≈ 3 nm) of both methods. Although we cannot explain the origin of this discrepancy, we speculate that it might arise from the different particle concentrations used for the measurements. Whereas FCS is a single-molecule-based method and thus requires extremely diluted particle solutions, thermophoresis is an ensemble-based method, and typically more concentrated particle solutions are used in order to obtain signals with sufficient intensity. Particle−particle interaction plays a different role under both conditions. Also the statistical effect of a certain amount of aggregated particles is different. We estimate the relative concentration of aggregates to contribute less than linearly to the diffusion coefficient measured by thermophoresis, since larger particles are depleted more strongly and the back diffusion is slower. Thus, the measured signal stems mostly from single-particle diffusion. The role of particle interactions will be analyzed in future experiments under optimized conditions with particle concentrations of less than 10 nM. This would allow direct comparison with FCS experiments. The values obtained with SEC in ensemble measurements of relatively concentrated particle solutions for plain polymer-coated particles correspond more to the values obtained with thermophoresis than those obtained with FCS, which also gives some indication about the importance of the particle concentration used for the measurements.

Thickness of Organic Coating Layers. In the following, we focus on the polymer-coated particles according to our own procedure (Tables 2 and 3). The mean value of all our different methods for the effective diameters of polymer-coated CdSe/ZnS is $<d_{eff,gel}, (d_{eff,FCS}), d_{eff,SEC}, d_{eff,Therm}> = <14.4, 12.6, (19.5), 12.2> = 13.1 \pm 1.2$ nm (14.7 ± 3.4 nm with the value obtained with FCS), and, for Au nanoparticles, it is $<d_{eff,gel}, d_{eff,SEC}, d_{eff,Therm}> = <12.5, 11.6> = 12.0 \pm 0.6$ nm. The hard core diameter as determined by TEM is 5.3 nm for CdSe/ZnS and 4.6 nm for the Au nanoparticles. This leads to an effective thickness of the organic shell of (13.1 − 5.3) nm/2 = 3.9 nm in the case of CdSe/ZnS and (12.0 − 4.6) nm/2 = 3.7 nm in the case of Au. Besides the values obtained with FCS, the values derived with the other techniques correspond well, and we conclude that, after polymer coating, the effective thickness of the organic layer around the inorganic particle core is around 3.5−4.0 nm. Whereas this value for the plain polymer-coated particles seems quite reliable, the uncertainties in absolute size determination get higher the larger the molecules attached to the polymer shell. The addition of a saturated layer of 20 kDa PEG molecules to the polymer surface increases the thickness of the organic layer by $<\Delta d_{eff,gel}, \Delta d_{eff,FCS}, \Delta d_{eff,SEC}>/2 = <$(34.8 − 12.6), (34.2 − 19.4), (40.0 − 12.2)>nm/2 = 10.8 ± 3.3 nm in the case of the CdSe/ZnS particles.

In Table 5, the thickness of the saturated layer of the PEG molecules bound to the particle surface is compared with the effective diameter of free PEG molecules as determined by Formula 3, whereby the thickness of the PEG layer was calculated as half of the difference in diameter of the PEG-coated and plain polymer-coated particles. All obtained values for the PEG molecules bound to the nanoparticles are slightly larger than those of free PEG molecules. This finding can be explained by a more stretched configuration of the random coil of the PEG molecules when they are attached by one end to the densely occupied surface of a saturated nanoparticle, compared to the presumably more symmetric configuration of PEG molecules in free solution. In any case, the agreement demonstrates that relative increments in particle size can be determined with much higher accuracy than absolute diameters.

Conclusions

The total particle diameter can be estimated by the core diameter plus 2 times the thickness of the organic layer, which is, for simple coatings, the length of the surfactant molecule. While this eventually works well for short molecules when the length of these molecules is small compared to the particle, it becomes more complicated for longer and more complex molecules or even complex polymer (multi)layers. Here the size depends strongly on assumptions about the steric configuration of the molecules on the curved nanoparticle surface. Furthermore, the effective hydrodynamic diameter also depends on hydration: interaction of the particles with the solvent results in larger effective sizes,[57] even in the most simple case where the stabilizer molecules form a monolayer around the inorganic core. Although several studies exist in which the effective diameters of particles have been measured, most of these studies are either based on only one method or only one type of particle surface.[24,58,59] A more detailed discussion can be found in the Supporting Information.

The more molecules are attached and thus the bigger the particles become, the more unreliable size measurements are. First, the hybrid nature of the particles with a rigid inner inorganic core and a soft organic shell becomes more pronounced, which eventually leads to problems for the methods in which the measurements take place in a matrix that can compress the particles. Especially, a random coil of a linear polymer such as PEG can be easily deformed depending on the technique used for the size determination. Second, for the

methods using calibration with size standards, there is the problem of a lack of appropriate size standards of sufficient size. Third, the charge composition can also change (in particular, if positively charged molecules are attached), which leads to the failure of gel electrophoresis but might also affect the other methods.

Thus, depending on the actual particle nature but also on the intended application, the adequate method for measurement has to be chosen with great care. For instance the measurement of the diffusive radius does not seem to be appropriate when particles are designed to enter into pores. In this case, the determination of the diameter by gel electrophoresis or SEC seems to be better suited.

Different methods to measure effective sizes of colloidal nanoparticles are based on different physical principles, resulting in deviations of the resulting particle diameters between the different methods. This finding is not surprising and points to a general problem and uncertainty: although within one measurement effective diameters can be determined in a consistent way with relatively small errors, bigger discrepancies arise between values obtained with different methods. This implies that the comparison with control samples (e.g., before and after a certain conjugation step) remains indispensable and that all derived absolute numbers for nanoparticle diameters have to be considered with care.

Acknowledgment. The authors would like to thank Andrea Rauh for help with the analysis of the TEM images and Dr. Fritz Simmel and Prof. Dr. Joachim Rädler for helpful discussion. The authors are grateful to Prof. Dr. Joachim Rädler for using the FCS setup and expertise of his institute. Quantum dots with organic and streptavidin coating were a gift from Quantum Dots Corp. The project was funded by the Deutsche Forschungsgemeinschaft (DFG Emmy Noether Grant) and the European Union (STREP NanoInteract grant). M.Z. is grateful for a fellowship from the International Doctorate Program Nano-Bio-Technology at the Center for Nanoscience.

Supporting Information Available: Details of particle synthesis, TEM analysis, gel electrophoresis, SEC, FCS, and thermophoresis experiments, and a comparison of the different methods. This material is available free of charge via the Internet at http://pubs.acs.org.

References and Notes

(1) Scher, E. C.; Manna, L.; Alivisatos, A. P. *Philos. Trans. R. Soc. London, Ser. A* **2002**, *361*, 241.
(2) Kumar, S.; Nann, T. *Small* **2006**, *2*, 316.
(3) Kudera, S.; Carbone, L.; Zanella, M.; Cingolani, R.; Parak, W. J.; Manna, L. *Phys. Status Solidi C* **2006**, *203*, 1329.
(4) Templeton, A. C.; Wuelfing, W. P.; Murray, R. W. *Acc. Chem. Res.* **2000**, *33*, 27.
(5) Michalet, X.; Pinaud, F. F.; Bentolila, L. A.; Tsay, J. M.; Doose, S.; Li, J. J.; Sundaresan, G.; Wu, A. M.; Gambhir, S. S.; Weiss, S. *Science* **2005**, *307*, 538.
(6) Pellegrino, T.; Kudera, S.; Liedl, T.; Javier, A. M.; Manna, L.; Parak, W. J. *Small* **2005**, *1*, 48.
(7) Fischer, C.-H.; Lilie, J.; Weller, H.; Katsikas, L.; Henglein, A. *Ber. Bunsen-Ges. Phys. Chem.* **1989**, *93*, 61.
(8) Fischer, C.-H.; Weller, H.; Katsikas, L.; Henglein, A. *Langmuir* **1989**, *5*, 429.
(9) Eychmüller, A.; Katsikas, L.; Weller, H. *Langmuir* **1990**, *6*, 1605.
(10) Wu, M. X.; Liu, H.; Liu, J.; Haley, K. N.; Treadway, J. A.; Larson, J. P.; Ge, N.; Peale, F.; Bruchez, M. P. *Nat. Biotechnol.* **2003**, *21*, 41.
(11) Pellegrino, T.; Manna, L.; Kudera, S.; Liedl, T.; Koktysh, D.; Rogach, A. L.; Keller, S.; Rädler, J.; Natile, G.; Parak, W. J. *Nano Lett.* **2004**, *4*, 703.
(12) Luccardini, C.; Tribet, C.; Vial, F.; Marchi-Artzner, V.; Dahan, M. *Langmuir* **2006**, *22*, 2304.
(13) Nann, T. *Chem. Commun.* **2005**, *2005*, 1735.
(14) Sperling, R. A.; Pellegrino, T.; Li, J. K.; Chang, W. H.; Parak, W. J. *Adv. Funct. Mater.* **2006**, *16*, 943.
(15) Zanchet, D.; Moreno, M. S.; Ugarte, D. *Phys. Rev. Lett.* **1999**, *82*, 5277.
(16) Fink, J.; Kiely, C. J.; Bethell, D.; Schiffrin, D. J. *Chem. Mater.* **1998**, *10*, 922.
(17) Yonezawa, T.; Onoue, S.-y.; Kimizuka, N. *Langmuir* **2001**, *17*, 2291.
(18) Zanchet, D.; Micheel, C. M.; Parak, W. J.; Gerion, D.; Alivisatos, A. P. *Nano Lett.* **2001**, *1*, 32.
(19) Parak, W. J.; Pellegrino, T.; Micheel, C. M.; Gerion, D.; Williams, S. C.; Alivisatos, A. P. *Nano Lett.* **2003**, *3*, 33.
(20) Pellegrino, T.; Sperling, R. A.; Alivisatos, A. P.; Parak, W. J. *J. Biomed. Biotechnol.*, submitted for publication, 2007.
(21) Pinaud, F.; King, D.; Moore, H.-P.; Weiss, S. *J. Am. Chem. Soc.* **2004**, *126*, 6115.
(22) Song, X.; Li, L.; Qian, H.; Fang, N.; Ren, J. *Electrophoresis* **2006**, *27*, 1341.
(23) Nehilla, B. J.; Vu, T. Q.; Desai, T. A. *J. Phys. Chem. B* **2005**, *109*, 20724.
(24) Pons, T.; Uyeda, H. T.; Medintz, I. L.; Mattoussi, H. *J. Phys. Chem. B* **2006**, *110*, 20308.
(25) Wilcoxon, J. P.; Provencio, P. P. *J. Phys. Chem. B* **2005**, *109*, 13461.
(26) Siebrands, T.; Giersig, M.; Mulvaney, P.; Fischer, C.-H. *Langmuir* **1993**, *9*, 2297.
(27) Fischer, C.-H.; Giersig, M.; Siebrands, T. *J. Chromatogr., A* **1994**, *670*, 89.
(28) Fischer, C.-H.; Kenndler, E. *J. Chromatogr., A* **1997**, *773*, 179.
(29) Wei, G.-T.; Liu, F.-K. *J. Chromatogr., A* **1999**, *836*, 253.
(30) Wei, G.-T.; Liu, F.-K.; Wang, C. R. C. *Anal. Chem.* **1999**, *71*, 2085.
(31) Jimenez, V. L.; Leopold, M. C.; Mazzitelli, C.; Jorgenson, J. W.; Murray, R. W. *Anal. Chem.* **2003**, *75*, 199.
(32) Al-Somali, A. M.; Krueger, K. M.; Falkner, J. C.; Colvin, V. L. *Anal. Chem.* **2004**, *76*, 5903.
(33) Krueger, K. M.; Al-Somali, A. M.; Falkner, J. C.; Colvin, V. L. *Anal. Chem.* **2005**, *77*, 3511.
(34) Kuga, S. *J. Chromatogr., A* **1981**, *206*, 449.
(35) Holtzhauer, M.; Rudolph, M. *J. Chromatogr., A* **1992**, *605*, 193.
(36) Magde, D.; Elson, E.; Webb, W. W. *Phys. Rev. Lett.* **1972**, *29*, 705.
(37) Eigen, M.; Rigler, R. *Proc. Natl. Acad. Sci. U.S.A.* **1994**, *91*, 5740.
(38) Schwille, P.; Bieschke, J.; Oehlenschläger, F. *Biophys. Chem.* **1997**, *66*, 211.
(39) Krichevsky, O.; Bonnet, G. *Rep. Prog. Phys.* **2002**, *65*, 251.
(40) Zhang, P.; Li, L.; Dong, C.; Qian, H.; Ren, J. *Anal. Chim. Acta* **2005**, *546*, 46.
(41) Liedl, T.; Keller, S.; Simmel, F. C.; Rädler, J. O.; Parak, W. J. *Small* **2005**, *1*, 997.
(42) Doose, S.; Tsay, J. M.; Pinaud, F.; Weiss, S. *Anal. Chem.* **2005**, *77*, 2235.
(43) Dong, C.; Bi, R.; Qian, H.; Li, L.; Ren, J. *Small* **2006**, *2*, 534.
(44) Jin, T.; Fujii, F.; Yamada, E.; Nodasaka, Y.; Kinjo, M. *J. Am. Chem. Soc.* **2006**, *128*, 9288.
(45) Duhr, S.; Arduini, S.; Braun, D. *Eur. Phys. J. E* **2004**, *15*, 277.
(46) Duhr, S.; Braun, D. *Phys. Rev. Lett.* **2006**, *96*, 168301.
(47) Duhr, S.; Braun, D. *Proc. Natl. Acad. Sci. U.S.A.* **2006**, *103*, 19678.
(48) Reiss, P.; Bleuse, J.; Pron, A. *Nano Lett.* **2002**, *2*, 781.
(49) Dabbousi, B. O.; Rodriguez-Viejo, J.; Mikulec, F. V.; Heine, J. R.; Mattoussi, H.; Ober, R.; Jensen, K. F.; Bawendi, M. G. *J. Phys. Chem. B* **1997**, *101*, 9463.
(50) Yu, W. W.; Qu, L.; Guo, W.; Peng, X. *Chem. Mater.* **2003**, *15*, 2854.
(51) Brust, M.; Walker, M.; Bethell, D.; Schiffrin, D. J.; Whyman, R. *J. Chem. Soc., Chem. Commun.* **1994**, 801.
(52) Mori, S.; Barth, H. G. *Size Exclusion Chromatography*; Springer: New York, 1999.
(53) Hagel, L. Gel Filtration. In *Protein Purification. Principles, High Resolution Methods and Applications*, 2nd ed.; Janson, J.-C., Ryden, L., Eds.; John Wiley & Sons: New York, 1998.
(54) Amediek, A.; Haustein, E.; Scherfeld, D.; Schwille, P. *Single Mol.* **2002**, *3*, 201.
(55) Fee, C. J.; Alstine, J. M. V. *Bioconjugate Chem.* **2004**, *15*, 1304.
(56) Sartori, R.; Sepulveda, L.; Quina, F.; Lissi, E.; Abuin, E. *Macromolecules* **1990**, *23*, 3878.
(57) Xu, X.; Rosi, N. L.; Wang, Y.; Huo, F.; Mirkin, C. A. *J. Am. Chem. Soc.* **2006**, *128*, 9286.
(58) Smith, A. M.; Duan, H.; Rhyner, M. N.; Ruan, G.; Nie, S. *Phys. Chem. Chem. Phys.* **2006**, *8*, 3895.
(59) Yu, W. W.; Chang, E.; Falkner, J. C.; Zhang, J.; Al-Somali, A. M.; Sayes, C. M.; Johns, J.; Drezek, R.; Colvin, V. L. *J. Am. Chem. Soc.* **2007**, *129*, 2871.

Publikation IX: Extreme Accumulation of Nucleotides in Simulated Hydrothermal Pore Systems, **PNAS, 104, 9346–9351 (2007)**, Philipp Baaske, Franz M. Weinert, Stefan Duhr, Kono Lemke, Michael J. Russel and Dieter Braun, (2007)

PNAS

Extreme accumulation of nucleotides in simulated hydrothermal pore systems

Philipp Baaske*, Franz M. Weinert*, Stefan Duhr*, Kono H. Lemke†, Michael J. Russell‡, and Dieter Braun*§

*Biophysics Department, Ludwig-Maximilians Universität München, Amalienstrasse 54, 80799 München, Germany; †Geochemistry Group, Institute for Mineralogy and Petrology, Swiss Federal Institute of Technology, ETH-Zürich, 8092 Zürich, Switzerland; and ‡Jet Propulsion Laboratory, California Institute of Technology, Pasadena, CA 91125

Edited by Howard Brenner, Massachusetts Institute of Technology, Cambridge, MA, and approved March 9, 2007 (received for review October 28, 2

We simulate molecular transport in elongated hydrothermal pore systems influenced by a thermal gradient. We find extreme accumulation of molecules in a wide variety of plugged pores. The mechanism is able to provide highly concentrated single nucleotides, suitable for operations of an RNA world at the origin of life. It is driven solely by the thermal gradient across a pore. On the one hand, the fluid is shuttled by thermal convection along the pore, whereas on the other hand, the molecules drift across the pore, driven by thermodiffusion. As a result, millimeter-sized pores accumulate even single nucleotides more than 10^8-fold into micrometer-sized regions. The enhanced concentration of molecules is found in the bulk water near the closed bottom end of the pore. Because the accumulation depends exponentially on the pore length and temperature difference, it is considerably robust with respect to changes in the cleft geometry and the molecular dimensions. Whereas thin pores can concentrate only long polynucleotides, thicker pores accumulate short and long polynucleotides equally well and allow various molecular compositions. This setting also provides a temperature oscillation, shown previously to exponentially replicate DNA in the protein-assisted PCR. Our results indicate that, for life to evolve, complicated active membrane transport is not required for the initial steps. We find that interlinked mineral pores in a thermal gradient provide a compelling high-concentration starting point for the molecular evolution of life.

concentration problem | hydrothermal vents | molecular evolution | origin of life problem | RNA world

Starting with Miller and Urey (1), a wide range of studies on the origin of life discuss the chemical synthesis of protobiomolecules (2–4). Concurrently, the studies of replication systems (5–8) culminated in the RNA-world proposal (9). All these approaches require fairly high concentrations of small proto-biotic molecules, whereas geochemical extrapolations indicate a dilute prebiotic ocean with concentrations comparable to contemporary values (10, 11). This discrepancy has been termed the concentration problem of the origin of life (10, 12). In the following, we describe a robust and efficient solution to the concentration problem, based on heat currents in porous mineral precipitates comprising a hydrothermal mound developed over a moderately warm submarine spring.

Living cells are crowded with small molecules which are accumulated as a result of highly evolved active transport mechanisms across the cell membrane (13). A comparably effective transport mechanism is required to solve the concentration problem of the origin of life. However, to accumulate molecules from a highly diluted prebiotic ocean (10, 11), a considerable entropic gap has to be bridged. In a rough estimate, at least a 10^6-fold accumulation is required for small protobiomolecules to interact. To fulfill the second law of thermodynamics, such states of exceedingly low entropies can only be siphoned from a larger nonequilibrium system. Contemporary life sustains the required high molecular concentration in a dissipative nonequilibrium state by a wide range of highly evolved strategies. For the evolution of life, an already existing protobiological dissipative environment is required (14). The most compelling would refer to an accumulation of molecules into preexisting abundant compartments of cellular dimensions (15). Both requirements are fulfilled by the accumulation mechanism we propose here.

Hydrothermal Setting

From a geological point of view, thermal gradients are the most abundant dissipative systems on the early earth. They drive convective water flow with a wide variety of geometries. Contemporary hydrothermal vents, both black smokers and "Lost City" type vents, are only extreme cases for heat dissipation. Hydrothermal vents are surrounded by highly porous mineral precipitates. Within these structures, we consider the ubiquitous millimeter to micrometer sized pores and syneresis cracks (Fig. 1*a*). A temperature gradient, typically along the horizontal direction, exists across such pore systems. We show that these natural settings can easily accumulate single nucleotides $>10^8$-fold at the bottom of a plugged pore system. Thus, this accumulation is sufficient to step up from the dilute hydrothermal solution to molar concentrations within the pore.

It is well known that probiotic reactions can be envisaged to foster molecular evolution and favor synthesis over hydrolysis only when concentrations are sufficiently high (16). Submarine hydrothermal environments were previously envisaged as potential sites for the emergence of life, partly because of their contemporary habitability and partly because essential basic materials can be found in such environments (14, 15, 17–20). The concentration mechanism described here considerably strengthens the scenario for a hydrothermal emergence of life.

Robust Exponential Accumulation

The mechanism of accumulation operates as follows. In a hydrothermal vent a plugged pore system is sandwiched between the hot vent interior and the cooling outside ocean (Fig. 1*b*). A temperature gradient across the pore drives two entangled processes: (*i*) molecules are shuttled up and down the cleft by laminar thermal convection and (*ii*) thermophoresis drives the molecules along the temperature gradient, i.e., perpendicular to the convection flow. Both processes are indicated by white arrows in Fig. 1*c*. In combination, they lead to a strong vertical accumulation toward the closed bottom of the cleft. This geological setting is analogous to a Clusius-tube or thermogravitational column (21). We simulate the behavior of rather rapidly diffusing single nucleotides. Even with conventional biotechnological or microfluidic laboratory methods, such small molecules

Author contributions: D.B. designed research; P.B., F.M.W., and S.D. performed research; P.B., F.M.W., S.D., K.H.L., M.J.R., and D.B. analyzed data; and P.B., K.H.L., M.J.R., and D.B. wrote the paper.

The authors declare no conflict of interest.

This article is a PNAS Direct Submission.

§To whom correspondence should be addressed. E-mail: dieter.braun@physik.lmu.de.

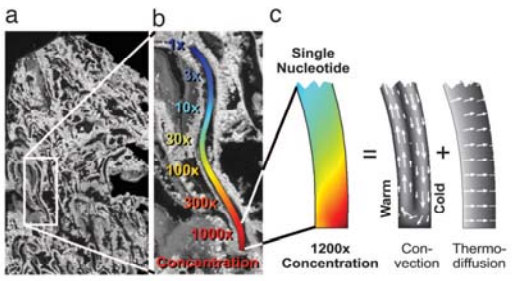

Fig. 1. Heat-driven molecular accumulation in hydrothermal pores. (*a*) Section through aragonite ($CaCO_3$) from the submarine hydrothermal vent field at Lost City (kindly provided by D. Kelley; ref. 20). (*b*) Simulation of a part of the pore system. If subjected to a horizontal thermal gradient of 30 K, a 1,200-fold accumulation of single nucleotides is expected (logarithmic concentration color scale). A concatenation of three of these pore sections leads to a 10^9-fold accumulation. (*c*) The mechanism of accumulation is driven by heat in a twofold way. Thermal convection shuttles the molecules vertically up and down and thermophoresis pushes the molecules horizontally to the right. The result is a strong molecular accumulation from the top to the bottom (linear concentration color scale).

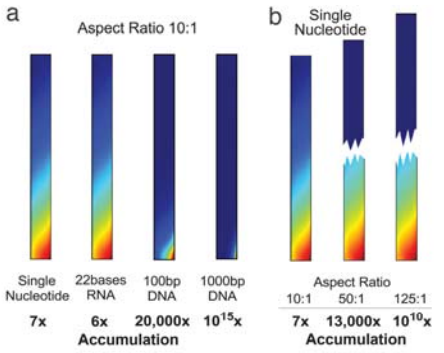

Fig. 2. Predicted effects of the molecule size and pore length on the accumulation level. The simulation results are based on the experimentally measured Soret coefficients and diffusion coefficients for DNA and RNA (see Table 1). (*a*) The accumulation increases exponentially with the size of the molecule. Whereas single nucleotides are accumulated 7-fold in a short cleft of aspect ratio 10:1, double-stranded DNA comprising 1,000 base pairs accumulates 10^{15}-fold. The equilibration takes 9 min for single nucleotides and 14 min for single stranded RNA comprising 22 bases. For DNA polynucleotides of 100 and 1,000 bp it takes 18 or 33 min, respectively. (*b*) Elongation of the cleft exponentially increases the accumulation. For example, the accumulation of single nucleotides is raised to a 10^{10}-fold level in a pore with an aspect ratio of 125:1. A linear concentration scale is used in both plots, scaled to the respective maximal concentration. The time to reach steady state is 9 min for $r = 10$, 4 h for $r = 50$ and 23 h for $r = 125$.

are hard to concentrate because of their considerable diffusion. The simulation shows a strong 1,200-fold downward accumulation of single nucleotides for the 5 mm short, bent cleft of Fig. 1*b*. As we will see later, a concatenation of three of these pores leads to a $1{,}200^3 = 1.7 \times 10^9$-fold accumulation.

We applied a 30 K temperature difference across the pore and found that maximal accumulation occurred in a pore with a cross-section of 145 μm. The diffusion of molecules in the convection flow was calculated by solving the combined Navier–Stokes, diffusion and heat transfer equations using commercial finite element software (Femlab, Comsol). The simulated pores feature a closed bottom and an open top end. The biomolecule concentration was fixed at the top, whereas the bulk fluid was subjected to gravity and restricted by the pore with nonslip boundary conditions. The heat transfer is barely affected by the slow laminar convection, and the temperature drops linearly across the pore structure.

Previously, we measured the thermophoretic characteristics of nucleotides using microfluidic fluorescence techniques (22). Molecules move along a thermal gradient ∇T with a drift velocity $v = -D_T \nabla T$. The ratio between the thermodiffusion coefficient D_T and the mass diffusion coefficent D is termed the Soret coefficient $S_T = D_T/D$, which typically determines the steady state concentrations. The values for single nucleotides are measured by using the fluorescent molecule 2′,7′-bis(carboxyethyl)-5 (6)-carboxyfluorescein (BCECF) in a 1 mM Tris buffer. BCECF and single nucleotides are of comparable size and charge. We also obtained S_T values for single stranded RNA of 22 bases in sodium chloride-sodium citrate-buffer with a monovalent salt concentration of 1.7 mM as well as double-stranded DNA of 100 and 1,000 bp in 1 mM Tris buffer. All measurements are performed at pH 7.8. In the experiments, the Soret coefficient S_T changes only by a factor of about three when the concentration of monovalent salt is increased from 1.7 to 170 mM. The Soret coefficient of a single nucleotide is comparable to the considerably larger single-stranded RNA of 22 bases. This is typical for thermodiffusion of charged particles smaller than the debye length and is due to reduced ionic shielding (22). Notably, single stranded RNA with 22 bases shows an ≈3-fold smaller thermodiffusion than single-stranded DNA of the same length. The experimental results are presented in Table 1.

A short pore with an aspect ratio of 10:1 accumulates single nucleotides 7-fold (Fig. 2*a*). A pore with the same aspect ratio accumulates a 22-bases-long single-stranded RNA to 6-fold, a 100-bases-long double-stranded DNA to 20,000-fold, and a 1,000-bases-long DNA to 10^{15}-fold levels. For these larger molecules, the short pore behaves like a molecule trap: once molecules enter the top of the pore, they are transported to the pore base and are accumulated to molar-level concentrations in a micrometer-sized spot in bulk water. As a result, the accumulated molecules diffuse freely and would find chemical reaction partners comparable to the situation within prokaryotic cells (13).

Pertinent to our argument is the fact that accumulation grows exponentially both with the size of the molecule and the length of a concatenated pore system. In concatenated pores accumulation of molecules increases exponentially, a result of the considerable concentration independence of thermophoresis below molar concentrations (23–25). Thus, although single nucleotides accumulate merely 7-fold in the short pore of Fig. 2*a*,

Table 1. Soret coefficient (S_T) and diffusion coefficient (D) for different molecules

Coefficient	Single nucleotide	ssRNA, 22 bases	ssDNA, 22 bases	dsDNA, 100 bp	dsDNA, 1,000 bp
S_T 1.7 mM salt, per K	0.015	0.014	0.044	0.075	0.3
S_T 170 mM salt, per K	0.006	0.003	0.01	0.019	0.09
D, $\mu m^2/s$	400	100	115	45	8

Table 2. Predicted accumulation depends on the type of molecule and pore aspect ratio

Aspect ratio	Single nucleotide	ssRNA 22 bases	dsDNA 100 bp	dsDNA 1,000 bp
10:1	7	6	2×10^4	10^{15}
25:1	120	89	10^{10}	(10^{37})
50:1	13,000	8,000	(10^{21})	(10^{75})
125:1	10^{10}	6×10^9	(10^{52})	(10^{187})

Accumulation levels that cannot be reached because of steric hindrance are denoted in brackets.

concatenating 12 of these pores using a wide variety of orientation angles exponentiate the accumulation to an extreme $7^{12} = 10^{10}$-fold level. Elongation of the pore has exactly the same effect. As shown in Fig. 2*b*, a pore system with a total aspect ratio of $r = 125{:}1$ accumulates single nucleotides 10^{10}-fold. Notably, the length of this pore system is only 18 mm, below the typical lengths of pore systems in hydrothermal settings. A compilation of the simulated accumulation values is given in Table 2.

The analytical solution for the accumulation in a rectangular cleft geometry confirms the above numerical findings. The analytical theory (26, 27) was originally developed for gas separation columns (21). The accumulation is found to be an exponential function given by

$$\frac{c_{\mathrm{BOTTOM}}}{c_{\mathrm{TOP}}} = \exp[0.42 \times S_{\mathrm{T}} \times \Delta T \times r] \qquad [1]$$

with the Soret coefficient S_{T}, the temperature difference ΔT and the aspect ratio r. For $0.42 \times S_{\mathrm{T}} \times \Delta T \times r \gg 1$, the molecular accumulation is large and rises exponentially with temperature difference ΔT or pore length. In pores with a sufficient aspect ratio r, substantial accumulation is reached even for small molecules with tiny Soret coefficients (Table 1). The exponential characteristic of Eq. **1** makes the accumulation robust because a small elongation of the pore leads to a large increase in molecular accumulation. Every linear decrease in the temperature difference ΔT can be compensated by a linear increase in pore aspect ratio r. For example, to achieve the same accumulation at just one tenth of the temperature difference, a 10-fold longer pore is needed. To illustrate this the accumulation versus the aspect ratio, r is plotted in Fig. 3 for single nucleotides, polynucleotides of 22 single stranded RNA bases, and double-stranded DNA comprising 100 and 1,000 base pairs.

The accumulation is highly robust with respect to the changes in the geometry of the pore. Fig. 4*a* shows various geometries that yield equal accumulations. We start with a rectangular pore with an aspect ratio of $r = 10{:}1$. The accumulation remains at the same level even if the pore is heavily dented, bent, incised, opened toward a bottom molecule repository, or strongly inclined. This insensitivity to geometric variation has two main reasons. First, mass diffusion bridges regions with inferior accumulation. This diffusion between the pores does not require any special geometries between the pore sections. Second, the slowing down of convection resulting from a tilt of the pore section can be easily compensated by a small increase in the pore width, because of the exponent 1/3 in Eq. **2**. For example, a tilt from 90° (vertical) to 1° (basically horizontal) enlarges the optimal cleft width only by a factor of four. Therefore, a wide variety of pore systems accumulate molecules with equal efficiency.

So far, we have discussed only two-dimensional pores with cleft-like geometries. We simulated the cross-section and assumed that the pore extends considerably further into the third dimension. However, equal accumulation is also found for pores

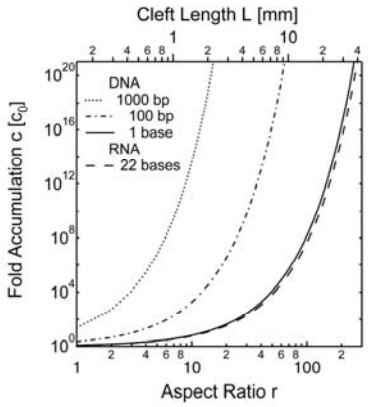

Fig. 3. Exponential accumulation. The accumulation depends exponentially on the aspect ratio r and the temperature difference ΔT, according to the analytical theory (Eq. **1**). Even for single nucleotides, it is remarkably easy to reach exceedingly large molecular accumulations. The accumulation is calculated for $\Delta T = 30$ K.

with only limited extension in the third dimension. Fig. 4*b* shows results for various pore cross-sections with comparable accumulation levels. Also, molecular accumulation is not seen to be significantly lowered over a variety of depths. As noted before, all of the geometries shown in Fig. 4 can be concatenated ad libitum, yielding a wide range of pore system geometries that are capable of an efficient molecular accumulation.

A critical parameter is the width of the pore. For an extended rectangular cleft (26, 27), the largest accumulation is found for an optimal width d_0 given by

$$d_0 = 8.4 \times (\mu D/\alpha\rho g_0 \Delta T \sin\Theta)^{1/3} \qquad [2]$$

with the viscosity of the fluid μ, the diffusion coefficient of the molecule D, the fluid volume expansion coefficient α, the fluid density ρ, the gravitational acceleration g_0, the inclination angle Θ to the horizontal plane, and the temperature difference ΔT. As the result of the exponent 1/3 in Eq. **2**, values for d_0 fall between

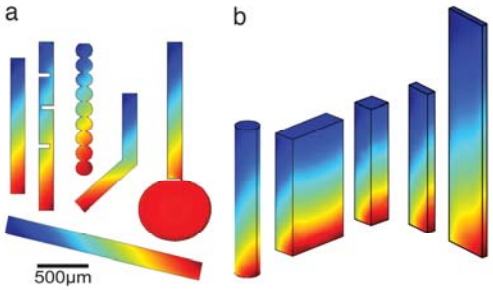

Fig. 4. Robustness of the accumulation. (*a*) Equally efficient accumulation is found for a large variety of geometries. Regions of reduced accumulation are bridged vertically by mass diffusion. Strongly inclined pores accumulate molecules equally well. A linear concentration scale is used in both plots. (*b*) Likewise, a wide range of pore cross-sections yields identical accumulations. As for two dimensional clefts, optimal accumulation is achieved if the convection speed balances the diffusion time across the pore.

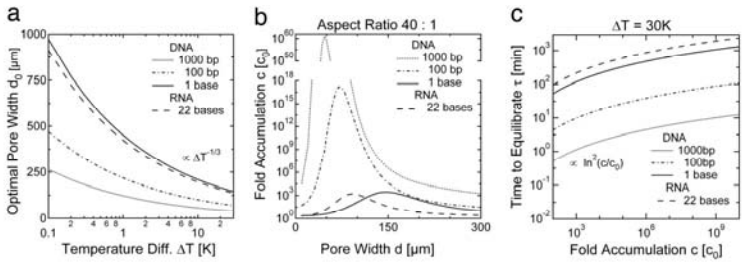

Fig. 5. Pore width and equilibration time. (*a*) The optimal cleft width depends moderately on the molecular size and temperature difference. The optimal cleft width is proportional to $D^{1/3}$ and $\Delta T^{-1/3}$ with the diffusion coefficient D and temperature difference ΔT. As a result, much longer nucleotides require only slightly narrower pores. (*b*) Accumulation drops considerably for pores with a nonoptimal width. Nucleotides are selectively accumulated in particularly narrow chambers. For a wider pore width $d \approx 150$ μm, the accumulation of molecules with different sizes reaches comparable levels. (*c*) The equilibration toward a 10^8-fold accumulation takes 14 h for single nucleotides and 25 h for single-stranded RNA comprising 22 bases. For DNA polynucleotides of 100 and 1,000 bp. it takes 70 or 8 min, respectively. This might be counterintuitive, but larger molecules accumulate faster because a considerably shorter cleft is sufficient to achieve the same level of accumulation.

40 and 400 μm for an extensive range of parameters D, Θ, and ΔT, as shown in Fig. 5*a*.

Fig. 5*b* illustrates the pore size dependence of the accumulation in more detail. DNA molecules of different length are selectively partitioned depending on the pore width. For an equivalent value of ΔT (30 K), single nucleotides accumulate best for a pore width of 145 μm, whereas a 1,000-bp DNA fragment accumulates best for a width of 40 μm. Therefore, the geometry determines the size of the preferentially accumulated molecules. On the other hand, the accumulation of longer polynucleotides is much more efficient, and pore widths $\approx$150 μm accumulate a wide range of different DNA lengths equally well. Monomers and polymers accumulate to similar levels under all these various pore conditions (Fig. 5*b*).

The time τ to reach a steady state concentration profile is given by the diffusion time along the pore

$$\tau = r^2 d_0^2 / \pi^2 D. \qquad [3]$$

As a result, a 10^8-fold accumulation of single nucleotides is achieved after $\tau = 14$ h, and for a 22-base single-stranded RNA, a 10^8-fold accumulation is achieved after $\tau = 25$ h. However, the time to reach a comparable accumulation for larger molecules drops to 70 min for 100-bp DNA and 8 min for 1,000-bp DNA (Fig. 5*c*), the reason being the much shorter cleft length required for longer DNA.

Notably, all these times are extremely short compared with the lifetime of a typical vent chimney, or even the Lost City vent system, which operates at least for 30,000 years (20, 28).

We also tested the robustness of accumulation against diffusive leakage from the pore. In general, a leak of molecules into an attached closed pore space does not inhibit accumulation. An example is shown in Fig. 4*a*, where a large extension is filled to the same high concentration at the pore base. Only the equilibration time slightly increases as a result of such an extension of the pore. However, leaks into permeable chambers can reduce the accumulation, depending on the concentration gradient ∇c and the resulting diffusive molecular flux, $j = -D\nabla c$. The distance between the leak and the surrounding background concentration $c = 1$ is crucial. This distance is expected to be relatively large for a hydrothermal mound. To characterize the effects of diffusive leaks, we simulated a worst case scenario. A wide diffusive leak is placed at the base of a pore and is connected to the outside over a distance of the pore length itself (Fig. 6*a*). Otherwise the same geometrical condition as illustrated in Fig. 2a is used, namely an aspect ratio of $r = 10{:}1$ with an optimal width d_0. Thus, we effectively simulate a tube which is open to both sides. Compared with a nonleaking pore, the resulting accumulation is reduced from 7 to 3 for single nucleotides, from 6 to 2.6 for single-stranded RNA, from 20,000 to 2,000 for 100-bp DNA and from 10^{15} to 10^{13} for 1,000-bp DNA. These reductions in accumulation that stem from leakage are quite easily compensated for by extending the length of the pore. We conclude that, even if the pore leaks through diffusion, accumulation is maintained at a high level.

In addition to diffusion, slow water flow through pore leakages might hinder accumulation. We focus on an upward flow because this direction is most probable in a hydrothermal mound. We use the same geometry as before (see Fig. 6*a*), but now add an upward flow at the lower end of the leak. This flow is fed with molecules from the outside concentration of $c = 1$. Obviously, such an upward flow through the pore directly competes with the downward accumulation. The accumulation versus flow rate is plotted in Fig. 6*b*. For comparison, the typical convection flow inside the pore is on the 1–10 μm/s scale. Fig. 6*b* shows that the accumulation of single nucleotides is quite robust against the upflow, probably because of the rapid diffusion of these molecules. Slower diffusing molecules are more vulnerable to pore flow drift, as can be seen from Fig. 6*b*. For a 22-base single-

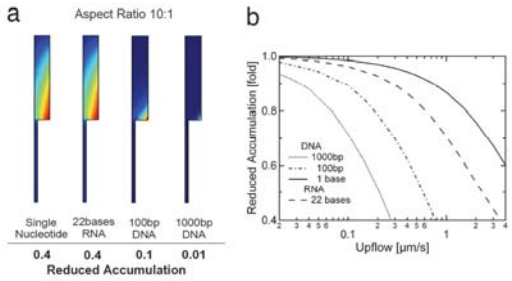

Fig. 6. Reduction of the accumulation by diffusive leakage and upflow. (*a*) A diffusive leak is introduced at the bottom of the pore over 1/5 of the pore width. The numbers beneath indicate the reduction of accumulation relative to the nonleaking pore in Fig. 2a. (*b*) Upflow is introduced into the cleft shown on the left side. For longer polynucleotides, the accumulation drops considerably faster with increasing upflow. Short molecules are less affected. The drop in accumulation for both diffusive leaks and upflow drift is readily compensated by a slight elongation of the pore.

stranded RNA, the accumulation drops by a factor of two for an upflow of ≈2.5 μm/s. For 100-bp DNA and 1,000-bp DNA, accumulation drops by the same factor for an upflow of 0.6 and 0.2 μm/s, respectively. These flow rates are comparable with the thermal convection speed in the pore. Flow rates in pores of hydrothermal mounds are hard to estimate but are probably slower than these values. As expected, strongest accumulation is found in pores that are well sealed at the bottom. According to our assessment, drift and diffusion in microscopic pore systems in hydrothermal precipitates do not, or only weakly, affect the proposed accumulation mechanism.

Discussion

We compare the assumptions on pore geometry with the geological record. As seen from the representative cross-section in Fig. 1*a*, an aspect ratio between 25 and 50 can be estimated for single elongated pore spaces in the mounds at the Lost City vent site (≈20–100 μm across and ≤1 mm long). Although, at Lost City, pore shapes may be governed by filamentous bacterial growth, chemical garden-like growth with even higher aspect ratios is likely to occur in comparable hydrothermal systems with moderate temperatures. For example, the 500-mm-long hydrothermal pyrite spires from the 352-million-year-old Tynagh zinc-lead sulfide deposit, Ireland, have central cavities that are ≈100 μm in diameter (aspect ratio $r \leq 5{,}000{:}1$) (ref. 29 and Fig. 3*b*). Similar structures have been realized in laboratory simulations (30). Thus, the projected extreme accumulation should be easily reached in natural settings. In any case, the accumulation is exponentiated when low aspect ratio clefts are interconnected. Note that pore concatenation is an especially interesting feature from a geological point of view. During hydrothermal dissolution pores enlarge, become more interconnected (i.e., the value of the aspect ratio increases), and can substantially promote the accumulation of molecules. Based on these results, and given the large number of clefts in any one of multitudinous submarine hydrothermal mounds on the early earth (29), the opportunities would have been manifold for a critical accumulation of organic monomers and polymers synthesized in the same milieu.

In the above calculations, we have assumed a temperature difference of $\Delta T = 30$ K. We anticipate that this is a realistic assumption, because temperature gradients are focused inside the clefts due to the considerably lower thermal conductivity of water (0.6 W/mK) as compared with the surrounding rock (>3 W/mK). The thermal conductivity measured for a hydrothermal pyrite–silica precipitate (31) is 14 W/mK, but the isolated pyrite and quartz minerals yield ≈20 W/mK and 3–4 W/mK, respectively, in laboratory tests (32). The resulting enhancement of the temperature gradient in the liquid part of the pores is 5- to 200-fold. Thus, to obtain the temperature difference of 30 K assumed in the above simulations, the required overall temperature gradient is of the order of 1–40 K/mm, well within reported values of ΔT for natural hydrothermal settings. However, focusing of the temperature gradient in the pores is not essential for the accumulation process. For lower thermal gradients, the same accumulation can be achieved if the pore system is elongated linearly for a decreased temperature difference.

The presented accumulation geometry surpasses previous approaches. Experiments with a circular, laser-heated geometry demonstrated that thermal convection could drive the DNA replicating PCR (33). In the same setting, we observed a considerable accumulation of long DNA (34). Although both of those experiments pointed toward the potential for convection to contribute to the emergence of life (35), no accumulation of short molecules was found or theoretically expected. We now know that this was due to the low aspect ratio of the chamber geometry ($r \approx 0.1$). The pore geometries studied here, however, demonstrate a strong accumulation of small molecules, such as single nucleotides, in a highly plausible geological setting on the early earth.

As we have seen, large molecules accumulate more efficiently. One may ask whether the strong accumulation of solvated organic molecules would lead to the tarring of the pore. This is not expected because thermophoretic coefficients become small for concentrations in the molar range (23–25). As a result, accumulation will level out at similar concentrations and will not lead to tarring. Also, a closing of the pore by microscopic solid particles is unlikely, based on our recent experimental findings (36). It was shown that, for low aspect ratio chambers ($r \approx 0.1$), 2-μm polystyrene spheres became highly concentrated, but still only formed two or three layers of a colloidal crystal. Further accumulation into the volume of the chamber was disrupted by flow interactions of the solid particles with the thermal convection current (36). As a result, convective flow itself is likely to prevent tarring of the pore by larger particles. On the other hand, a minor accumulation of sticky particles at the pore bottom could contribute to the sealing of the leaks (see Fig. 6). Moreover, in this process, any pore shortening would be negligible.

The mechanism provides concentrated molecules in bulk water without requiring molecules to adsorb onto surfaces. Surface-assisted accumulation is often thought to solve the concentration problem, either via drying or specific adsorption. However, biological systems complex enough to evolve a replicating machinery would most likely need to disconnect, at least temporarily, from such restricting adsorbing surfaces (37). During this desorption or wetting process, there is a high risk of losing the replicated molecules into the bulk water (38). In the present scenario, where they would simply be reaccumulated from the pore solution and the catalytic activity of surfaces can be efficiently used. Our approach has the advantage of offering an active concentration mechanism in an already existing, robust enclosure. Because thermophoretic drift is common for molecules, the accumulation scheme applies similarly to nucleic acids, amino acids, and lipids.

The described accumulation in semiclosed microscopic pores has several synergistic advantages that pertain to the molecular evolution of early life. The enclosure of pore space by mineral precipitates frees life from the need to build a semipermeable organic membrane in its very first evolutionary steps. Microbiological evidence indicates that membrane synthesis appears to be a rather late development (15, 18). Moreover, active transport across a membrane to accumulate molecules in a cell is well known to be a highly evolved process, requiring complex proteins to form vesicles and to actively pump molecules across the membrane.

Notably, the mineral pores that we propose as accumulation centers for the emergence of life are presently populated with thermophilic prokaryotes, and it is speculated that these sites could have been inhabited by the last common ancestor and its biochemical precursors (15, 39). Rapid thermal quenching was demonstrated to be able to polymerize both nucleic (40) and amino (16) acids in a setting in which hydrothermal fluids were injected into cooled (4°C) water. The discussed setting of thermal convection provides comparable temperature interfaces, but now within a single pore. Therefore, both the temperature drop and the needed molecule concentration could be found in an enclosure instead of an open flow reactor.

The water inside the pore network is permanently shuttled by laminar thermal convection. Molecules that stochastically escape the accumulation at the bottom of the pore by diffusion are subjected to a rapid periodic temperature variation within a wide range of temperature amplitudes and cycle times inside a single pore. Equally, freshly precipitated mesoscopic mineral grains are subjected to thermal cycling by the convection. Their catalytic surfaces might generate nucleic acid multimers by thermally triggered periodic condensation (4) and unbinding reactions. In

this context, we note that, in a comparable thermal convection setting, DNA was shown to replicate exponentially by using the, albeit protein-catalyzed, PCR (33, 41).

In conclusion, we propose a type of mechanism, driven solely by a temperature gradient, which strongly accumulates even small protobiological molecules in semiclosed hydrothermal pore systems. This setting provides a compelling, dissipative microenvironment to promote the first steps in the molecular evolution of life.

Materials and Methods

Combined solutions of the Navier-Stokes equation (velocity $\vec{u}$, pressure p, density ρ, viscosity η), molecule diffusion (concentration c, diffusion coefficient D), and heat transfer (temperature T, heat conductivity k) were simulated in two dimensions by a finite element solver (Comsol, Femlab). Cross terms induce the thermal convection with the expansion coefficient α and the gravitational acceleration g_0, trigger thermophoresis with the thermodiffusion coefficient D_T and consider the flow-induced heating with the heat capacity c_P. Boundary conditions were nonslip for $\vec{u}$, neutral for c except for fixing the concentration to $c = 1$ at the top opening of the column and a horizontal temperature difference of ΔT across the cleft. Material parameters were as follows: density of water 1,000 kg/m^3, viscosity 0.0012 ($N \times$ s)/m^2, heat capacity 4,200 J/(kg $\times$ K), heat conductivity 0.6 W/(m $\times$ K), volume expansion 3.2×10^{-4}, cold temperature 293 K, temperature difference 30 K, and gravitational acceleration 9.8 m/s^2. The temperature dependence of the above parameters is not significant in the simulations. The Femlab simulation files can be obtained from the authors.

We thank Ludmilla Mendelevitch for initial simulations and Hermann Gaub for hosting D.B.'s Emmy–Noether Nachwuchsgruppe, which was funded by the Deutsche Forschungsgemeinschaft. M.J.R.'s work was conducted at the Jet Propulsion Laboratory, California Institute of Technology, under contract with the National Aeronautics and Space Administration.

1. Miller SL (1953) *Science* 15:528–529.
2. Drobner E, Huber H, Wächtershäuser G, Rose D, Stetter KO (1990) *Nature* 346:742–744.
3. Zubay G (2000) *Origins of Life on the Earth and in the Cosmos* (Academic, New York), 2nd Ed.
4. Ferris JP (2002) *Origins Life Evol Biosph* 32:311–332.
5. Eigen M (1971) *Naturwissenschaften* 58:465–523.
6. Kuhn H (1976) *Naturwissenschaften* 63:68–80.
7. Sievers D, von Kiedrowski G (1994) *Nature* 369:221–224.
8. Joyce GF (1989) *Nature* 338:217–224.
9. Cech TR, Atkins JF, Gesteland RF, eds (2000) *The RNA World* (Cold Spring Harbor Lab Press, Plainview, NY).
10. Dose K (1975) *Biosystems* 6:224–228.
11. Mojzsis SJ, Harrison TM, Pidgeon RT (2001) *Nature* 409:178–181.
12. de Duve C (1991) *Blueprint for a Cell: The Nature and Origin of Life* (Neil Patterson, Burlington, NC).
13. Ellis RJ (2001) *Trends Biochem Sci* 26:597–604.
14. Corliss JB (1990) *Nature* 347:624.
15. Koonin EV, Martin W (2005) *Trends Genet* 21:647–654.
16. Imai E, Honda H, Hatori K, Brack A, Matsuno K (1999) *Science* 283:831–833.
17. Russell MJ, Hall AJ, Cairns-Smith AG, Braterman PS (1988) *Nature* 336:117.
18. Russell MJ, Hall AJ (1997) *J Geol Soc London* 154:377–402.
19. Nisbet EG, Sleep NH (2001) *Nature* 409:1083–1091.
20. Kelley DS et al (2001) *Nature* 412:145–149.
21. Clusius K, Dickel G (1938) *Naturwissenschaften* 26:546.
22. Duhr S, Braun D (2006) *Proc Natl Acad Sci USA* 103:19678–19682.
23. Duhr S, Arduini S, Braun D (2004) *Eur Phys J E* 15:277–286.
24. Piazza R, Iacopini S, Triulzi B (2004) *Phys Chem Chem Phys* 6:1616–1622.
25. de Gans BJ, Kita R, Wiegand S, Luettmer-Strathmann J (2003) *Phys Rev Lett* 91:245501.
26. Furry WH, Jones RC, Onsager L (1939) *Phys Rev* 55:1083–1095.
27. Debye P (1939) *Annalen der Physik* 36:284–294.
28. Kelley DS, Karson JA, Fruh-Green GL, Yoerger DR, Shank TM, Butterfield DA, Hayes JM, Schrenk MO, Olson EJ, Proskurowski G, *et al* (2005) *Science* 307:1428–1434.
29. Russell MJ, Hall AJ, Boyce AJ, Fallick AE (2005) *Econ Geol* 100:419–438.
30. Stone DA, Goldstein RE (2004) *Proc Natl Acad Sci USA* 101:11537–11541.
31. Rona PA, Davis EE, Ludwig RJ (1998) *Proc Ocean Drilling Prog Sci Results* 158:329–336.
32. Clauser C (2006) in *Landolt-Börnstein: Numerical Data and Functional Relationships*, ed Heinloth K (Springer, Heidelberg).
33. Braun D, Goddard NL, Libchaber A (2003) *Phys Rev Lett* 91:158103.
34. Braun D, Libchaber A (2002) *Phys Rev Lett* 89:188103.
35. Braun D, Libchaber A (2004) *Phys Biol* 1:1–8.
36. Duhr S, Braun D (2005) *Appl Phys Lett* 86:131921.
37. Duve CD, Miller SL (1991) *Proc Natl Acad Sci USA* 88:10014–10017.
38. Wächtershäuser G (1994) *Proc Natl Acad Sci USA* 91:4283–4287.
39. Martin W, Russell MJ (2003) *Philos Trans R Soc London B* 358:59–85.
40. Ogasawara H, Yoshida A, Imai E, Honda H, Hatori K, Matsuno K (2000) *Origins Life Evol Biosph* 30:519–526.
41. Krishnan M, Ugaz VM, Burns MA (2002) *Science* 298:793.

Publikation X: Melting Curve Analysis in a Snapshot, **Applied Physics Letters**, **in prep.**, Philipp Baaske, Stefan Duhr and Dieter Braun

Melting Curve Analysis in a Snapshot

Philipp Baaske,[1] Stefan Duhr,[1] and Dieter Braun[*]

Chair for Applied Physics, Ludwig-Maximilians-University,

Amalienstrasse 54, 80799 Munich, Germany

[1]contributed equally

[*]Corresponding author: dieter.braun@physik.lmu.de

We present here a novel method for measuring the melting curve of biomolecules within 50 ms. It is based on fluorescence microscopy extended by an infrared laser scanning unit for optical heating of aqueous solutions. The spatial temperature distribution obtained in solution bypasses the time limiting step of ordinary thermal denaturation experiments. The method is of great interest for high throughput screening of single nucleotides Polymorphisms (SNP) in biotechnology and for fast genotyping in medicine.

Measuring stabilities of biomolecules and especially oligonucleotides is of great importance in the field of life science and biotechnology. In most cases thermal denaturation experiments are used [1] to obtain information about sequence and structure of a molecule. The state of a molecule is recorded optically and plotted against the respective temperature, yielding a so called melting curve [2, 3].
A characteristic feature of DNA melting curves is that the transition from a double stranded to a single stranded form takes place in a narrow temperature range. An appropiate description for this transition is a two state model allowing the determination of thermodynamic properties like change in free enthalpy and entropy of reaction. However for any quantitative analysis the denaturation experiment must contain information about a wide temperature range, since to obtain the midtransition value the completely closed and open states have to be measured.

In well established fluorimeter setups heating of a tiny sample volume inside a comparably large cuvette is achieved by mechanical contact to a heat bath. Since the whole system has to be equilibrated thermally at each temperature, the whole process

is very time consuming. In currently available systems the measurement of a melting curve takes more than 30 min.
We developed an all optical method to determine thermal stabilities of biomolecules in less than 50 ms. The slow heating of well established methods is bypassed by generating the temperatures optically by an infrared (IR) Laser within a sub microliter volume. The temporal separation of temperatures is replaced by a spatial temperature distribution.

As a side effect, temperature field induce a directed motion of molecules, a process termed thermophoresis or Soret-effect. Only with the precise knowledge [6] of this effect it is possible to find optimized the experiments.
In experiments an optical signal which reports the conformation of a molecule is recorded. As a model system to test the method presented here a DNA hairpin labelled with a fluophore quencher pair was chosen. The molecule is of great biological interest [4] and exhibits strong fluorescence increase upon thermal denaturation [5].

The method described within this work generates broad spacial temperature distributions by focussing infrared laser radiation into an aqueous solution of 20 µm in height. Temperatures spanning the whole range between ambient temperature and 100°C are created almost instantaneously in a field of view of 200x200 µm imaged on a CCD device. This way a complete denaturation experiment is obtained within 50 ms in a volume of 100 nl (Fig. 1).
As a local heat source a continous wave infrared laser (IR laser) is focussed in a 20 µm thin microfluidic chamber. The temperature dependent fluorescence signal of tetramethylrhodamine (TAMRA, Invitrogen) in 1x sodium chloride-sodium citrate-buffer is measured. The decrease of fluorescence with temperature is used to determine the temperature created in the microfluidic chamber. The temperature dependence of the fluorescence is known from an independent fluorimeter measurement.

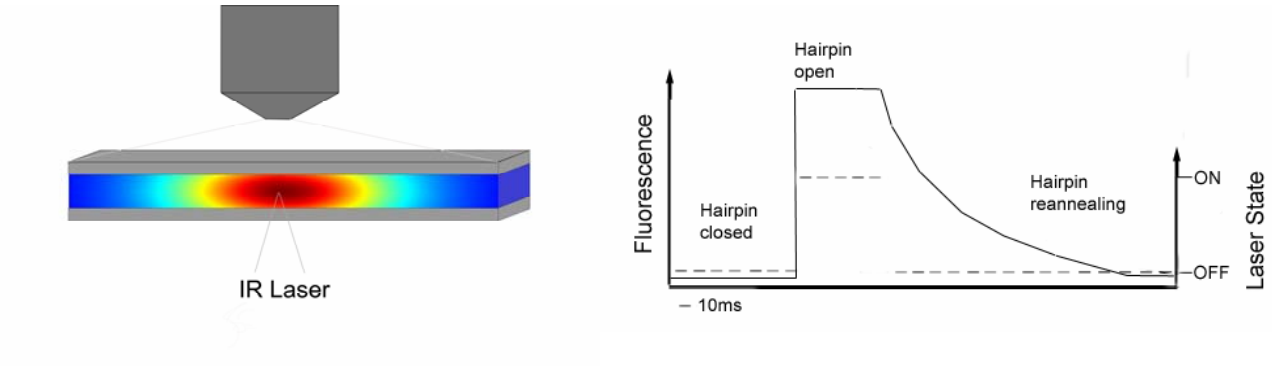

Figure 1 Experimental setup and time course of experiment. (a) Fluorecence from molecules in a 20 µm thin sheet of water is imaged on a CCD camera. An almost two dimensional temperature distribution is created within the solution by focussing an infrared laser into the solution. Structural changes induced by temperature are montiored by a fluorescence change.(b) To determine a melting curve within 50 ms a precise synchronisation between laser heating and time point of exposure is crucial. In this figure the fluorescence change of a single pixel (e.g. in the center of a heat spot) due to an increase and a following decrease in temperature is shown. The temperature increase is very fast as is the response of the hairpin. After the laser is turned off the temperature relaxes and the hairpin changes to its double stranded form. The reannealing is presented disproportionate slow in this figure.

The state of the DNA hairpin is observed by fluorecence microscopy of the fluorophore quencher pair. Strand separation is reported by an increase of the probes' fluorescence (Fig 1b. solid line).

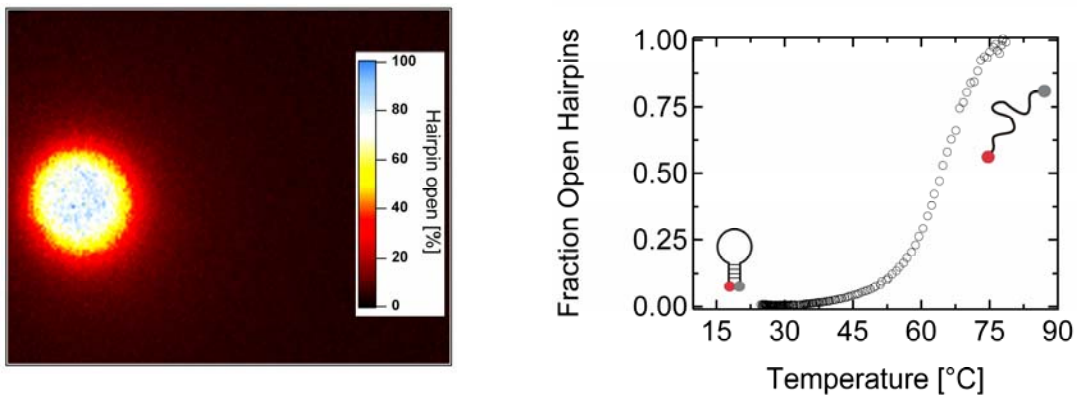

Figure 2 Melting curve from spatial temperature distribution. (a) A temperature distribution is imposed on a DNA hairpin containing solution. The fraction of open hairpin strongly increases close to the melting temperature. This leads to a distinct increase in fluorescence. (b) Since the temperature distrinution is known from an independent measurement, a melting curve is easily obtained from the radial averages.

To obtain reliable experimental data a precise triggering of events is necessary (Fig.1b). First an image of the fully closed hairpin is taken at room temperature by the CCD device and 40 ms after laser irradiation is started a second image with 10 ms

exposure time is taken to determine the distribution of open and closed states of the hairpin. Though only a trigger signal and no high frame rate is needed. The first image is taken to determine the base line and to correct for inhomogenous illumination.
Since the laser heat spot is of circular symmetry, a radial average of fluorescence intensity is used for the analysis. Figure.2b shows the baseline corrected [1] “Snapshot” melting curve and the corresponding thermal denaturation experiment measured in a standard fluorimeter. Within the error of experiment melting curve measured in 50 ms is in good agreement with the 1h control experiment.

However, the use of spatial temperature distributions poses important boundary conditions on the measurement protocol regarding the length and point in time of exposure: Each subvolume imaged on a pixel of a CCD camera should report the structural state of a molecule at the temperature assigned to that respective part of the system. Therefore the exposure time should be well below the characteristic time the molecules need to diffuse into a segment of different temperature.

$$x = \sqrt{2Dt}$$

Within the exposure time a molecule diffuses approximately 1.5 µm which is about the size of a pixel. This indicates that a molecule of the size of a DNA hairpin stays during the measurement within the spatial domain imaged on a single pixel of the camera device. However since the opening an closing rates of the molecule are within the microsecond to 1 ms range [5], the molecules immediately respond on the temperature change of their surrounding. So no severe deviation from the results of other techniques is expected.
A second concern is that the concentration of molecules within a segment has to be constant until the second image is taken. During laser irradiation concentration is changed due to a directed molecule flow induced by the temperature gradients. This effect is known as thermophoresis or Soret effect [Ref Ludwig]. Only through the knowledge of DNA thermophoresis [6] it was possible to optimize conditions were the directed movement can be neglected. The molecule drift induced by thermophoresis can be described as follows:

$$v = -D_T \nabla T \qquad (1)$$

with the thermophoretic mobility D_T. The molecule concentration in steady state for a given temperature difference is given by [3]:

$$\frac{c}{c_0} = \exp^{(-S_T \Delta T)} \tag{2}$$

with the Soret Coefficient ($S_T = \frac{D_T}{D}$). Assuming a negligible concentration gradient at the beginning of laser irridation, a typical time scale for the thermophoretic movement can be derived. This timescale is given by the thermophoretic mobility and the curvature of the temperature:

$$\tau_s \approx (D_T \Delta T)^{-1} \tag{3}$$

It turns out that the temperature gradients in z-direction, towards the glass surfaces influence the results more strongly than comparably low temperature gradients in the radial direction. Molecules are driven to the cold glass surfaces by thermophoresis, changing the distribution of states by increasing the amount of closed states. Numerical simulations of the parabolic temperature distribution (Femlab, Comsol) within the microfluidic chamber result in a curvature of 0.17 K/µm^2. For a temperature difference of 20 K in the center of the heat spot a characteristic time for short oligonucleotides to reach steady state is 1.2 s. Therefore the concentration change in the center after 40 ms is only 3%. Please note, that this is a worst case scenario, since diffusion counteracts this effect. At positions with a lower temperature difference this effect is even less pronounced.

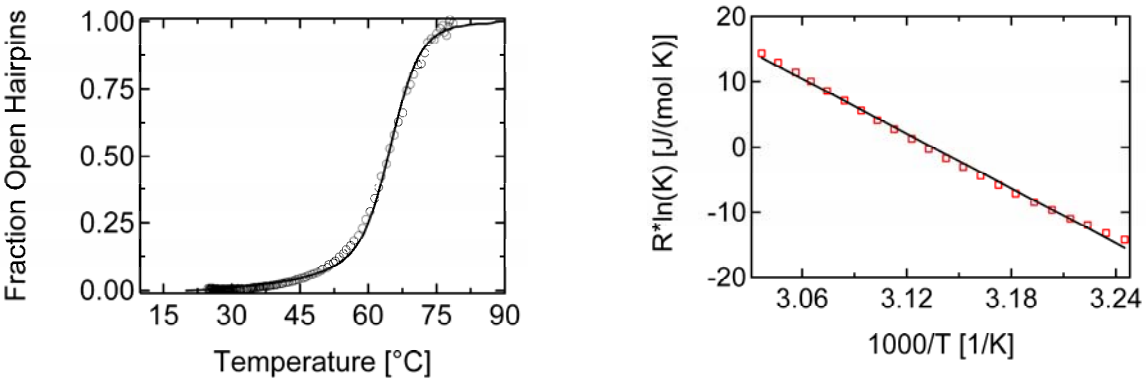

Figure 3 Melting curve compared to standard techniques. (a)The melting curve obtained in 50 ms by the "snapshot" technique coincides very well with a curve obtained in an 1h fluorimeter measurement (solid line). (b) The same is true for the quantitatification of the thermodynamic parameters.

In a setting with spatial inhomogenous temperatures, also convection has to be taken into account. According to recent simulations of our experimental setting [3,7] a convection speed of about 10 µm/s in the vicinity of the heat spot is possible. However within the measurement time of 50 ms the convection is negligible.

The rate constants for opening and closing reaction of the hairpin are well known and are within the microsecond to 1 ms range. Therefore the melting reaction can be considered as equilibrated allowing for the determination of standard enthalpy (ΔH^0) and entropy (ΔS^0) of reaction (Fig. 2b):

$$\Delta G^0 = -RT \ln(K_a) = \Delta H^0 - T\Delta S^0 \qquad (4)$$

The value of the association constant (K_a) is extracted by determining the fraction of closed to open states of the hairpin molecules. K_a can be dervied from the fraction of open states □as $K_a = \phi/(1-\phi)$. Where □ can be derived from the fluorescence signal F: $\phi = \frac{F-a}{b-a}$, where a is the fluorescence signal of the fully closed state and b the fluorescence signal of the fully open state. Plotting of $\ln(K_a)$ versus the inverse Temperature yields the value for ΔH^0 as slope and ΔS^0 as intercept:

$$R \ln(K_a) = -\Delta H^0 / T + \Delta S^0 \qquad (5)$$

To conclude, we developed a method for fast high precision melting curve analysis. Based on optical generated spatial temperature distributions the method circumvents the rate limiting steps of conventional melting curve analysis and accelerates the analysis more than 10.000 times. This is of particular interest for the area of high throughput screening in biotechnology and fast genotyping in medicine.

Beside determination of thermodynamic properties, this technique will allow the evaluation of complete kinetic schemes since melting curves for bimolecular reactions will be out of equilibrium entirely governed by the denaturation rate, while the reannelaing after denaturation (Fig. 1a) contains both, the on and off rate.

Material. The used DNA was bought from biomers.net. We used DNA of the following sequences: HpAlpha: 5'-Hex-GCAC GCA T CG CTC TT CAT TAG AAC T A TGC GTGC-Dabcyl-3'.

Infrared Temperature Control. The spatial temperature distribution was generated by aqueous absorption of a fibre coupled IR-Laser with a wavelength of 1455nm and a maximum output power of 5 W cw (Raman Fibre Laser RLD-5-1455; IPG Photonics Corporation). Water has a strong absorption at this wavelength with an attenuation length of 305µm. In the experiments we used a maximum laser power of 1 W. The laser beam was moderately focused with a lens of 8 mm focal distance. Typically the temperature at the laser spot was raised by 60K whereas the temperature stays near room-temperature at a distance of 200µm to the spot. The temperature was measured with the use of a temperature-dependend fluorescence signal of the dye tetramethylrhodamine in 1x sodium chloride-sodium citrate-buffer.

Fluorescence Detection. We performed the experiments with a fluorescence microscope (AxioTech Vario; Zeiss) featuring an oil immersion objective (40x magnification, 1.3 numerical aperture, Zeiss "FLUAR" corrected for 170µm cover slips). As light source xxx is used. We used a filter set consisting of an excitation filter (HQ545/30; AHF), beamsplitter (Q570lp; AHF) and emission filter (HQ585/40; AHF). Detection was provided with a 12-bit ccd camera (Sensicam QE; PCO AG). Both detection and illumination were conducted through the same objective. Images were taken with non saturated pixels.

References:

[1] J-L Mergny and L. Lacroix, Analysis of thermal Melting Curves, Oligonucleotides 13: 515-537 (2003)
[2] J. Marmur and P. Doty, "Determination of the base composition of deoxyribonucleic acid from its thermal denaturation temperature," J Mol Biol **5**, 109-118 (1962).
[3] Stefan Duhr and Dieter Braun, Thermophoretic Depletion Follows Boltzmann Distribution PRL 96, 168301 (2006)
[4] Zazopoulos, E., Lalli, E., Stocco, D.M. and Sassone-Corsi, P. Nature (London) 390, 311-315 (1997)
[5] Bonnet, G., Krichevsky, O. and Albert Libchaber PNAS 95, pp. 8602-8606 (1998)
[6] S. Duhr and D. Braun, “Why molecules move in a temperature gradient,” PNAS ,103, 19678-19682 (2006)
[7] Stefan Duhr, Silvia Arduini and Dieter Braun, Thermophoresis of DNA determined by microfluidic fluorescence**,** Europ. Phys. J. E 15, 277-286 (2004)

Erklärung

Hiermit versichere ich, die vorliegende Arbeit selbstständig ausgeführt und keine weiteren Hilfsmittel als die im Text und im Literaturverzeichnis aufgeführten verwendet zu haben.

München, den

_____

Stefan Duhr